Development of a 1.8mm Percutaneous Applicator with Closed Cycle Cooking for Microwave Tumour Ablation

Wieland, Ines

Award date:
2009

Awarding institution:
University of Bath

DEVELOPMENT OF A 1.8 MM PERCUTANEOUS APPLICATOR WITH CLOSED CYCLE COOLING FOR MICROWAVE TUMOUR ABLATION

Ines Wieland
A thesis submitted for the degree of
Doctor of Philosophy (PhD)
University of Bath
Department of Physics
August 2009

Signature of Author.....

Ines Wieland

Contents

List of Figures

List of Tables

Acknowledgements

Above all, I would like to thank Prof Nigel Cronin for his support, guidance and commitment throughout this work. Without his leadership and discernment this research would not have progressed to the stage it did.

I would also like to express my gratitude to Dr Peter Clegg whose support, readiness to help at all times, and enthusiasm made the work enjoyable.

Furthermore, I would like to thank many individuals of the Department of Physics at the University of Bath, Dr Benjamin Lepers, and my husband Dr Donald Hardie for their support and involvement at different times and phases during my PhD.

Finally, I am very grateful for the funding provided by Microsulis Medical Ltd., for without it this research project would not have been possible in the first place.

Abstract

This thesis reports the development of a novel microwave ablation system for tumour destruction. In addition, a computer model simulating the electromagnetic and thermal behaviour of the designed microwave applicator is presented. Concerning the microwave ablation system development, novelty is seen in four aspects of the work: firstly, in the design of a new percutaneous microwave applicator of 1.8 mm diameter; secondly, in the development of a novel closed-cycle cooling system for the microwave applicator and microwave applicator feed cable; thirdly, in the development of a novel integrated thermocouple as part of the applicator design; and lastly, in the design and development of the complete microwave ablation system consisting of applicator, feed cable and cooling system. Regarding the computer simulations of the developed microwave applicator, novelty is also seen in the definition of new non-linear temperature-dependent material properties of ex-vivo bovine liver up to 300 °C which significantly improved the accuracy of the simulation. Figure 1 displays the latest version of the applicator developed within the scope of this thesis which is currently being developed into a commercial product by Acculis Limited and Runfold Medical Limited.

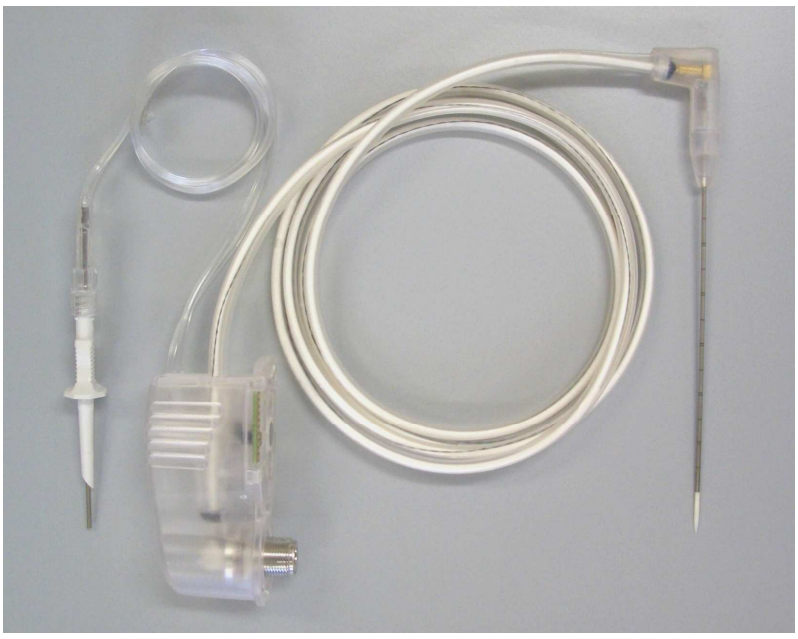

Figure 1: Latest version of 1.8 mm percutaneous microwave applicator with internal closed-cycle cooling system developed as part of a microwave ablation system within the scope of this thesis.

Nomenclature

List of abbreviations:

MWA Microwave ablation

CT Computed tomography

EM Electromagnetic

HCC Hepatocellular carcinoma

RFA Radiofrequency ablation

PEI Percutaneous ethanol injection

PAAI Percutaneous acetic acid injection

HIFU High-intensity focused ultrasound

ILA Interstitial laser ablation

MRI Magnetic resonance imaging

SAR Specific absorption rate (W/kg)

PDE Partial differential equation

FEM Finite element method

MDTG Medical Device Technology Group (University of Bath)

FEA Finite element analysis

ID Inner diameter

OD Outer diameter

TC Thermocouple

LCS Local control station

TM Transverse magnetic (wave)

BHE Bioheat equation

TEM Transverse electromagnetic

PEC Perfect electric conductor

Chapter 1

Introduction

1.1 Thesis Subject and Outline

The subject of this thesis was the development of a novel thin microwave ablation system for the treatment of cancerous tissues. Since several microwave ablation systems already existed at the onset of this research project, the objective was narrowed to the thesis that it was regarded possible to design a percutaneous applicator with a diameter below 2 mm for high power microwave ablation by design and incorporation of an effective cooling system. In addition, a computer simulation of the device was to be generated to model the electromagnetic and thermal behaviour of the applicator during operation.

1.2 Introduction to Microwave Tumour Ablation (MWA)

Microwaves are electromagnetic waves with a frequency ranging from 300 MHz to 300 GHz; corresponding wavelengths at these frequencies are 1 m and 1 mm in vacuum [1]. In the electromagnetic spectrum, microwave radiation lies between the higher frequency infra-red radiation and lower frequency radio waves.

In medicine, the word ablation refers to the removal or destruction of a body part or tissue or its function. Ablation may be performed using surgery, hormones, drugs or heat. In the case of microwave ablation, destruction is achieved by the interaction of microwaves with biological tissue which generates heat. Electromagnetic radiation at microwave frequencies causes polar molecules such as water to rotate, as the dipoles try to constantly realign themselves to the alternating electric field. Higher levels of molecular rotation and vibration mean increasing kinetic energy of the tissue which is directly related to the macroscopic tissue temperature. Once tissue is heated above the cytotoxic threshold, cells begin to die. The destruction of tissue in this way is irreversible.

Microwave energy is delivered to the target site inside the human body via specifically designed applicators. The applicator tip is hereby inserted into the tumour mass and the treatment initiated. During the operation of the applicator, microwave energy is radiated into the tissue surrounding the tip causing the desired heating effect. Depending on the tumour size to be treated, a microwave power between 30 W and 100 W is

applied for a length of time between a few minutes and a maximum of about 10 min.

There are several types of microwave applicator designs that are commonly used for MWA; these are monopole antennas [2, 3, 4], dipole antennas [5], slot antennas [6], tri-axial antennas [7], cap-choke antennas [8], and antenna arrays [6, 9, 10, 11]. Previous applicators designed at the University of Bath were of type monopole and dipole; the development described in this thesis continued one of the previous dipole designs (2.4 mm percutaneous applicator) and hence retained the dipole type antenna.

A typical microwave ablation system consists of three major parts: a microwave source generating the electromagnetic radiation at a set frequency, a hand-held applicator emitting the microwave energy into tissue, and transmission lines, mainly coaxial cables, delivering energy from source to applicator. Figure 1.1 illustrates the components of a MW system. Microwave applicators usually operate at frequencies between 0.915 GHz to 10 GHz with 2.45 GHz being the most commonly used one. The reason for that is that 2.45 GHz is an allocated medical frequency. Furthermore, commercially available microwave ovens operate at 2.45 GHz resulting in readily available and inexpensive equipment.

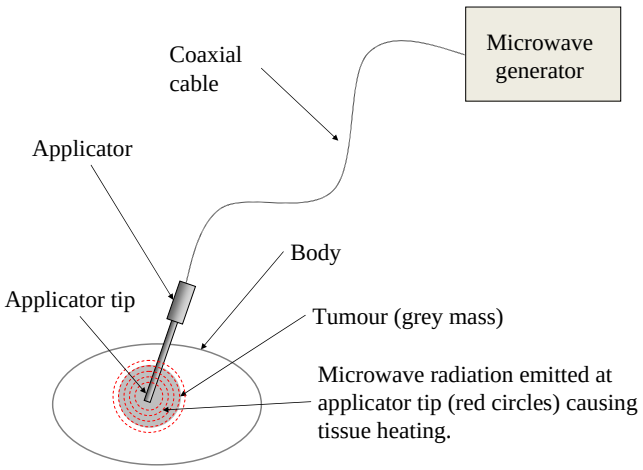

Figure 1.1: Components of microwave ablation system including microwave generator, coaxial cable, and applicator.

Over the past few years, MWA has become increasingly popular for the treatment of liver tumours. It is still considered a relatively new technique and published data regarding its clinical effectiveness in terms of complications, local tumour control, and patient survival is rare. Also, much of the current literature is dominated by early Asian studies conducted with old technology. However, MWA is on the increase due to several theoretical advantages over other local ablative techniques including [12, 13]:

- Higher intra-tumoral temperatures
- Deeper tissue heating [14, 15], leading to
- Larger ablation volumes
- Less affected by heat sink effect of large vessels
- Faster ablations

- Repeatable ablation shapes
- Possible use of multiple simultaneous applicators

The primary area of application for the microwave applicator developed in the context of this thesis was the treatment of human liver tumours. Figure 1.2 shows pre and post ablation CT scans [16] of a typical treatment in liver using MWA. The pre ablation scan revealed a 6 cm metastasis located in the lower left part of the liver; the post ablation CT scan displays the ablated volume. A MWA procedure in liver is shown in figure 1.3 [17], together with an image of an ablated liver tumour that was resected post ablation [16].

(a) Pre CT scan showing liver tumour.

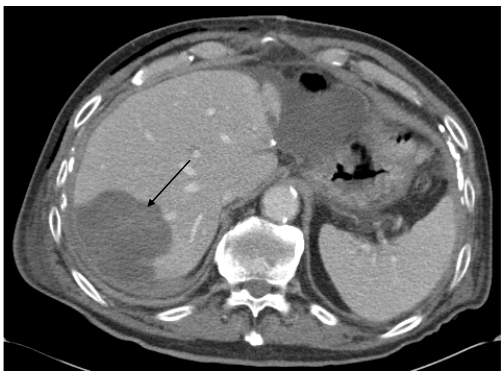

(b) Post CT scan showing microwave ablation of tumour mass.

Figure 1.2: Pre ablation scan (figure 1.2(a)) reveals 6 cm liver metastasis. Post ablation CT scan (figure 1.2(b)) displays resulting ablation (100 W; 8 min).

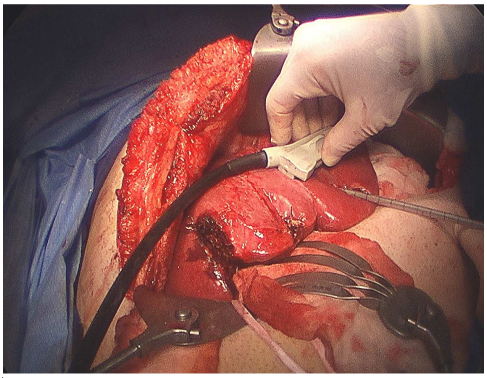

(a) Typical microwave ablation procedure in liver. Microwave applicator inserted into liver from the right; ultrasound probe for applicator guidance seen on liver surface.

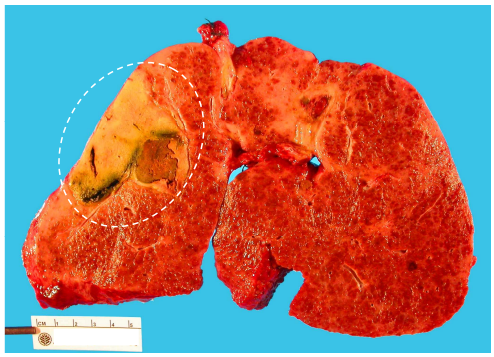

(b) Resected liver showing ablated tumour (dashed line).

Figure 1.3: Microwave ablation procedure in human.

Good results in the treatment of hepatic tumours were reported with a device developed by the group over the past decade, however owing to the relatively large dimension of the applicator (5.6 mm), the development of thinner devices had been pursued over the last few years which led to the design of a 2.4 mm diameter applicator for less invasive, or minimally invasive, treatments. Minimally invasive treatments are often associated

with lower complication rates, faster treatment times, faster patient recovery and shorter hospital stays [18, 19, 20].

In order to be able to place the work presented in this thesis into context it was seen appropriate to give an overview of the medical conditions targeted and existing treatment options.

1.3 Introduction to Liver Tumours and Treatment Options

Primary cancer of the liver, called hepatocellular carcinoma (HCC), is the fifth most common cancer in the world [21] with an estimated number of 564 000 new cases in the year 2000 [22]. It occurs predominantly in Asia and Africa, however its incidence in the Western world is rising [23, 24] due to the increasing number of cases of Hepatitis C [25]. Hepatitis B virus, hepatitis C virus, and alcohol related cirrhosis are the primary causes of the development of HCC [26] and account for up to 80 % of all new cases [22].

In addition, colorectal carcinoma (cancer of the colon or rectum) is a worldwide problem with an annual incidence of approximately 1 million cases and an annual mortality of over 500 000 [27]. Furthermore, these numbers are expected to rise over the coming decades due to an ageing and increasing population in both developed and developing countries. Since colorectal carcinoma is most common in parts of Europe, North America, Australia and New Zealand, it is considered a disease associated to western lifestyle [28, 29, 30]. This is significant for the topic of liver cancer as approximately 25 % of those patients also show metastatic spread to the liver, and a further 25% will develop metastases at a later date. In the latter case, the progressive involvement of the liver may be the major factor of survival [21].

The prognosis of HCC is generally poor. Data regarding the overall survival of untreated HCC range from 0 % for the 5-year survival rate to 30 % for the 3-year survival rate [31, 32]. In the treatment of HCC, surgery still presents the best curative option. Two surgical procedures are available; partial liver resection and liver transplantation. Liver transplantation is a treatment with good survival rates, however the restricted availability of donor organs must be kept in mind as it limits the possible number of liver transplants [33]. Surgical resection can result in a significant benefit in terms of long-term survival; 5-year survivals of 40 % and 50 % were reported for colorectal hepatic metastases [34] and HCC [35], respectively. However, only an approximate 20 % of patients with HCC or liver metastases are candidates for surgical resection due to a number of reasons [36, 37]:

- Occurrence of multiple liver tumours
- Extrahepatic disease or advanced age renders patient too ill for major surgery
- Remaining liver volume inadequate to sustain liver function
- Inability to obtain an optimal tumour-free margin
- Tumour involves or is in proximity to major vessels

In light of these limitations for surgical resection and the previously mentioned shortage of donor organs, alternative treatment options have been developed and assessed over the years including systemic and regional chemotherapy, chemo-embolisation, im-

munotherapy, and ablative techniques. Significant disadvantages have been found for chemotherapy, immunotherapy and chemo-embolisation in that long-term patient survival did not increase due to poor complete tumour responses [21]. However, chemotherapy and chemo-embolisation are commonly used to shrink tumours for short-term benefits or prior to local ablative treatments [26]. Local ablative techniques can be performed at laparotomy where the abdomen is opened during surgery, during laparoscopy (keyhole surgery), or percutaneously. In percutaneous treatments, devices are inserted minimally-invasive through a small puncture in the skin. Local ablative therapy has the advantage of preserving uninvolved liver tissue surrounding the tumour mass. Furthermore, it can be used to control tumour sizes in patients awaiting liver transplantation and so help sustain the patient's life until a donor organ becomes available. However, tumours located too close to vital structures, for instance bile ducts, major blood vessels, stomach, or gut, are usually excluded from local ablative treatment [38]. Figure 1.4 displays the complex algorithm for decision making in the management of patients with hepatocellular carcinoma. The figure highlights surgical resection and transplantation as first choices where possible, and shows when and under which circumstances local ablative therapies are applicable.

1.4 Overview of Local Ablative Techniques

1.4.1 Introduction

There are several local ablative techniques in use for the treatment of HCC or hepatic metastases. Depending on their mechanism of cell destruction these treatments can be divided into six groups:

1. Injection of cyto-toxic (cell-killing) agents:
    - Ethanol injection
    - Acetic acid injection
2. Generation of intense cold leading to hypothermic cell death (cell freezing):
    - Cryotherapy
3. Generation of heat leading to hyperthermic cell death:
    - High-intensity focussed ultrasound
    - Radiofrequency ablation
    - Interstitial laser photocoagulation
    - Microwave coagulation
    - Hot saline injection
4. Mechanical shock; cavitation
    - High-intensity focussed ultrasound. Cavitation describes the formation and instantaneous collapse of innumerable tiny voids or cavities within a liquid subjected to rapid and intense pressure changes.
5. Generation of cyto-toxic intermediaries:
    - Electrolysis
6. Permanent permeabilisation of cell membranes:

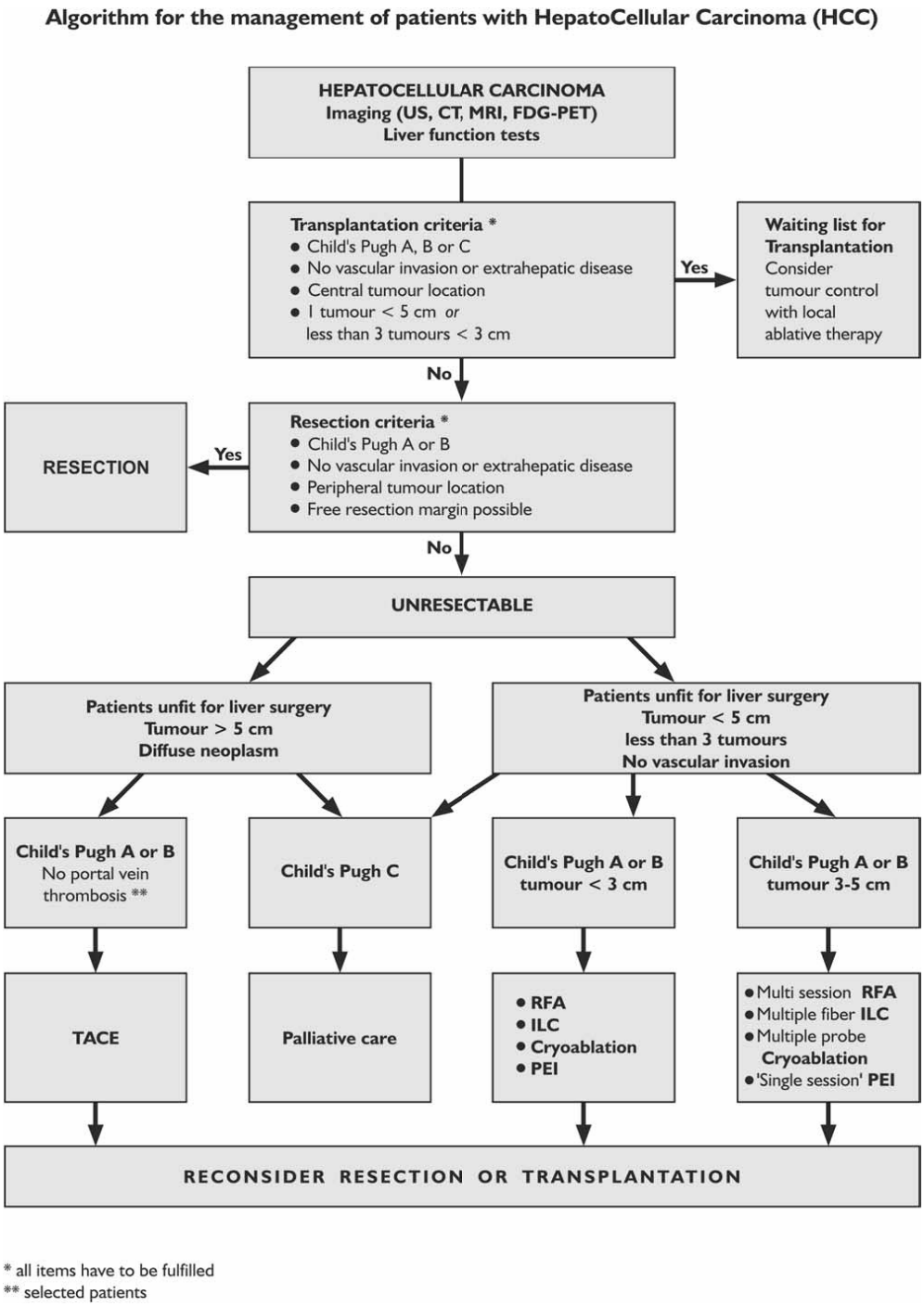

Figure 1.4: Algorithm for decision-making in the management of patients with HCC. Ablative techniques include radiofrequency ablation (RFA), interstitial laser coagulation (ILC), cryoablation, and percutaneous ethanol injection (PEI) [26].

- Electroporation

In general, the desired outcomes and qualities of all ablative techniques are alike. In order to be of clinical use they must offer as many of the following characteristics as possible:

- Predictable cell-killing
- Repeatable zones of cell-killing
- Dose-response behaviour, meaning the application of a greater amount of the cause (heat, cold, fluid) changes the effect, that is, results in a larger ablation zone; and vice versa.
- Fast ablation procedure
- Localised ablation zone
- Real-time monitoring of ablation growth
- Percutaneous or laparoscopic delivery
- Little or no systemic (whole-body) response

Below, each local ablative technique is described in more detail regarding its cyto-toxic mechanism, advantages, limitations, and current state of clinical usage where possible.

1.4.2 Percutaneous Ethanol Injection (PEI)

PEI was first recommended for the treatment of HCC by Suguira and colleagues in 1983 [39]. In PEI, ethanol of 95 % to 99.5 % is slowly injected into the entire tumour mass. Absolute alcohol has the ability to diffuse into cells where it subsequently induces non-selective protein denaturation (proteins loose their structure) and cellular dehydration. Both events lead to localised cell death called coagulative necrosis. Advantages of PEI include efficiency in the treatment of small HCC ($\leq$ 3 cm), simplicity of technique, cost effectiveness, and repeatability. Furthermore, it can be used for the ablation of tumours located in close proximity to vital structures where thermal ablation can be problematic. Disadvantages of PEI include the small tumour size of $\leq$ 3 cm that can be routinely treated, as well as the unpredictability associated with the distribution of ethanol. In the latter case, viable tumour cells may remain after PEI in areas isolated by a capsule or intra-tumoural septa. Such incomplete tumour necrosis is the main reason for the relatively high rate of local tumour recurrence for PEI [26]. Yet, no randomised controlled trials comparing the survival rates after PEI and partial liver resection have been conducted to date.

1.4.3 Percutaneous Acetic Acid Injection (PAAI)

The method of cell destruction in PAAI, where 50 % acetic acid is injected into the tumour, is identical to that of PEI. A proposed advantage over PEI is a greater necrotising ability, hence reducing the volume of liquid necessary. First positive results have been published [40], but serious complications such as hepatic failure, which describes the inability of the liver to perform its normal functions as part of normal physiology, have also been noted [41]. More data is hence needed before conclusions regarding efficacy and safety can be drawn.

1.4.4 Cryotherapy

Cryoablation induces cell death by repeated freeze-thaw cycles. Cryoablation devices use circulating liquid nitrogen to cool down the applicator tip to temperatures between -20 °C and -60 °C. During freezing, intra- and extracellular ice formation takes place causing injury of intracellular structures, membrane rupture, osmotic dehydration, and anoxia (lack of oxygen), all of which lead to cell death [42, 43]. Cryoablation has been a popular technique for some time. However, a relatively high complication rate of approximately 20 % as well as a high local tumour recurrence due to incomplete tumour destruction have been associated with cryoablation in recent years. A specific complication, called 'cryoshock', occurred in 1 % of the treatments and was responsible for 18 % of deaths following cryotherapy [44]. It hence is a rare but severe complication whereby multiple organ failure, severe coagulopathy (blood does not clot normally), and disseminated intravascular coagulation occurs. All those issues have led to other local ablative techniques being favoured over cryoablation in recent years, especially RFA [26].

1.4.5 High-Intensity Focused Ultrasound (HIFU)

HIFU is an extracorporeal method of tissue heating whereby sound waves of high amplitudes are focused on a tumour target inside the body. The two main modes of cell destruction are coagulative necrosis due to heat and cavitation processes [45]. The main advantage of HIFU is the non-invasiveness of the technique, its safety and sharply demarcated ablation boundaries. Limitations include local tumour recurrence as well as skin burns and long ablation times (2 h for a 2-3 cm tumour) and small ablation sizes [46, 47]. Furthermore, ultra-sound scanning is usually required during treatment to monitor tissue response and ablation growth. A recent study conducted in porcine models with an improved HIFU system achieved average ablation diameters of 2 cm in 40 s [48]. In addition, the study claimed to produce larger lesions up to 6 cm by placing ablation next to ablation without any major complication. However, data is still limited regarding HIFU ablations in humans.

1.4.6 Hot Saline Injection

The injection of hot saline into a tumour causes coagulation necrosis due to heat. The advantage of saline over PEI or PAAI is seen in the more physiological nature of saline which renders larger application volume for the treatment of large tumours up to 7 cm possible. However, the number of cases using hot saline injection is still too small for drawing definite conclusions.

1.4.7 Radiofrequency Ablation (RFA)

Radiofrequency ablation uses alternating current in the frequency range of approximately 100 kHz to 500 kHz to cause Joule heating. During RF ablation, agitation of ions in the electric field between two electrodes leads to intense heating at locations

of highest field densities. Highest field densities are found at the surface of the RF applicator electrode where temperatures hence rise to approximately 100 °C leading to localised cell death. Further radial ablation growth is achieved by continued voltage application and thermal conduction of heat from the applicator surface outwards. Typical treatment times in RFA are 10 min to 20 min. Initially, monopolar devices required a grounding electrode (pad) placed on the patient's skin to close the electric circuit. Recently, improvements in device design led to bipolar devices able to create larger and more repeatable ablation zones. Modern RFA system designs include more powerful generators, pulsed application, cooled-tip electrodes, multiple needle application, expandable array systems, clustered electrodes or saline perfused RFA needles. Typical sizes of single ablations performed with modern devices are approximately 30 mm x 50 mm achieved within 10 min and 15 min [49], although 5 cm lesion were claimed to be achieved by high-power umbrella or multiple needle devices. Several limitations concerning RFA exist [38, 21, 50] including:

- Efficiency of RFA depended on tissue conductivity.
- Conductivity values vary for different soft tissue organs.
- Often, multiple needle ablation required for complete ablation of larger tumours ($\geq$ 3 cm).
- RF heating diminished by tissue charring occurring at the electrode once temperatures exceed 100 °C.
- Long ablation times between 10 min to 20 min.
- Unreliable ablation geometry due to tine deployment and unpredictable current flow path.
- Ineffective when placed close to heat sinks, for instance major blood vessels.
- Ill-defined margin precludes distinction between ablated tumour and residual disease.
- Possibility of skin burns in monopolar setups.

The main disadvantage of RFA is a markedly high local tumour recurrence rate of 37 % [51]. Reasons for tumour recurrence is incomplete ablation in the first place which could be caused by several of the listed RF limitations above or a misplaced RF probe.

1.4.8 Interstitial Laser Ablation (ILA)

In ILA, light from a Nd:YAG laser of wavelength 1064 nm is guided to the centre of the tumour using optical fibres. The absorption of photons creates heat which leads to coagulative necrosis of the tumour tissue. Photons are either directly absorbed or after scattering processes. The latter creates a deeper penetration and hence greater energy distribution [52]. The advantage of ILA is the small size of the fibres of below 1 mm, the option to use multiple fibres, and the possibility to monitor real-time ablation size with magnetic resonance imaging (MRI). Good results have been obtained especially for smaller tumours (2 cm). An ablation size of up to 1.5 cm in diameter can generally be achieved using a single fibre, whereas larger lesions require the use of multiple fibres. The number and size of lesions that can be treated with ILA are similar to those resulting from PEI and RFA [38]. Hence, ILA is generally limited to the treatment of small tumours ($\leq$ 3 cm).

1.4.9 Electrolysis

Electrolysis is a relatively new treatment that uses direct current (DC) to produce tissue destruction. Direct currents (80 mA to 100 mA) are passed between two electrodes inserted into the liver tissue producing a pH gradient and cyto-toxic chemicals, hydrogen chloride (HCL) and chlorine gas (Cl_2), leading to tissue necrosis. Initial studies of electrolysis in animal models and humans have shown that it is a safe, predictable and effective process for destroying normal and tumour-bearing liver in a linear, dose-dependent manner. However, a disadvantage of electrolysis represents the long ablation time; to ablate an 8 cm tumour a three-hour treatment was needed [21].

1.4.10 Electroporation

The first successful use of irreversible electroporation for tumour ablation in animals was reported by Al-Sakere et al in 2007 [53]. Electroporation is a technique in which short electrical impulses are sent through a target tissue causing permanent damage to cells by causing irreversible permeabilisation (cell membranes are made permeable). Irreversible electroporation is described as a non-thermal technique since analyses showed that time delays between different pulse trains allowed for significant heat dissipation through the electrodes. Best results were achieved using 80 pulses of 100 ms at 0.3 Hz with an electrical field magnitude of 250 kV/m [53]. The main limitation of electroporation, apart from its early stage development, is seen in the required experimental setup and patient safety. In order to ensure a homogeneous electrical field throughout the tumour, access to the tumour mass must be provided, parallel plates placed around the tumour tissue, and direct contact with the tissue retained throughout the experiment. In terms of patient safety, accurate electrode placement is mandatory to prevent serious damage to neighbouring tissues and organs.

1.4.11 Discussion

Partial surgical liver resection and liver transplantation remain the 'gold standard' in the treatment of HCC and hepatic metastases. For patients that are considered unfit for resection and transplantation, local ablative techniques have been on the increase. PEI was considered one of the major local ablative technique for the treatment of small HCC a few years ago [26]. In recent years however, RFA, ILC, and MWA have evolved rapidly and are now the most popular thermal ablative techniques [26] with the exception of tumours located close to vital structures where PEI is still used. Similarly, cryoablation had been popular but has come out of fashion due to a relatively high mortality rate compared to other local ablative techniques. Currently, the most commonly used local ablative technique is RFA.

1.4.12 Conclusion

So far, long-term clinical results are scarce for all of the local ablative techniques discussed. Due to the popularity of RFA and promising results of the emerging MWA

technique, comparative studies are now needed to assess and compare the risks and benefits of RFA and MWA, or even MWA and resection. This is the purpose of large-scale randomised clinical trials, where data regarding type and number of lesions, mean survival, long-term patient survival ($\geq$ 5 years), complication rates during procedure, completeness of tumour ablation, and local tumour recurrence are recorded. A major factor in such clinical trials is patient selection, since healthier patients with a single tumour often qualify for surgical resection with better survival rates whereas patients with multiple tumours are considered 'unresectable' and so become candidates for ablation treatments. However, the choice of treatment offered to a patient must remain ethical, in that the technique with the highest survival rate for a particular patient is chosen. It can be seen that the assessment of clinical treatment techniques often presents a complex, risky, and long-term task.

Chapter 2

Theory

2.1 Introduction

This chapter presents some basic theory concerning microwave ablation. The background to microwave radiation and its propagation in various media is given in the first section 2.2 on electromagnetic theory. In the second part, section 2.3, the so-called bioheat equation, which is often used to predict heat transfer in biological tissue, is introduced and derived.

2.2 Electromagnetic Theory

2.2.1 Maxwell's Equations

The general form of Maxwell's equations in differential format are given by the following equations [1, 54]:

$$\nabla \cdot \vec{D} = \rho \tag{2.1}$$

$$\nabla \cdot \vec{B} = 0 \tag{2.2}$$

$$\nabla \times \vec{E} = -\frac{\partial \vec{B}}{\partial t} \tag{2.3}$$

$$\nabla \times \vec{H} = \vec{J} + \frac{\partial \vec{D}}{\partial t} \tag{2.4}$$

Here, $\vec{D}$ is the electric flux density, also known as displacement current density, in $\mathrm{C/m^2}$, ρ the charge density in $\mathrm{C/m^3}$, $\vec{B}$ the magnetic flux density in T, $\vec{E}$ the electric field intensity in V/m, $\vec{H}$ the magnetic field intensity in A/m, and $\vec{J}$ the conduction current density in $\mathrm{A/m^2}$. Solutions of Maxwell's equations describe the behaviour of electric and magnetic fields as well as their interaction with matter. Equation 2.1, also known as Gauss' law, describes how electrical charges produce electrical fields; equation 2.2 states the absence of magnetic monopoles. The Maxwell-Faraday equation 2.3 describes how changing magnetic fields produce electric fields. Lastly, the Ampere-Maxwell law, given in equation 2.4, expresses how currents and changing electric fields produce magnetic fields.

Furthermore, the continuity equation 2.5 states that the divergence of the current density is equal to the negative rate of change of the charge density:

$$\nabla \cdot \vec{J} = -\frac{\partial \rho}{\partial t} \tag{2.5}$$

2.2.2 The Constitutive Equations

The constitutive equations define the relationship between the field quantities in a medium. In a uniform medium where ε and μ are scalars these equations can be written as:

$$\vec{J} = \sigma \cdot \vec{E} \tag{2.6}$$

$$\vec{D} = \varepsilon \cdot \vec{E} \tag{2.7}$$

$$\vec{B} = \mu \cdot \vec{H} \tag{2.8}$$

where ε is the electric permittivity of the medium in F/m, $\varepsilon_0 = 8.854{\cdot}10^{-12}$ the permittivity of free space in F/m, σ the conductivity in S/m, μ the magnetic permeability of the medium in H/m, and $\mu_0 = 4\pi{\cdot}10^{-7}$ the permeability of free space in H/m. In this document, the conductivity σ denotes the DC conductivity of a material due to the movement of free charge and measurable with a multimeter. For reasons of clarity, losses due to dipole oscillations at microwave frequencies are treated using a complex permittivity rather than a high-frequency conductivity in order to avoid confusion of these two distinctly different loss mechanisms.

2.2.3 The Wave Equation

The propagation of an electromagnetic field in a uniform conducting but source-free medium is governed by the so-called wave equation. The wave equation is derived by substituting the curl of equation 2.3 into equation 2.4 using the vector identity $\nabla \times \nabla \times \vec{E} = \nabla(\nabla \vec{E}) - \nabla^2 \vec{E}$ and assuming that there are no free electric charges in the region of interest, giving:

$$\nabla^2 \vec{E} = \mu\sigma \frac{\partial \vec{E}}{\partial t} + \mu\varepsilon \frac{\partial^2 \vec{E}}{\partial t^2} \tag{2.9}$$

The presence of the first-order derivative indicates that the field decays as it propagates through a conducting medium ($\sigma \neq 0$), that is the wave loses energy. However, this is not the only manner in which an electromagnetic wave can decay as it propagates through a medium. How an electromagnetic wave can lose energy despite the fact that $\sigma \approx 0$ will be discussed in the following sections.

2.2.4 Propagation of Electromagnetic Waves in Biological Tissues

Introduction

Most organic materials as well as human soft tissues contain approximately 70 % water [55]. In addition, ionic compounds such as sodium chloride (Na^+, Cl^-) are found in

the extracellular fluid. Electromagnetic radiation at microwave frequencies interacts with polar molecules, mainly water, and ionic molecules. The water molecule features a permanent electric dipole due to the positively charged hydrogen atoms (H^+) and the negatively charged oxygen (O^-). In an electric field, the dipole molecule aligns in the direction of the applied field. As the electric field changes direction due to the high frequency, water molecules constantly re-align themselves and start oscillating. These oscillations are counteracted by hydrogen bonds which form between neighbouring water molecules; energy is hence transferred from the electromagnetic wave to tissue in the form of heat. This loss mechanism of dipolar coupling is dominant for higher frequencies, whereas conduction losses due to ionic transport are responsible for losses at lower frequencies, for instance at frequencies utilised for RF heating.

The interaction of an electromagnetic wave with biological tissue can be mathematically described by the solution of Maxwell's equations of a plane wave propagating through the material. From an electromagnetic point of view, biological tissue is a lossy dielectric material and can be fully characterised by its electrical material properties of conductivity, permittivity, and permeability. The materials considered in the context of this work have magnetic permeabilities equal to one; the magnetic properties are hence not studied further. Conductivity in the context of this work is defined as the DC conductivity; permittivity however, is a frequency-dependent material property which is important to the understanding of the heating mechanisms at different frequencies.

Complex Permittivity

The permittivity ε of a medium can be expressed as the product of relative permittivity ε_r, also known as dielectric constant, and the permittivity of free space ε_0:

$$\varepsilon = \varepsilon_r \cdot \varepsilon_0 \tag{2.10}$$

In the case when permittivity is a function of frequency ω, a frequency-dependent relative complex permittivity $\varepsilon_r(\omega)$ results which can be written as a function of its real and imaginary parts $\varepsilon'_r(\omega)$ and $\varepsilon''_r(\omega)$, also referred to as dielectric constant and dielectric loss factor:

$$\varepsilon_r(\omega) = \varepsilon'_r(\omega) - i \cdot \varepsilon''_r(\omega) \tag{2.11}$$

or simply:

$$\varepsilon_r = \varepsilon'_r - i \cdot \varepsilon''_r \tag{2.12}$$

The real part ε'_r of the complex permittivity is a measure of the material's ability to store electrical energy, the imaginary part ε''_r quantifies the efficiency with which electromagnetic energy is converted to heat due to loss mechanisms.

Using Maxwell's equation 2.4 together with the constitutive equation 2.6 and the equation for the complex permittivity 2.12 and assuming the electric field is a sinusoidal

function of time, $E = E_0 \exp(i(\omega t - kx))$, gives:

$$\begin{aligned} \nabla \times \vec{H} &= \vec{J} + \frac{\partial \vec{D}}{\partial t} \\ &= \sigma \vec{E} + \varepsilon \frac{\partial \vec{E}}{\partial t} \\ &= \sigma \vec{E} + \varepsilon' \frac{\partial \vec{E}}{\partial t} - i\varepsilon'' \frac{\partial \vec{E}}{\partial t} \\ &= \sigma \vec{E} + i\omega\varepsilon' \vec{E} + \omega\varepsilon'' \vec{E} \\ &= i\omega\varepsilon' \vec{E} + (\sigma + \omega\varepsilon'') \vec{E} \end{aligned} \tag{2.13}$$

Thus, the imaginary part of the complex permittivity or loss factor ε'' leads to an additional term in phase with the electric field besides the DC conductivity σ. The total loss hence comprises $\sigma + \omega\varepsilon''$. The power dissipated per unit volume is given by $(\sigma + \omega\varepsilon'')E^2$.

However, when studying dielectric materials, the conductivity value is usually negligible. The loss is then given by $\omega\varepsilon''$ whose value is often determined experimentally. It is this term $\omega\varepsilon'' E^2$ that is the basis for microwave heating of dielectric materials. Dielectric materials are usually characterised by their respective values of dielectric constant ε'_r and loss tangent $tan\delta$. The loss tangent $tan\delta$ is defined as the ratio of imaginary to real part of the complex permittivity:

$$tan\delta = \frac{\varepsilon''}{\varepsilon'} \tag{2.14}$$

The loss tangent can be related to the total conductivity σ_t, defined as $\sigma + \omega\varepsilon''$, via:

$$tan\delta = \frac{\varepsilon''}{\varepsilon'} = \frac{\sigma_t}{\omega\varepsilon'} \tag{2.15}$$

Wave Propagation in Media

In one dimension, the general wave equation can be written as (see equation 2.9):

$$\frac{\partial^2 \vec{E}}{\partial z^2} - \mu\sigma \frac{\partial \vec{E}}{\partial t} - \mu\varepsilon \frac{\partial^2 \vec{E}}{\partial t^2} = 0 \tag{2.16}$$

A general solution to a differential equation of this form is given by the equation of a linearly polarised plane wave, for instance in x-direction:

$$E_x(z) = E_0 \exp(i(\omega t - kz)) \tag{2.17}$$

which is equivalent to:

$$E_x(z) = E_0(cos(\omega t - kz) + i \sin(\omega t - kz)) \tag{2.18}$$

where E_0 is the amplitude of the wave, ω the angular frequency, and k the wavenumber defined as $2\pi/\lambda$. Differentiation of equation 2.17 and subsequent substitution into wave

equation 2.16 yields:

$$k^2 = \varepsilon\mu\omega^2 - i\mu\sigma\omega = \omega^2\mu\varepsilon[1 - i(\sigma/\omega\varepsilon)] \tag{2.19}$$

Depending on the type of media – free space, lossless dielectrics, lossy dielectrics or good conductors – different results for k are obtained.

In free-space, the medium is non-conducting; hence $\sigma = 0$. Equation 2.19 therefore becomes:

$$k^2 = \varepsilon\mu\omega^2 \tag{2.20}$$

The phase velocity v_p of a wave is defined as ω/k. The resulting speed of the wave in free space is hence the speed of light c:

$$\frac{\omega}{k} = \frac{1}{\sqrt{\varepsilon\mu}} = \frac{1}{\sqrt{\varepsilon_0\mu_0}} \equiv c \tag{2.21}$$

Since k is purely real, the wave does not decay over time (see equation 2.18) but propagates lossless through free space.

In lossless dielectrics however, the permittivity $\varepsilon = \varepsilon_0\varepsilon_r$ of the medium is greater than unity. This leads, for $\sigma = 0$, to a phase velocity of:

$$\frac{\omega}{k} = \frac{1}{\sqrt{\varepsilon\mu}} = \frac{1}{\sqrt{\varepsilon_r}} \cdot \frac{1}{\sqrt{\varepsilon_0\mu_0}} = \frac{1}{\sqrt{\varepsilon_r}} \cdot c \tag{2.22}$$

The speed of the wave is therefore reduced by a factor of $1/\sqrt{\varepsilon_r}$ compared to c. Since the frequency of the wave remains constant, the wavelength experiences the same reduction of factor $1/\sqrt{\varepsilon_r}$.

In the case of a lossy medium with complex permittivity ε and finite conductivity σ, the wavenumber k becomes complex:

$$\begin{aligned} k^2 &= \varepsilon\mu\omega^2 - i\mu\sigma\omega \\ &= (\varepsilon' - i\varepsilon'')\mu\omega^2 - i\mu\sigma\omega \\ &= \varepsilon'\mu\omega^2 - i\mu\omega(\omega\varepsilon'' + \sigma) \\ &= \omega^2\mu\varepsilon'\left(1 - i\left(\frac{\omega\varepsilon'' + \sigma}{\omega\varepsilon'}\right)\right) \end{aligned} \tag{2.23}$$

The complex propagation constant for the medium γ is defined as ik and is split in real and imaginary parts according to:

$$\gamma = \alpha + i\beta = i\omega\sqrt{\mu\varepsilon'}\sqrt{1 - i\left(\frac{\omega\varepsilon'' + \sigma}{\omega\varepsilon'}\right)} \tag{2.24}$$

where the attenuation constant α (1/m) is given by:

$$\alpha = \frac{\omega\sqrt{\mu_0\varepsilon'}}{\sqrt{2}}\sqrt{\sqrt{1 + \left(\frac{\sigma + \omega\varepsilon''}{\omega\varepsilon'}\right)^2} - 1} \tag{2.25}$$

and the phase constant β (radian/m) by:

$$\beta = \frac{\omega\sqrt{\mu_0\varepsilon'}}{\sqrt{2}}\sqrt{\sqrt{1+\left(\frac{\sigma+\omega\varepsilon''}{\omega\varepsilon'}\right)^2}+1} \tag{2.26}$$

Skin depth δ is defined as the depth of penetration at which the electromagnetic field has been attenuated to 1/e ($\approx$ 37 %) of its original value. It is given by:

$$\delta = \frac{1}{\alpha} \tag{2.27}$$

Assuming again an electric field only in x direction, solutions to the wave equation (equation 2.16) are:

$$\begin{aligned} E_x(z) &= E_0\exp(i(\omega t - kz)) \\ &= E_0\exp(i(\omega t - (\gamma/i)z)) \\ &= E_0\exp(i\omega t)\exp(-\alpha z)\exp(-i\beta z) \end{aligned} \tag{2.28}$$

which, in the time domain, is of form:

$$E_x(z) = E_0\exp(-\alpha z)\cos(\omega t - \beta z) \tag{2.29}$$

This wave travelling in the $+z$ direction has a phase velocity of $v_p = \omega/\beta$, a wavelength $\lambda = 2\pi/\beta$, and an exponential damping factor $\exp(-\alpha z)$. The rate of decay over distance is given by the attenuation constant α. It can be seen that the total loss still comprises the two components σ and $\omega\varepsilon''$ responsible for conductive and dielectric loss. Furthermore, it can be seen that if $\sigma = 0$, the heating of the material is due to its complex permittivity.

For good conductors, the conductive current is much greater then the displacement current, or $\sigma \gg \omega\varepsilon''$. The complex propagation constant γ can then be approximated by ignoring the displacement current term, to give:

$$\gamma = \alpha + i\beta \simeq i\omega\sqrt{\varepsilon'\mu}\sqrt{\frac{\sigma}{i\omega\varepsilon'}} = (1+i)\sqrt{\frac{\omega\mu\sigma}{2}} \tag{2.30}$$

The skin-depth, or characteristic depth of penetration, it then given by:

$$\delta_s = \frac{1}{\alpha} = \sqrt{\frac{2}{\omega\mu\sigma}} \tag{2.31}$$

This means, that the amplitude of the fields travelling in the conductor decays by 1/e or 36.8 % after a distance of one skin depth, since $\exp^{-\alpha z} = \exp^{-\alpha\delta_s} = \exp^{-1}$. At microwave frequencies, this distance is very small, which makes it possible to obtain a low-loss component by simply plating that component with a thin layer of a good conductor such as gold or silver.

2.2.5 Specific Absorption Rate (SAR)

Electromagnetic waves emitted by the applicator antenna are absorbed by the surrounding tissue causing an increase in tissue temperatures. A measure commonly used for quantifying this power deposition in the tissue is the specific absorption rate (SAR) in W/kg. SAR is a scalar quantity and a function of position denoting the electrical power W absorbed per kg of tissue. It is derived from the space-dependent magnitude of the electric field $|\vec{E}(r,z)|$, imaginary part of the complex permittivity ε'', angular frequency ω, and tissue mass density ρ according to:

$$SAR(r,z) = \frac{\omega \varepsilon_0 \varepsilon_r'' |\vec{E}(r,z)|^2}{\rho} \tag{2.32}$$

2.3 Heat Transfer in Biological Tissue

2.3.1 Introduction

Heat transfer is generally defined as energy transit due to a temperature difference [56]. There are three basic modes of heat transfer; conduction, convection and radiation. Conduction describes the exchange of internal energy between one body which is in perfect contact with another, or from one part of the body to another part due to a temperature gradient. In contrast, the term convection refers to energy exchange that takes place between a body and a surrounding fluid. The third mode of heat transfer, radiation, is the energy transfer from a body or between two bodies by electromagnetic waves.

In most cases, heat transfer problems consist not only of one mode but of a combination of different modes. In order to understand heat transfer in tissue, several general factors have to be considered, for instance the thermal properties of the target tissue, such as specific heat and thermal conductivity, the geometry of the target, the heat production due to absorption of electromagnetic radiation, heat production due to metabolic processes, heat flow due to perfusion of blood and thermoregulatory mechanisms. The next sections present the derivation of a partial differential equation (PDE) describing the heat transfer in tissue. This PDE is often called the tissue bioheat equation and was first proposed by Pennes [57].

2.3.2 Pennes Bioheat Equation

The first law of thermodynamics (conservation of energy) states that the rate of change in heat energy in time for a given volume is always equal to the heat energy flowing across the boundaries in time plus the heat energy generated inside per unit time. Considering a finite segment of a one-dimensional rod (see figure 2.1(a)), the conservation of energy can be expressed as follows:

$$\frac{d}{dt}\int_a^b E(x,t)A dx = A(\phi(a,t) - \phi(b,t)) + \int_a^b Q(x,t)A dx \tag{2.33}$$

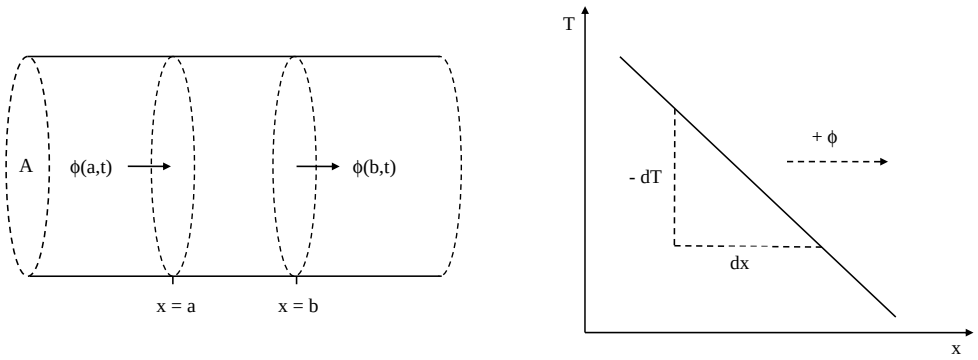

(a) First law of thermodynamics (conservation of energy) for a finite segment of a one-dimensional rod.

(b) Fourier's law of heat conduction. The direction of heat flux ϕ is opposite to the thermal gradient dT/dx.

Figure 2.1: First law of thermodynamics and Fourier's law of heat conduction.

where $E(x,t)$ is the thermal energy density in J/m^3, A the cross-sectional area in m^2, $\phi(x,t)$ the heat flux in J/(s· m) and $Q(x,t)$ internal heat sources in J/(s· m^3). Taking the time derivative into the integral and writing the heat flux in integral form yields:

$$\int_a^b \frac{\partial E(x,t)}{\partial t} dx = -\int_a^b \frac{\partial \phi(x,t)}{\partial x} dx + \int_a^b Q(x,t) dx \tag{2.34}$$

or,

$$\int_a^b \left(\frac{\partial E(x,t)}{\partial t} + \frac{\partial \phi(x,t)}{\partial x} - Q(x,t) \right) dx = 0 \tag{2.35}$$

Equation 2.35 only holds true if the integrand equals zero, hence:

$$\frac{\partial E(x,t)}{\partial t} = -\frac{\partial \phi(x,t)}{\partial x} + Q(x,t) \tag{2.36}$$

Generally, the thermal energy of an object can be expressed in terms of the object's temperature using the following equation:

$$E(x,t) = c\rho \cdot T(x,t) \tag{2.37}$$

where $T(x,t)$ is the object's temperature in K, c the specific heat capacity in J/(kg· K) and ρ the mass density in kg/m^3. Substitution of equation 2.37 into equation 2.36 yields:

$$c\rho \frac{\partial T(x,t)}{\partial t} = -\frac{\partial \phi(x,t)}{\partial x} + Q(x,t) \tag{2.38}$$

Equation 2.38 is known as the equation of conservation of thermal energy.

Thermal conduction of heat energy inside a finite segment of a test rod is taken into account using Fourier's law of conduction which is defined according to:

$$\phi = -k \frac{\partial T}{\partial x} \tag{2.39}$$

where ϕ is the heat flux, k the thermal conductivity in x-direction in W/(m· K), and $\partial T/\partial x$ the thermal gradient in W/m in the x direction. The negative sign indicates

that heat always flows in the opposite direction of the gradient, that is, from hot to cold. Fourier's law of conduction is illustrated in figure 2.1(b). Substitution of equation 2.39 into equation 2.38 yields:

$$c\rho\frac{\partial T}{\partial t} = k\frac{\partial^2 T}{\partial x^2} + Q \tag{2.40}$$

and for $Q = 0$:

$$\frac{\partial T}{\partial t} = \frac{k}{c\rho}\frac{\partial^2 T}{\partial x^2} \tag{2.41}$$

Equation 2.41 is known as the heat equation or the diffusion equation as it describes how heat energy spreads out (diffuses) over time from initially being concentrated in one place. Accordingly, the diffusion equation in three dimensions used for further considerations is given by equation:

$$\frac{\partial T}{\partial t} = \frac{k}{c\rho}\nabla^2 T \tag{2.42}$$

In addition to heat conduction and transient heat storage covered by the diffusion equation, terms taking into account microwave heating, metabolic heating, and blood perfusion are needed in order to obtain a differential equation characterising the heat transfer during microwave ablation. The heat generation due to metabolic processes in the body can be represented by a term Q_m in units of $\mathrm{W/m^3}$. A term accounting for microwave heating can be added using SAR (see section 2.2.5). To be expressed in correct units of $\mathrm{W/m^3}$, SAR is multiplied by tissue density. Finally, a term accounting for heat transfer due to blood perfusion can be added given by:

$$\varepsilon_b\dot{\omega}_b\rho_b c_b \cdot (T - T_a) \tag{2.43}$$

where ε_b represents a heat transfer efficiency accounting for the possibility that blood in capillaries might not be completely equilibrated, $\dot{\omega}_b$ a volume flow of blood per unit volume of tissue per second (1/s), ρ_b the blood mass density, c_b the blood specific heat capacity, and T_a the arterial blood supply temperature [58]. Pennes first introduced the term given in equation 2.43 assuming that thermal equilibrium between blood and surrounding tissue only occurs in the capillary bed. The capillary bed is a layer of tissue densely packed with the smallest of the body's blood vessels. Furthermore, it was assumed that arterial blood – blood vessels carrying oxygenated blood from the heart to the rest of the body – is of constant temperature. In summary, Pennes assumed that blood at arterial temperature enters a region of elevated temperatures and removed heat from that region with a certain efficiency.

Combining all terms introduced results in Pennes bioheat equation (see equation 2.44), taking into account of transient heat storage, heat conduction, heat transfer due to blood perfusion, heat generation caused by the microwave field and metabolic heat generation:

$$\rho_t c_t\frac{\partial T}{\partial t} = k\nabla^2 T - \varepsilon_b\dot{\omega}_b\rho_b c_b \cdot (T - T_a) + \rho_t \cdot SAR + Q_m \tag{2.44}$$

where ρ_t and c_t are tissue density and tissue specific heat; all other variables have been

defined previously. In order to obtain the actual transient temperature distribution $T = T(\vec{r}, t)$, Pennes bioheat equation can be solved using the finite element method (FEM) which will be introduced later.

Chapter 3

Detailed Design Brief of 1.8 mm Applicator

3.1 Introduction

This chapter addresses the methodology of the device development. At first, the design approach is outlined (section 3.2), followed by the identification of desired applicator performance in section 3.3. Identified desired outcomes are then explicitly stated as applicator performance requirements in section 3.4, which are summarised again in section 3.5.

3.2 Design Approach

The development of a medical device is a complex and challenging task as it is reliant on the combination and application of knowledge of a diverse range of disciplines outside the main subject area. The development of a device for hyperthermia treatments requires specialised know how in disciplines such as fundamental physics, computational science, engineering, materials science, surface mechanics, medical knowledge, chemistry, and biology, all of which are essential for a successful design. In addition to that, the range of materials with suitable engineering characteristics is highly constrained due to regulatory requirements. Devices that are in contact with the human body must be made of materials certified as biocompatible. Furthermore, the possible occurrence of bacteria or germs on the device has to be eliminated by appropriate cleaning, disinfection, or sterilisation procedures.

The design approach for the development of this microwave applicator consisted of the following design steps:

1. Identification of desired device performance.
2. Definition of device requirements.
3. Initial applicator design.
4. Theoretical analysis of electromagnetic performance of initial applicator design in terms of:

- Match $S11$ ($S11$ defines the fraction of reflected power to input power and is used as a measure of power transmission)
- Field shape (SAR)

5. Applicator fabrication.
6. Validation of electromagnetic performance ($S11$).
7. Applicator testing of thermal performance in terms of:
   - Ablation size
   - Ablation shape
   - Applicator service temperatures
8. Theoretical modeling of thermal performance of applicator design (ablation size and shape, applicator service temperatures)
9. Applicator batch built and subsequent electromagnetic and thermal validation

Generally, the process of validation is defined as the task to ensure that a device is fit for purpose. It is achieved by performing suitable tests throughout the entire development phase proving that the device meets the users' needs. Validation ensures that functionality, as defined in requirements, is the intended behavior of the device in question. In contrast to that, the process of verification, which also occurs within each stage of the development, but should not be confused with validation, ensures that the device is designed to deliver all functionality demanded by an end user. It typically involves reviews and meetings to evaluate requirements and specifications [59].

At any stage in the design process, it may become necessary to re-work the design in order to obtain a satisfactory performance. Appropriate tests or analysis are then repeated until the required performance is achieved.

3.3 Identification of Desired Applicator Performance

Aspects of desired applicator performance were identified in communication with interventional radiologists, medical staff, and medical physicists. The desired performances can roughly be divided into clinical and technical demands.

In order to satisfy demands concerning its use in the clinical environment, the applicator must be designed for:

1. Percutaneous use
2. Use in interventional radiology (IR) suites and operating theatres
3. Use in computed tomography (CT) gantries
4. Induce cell death locally and at target site only
5. Allow the treatment of tumours at different sites
6. The applicator design must comply with existing healthcare regulations
7. The applicator must not radiate in air

To be effective for the treatment of tumours, the applicator must offer the following technical performances:

1. Delivery of microwave energy into biological tissue
2. Effect appropriate ablation sizes in acceptable times

3. Generate ablations of required shape
4. Ablation procedure must be safe for patient and staff
5. Device must deliver the same performance repeatedly
6. Structural ruggedness adequate to withstand common usage

All issues raised were then discussed and, where appropriate and doable, included into the list of device requirements presented below.

3.4 Device Requirements

Following the identification of desired clinical and technical device performance, a list of design requirements can be proposed including clinical, technical, and mechanical design attributes.

Requirements for Percutaneous Use

Percutaneous use imposes restrictions on the applicator design in terms of device diameter and tip geometry. The device diameter was defined with respect to existing applicators and should present an improvement thereof. The smallest existing applicators of the Medical Device Technology Group at the University of Bath at the onset of the project was a 2.4 mm diameter applicator, consisting of a 1.8 mm diameter coaxial cable (UT 70-LL from Micro-Coax). Therefore, the next smaller cable size was chosen for this design measuring 1.2 mm in diameter (UT 47C-LL from Mico-Coax). Taking into account a necessary supporting structure, an overall device diameter of 1.8 mm was envisaged. The required diameter was thus set to 2 mm maximum, with a target diameter of 1.8 mm.

Percutaneous devices can be used in conjunction with insertion aiding equipment such as trocars or tubes. More flexibility is provided to the user however, if the device itself is capable of penetrating necessary tissue types. Devices suitable for percutaneous use without further aid exhibit needle type tip designs in order to allow easy penetration through multiple tissue layers. The trocar tip design of the previous 2.4 mm applicator had satisfied those demands in the past and was therefore retained. The sharpness of the tip was not quantified but must allow effortless applicator insertion.

Requirements for Use in Interventional Radiology Suites and Operating Theatres

Suitability for use in IR suites and operating theatres requires compliance with aspects of safety and dimensional restrictions. Devices utilised in these environments must be provided in sterile condition [60, 61]. The applicator design therefore required the use of suitable materials in order to allow appropriate sterilisation processes. Secondly, all patient-contacting parts must be made of biocompatible materials to avoid harmful device-body reactions and kept below a certain temperature limit specified in the European Standard EN 60601-1 in order to prevent unwanted tissue damage or superficial skin burns [62, p. 154]. The allowable maximum temperature for a specific device or part of a device depends on several factors: the type of contact (direct skin contact or

likely to be touched), the length of time the part is in contact with the patient, and the type of material that device or part is made of. Applying these criteria to a coated applicator shaft in direct contact with the patient for up to 10 min results in a maximum allowable temperature of 48 °C. The same limit applies to the handle part. The feed cable falls in the category 'likely to be touched' for a plastic material and contact times greater than 1 min. Although it is a slightly different case, the same maximum allowable temperature of 48 °C results for its surface temperature.

The feed cable of the applicator is subject to several additional constraints concerning the use in respective environments. A certain length of feed cable between stationary microwave generator and applicator is required to allow necessary flexibility during use and provide a connection between non-sterile (location of microwave generator) and sterile field (location of patient). The required length of cable was therefore set to 1 m to 3 m. Also, the feed cable had to be thin, highly-flexible, and light-weight in order to facilitate handling. Thus, a feed cable with maximum diameter of 4 mm and surface temperatures below 48 °C was envisaged.

Requirements for CT Gantry Compatibility

The applicator design has to be compatible for use in CT gantries as mentioned earlier. An average opening of a CT unit measures approximately 90 cm. During the course of an ablation treatment, the patient can undergo several scans, for instance to determine correct applicator placement. In order to perform a CT scan, the operating table, patient and applicator has to be driven into the scanner. The applicator shaft thus has to be of correct length to allow access into the gantry whilst placed in the patient. Furthermore, a sufficient length of feed cable is required to allow lateral movement into the gantry with respect to the stationary microwave generator unit. Also, a lightweight feed cable reduces the risk of injury caused by the torsional moment exerted by the cable on the volume of tissue locating the applicator.

Required Safety Trip

The applicator must be designed for operation in soft tissue only. In air, the applicator must be prevented from radiating in order to satisfy safety regulations concerning the exposure of medical staff to possibly high-level radiation. The applicator system should therefore incorporate a suitable mechanism disconnecting the supply of microwave power to the antenna and thus avoiding operation when not inserted into tissue.

Requirements for the Treatment of Deep-Seated Tumours

Deep-seated tumours require a greater applicator shaft length in order to deliver microwave energy to the target site. However, a compromise in shaft length has to be made since greater lengths conflict with requirements stated in the previous section. The required shaft length was therefore set to approximately 20 cm. In addition to this device, a second applicator could be made at a later date with a longer shaft in order to meet demands for the treatment of deep-seated tumours.

Required Energy Delivery

The applicator antenna has to feature an appropriate impedance match to ensure efficacy. The required return loss of the device was set to be -10 dB or lower, corresponding to minimum transmitted power of 90 %.

Required Ablation Size and Shape

The device must be capable of producing ablation diameters ranging from approximately 20 mm to 50 mm in times up to 8 min to be clinically effective. In order to achieve such, input powers of 60 W or more would be required. The resulting coagulation geometry should be close to spherical, and occur around the distal end of the applicator, embedding the applicator tip in the ablation. The sphericity of the ablation should feature a minimum short-axis to long-axis diameter ratio of 0.73 corresponding to, for instance, 40 mm and 55 mm. Sphericity will also be determined later using appropriate equations and should be above 0.98.

Required Cooling System

Efficient cooling of the device is required due to several reasons. Firstly, due to a loss of 1.61 dB/m in the 1.2 mm semi-rigid coaxial cable, temperatures of up to 250 °C were expected for a source level of approximately 55 W. As power levels of 60 W and above would be required for sake of maximising ablation sizes, the cable had to be cooled during operation. Secondly, skin burns caused by hot feed cable or shaft sections must be avoided as mentioned before. Furthermore, cooling of critical materials such as solder joints, plastic handle parts, adhesives, tip structure, and coating assist in the aim of high power operation and increase device reliability since respective service temperatures can be lowered by the cooling. Efficient cooling of the shaft was also regarded necessary to improve the sphericity of the ablation. Most microwave ablation devices suffer to some degree of back radiation travelling along the outside of the shaft giving rise to pear-shaped coagulation zones [63]. Such tails in ablation shape could possibly be reduced by efficacious shaft cooling.

In order to eliminate the insertion of coolant into the ablation zone, as is the case in the 2.4 mm open-cooled applicator, a close-cycle cooling system was preferred. However, the existing restriction on device diameter must be complied with when implementing a cooling solution. Consequently, a efficacious closed-cycle cooling system was required for safe and high-power operation of the semi-rigid coaxial cable, for prevention of skin burns along shaft or feed cable, for facilitation of material selection, and high quality ablation shapes. The only requirement quantified was the maximum temperature of 48 °C on all external device surfaces outside the ablation zone and the required closed-cycle cooling concept.

Requirements for Device Reliability

The requirements on applicator reliability can be divided into three categories – structural strength, bond strength, and non-stick surface. The structural strength of applicator shaft and tip must be sufficiently high to endure customary device handling, device placement, and device withdrawal. No quantified requirement was defined. However, handling practices during experimental validation of prototype devices were considered comparable to those during clinical use and would highlight structural weaknesses.

All interfaces, joints, and bonds in the device have to withstand conditions during operation, in addition to those encountered during common usage. Possible challenges regarding bond strength are seen regarding:

- Limited bonding area and thickness in applicator shaft and tip:
  - Structure dimensionally constrained to maximum shaft diameter and coaxial cable
  - Possible glue lines thickness minimal; only very fine pastes suitable
  - Compromise between wall thickness of material and glue line thickness
- Range of usable bonding and coating materials for tip structure limited due to:
  - Exposure to high-power microwave fields
  - Operation under high temperature
  - High-strength bond required
  - Operation in the presence of water and steam
  - Issues of biocompatibility and sterilisation
  - Curing temperatures limited to 250 °C
- Limited range of usable bonding materials around handle structure due to requirements of:
  - Sterilisation resistance
  - Water-proofing of seals

Furthermore, the applicator surface was required to feature superior non-stick properties in order to prevent tissue adhesion during and after an ablation. The non-stick properties have to remain intact for several ablations of maximum duration and power and have to withstand withdrawal from hardened, carbonised tissue. Since peak temperatures around the applicator tip are likely to reach as high as 300 °C, exceeding the operating range of the widely-used non-stick material Teflon, finding a suitable non-stick coating was of importance.

All attributes listed above affect applicator reliability. Suitability of materials as well as certain design aspects will be tested during repeated ablation experiments performed at the maximum usable device input power. The target number of maximum ablation repetitions per applicator was 8-10, the maximum power level in the order of 60 W to 80 W, and the maximum time of each ablation approximately 8 min. All aspects discussed were hence tested simultaneously during those applicator reliability tests of maximum power and time.

3.5 Summary of Applicator Requirements

Table 3.1 summarises the requirements on the applicator design established in this chapter. The design approach introduced for the development of the microwave applicator

Table 3.1: Summary of applicator design requirements.

Design Requirement	Description
Device diameter	≤ 2.0 mm; target 1.8 mm
Sharp cutting tip	allow effortless percutaneous use
Sterility	suitable for sterilisation process
Biocompatibility	all patient-contacting parts
Safety Trip Mechanism	avoid radiation leakage
Length of feed cable l	$(1 \leq l \leq 3)$ m
Feed cable diameter	≤ 4 mm
Feed cable flexibility	highest flexibility offered
Feed cable weight	lightweight
Cable and shaft surface temperatures	≤ 48 °C
Applicator shaft length	16 cm and approx. 26 cm
Return loss	≤ -10 dB
Ablation diameter	≥ 50 mm
Ablation location	encompass applicator tip
Ablation sphericity	≥ 0.98
Maximum ablation time	8 min
Input power	≥ 60 W
Applicator reliability	survival of 8 ablations at maximum settings
Closed-cycle cooling system	eliminate coolant leakage
Rigidity of applicator tip and shaft	retain device integrity
Required joint and bond strengths	retain device integrity
Non-stick applicator surface	retain device integrity

is reflected in the structure of this thesis. Design requirements are dealt with individually where possible and are organised into different chapters, beginning with the electromagnetic applicator design in the subsequent chapter 4.

Chapter 4

First 1.8 mm Applicator Design and Electromagnetic Analysis

4.1 Introduction and Objectives

A detailed description of the design and testing of the first 1.8 mm applicator is given in this chapter. Firstly, the applicator design is presented, followed by a theoretical analysis of the electromagnetic performance in terms of return loss and localised energy absorption. Next, the applicator manufacture is described. Device validation is performed in the last section by comparing predicted to measured results.

The objectives of the design, manufacture and validation studies presented in this chapter were threefold:

- To assess the prospects of an applicator design of reduced diameter
- If applicable to optimise given applicator design
- If applicable to validate the electromagnetic performance of the device

4.2 Design Description

4.2.1 Introduction and 2.4 mm Applicator

The design of the 1.8 mm applicator presented in this chapter was based on an existing 2.4 mm percutaneous applicator with open-cycle cooling developed by Prof N Cronin, Dr P Clegg and M Boix of the MDTG at the University of Bath between 2003 and 2006. In addition to extensive testing during the development phase, the 2.4 mm applicator has been used in clinical trials. Figures 4.2 and 4.1 display the design and dimensions of the 2.4 mm applicator. The operating principle and general associated applicator components of the 2.4 mm applicator were retained for the design of the 1.8 mm applicator. For further information regarding the 2.4 mm applicator see [64, p.45–53].

A number of design modifications of the 2.4 mm device were necessary in order to meet the required specifications of the new applicator including the use of an appropriate

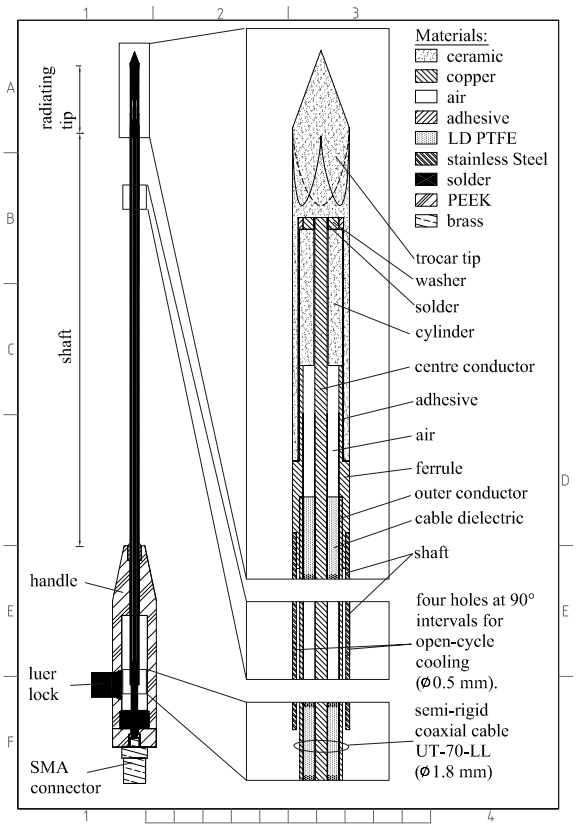

Figure 4.1: Design of 2.4 mm applicator featuring open cycle cooling.

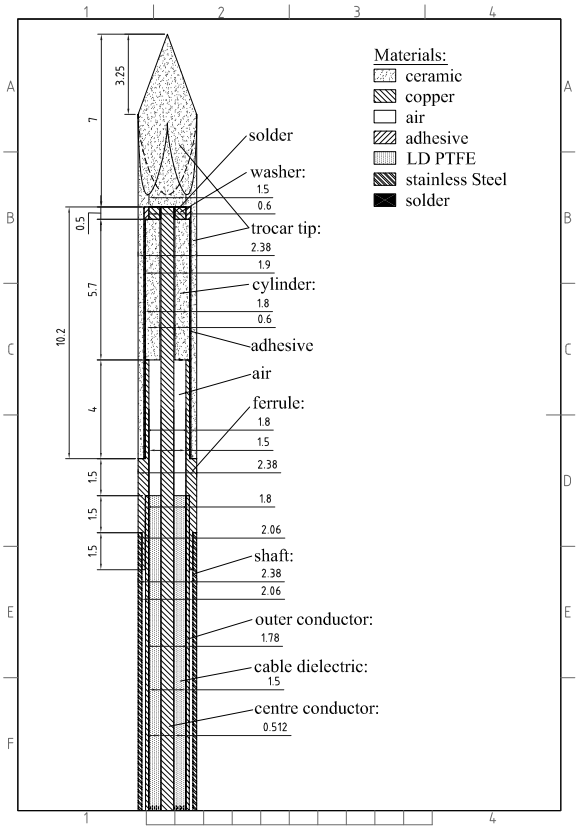

Figure 4.2: Engineering drawing of 2.4 mm applicator featuring open cycle cooling.

coaxial cable and the resulting reduction of component and antenna diameters from 2.4 mm to 1.8 mm. Minor alterations were necessary with regards to manufacture and selection of appropriate adhesives and bonds, the latter due to decreasing bond gaps and glue lines.

4.2.2 Operating Principle

The efficacy of the applicator, namely to deliver heat into the medium surrounding the vicinity of applicator tip, is based on the operating principle of a $\lambda/2$ dipole antenna that is matched into human soft tissue.

An ideal thin linear $\lambda/2$ dipole antenna is depicted in figure 4.3(a). It consists of two quarter-wave long conductors (elements) that are fed centrally, in this instance by a coaxial waveguide. The unbalanced voltage of the coaxial cable is hereby transformed to a balanced voltage distribution on the dipole using a balun transformer. The total antenna length measures approximately half a wavelength or $\lambda/2$. The voltage differential U is maximum over a length of $\lambda/2$, as one end of the antenna is at a node while the other is at an antinode of the wave, resulting in a voltage difference of $+2U_{max}$ over $\lambda/2$. The voltage differential gives rise to current flow between the elements. The resulting current distribution I of the antenna is approximately sinusoidal as indicated in the figure. The currents are in phase over each $\lambda/2$ section and in opposite phase over the next, if present. The radiation pattern for such an ideal $\lambda/2$ antenna positioned

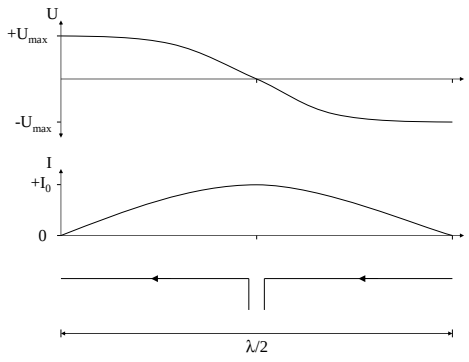

(a) $\lambda/2$ dipole antenna with voltage distribution and resulting current distribution.

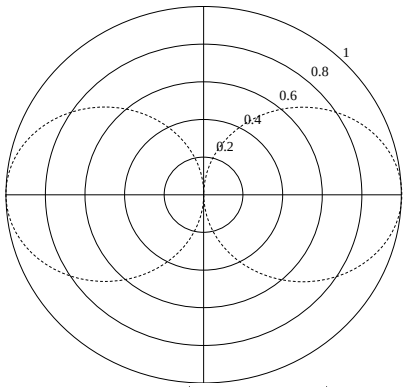

(b) Radiation pattern (dashed lines) of ideal $\lambda/2$ dipole antenna on linear scale.

Figure 4.3: $\lambda/2$ dipole antenna with voltage and current distributions 4.3(a) and radiation pattern 4.3(b).

vertically is shown in dashed lines in figure 4.3(b). It can be seen that it takes the form of a slightly flattened torus whereby the axis of the torus is aligned in the direction of the dipole elements.

However, there are several differences between the ideal $\lambda/2$ dipole discussed and the applicator antenna. Figure 4.4 shows the approximated $\lambda/2$ dipole of the applicator. The first $\lambda/4$ element is implemented by the extended centre conductor of the coaxial waveguide, the second by a copper ferrule. The copper washer at the end of the centre conductor acts as an end plate providing additional loading without seriously altering the pattern. With figure 4.3(a) in mind, the applicator antenna can now be produced

from the ideal dipole by bending both antenna elements by 90 degrees relative to the feed line, yielding both antenna and feed line in the vertical position. Yet, even in this alignment, the applicator antenna does not entirely emulate the $\lambda/2$ wire dipole antenna due to the radial extent of the copper ferrule. However, being of cylindrical form the ferrule retains the necessary symmetry in the antenna design, assuring symmetry in the radiation pattern.

In addition, the general assumption in antenna theory whereby antennas are designed to radiate into air is not applicable to the applicator. The applicator ought to radiate into human tissue which is, contrary to air, a lossy medium. As a direct consequence, the antenna length had to be redefined in terms of the wavelength in the surrounding medium. The wavelength in a medium λ_m can be calculated from the wavelength of free space λ_0 and the refractive index n of the medium according to $\lambda_m = \frac{\lambda_0}{n}$, where λ_0 is defined by speed of light c divided by frequency ν. The refractive index of the medium n can be derived from $n = \sqrt{\epsilon'_r \mu_r}$. Substituting the latter equations into the former and using $c = 3 \cdot 10^8$ m/s, $\epsilon'_r = 62.44$ [65], $\nu = 2.45 \cdot 10^9$ Hz, and $\mu = 1$, results in a wavelength of $\lambda_m = 15$ mm for in-vivo malignant human liver (see equation 4.1). The length of each $\lambda/4$ element should therefore be approximately 3.8 mm.

$$\lambda_m = \frac{\lambda_0}{n} = \frac{c}{\nu \cdot n} = \frac{c}{\nu\sqrt{\epsilon'_r}} = 0.015 \tag{4.1}$$

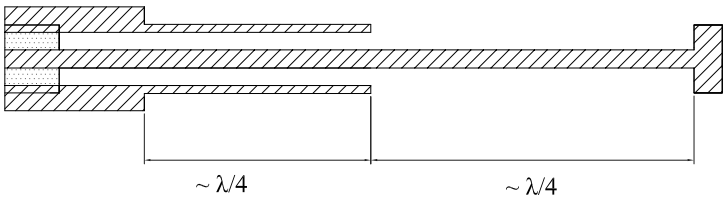

Figure 4.4: Actual dipole of applicator.

As a direct consequence of wave propagation through a lossy medium (n>1), the radiation pattern of the ideal $\lambda/2$ dipole (see figure 4.3(b)) displaying the far field does not represent the radiation process of the applicator. In order to accurately determine the electric field distribution around microwave or RF applicators, computer models using the finite element method (FEM) are commonly used [66, 67, 68]. The magnetic field of the applicator resembles that of the dipole, that is, it does not exhibit any radial components. It is therefore confined to planes perpendicular to the antenna axis, running in concentric circles. This assumption was used in defining known boundary conditions in the computer model.

4.2.3 Components and Materials

Figure 4.5 shows the design of the first 1.8 mm applicator with open-cycle cooling. A drawing of the entire applicator approximately to scale is shown on the left hand side of the figure. On the right hand side, two view ports are visible enlarging the areas

around the applicator tip and around the end of the shaft. The legend in the top right corner of the figure identifies the materials of the applicator. The following sections detail individual components of the design including function, choice of material and geometry.

Coaxial Cable and Connector

Transmission of electromagnetic energy from source to load was realised by use of coaxial cables together with appropriate connectors. Coaxial cables consist of outer conductor, dielectric, and centre conductor, as depicted in figure 4.6(a). Electromagnetic energy in coaxial cables in confined by the inner and outer conductors. Transmission of electromagnetic energy hence occurs only in the cable dielectric. The mode of propagation is in transverse electric magnetic (TEM) mode, that is, both electric and magnetic fields are perpendicular to the direction of propagation (see figure 4.6(b)). The electric field is orientated in radial direction only, the magnetic field in concentric circles around the centre conductor. The magnitude of both electric and magnetic field varies sinusoidally from minium to maximum over half a wavelength. The radial restriction of the device to below 2 mm severely limited the choice of suitable cables. The applicator was therefore designed on the basis of the semi-rigid coaxial cable UT-047C-LL (from Micro-Coax [69]), a low-loss cable with outer conductor diameter of (1.194 ± 0.025) mm, dielectric diameter of (0.940 ± 0.025) mm, and centre conductor diameter of (0.320 ± 0.013) mm. Its electrical characteristics comprises an impedance of (50 ± 2.0) Ω, a frequency range of DC to 115 GHz. The typical insertion loss of the cable in dB/m is plotted in figure 4.7(a) as a function of frequency. Furthermore, figure 4.7(b) displays the average power handling for continuous wave (CW) in W at 20 °C and sea level. The maximum operating temperature of the cable is defined as 250 °C. At the target frequency of 2.45 GHz, the typical insertion loss and average power handling amount to 1.61 dB/m and 55.5 W, respectively. The respective materials of outer conductor, dielectric, and centre conductor are copper, low density polytetrafluoroethylene (LD PTFE), and silver plated copper (all data taken from the manufacturer [69]). The design shown in figure 4.5 required a customised cable assembly of defined total length, exposed centre conductor of given length, and termination with a female SMA connector.

Ferrule and Washer

The ferrule forms an integral part of the applicator. It serves as a mechanically strong connection between tip and applicator shaft. It also acts as a waveguide extending the coaxial cable, and as one of the dipole elements. The ferrule is to be electrically connected to the coaxial cable and mechanically to shaft, cylinder and tip. The washer, located at the distal end of the extended centre conductor shortens the required length of the dipole element made up by the centre conductor. Both ferrule and washer were made of copper offering high electrical conductivity, ease of manufacturing and workability.

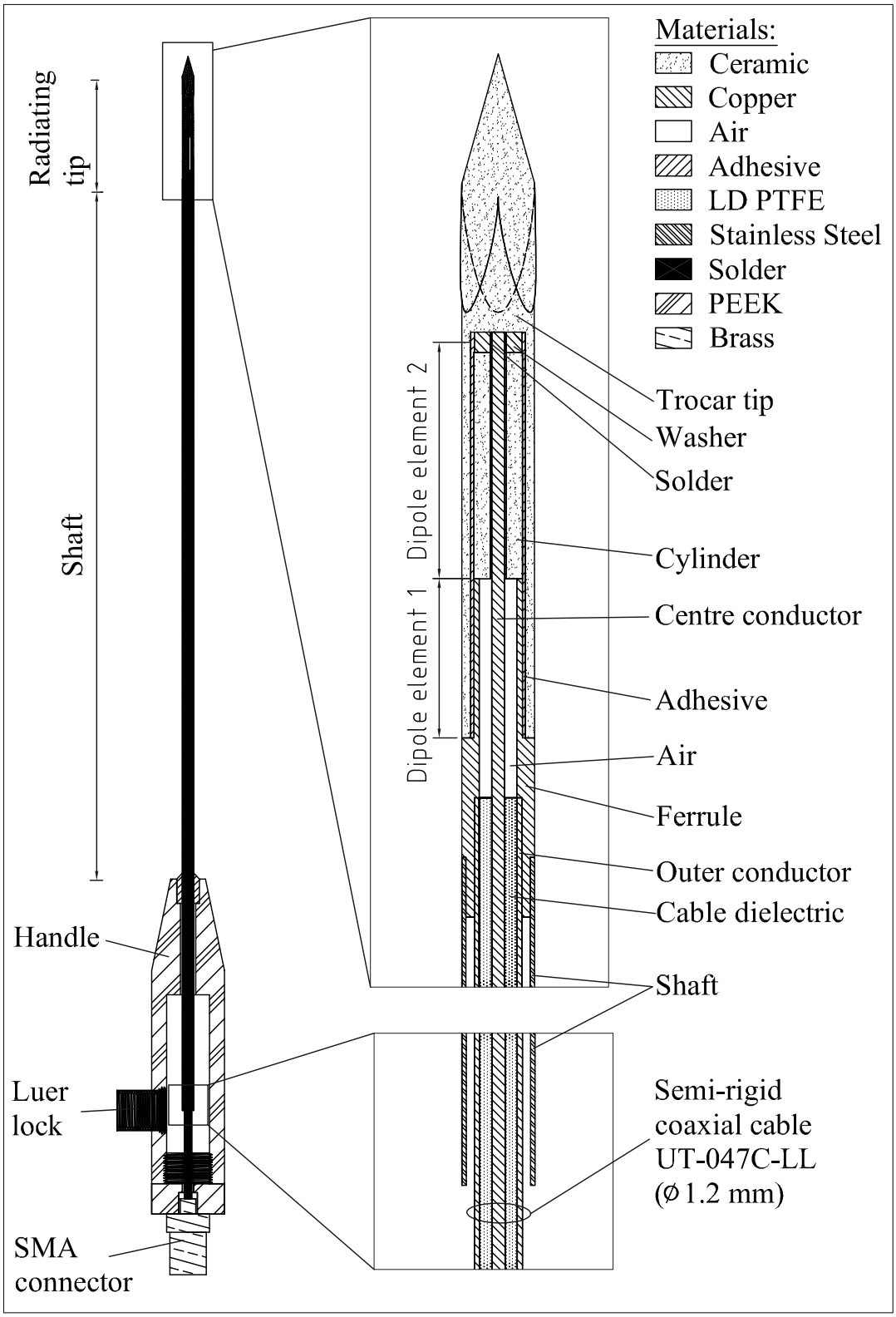

Figure 4.5: Design drawing of first 1.8 mm applicator with open-cycle cooling.

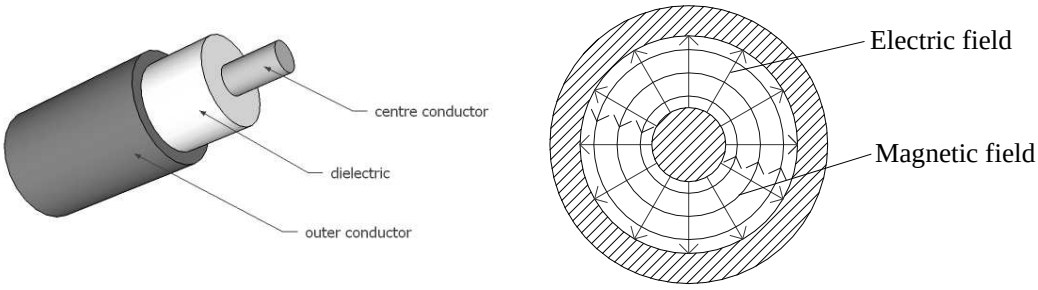

(a) Composition of semi-rigid coaxial cable.

(b) Electric and magnetic field lines of TEM mode in coaxial cable; fields confined to cable dielectric.

Figure 4.6: Composition of semi-rigid coaxial cable 4.6(a) and fields of TEM mode 4.6(b).

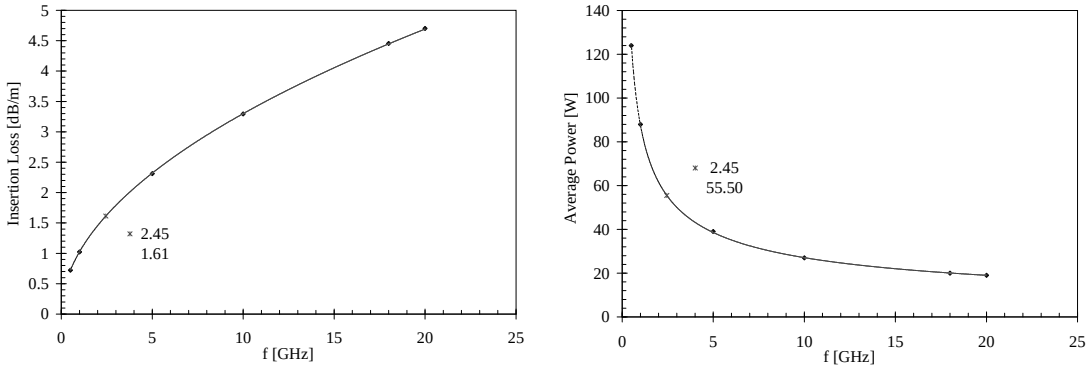

(a) Typical insertion loss (dB/m) versus frequency.

(b) Average power handling (W) versus frequency.

Figure 4.7: Typical insertion loss and average power handling of semi-rigid coaxial cable UT-047C-LL utilised in the applicator design versus frequency.

Cylinder and Tip

Both cylinder and trocar tip (see figure 4.5) were made of a particular ceramic: yttrium stabilised tetragonal zirconia (Y-TZP). This type of ceramic features a high dielectric constant of approximately 18 at 2.45 GHz and superior mechanical strength.

The main function of the cylinder is to provide a material of high dielectric constant ϵ'_r in the vicinity of the upper dipole element. As described in section 4.2.2, the wavelength of an electromagnetic wave decreases in materials of higher ϵ'_r, reducing the required dipole element length and hence applicator tip. The same function is achieved by the ceramic tip loading both dipole elements. This effect however, is expected to be reduced in the case of the 1.8 mm applicator when compared to larger devices due to decreasing wall thicknesses resulting in lesser material present. Another important feature of the zirconia ceramic lies in its superior mechanical hardness necessary for percutaneous application. The particular trocar shape maximises the cutting force of the tip through biological tissues.

Handle

The applicator handle facilitates device handling during operation. It also provides a connection for coolant supply via a luer lock. The coolant enters through the luer lock into the handle reservoir from where it is fed into the space between shaft and coaxial cable. The handle design was adopted from the 2.4 mm applicator and was made of PEEK (polyetheretherketone), a biocompatible plastic. PEEK offers a high melting point of 350 °C and high tensile strength.

Shaft

The applicator shaft provides structural strength to the device and mechanical protection to the enclosed semi-rigid coaxial cable. It also guides the coolant along the applicator length towards the tip, thereby cooling the applicator and neighbouring tissue. The coolant then exits through small holes made in the shaft approximately 1 cm below the ferrule into the ablation zone. An extra thin-walled hypodermic tube made of stainless steel and dimensions of (1.83 ± 0.01) mm for outer diameter and (1.59 ± 0.03) mm for inner diameter was chosen as shaft. These shaft dimensions allowed the insertion of the coaxial cable and lower ferrule shoulder while keeping the applicator diameter to a minimum.

Adhesive and Solder

A suitable strong and low loss adhesive was to be found to bond the ceramic tip to both ferrule and cylinder. Due to the very small gap sizes involved the choice was limited. A urethane methacrylate adhesive (Loctite 638, [70]) was chosen due to its anaerobic cure condition. Both solder joints, washer to centre conductor and ferrule to coaxial cable, were performed with a solder paste of melting point 180 °C.

4.2.4 Dimensions

The dimensions of the first applicator design are displayed in figure 4.8. The radial dimensions of components are listed below the respective component label on the right hand side relative to the applicator; longitudinal dimensions are shown on the left hand side. The outer device diameter is 1.83 mm.

Radial dimensions of all parts were reduced in order to meet the required device diameter. The internal diameter of the ferrule, for instance, was defined to be 0.47 mm as this is the diameter of the semi-rigid cable dielectric serving as extension of the outer conductor. Most other part dimensions were defined by compromising between maximising wall thickness and glue line thickness, as greater wall thickness yield increased mechanical strength and greater glue line thickness improved bond strength. Part lengths were only provisionally defined at this stage. A separate analysis was conducted later with the aim of optimising the major part lengths (see section 4.3.8).

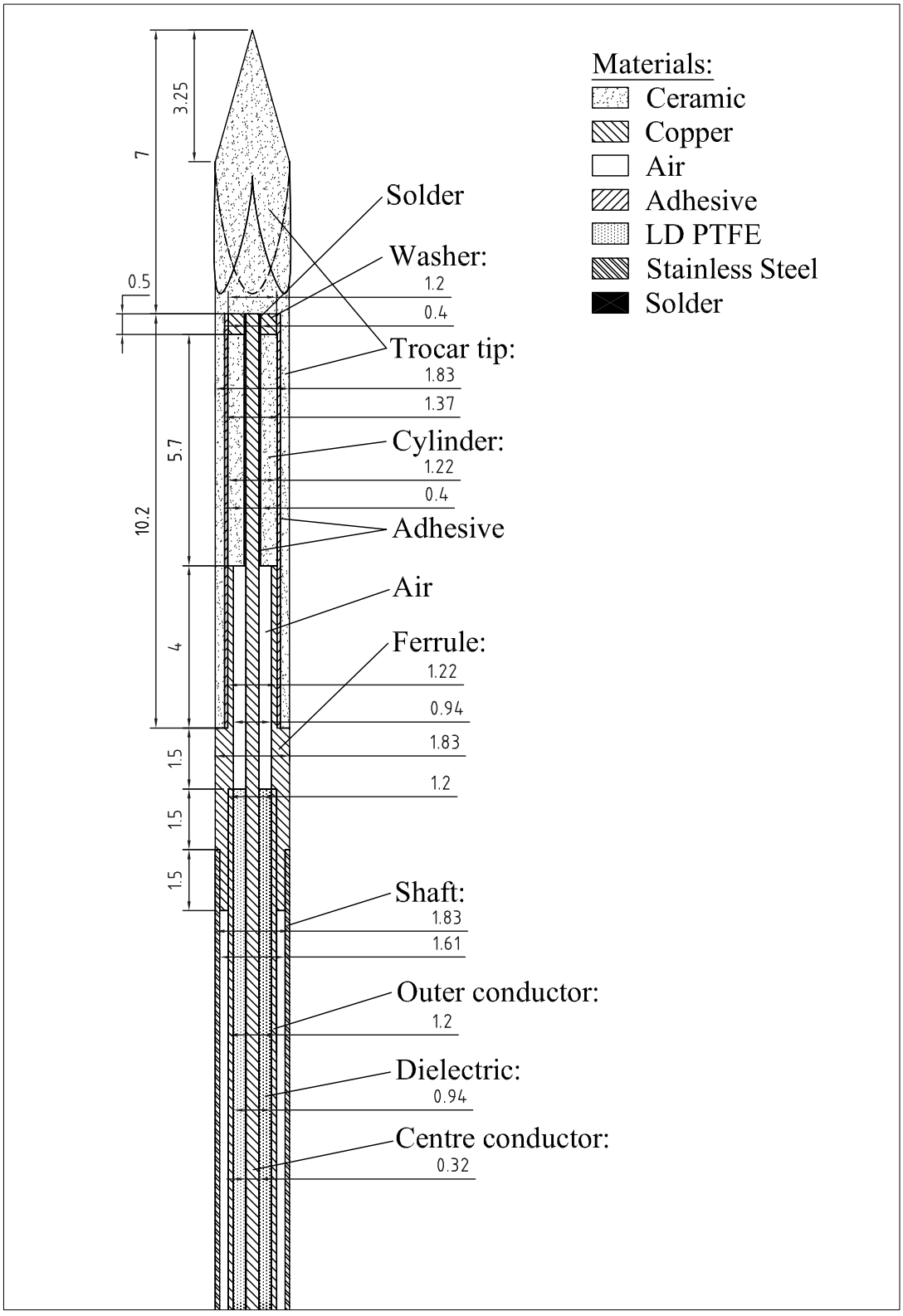

Figure 4.8: Dimensions of first 1.8 mm applicator design in mm.

4.3 Theoretical Analysis of 1.8 mm Applicator Design

4.3.1 Introduction

A theoretical analysis of the electromagnetic performance of the design was performed using the finite element method (FEM) or finite element analysis (FEA). A FEA model was created in a high-frequency 3D electromagnetic field simulator (HFSS ^{TM} from ANSYS, Inc.; [71]). The objective of the analysis was to extract the scattering parameter S11 and the SAR distribution of the device in order to validate the device against later measurements.

4.3.2 Background

Return Loss and S11

In high frequency systems, reflections occur at a discontinuity or impedance mismatch. Quantitative measures of such reflections are return loss RT or S-parameters. The return loss of a single input/output transmission line is defined as the ratio of incident or forward signal power P_f to reflected signal power P_r given in dB:

$$RT(dB) = 10\log(\frac{P_r}{P_f}) \tag{4.2}$$

A standing wave on a transmission line consists of voltage components for forward (V_f) and reflected wave (V_r) which are superimposed. The reflection coefficient Γ of that line is defined as:

$$\Gamma = \frac{V_r}{V_f} \tag{4.3}$$

Since both voltage components are complex numbers, Γ is also complex and contains the information of both magnitude and phase shift of the reflection. If $\Gamma = -1$ the line is short-circuited, if $\Gamma = 0$ the line is perfectly matched, and if $\Gamma = 1$ the line is open-circuited. For a single input/output transmission line Γ is equal to the S_{11} parameter.

Often, only the magnitude of a reflection coefficient is of interest. In this case the following equation applies:

$$|\Gamma| = \frac{|V_r|}{|V_f|} = |S_{11}| \tag{4.4}$$

Furthermore, forward and reflected power can be derived from the respective voltage and the characteristic impedance of the line Z_0 as follows:

$$P_i = \frac{1}{2}\frac{V_i^2}{Z_0} \tag{4.5}$$

Hence, the return loss of a line is related to the magnitude of the reflection coefficient through:

$$RT(dB) = 10\log(\frac{P_r}{P_f}) = 10\log(\frac{V_r^2}{V_f^2}) = 10\log(|S_{11}|^2) = 20\log|S_{11}| \tag{4.6}$$

Both the return loss in dB and $|S_{11}|$ in dB are derived from the ratio of reflected and forward power. If $|S_{11}|$ is displayed on a linear scale however, then it is the ratio of respective voltages rather than powers that are used and the two parameters $|S_{11}|$ (dB) and $|S_{11}|$ (linear) are not interchangeable. However, $|S_{11}|$ (dB), S11 (dB) or $magS11$ (dB) all denote the same quantity. It is those that are of concern in the context of this work.

Return losses of -3 dB, -10 dB, and -15 dB are hence equivalent to ratios of reflected power to input power of 0.5, 0.1, and 0.03, or a transmission of power by 50 %, 90 %, and 97 %, respectively.

Finite Element Analysis (FEA)

FEA is a computer-based simulation technique used in many different areas of engineering analysis. It utilises a numerical technique called the finite element method (FEM). In its application, the object in an FEA is represented by many discrete regions called finite elements; together those elements form the entire physical structure. The relevant laws and equations of a particular discipline are applied to each element constructing a set of simultaneous equations. The set of equations are solved for unknown values using appropriate techniques and solvers. Each element has a certain number of corners set by its shape, dimension and type of the element. Those corners are called nodes and are the locations in the model where unknown values are calculated during the solution process. Since the FEM is an approximate method, the accuracy of the solution can be improved by refining the mesh of the object modelled, corresponding to an increase in the number of elements and hence nodes. FEM models can provide quick, accurate solutions to multiple systems of differential equations and are therefore well suited to heat transfer problems like ablation.

An FEA model is usually constructed in a sequence of steps. They consist of:

1. Creating the solid model
2. Choice of appropriate element type; this depends on the type of analysis, for instance, thermal, electromagnetic or mechanical
3. Assigning material properties
4. Assigning materials and element types to model volumes
5. Creating a Mesh
6. Applying load, boundary and initial conditions
7. Defining the solution process; for instance, solver type, load step size, and convergence criteria
8. Solving the model
9. Post processing of results

For more information on the finite element method in electromagnetics consult [72].

4.3.3 Model Geometry

Due to the unavailability of 2D axially symmetric elements, a 3D model geometry of the applicator design had to be created. However, existing symmetry planes in the design

rendered possible the use of a 60° model section instead of the full 360° one, hence reducing the necessary computational power. The 60° symmetry stems from the trocar tip geometry as the very tip of the trocar tip features a three sided design with a 120° symmetry. This 120° symmetry, when halved once more, results in the 60° symmetry utilised in the model. The utilised model geometry is shown in figure 4.9 consisting of the physical structure of the applicator plus a surrounding load volume.

The model was built using variables for all major part dimensions in order to render possible automatic modifications at later times. These variables are defined in figure 4.10. Table 4.1 lists those variables and their respective values.

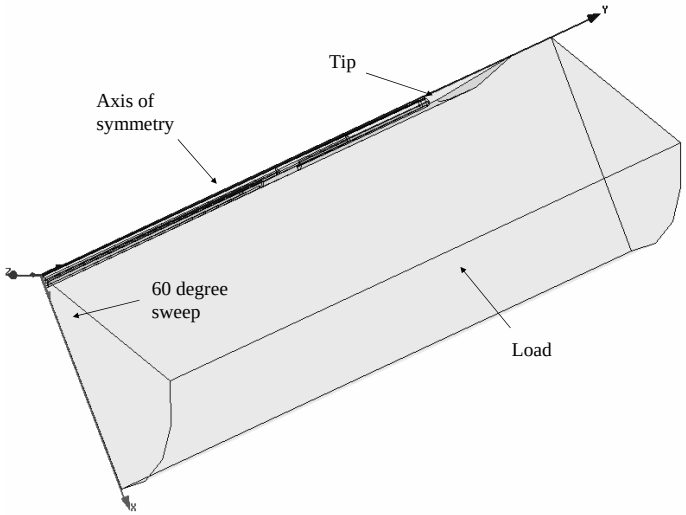

Figure 4.9: FEA model geometry for electromagnetic analysis of applicator.

4.3.4 Material Properties

The computer simulation software required the assignment of dielectric constant ε'_r and either loss tangent $tan\delta$ or conductivity σ at 2.45 GHz for each material, defining both real and imaginary part of each material's complex permittivity. The conductivity term was hereby defined by the material's complex permittivity via $\omega\varepsilon''$ which does not relate to the DC conductivity of the material. All materials, properties, and source references are listed in table 4.2. Material properties were assumed linear throughout.

Three load materials were considered in the model: in-vivo human malignant liver, saline solution with a concentration of 0.58 % w/v (equivalent to 0.1 M), and ex-vivo bovine liver. The first material, in-vivo human malignant liver was chosen since it presented the ultimate target tissue type of live human cancerous liver. The applicator therefore had to be designed with the aim of operating in this load type.

During the development process however, the use of a substitute or tissue phantom which closely mimics the related material properties was more convenient. For this reason, a saline solution of given concentration was used for comparison of theoretical and experimental results, for instance $|S11|$. The material properties of saline solutions are well defined over ranges of concentrations, temperatures, and frequencies [74]. Fur-

Table 4.1: Names and values of variables employed in FEA model for electromagnetic analysis of applicator. Some variables are defined in relation to other variables.

Variable Name	Value	Unit	Calculated Value
r_centre_cond	0.16	mm	0.16 mm
l_centre_cond	30	mm	30 mm
$r\_dielectric\_coax$	0.47	mm	0.47 mm
$l\_dielectric\_coax$	18.3	mm	18.3 mm
r_outer_cond	0.6	mm	0.6 mm
l_outer_cond	$l\_dielectric\_coax$	mm	18.3 mm
r_shaft_inner	0.805	mm	0.805 mm
r_shaft	0.915	mm	0.915 mm
l_shaft	16.8	mm	16.8 mm
l_air_shaft	15.3	mm	15.3 mm
$r\_ferrule\_1\_outer$	r_shaft_inner	mm	0.805 mm
$l\_ferrule\_1$	19.8	mm	19.8mm
$r\_ferrule\_3\_inner$	$r\_dielectric\_coax$	mm	0.47 mm
$r\_ferrule\_3\_outer$	0.61	mm	0.61 mm
$l\_ferrule\_3$	23.8	mm	23.8 mm
$r\_ferrule\_2\_outer$	r_shaft	mm	0.915 mm
r_cyl_inner	0.2	mm	0.2 mm
r_cyl_outer	0.61	mm	0.61 mm
r_washer_inner	0.2	mm	0.2 mm
r_washer_outer	0.6	mm	0.6 mm
dy_washer	0.5	mm	0.5 mm
dy_solder	dy_washer	mm	0.5 mm
r_tip	r_shaft	mm	0.915 mm
r_tip_inner	0.685	mm	0.685 mm
dy_tip	7	mm	7 mm
r_load	15	mm	15 mm
l_load	l_centre_cond+dy_tip+3	mm	40 mm
$sweep\_angle$	60	deg	60 deg

Table 4.2: Material properties used in electromagnetic FEM model of first applicator.

Material	ε_r	$tan\delta$	σ [S/m]	Reference
LD PTFE	1.7	0	N/A	[69]
Copper	1	0	58e6	N/A
Air	1	0	0	N/A
Adhesive	3	0.03	0	approx.
Y-TZP Zirconia	18	1e-3	0	[73]
Solder	1	0	7e6	N/A
Stainless steel	1	0	1.1e6	N/A
In-vivo human malignant liver	62.4	0.26	0	[65]
Saline	77	0.23	0	[74]
Ex-vivo bovine liver	46.9	0.249	0	[73]

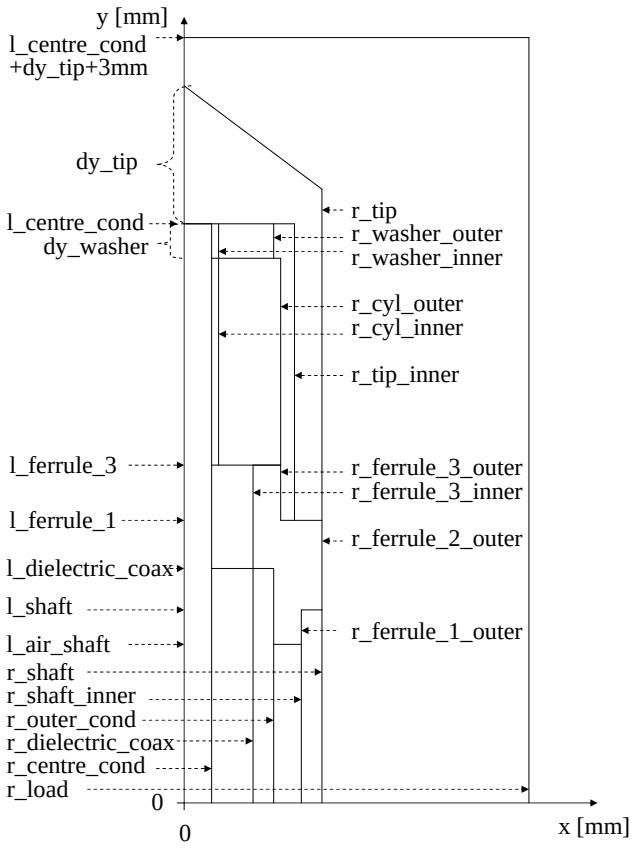

Figure 4.10: Definition of FEA model variables for electromagnetic analysis of applicator.

thermore, it is a homogenous solution reducing the random error in repeated sets of experiments. 0.58 % w/v denotes the weight-volume percentage of the saline solution, meaning that a mass of 0.58 g of sodium chloride (NaCl) was dissolved per 100 mL of water.

The third load, ex-vivo bovine liver, was chosen in order to allow ex-vivo bench tests for general device testing and measurements of ablation size. Both material properties of saline and ex-vivo bovine liver are given for 2.45 GHz and 20 °C.

4.3.5 Excitation

All model interfaces between 3D objects and the background are assigned 'perfect E' boundaries (see section 4.3.6) by default. As a consequence, no energy may enter or exit through them. In order to provide a window that couples the modelled device to the external world a wave port type excitation must be placed across one of these interfaces. In this model, the wave port was assigned across the interface of the waveguide dielectric. The natural field pattern associated with the given cross-section is then assumed by the model when calculating the S-parameter during the solution process. The input power

of this port was set to 1 W, and a scaling factor to 1/6 assigned in order to take into account the model symmetry, giving a total input power of 1 W for a full 360° model.

4.3.6 Boundary Conditions

A radiation boundary was applied on all outer surfaces of the model except the cross-sectional area of the waveguide. A radiation boundary allows a wave to radiate infinitely far into space by simulating an open problem. A wave at this boundary is absorbed by the model eliminating reflections from it.

Symmetry boundaries were assigned on all non-metallic surfaces within the symmetry planes. Assigning symmetry boundaries accounts for the reduced model geometry of only 60°. The correct symmetry type for this model was 'perfect H', defining the boundaries as natural boundaries through which the field propagates, that is, the tangential component of $\vec{H}$ is the same on both sides of the surface, and the electric field $\vec{E}$ is tangential to the symmetry planes.

4.3.7 Analysis Setup

The software utilised uses convergence in order to obtain an accurate solution. After creating an initial mesh and obtaining the initial solution being the S-matrix, HFSS begins to refine the mesh and resolve the problem during a number of subsequent adaptive passes. This process is repeated until the discrepancy between previous and current S-matrix falls below a certain limit. This limit is called 'maximum delta S' and is computed as a percentage. For instance, if the maximum error is found to be 5 %, but the defined 'maximum delta S' 3 %, the software will continue to refine the mesh and resolve the problem. If however, the maximum error is found to be 2 %, the solution has converged and the simulation finishes.

In order to influence the solution process and resulting solution accuracy, a number of parameters related to the process can be defined. The following settings were specified in the analysis setup in this model:

- Solution type: driven modal. The driven modal solution type was chosen as it allows the computation of S-parameters. The S-parameter solution will be expressed in terms of the incident and reflected powers of the waveguide mode.
- Solution frequency: 2.45 GHz.
- Maximum number of passes: 18. The simulation is forced to stop after a maximum number of 18 passes even if the solution did not converge. It prevents the model from refining the mesh endlessly.
- Minimum number of 3 passes; minimum number of 2 converged passes. Ensures that convergence is persistent.
- Adaptive mesh options: maximum refinement of 20 % per pass.
- Convergence per pass: maximum delta S of 0.001.
- Sweep setup: A 'fast sweep' is defined over a frequency range of 1 to 10 GHz in 50 MHz steps. When using a 'fast sweep' field solutions are available for all frequencies.

4.3.8 Parametric Analysis Setup

A parametric analysis was set up for three critical applicator component dimensions in order to predict the effects of dimensional changes on device performance. Critical applicator components were identified on the basis of the antenna structure being of dipole type. Hence, changes in the length of the dipole elements were expected to induce significant changes in resonant frequency. Furthermore, variations in radial washer dimensions had been shown to affect S11 in the 2.4 mm applicator.

Following those considerations, the variables chosen for parametric analysis were l_centre_cond, $l\_ferrule\_3$, and r_washer_outer. The model was created such that alterations in l_centre_cond stretched or compressed the cylinder length as indicated in figure 4.11, $l\_ferrule\_3$ the length of the ferrule representing the dipole element, and r_washer_outer the outer diameter of the washer. The values of the first and second variables were varied around the expected calculated dipole element length of approximately 3.8 mm; the other variables within the limits given by the proposed design.

Table 4.3 lists these variables together with the respective ranges and increments, resulting in a total of 16 analyses. A length of 28 mm for variable l_centre_cond hereby corresponds to a cylinder length of 3.7 mm, a value of 21.8 mm for $l\_ferrule\_3$ to a ferrule dipole length of 2 mm. Solving one analysis required approximately 15 min, 21 000 tetrahedra, and a number of 9 passes for convergence on a Dell 2.66 GHz workstation with 3 GB RAM.

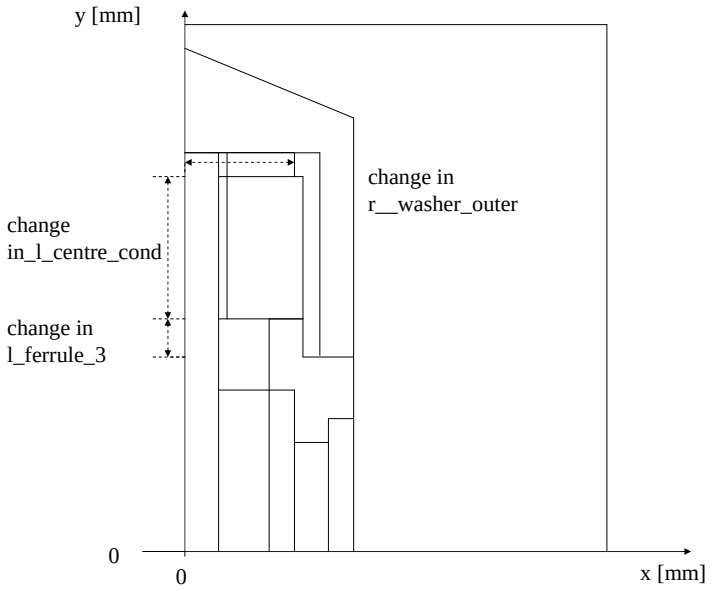

Figure 4.11: Model variables employed for parametric analysis.

Table 4.3: Values of optimisation variables.

Variable	Range [mm]	Step size [mm]
l_centre_cond	28-33	1
$l\_ferrule\_3$	21.8-25.8	1
r_washer_outer	0.3-0.6	0.15

4.3.9 Results

S11

Figures 4.12, 4.13, and 4.14 display the applicator's $S11$ for the parametric analyses of 28 mm to 33 mm for l_centre_cond, 21.8 mm to 25.8 mm for $l\_ferrule\_3$, and 0.30 mm to 0.60 mm for r_washer_outer, respectively.

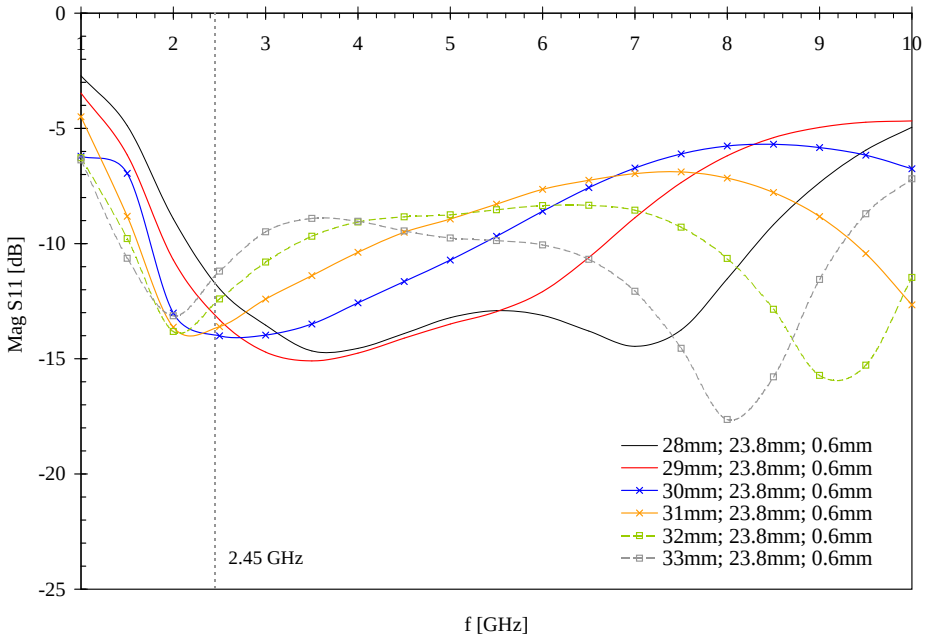

Figure 4.12: S11 of the applicator for various lengths of extended centre conductor: 28 mm to 33 mm in steps of 1 mm.

It can be seen from figure 4.12 that longer cylinder lengths, or l_centre_cond, shift the resonant frequency toward lower frequencies. A value of 30 mm for l_centre_cond was chosen since it offered a broad resonance with -14 dB at 2.45 GHz.

Figure 4.13 shows a decrease in S11 from -11 dB for $l\_ferrule\_3 = 21.8$ mm to -16 dB for $l\_ferrule\_3 = 24.8$ mm. For the final value of 25.8 mm, the S11 increased to -12 dB again. For reasons of design stability the value of $l\_ferrule\_3 = 23.8$ mm was hence chosen over the next longer one.

The effect of increasing the washer diameter can be seen in figure 4.14, whereby a greater diameters shift the resonance toward a lower frequency. The maximum possible value of 0.6 mm was hence selected for r_washer_outer.

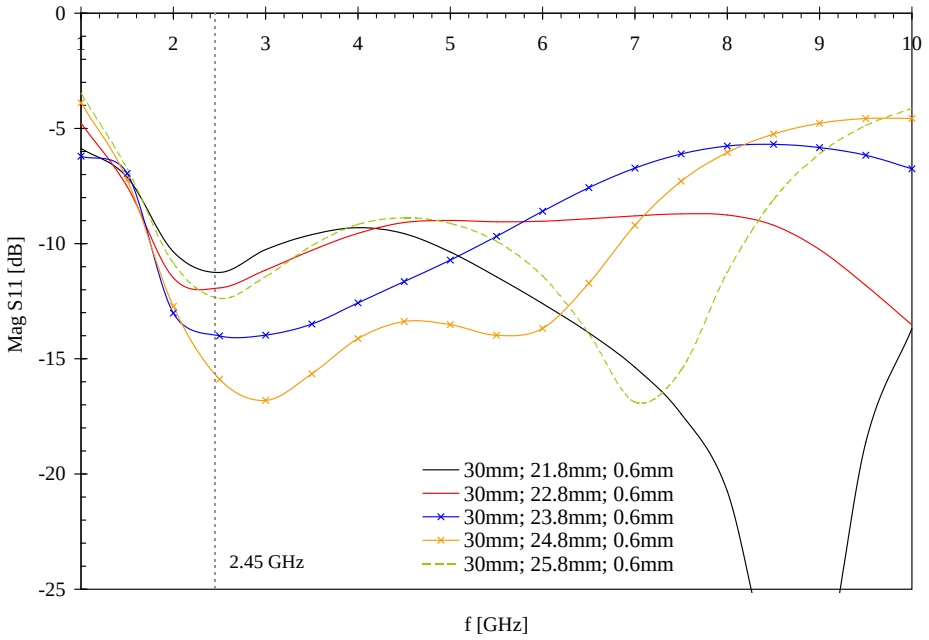

Figure 4.13: S11 of the applicator for various lengths of variable $l\_ferrule\_3$: 21.8 mm to 25.8 mm in 1 mm steps.

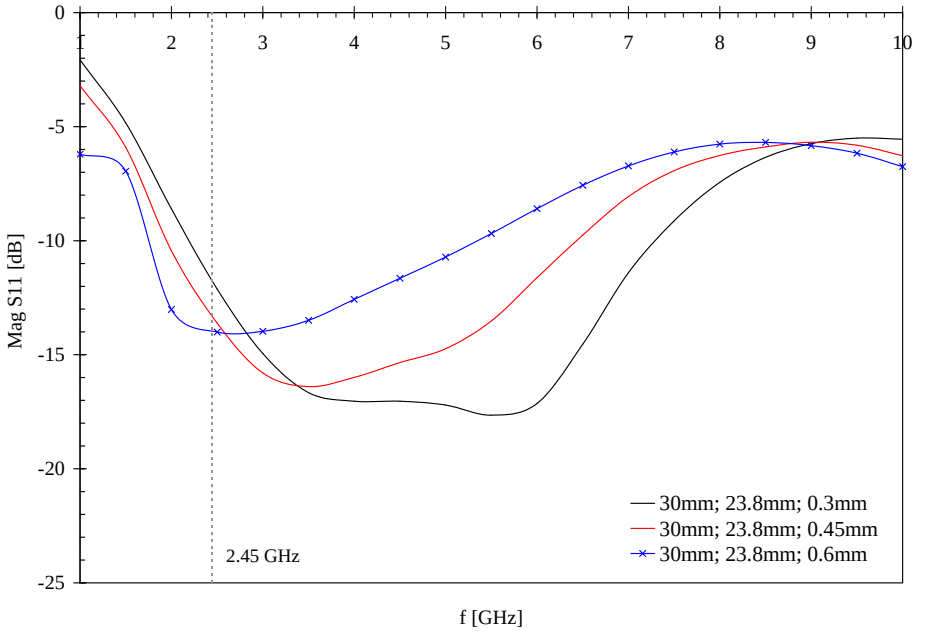

Figure 4.14: S11 of the applicator for various washer diameters r_washer_outer: 0.3 mm, 0.45 mm, and 0.6 mm.

The best design was therefore achieved with dipole lengths of 5.7 mm for the extended centre conductor and 4 mm for the ferrule, differing from the expected calculated length of a quarter wavelength of 3.8 mm (see section 4.2.2). This discrepancy can be explained by the fact that the load material is in fact a combination of adhesive, ceramic, and saline properties. Table 4.4 lists the wavelengths of a wave of frequency 2.45 GHz in the mediums concerned: adhesive, Y-TZP zirconia, and saline. The dipole element made

Table 4.4: Values of $\lambda/4$ for adhesive, zirconia, and 0.1M saline at 2.45 GHz.

Medium	$\varepsilon_r^{'}$	λ_m [mm]	$\lambda_m/4$ [mm]
Adhesive	3	70.1	17.7
Y-TZP zirconia	18	28.9	7.2
0.1M saline	77	14.0	3.5

up by the extended centre conductor is surrounded by a significant volume of ceramic material. The optimum length of 5.7 mm thus lies between that for ceramic and saline. In the case of the ferrule dipole element, the ceramic layer is less than half the thickness, hence mainly surrounded by the load. The optimum length of the ferrule dipole, 4 mm, is thus closer to the $\lambda_m/4$ value for saline.

The optimised applicator design was then solved for the remaining load materials, in-vivo malignant human liver and ex-vivo bovine liver tissue in order to assess the effects on applicator S11. Figure 4.15 displays the resulting $S11$ for all three loads - in-vivo malignant human liver, saline, and ex-vivo bovine liver. $S11$ is plotted in dB over a frequency range of 1 to 5 GHz, reading -14.8 dB, -14.1 dB, and -15.8 dB at 2.45 GHz for human liver, saline, and bovine liver, respectively. The frequency range of all three loads in which $S11$ is below -10 dB spans approximately 1.7 GHz to 5 GHz. It can hence be seen that there are no significant differences in $S11$ for the three similar load materials.

Electric Field Distribution

The magnitude of the electric field emitted by the antenna immersed into saline is displayed in figure 4.16 for phases ranging from 0° to 180° in 20° steps. It can be seen that microwave radiation is emitted at the antenna travelling radially outwards. In addition, the figure shows that some radiation is travelling back along the shaft.

SAR Distribution

The normalised SAR distribution (dB) of the optimised applicator design is shown in figure 4.17. Is was derived from the solution for 1 W input power, 2.45 GHz, and in-vivo human malignant liver load and is depicted on a logarithmic scale in colour-coded intervals of 5 dB from 0 dB to -45 dB. The irregularity in the contour lines, shown in black in the figure, stems from artefacts in the software. Sites of maximum SAR are located around the washer, distal and middle sections of the ferrule. The figure was generated by normalising local values of SAR, $LocalSAR$ in W/kg, to the maximum local SAR, SAR_{max} in W/kg, found inside the tissue. SAR_{max} was determined to 10

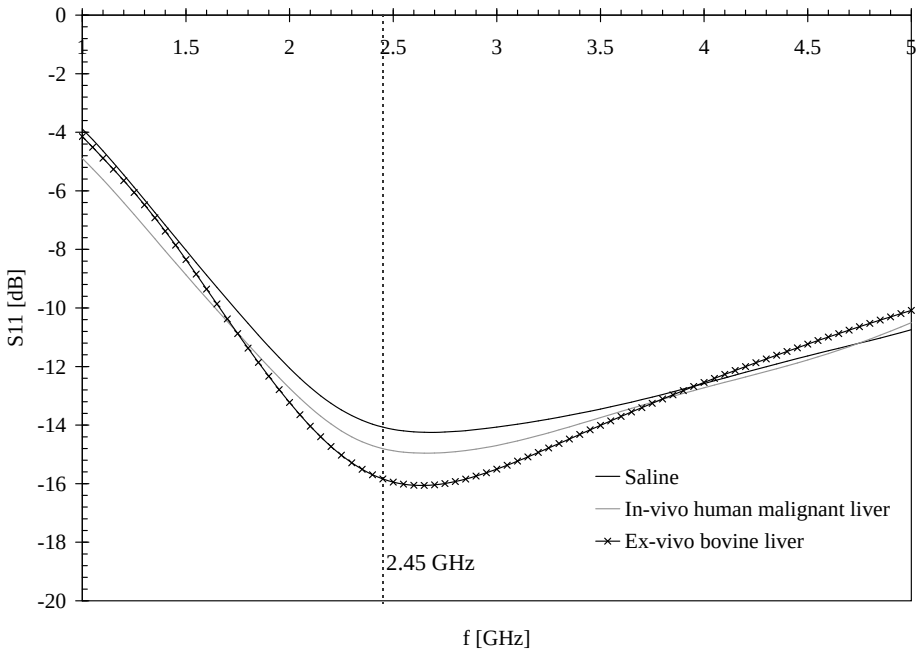

Figure 4.15: Modelled S11 of applicator in three load materials: in-vivo human malignant liver, saline, and ex-vivo bovine liver. Solution error ±0.1 dB.

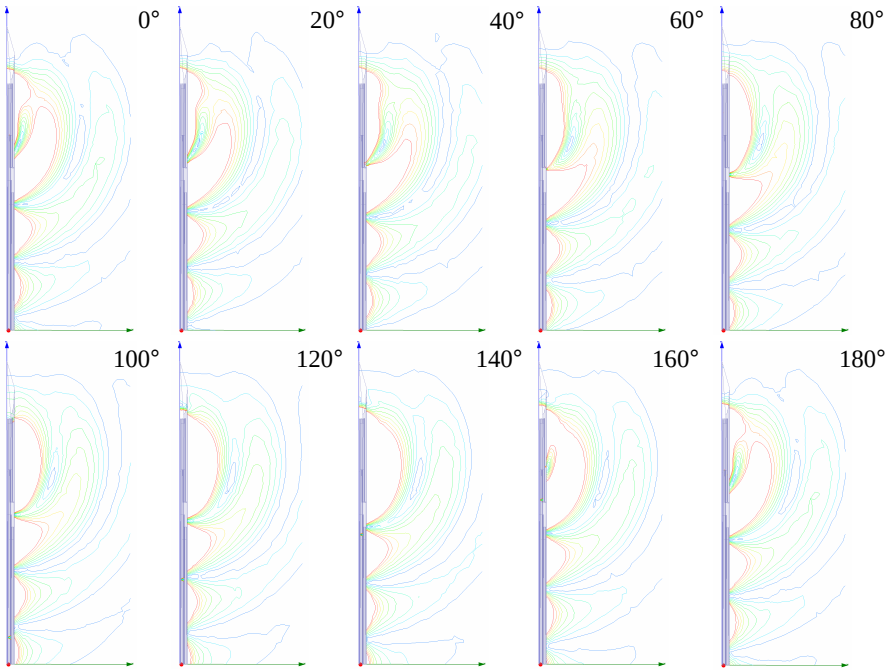

Figure 4.16: Modelled electric field distribution of the applicator in saline for phases from 0° to 180° in steps of 20°; magnitude of the electric field shown in colour-coded contours from 10 V/m (blue) to 500 V/m (red) in linear steps.

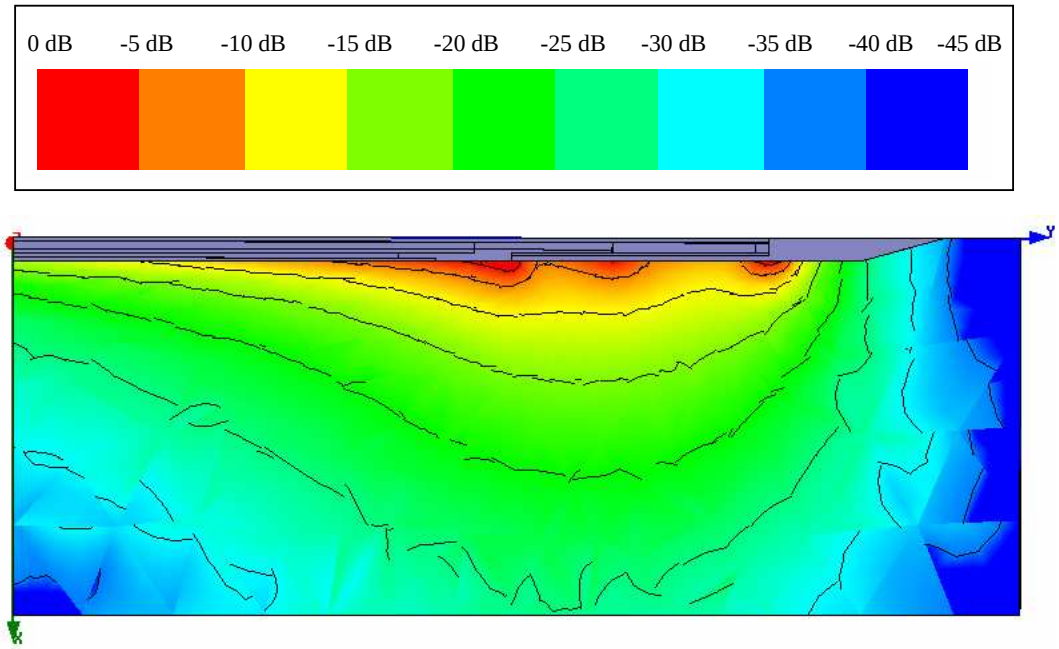

Figure 4.17: Normalised SAR distribution (dB) of applicator in dB for in-vivo human malignant liver; 1 W input power; 2.45 GHz; normalised to 10,000 W/kg. Irregularity in contour lines due to artefacts in software.

000 W/kg, the maximum value recorded at a node located inside the tissue and near the ferrule, that is not on one of the applicator surfaces. The resulting normalised SAR, SAR_{norm}, was then calculated via:

$$SAR_{norm} = 10 \cdot \log(LocalSAR/SAR_{max}) \tag{4.7}$$

4.3.10 Discussion

S11

Figure 4.15 shows that the applicator's $S11$ was (-15 ± 1) dB for all three materials considered. The antenna was therefore regarded resonant at 2.45 GHz.

Using an acceptance threshold of -10 dB, corresponding to 90 % transmission of input power, it can be seen that the device is well matched between 1.7 to 5.0 GHz. This was of importance as it had been suggested that the resonant frequency can shift during operation [64]. This can be explained by virtue of rising temperatures in the ablation zone which in turn alter tissue material properties due to decreasing water content. However, the extent of such a shift was not quantified. Therefore, a broad resonance was sought in order to ensure operation throughout the ablation.

SAR Distribution

Figure 4.17 gives a indication of an expected ablation size as it marks out the locations of direct and intense electromagnetic heating. It cannot predict a precise shape or size however, due to several reasons. Firstly, SAR identifies the locations of direct EM heating but neglects energy transfer due to heat conduction from nearby tissue. In addition, the ablation size is not only a function of temperature but rather temperature and time. Lastly, the shown SAR distribution is only correct for the very beginning of an ablation as temperatures close to the applicator rise beyond 100 °C within about ten seconds, drastically altering material properties and hence radiation pattern and SAR distribution. Despite all these complexities, an SAR distribution is the major indicator for ablation shape in the design of microwave ablation antennas.

Furthermore, it can be seen that the radiation pattern of the applicator does not greatly resemble that of an ideal dipole, in that it shows three distinct regions generating high fields (washer, distal end of ferrule, middle section of ferrule). These overlap for greater distances from the applicator. The figure also shows the SAR trailing back along the shaft. This is caused by electromagnetic waves travelling back on the outside of the shaft as shown in figure 4.16, an event common to many microwave applicators [75]. Efforts have been made by researchers to suppress this tail [76]. However, no further consideration was given to it at this stage, since no real ablations assessing its significance had been performed with the applicator as yet.

4.3.11 Conclusion

The applicator design was optimised with regards to three critical design variables using FEM models in order to determine the best return loss. Using a -10 dB threshold, the return loss of the optimised design was (-15 ± 1) dB at 2.45 GHz, hence meeting the acceptance criterion. Furthermore, the SAR distribution of the applicator in tissue was determined which indicated a pear-shaped ablation zone; however active cooling of the applicator shaft, which is expected to reduce the tail in an ablation, had been neglected so far since it belongs to the thermal analysis of the applicator performance. The modelled applicator $S11$ and SAR hence met the defined performance criteria, which lead to the subsequent applicator manufacture and testing described below.

4.4 Manufacture

4.4.1 Introduction

Following the theoretical investigations, the next step was the manufacture of devices in order to perform validation experiments. Hence, two applicators were built manually at the University of Bath. Device components, manufacturing processes, and experimental results are discussed in the following sections.

4.4.2 Components

The materials and components presented in section 4.2 were ordered according to the dimensions obtained from the theoretical optimisation. Machining tolerances were taken into account to guarantee fit between individual components. All items together with their respective materials, manufacturers, and part numbers if applicable are listed in table 4.5. The complete engineering drawings of all components can be found in appendix A.

Table 4.5: Components for manufacture of first applicator.

Item	Material	Supplier/Manufacturer	Part number
Cable assembly	Refer to 4.2.3	Rhophase Microwave Ltd.	N/A
Ferrule	Copper	Datum Precision Eng.	N/A
Washer	Copper	Datum Precision Eng.	N/A
Cylinder	Y-TZP ceramic	Astro-Med, Inc.	N/A
Tip	Y-TZP ceramic	Astro-Med, Inc.	N/A
Handle	PEEK	Datum Precision Eng.	N/A
Shaft	304 stainless steel	Small Parts, Inc.	HTX-15X
Adhesive tip	Urethane methacrylate	Henkel	Loctite 638
Solder paste	63Sn/35Pb/2Ag	Electrolube	N/A
Coating	Silicone dispersion	NuSil	MED10-6607

4.4.3 Manufacturing Procedure

The top half of figure 4.18 displays a set of applicator parts, including the semi-rigid coaxial cable assembly, shaft, ferrule, cylinder, washer, and tip (handle parts not shown). A picture of the finished applicator is depicted below including a magnification of the tip. The applicator was built according to the manufacturing procedure specified in appendix B.

4.5 Measurement of Scattering Parameter $S11$

Validation consisted of the measurement of the device's scattering parameter $S11$. Although SAR was utilised for design development it could not be measured due to the lack of necessary equipment.

S11 was measured using a network analyser (Wiltron 37269A) of frequency range 40 MHz to 40 GHz. S11 measurements of type log magnitude were undertaken from 1 GHz to 10 GHz in saline. The saline solution was of concentration 0.58 % w/v and at room temperature, the same conditions as applied in the FEM model.

Figures 4.19 and 4.20 display the recorded S11(dB) data together with the results obtained from the FEA on logarithmic and linear scales, respectively. The measured data was subjected to a smoothing routine in order to eliminate high-frequency oscillations caused by reflections at connectors and interfaces. The solid black lines with markers depict the smoothed measured data; black dashed lines the modelled data. S11 at 2.45

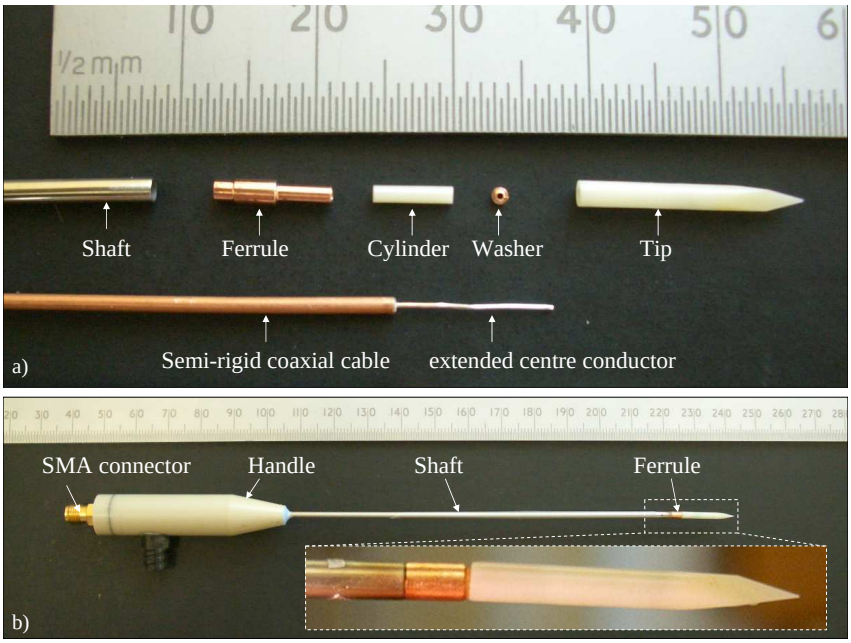

Figure 4.18: Components for manufacture of first applicator (a). Fabricated applicator with magnified tip section (b).

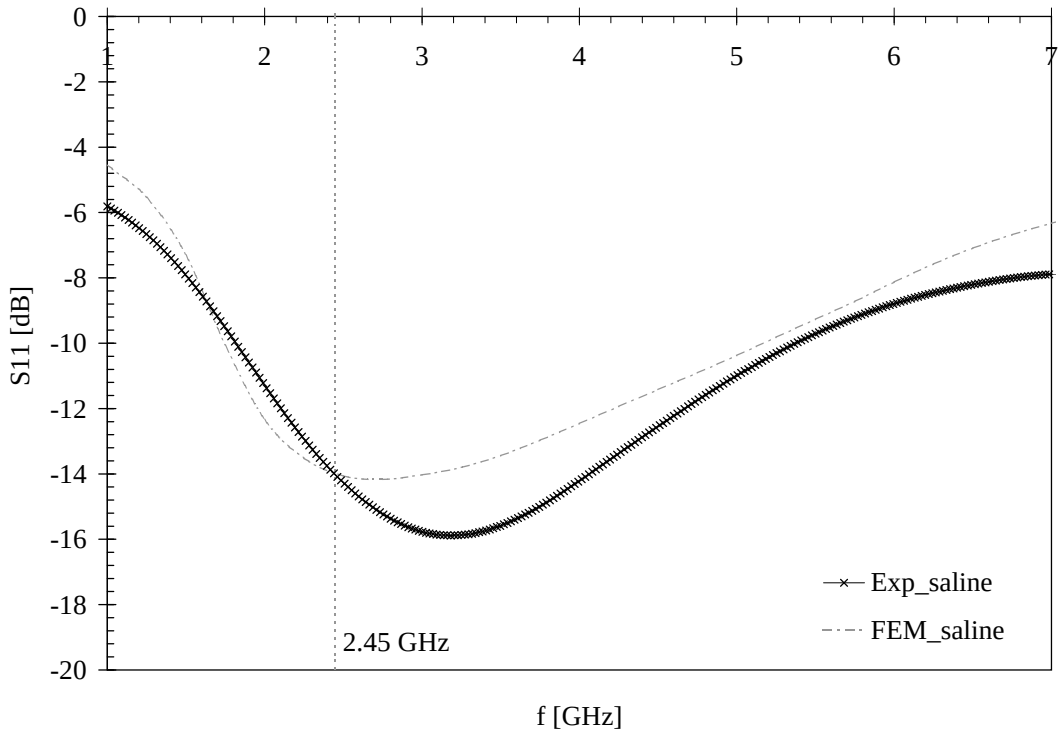

Figure 4.19: Measured (exp) and modelled (FEM) $S11$(dB) of 1.8 mm applicator in 0.58 % w/v saline. $S11$(dB) on log scale.

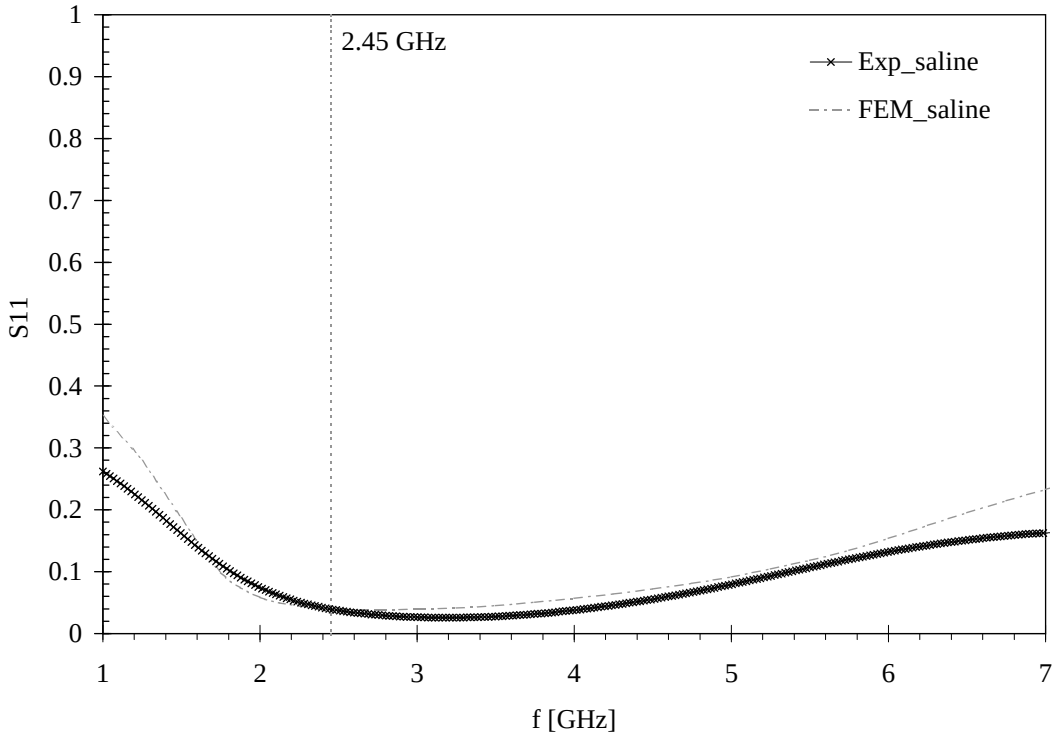

Figure 4.20: Measured and modelled $S11$(dB) of 1.8 mm applicator in 0.58 % w/v saline on linear scale.

GHz was measured to −14.2 dB in saline. The corresponding value from the FEA was −14.0 dB.

Although measured and modelled data agreed well at 2.45 GHz, they differed in value for frequencies above 2.45 GHz. This discrepancy in measured to modelled $S11$ is amplified in figure 4.19, as the logarithmic scale magnifies small changes at low values. For this reason, S11 was also plotted on a linear scale. It can be seen, that the discrepancy between model and measurements for higher frequencies appears less significant. Nevertheless, differences in the data indicate that some characteristic of the applicator had not been taken into account in the model. Possible parameters include dimensional differences and differences in material properties. Consequently, the FE model was run for a number of changes in the model in order to determine the source of the discrepancy in modelled and recorded S11 data.

The first analysis consisted of an identical setup and geometry but included frequency-dependent saline properties. The saline properties used are given in table 4.6 and were taken from [74] for 20 °C and 0.1 N saline. The second analysis included a glue gap

Table 4.6: Frequency-dependent properties of 0.1 N saline from 1 GHz to 10 GHz for 20 °C [74].

f/GHz	1	2	3	4	5	6	7	8	9	10
ε_r'	77.77	76.94	75.60	73.81	71.64	69.18	66.49	63.65	60.74	57.81
$-\varepsilon_r''$	22.55	18.08	19.28	21.68	24.35	26.95	29.31	31.38	33.13	34.57

between washer and tip of 0.1 mm height. The resulting S11 for both analyses are shown in figure 4.21.

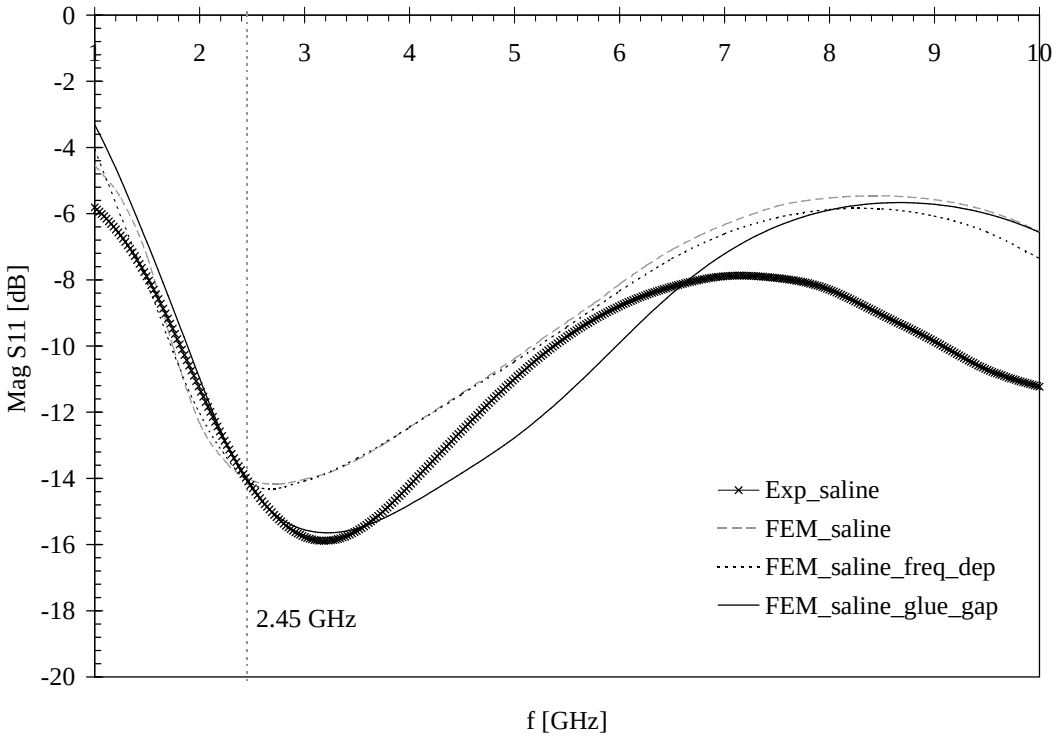

Figure 4.21: Modelled S11 of applicator for frequency-dependent saline properties and glue gap between washer and tip of height 0.1 mm.

It can be seen that the input of frequency-dependent saline properties did not change the $S11$ significantly. However, the inclusion of a glue gap between washer and tip, although extremely small, altered the applicator's $S11$. Figure 4.22 highlights the reason for this change in $S11$: any space or glue gap behind the washer will allow the field to continue around the washer and into the space behind it leading to high intensity fields in this area. The figure plots the electric field magnitude in the applicator antenna for a sequence of phases ranging from 0° to 160° in 20° steps. Highest values of electric field magnitude are displayed in red, lowest values in blue. The electric field magnitude oscillates from minimum to maximum in the area behind the washer, that is in the glue gap. The existence of such a thin layer of glue between washer and tip is very likely as glue is applied to the entire tip structure during the assembly. It was hence concluded that the initial discrepancy between modelled and measured data was largely due to neglecting glue gaps such as the one investigated between washer and tip.

4.6 Conclusion

This chapter presented the theoretical background to the operation of the proposed applicator design. The design of the developed 1.8 mm applicator was derived from the design of an existing 2.4 mm device and adapted where necessary. FEM computer simulations were created and utilised to optimise critical applicator components by means

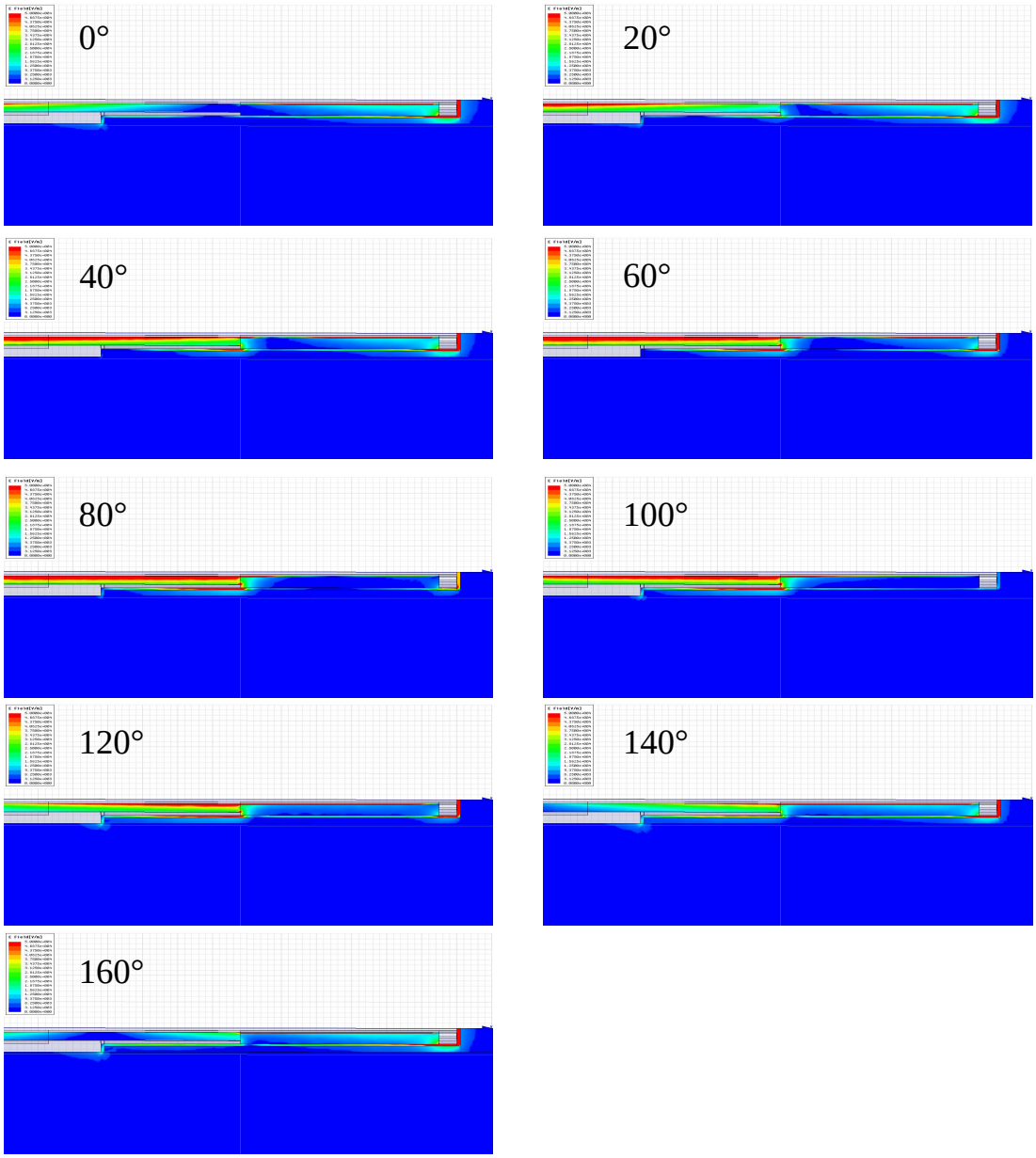

Figure 4.22: Electric field magnitude in the applicator antenna for a sequence of phases ranging from 0° to 160°; step size 20°.

of $S11$ comparison. The optimised applicator design was then analysed in terms of its $S11$ and SAR, whereby $S11$ was determined for three different load materials. The SAR was pear-shaped, which was regarded as a satisfactory indication of the desired spherical zone of heating at this stage, since active cooling would improve ablation shape further. Two applicators were then built and their $S11$ measured. Comparison of modelled and measured $S11$ data showed an initial discrepancy. Further computer simulation showed that the discrepancy was likely due to minute glue gaps in the assembled device. The applicator showed a broad resonance with $S11$ below $-$ 10 dB from approximately 2 GHz to 5 GHz. The applicator design presented hence met four

of the design requirements listed in table 3.1– a device diameter below 2 mm, a sharp cutting tip, an appropriate shaft length, and a return loss below −10 dB at 2.45 GHz.

In order to be able to test the applicator in operation with high input powers, as would ultimately be required, the current open cycle cooling system had to be improved. A significant amount of work was therefore undertaken to develop a suitable cooling system for the applicator. The design process and design sequence of cooling solutions developed will be discussed in detail in the following chapter 5.

Chapter 5

Development of Applicator with Integrated Closed Cycle Cooling System

5.1 Introduction

The applicator design presented in chapter 4 showed good electromagnetic performance and a device diameter of 1.8 mm, meeting the first set of requirements. However, the current cooling system of the device consisted of a simple open-cycle cooling system created by guiding coolant through the applicator shaft and then through holes in the shaft close to the ferrule out into surrounding tissue. Saline, which could simply be seen as surplus free water, was therefore injected directly into the ablation zone where intense MW heating occurs. Such extra free water is quickly heated above the boiling point and hence turned into water vapour spreading uncontrollably in the tissue.

Using open-cycle cooling, the probability of creating irregular ablation shapes is therefore high and has occurred regularly as part of this work during applicator bench testing in ex-vivo bovine liver. Alarming results were also published by Goldberg et al following animal studies using RF ablation stating that the injection of saline in an ablation zone may increase the coagulation of normal liver tissue significantly, however the degree and shape of the final ablation zone were unpredictable [77]. Unpredictable coagulation zones however should be avoided as they pose a serious health risk for patients since healthy tissue or vital organs may be damaged during the process.

Furthermore, an experiment conducted by Hardie several years ago visualised the extent of surplus water or vapour movement during an ablation [73]. In the experiment, a small amount of the radioactive isotope technetium, which is a radioactive metallic element used as a diagnostic radiopharmaceutical, was injected into tissue close to the applicator tip prior to the commencement of an ablation. A 100 W, 3 min ablation was then performed during which the technetium was tracked by recording the emitted radiation from the ablation zone using a gamma camera. The resulting locations of the injected isotope are displayed in figure 5.1 at three different times – immediately before the ablation, after 90 s, and at the maximum ablation time of 3 min. It can be seen that the largest distance travelled by the radioactive isotope was 23 cm, recorded at the very end of the 3 min ablation. In this instance, blood vessels were responsible for

guiding the fluid and steam along the path of least resistance to locations in the liver tissue as far away as four to five times its actual ablation radius.

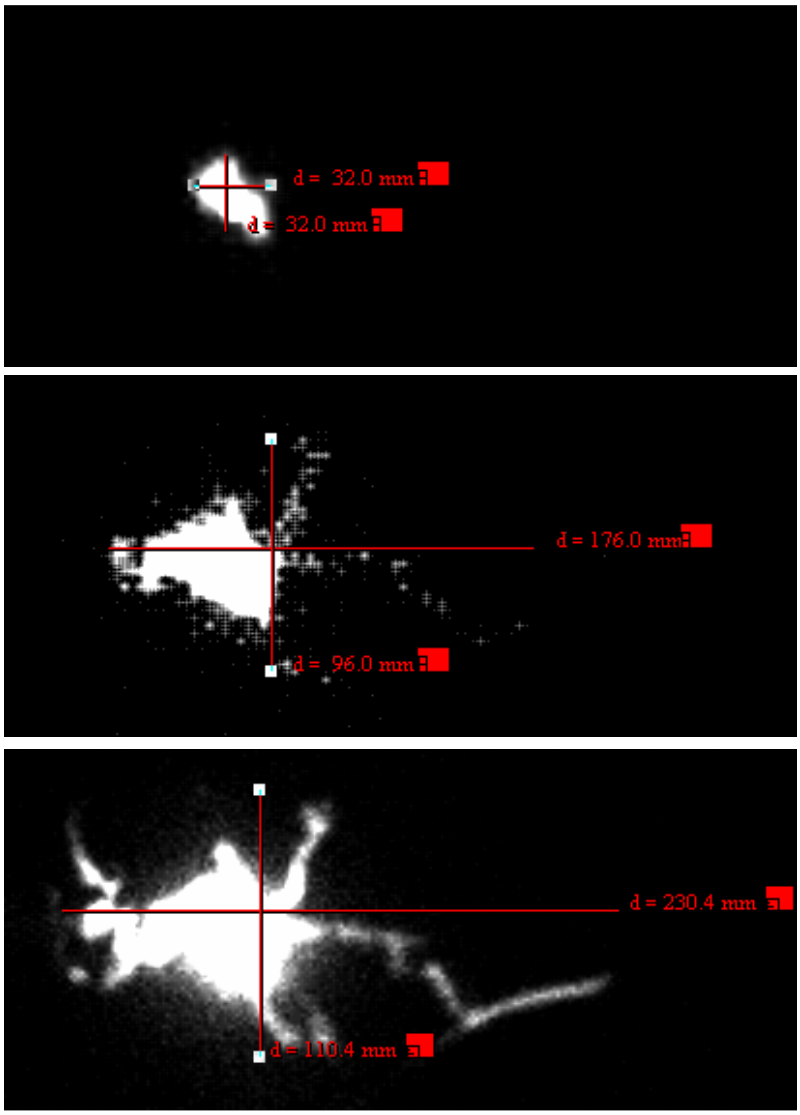

Figure 5.1: Visualisation of fluid and steam movement during an ablation by tracking of a radioactive isotope injected prior to the ablation using a gamma camera; pictures recorded at 0 s, 90 s, and 180 s.

Although air-filled blood vessels are not relevant during in-vivo treatments, blood vessels nevertheless often present the path of least resistance for fluids and steam in biological tissues. It was hence concluded that the injection of unnecessary and surplus fluid into an ablation zone presents a serious health risk for patients; it should therefore be avoided whenever possible.

In addition to that, a closed-cycle applicator cooling system was required in order to meet the requirements posed on the applicator design (see page 40) regarding the maximum allowable temperature of 48 °C applying to all external applicator surfaces

of shaft, handle, and feed cable. The feed also had to satisfy demands concerning its length (1 m to 3 m), flexibility and weight. The latter two were specified via a maximum allowable feed cable diameter of 4 mm. Since a flexible coaxial cable of those dimensions would heat up to temperatures above the set limit, the cooling system also had to include the handle and feed cable portions of the applicator.

5.2 Review of Existing Closed-Cycle Cooling Concepts

Cooling of RFA and MWA applicators has become more and more significant in the development of a new device which is mainly due to the demand for more powerful devices. In addition to a number of existing traditional closed-cycle cooling concepts more complex systems have emerged recently for the cooling of applicator shafts. The following section will give an overview of these existing closed-cycle cooling systems and comment on their suitability for integration into the applicator design. It will also comment of the main types of feed cable cooling.

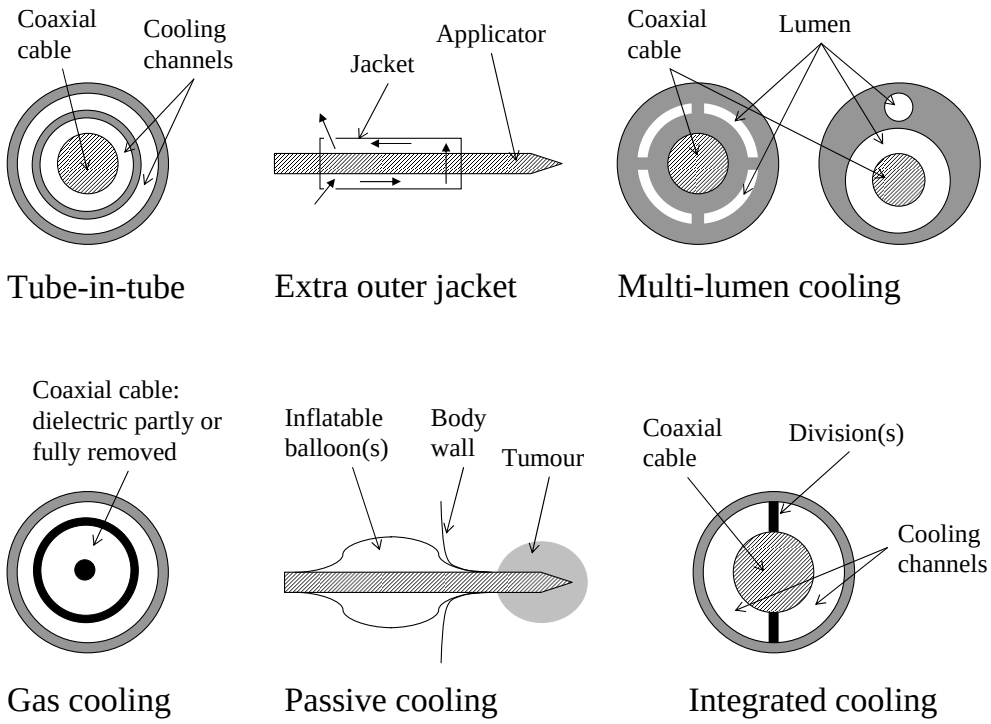

Figure 5.2: Selection of existing cooling systems for thermal ablation devices.

Tube-In-Tube Cooling System

A tube-in-tube cooling system consists of two nested tubes with the applicator going through both of them. The coolant flows toward the applicator tip in an annular space between outer and inner tube and returns in the space between inner tube and coaxial cable as indicated in figure 5.2 in the top left corner.

The tube-in-tube design is a popular simple yet powerful cooling solution and was considered as a possible applicator cooling concept. The main challenges in incorporating a tube-in-tube cooling system into the applicator lay in the existing restriction of the applicator diameter and the simultaneous requirement for mechanical shaft stability. Two tubes were needed for this design; an outer tube featuring an OD of ≤ 2 mm and an inner tube having an OD smaller than the ID of the outer tube. Furthermore the ID of the inner tube must be ≥ 1.2 mm as this is the outer diameter of the coaxial cable. Hence, a tube of wall thickness ≤ 0.15 mm was required. Extra thin-walled hypodermic tubing was found (Small Parts, Inc.); however the minimum wall thickness still measured 0.20 mm. The concept of a tube-in-tube was hence regarded unfeasible for this particular device and another solution was sought.

Extra Outer Jacket Cooling System

In this design, an applicator is surrounded with an extra outer jacket through which the coolant is forced. There are two main jacket types – cylindrical as shown in figure 5.2, or tubing coiled around the applicator shaft. Advantages of this design include simplicity, low costs and adaptability. However, an extra outer cooling jacket system is unsuitable for the current applicator design as cooling is needed as close to the tip as possible which would hence drastically increase the outer diameter of the device.

Multi-Lumen Cooling System

The use of multi-lumen tubing often presents a simple and elegant solutions for a variety of problems where separate pathways are needed. A large number of different tubing offering many shapes and sizes are available from commercial sources; for further examples consult [78, 79]. Figure 5.2 shows the cross-sections of two types of multi-lumen tubing with fluid channels displayed in white. Depending on the problem, any configuration of channels utilised as in- and output is generally possible.

The feasibility of a multi-lumen cooling system for the applicator was investigated and suitable tubing searched. However, no fitting size could be found in the pool of available standard tubing and since custom made tubing is costly, the use of multi-lumen tubing was put aside at that time.

Gas Cooling System

Another cooling concept utilises gases instead of fluids as coolants. In gas cooling systems, the dielectric of the coaxial cable is partially or fully removed in order to allow gas or air to circulate through the coaxial cable cooling the applicator.

Prior to this work, the latest research of the MDTG at the University of Bath focussed on the development of such a cooling system resulting in the manufacture of two gas cooled applicators [64]. In these applicators, centricity of the centre conductor was warranted within limits by the introduction of spacers along the cable length. The concept was validated successfully by Lepers [64] in applicators of 5 mm and 2.4 mm diameter. In the case of the 5 mm applicator, the air cooling stabilised the temperatures

at the shaft, measured at a distance of approximately 5 cm from the radiating tip, to (45 $\pm$ 2) °C during ablations of 100 W, air flow rate of 10 l/min, and air input temperature of 10 °C. In tests with the 2.4 mm device, the cooling effect was amplified by using CO_2 gas of flow rate 3.25 l/min and a gas input temperature of (-14 ± 2) °C. In ex-vivo ablations of 80 W this setup resulted in shaft temperatures of (16 $\pm$ 2) °C, measured at the same location as before.

Advantages of gas cooling include narrow device diameter and readily available coolant (in the case of air). However, gas cooling was considered unsuitable in the context of this work due to two reasons. Firstly, the gas-cooled system required the use of pressurised gas (air or CO_2) usually supplied in gas cylinders. For cooling the 2.4 mm device, the gas had to be guided through a heat exchanger in order to significantly lower the gas input temperature to around -20 °C. The experimental setup and requirements for the gas cooling were hence considered unfavourable for use in operating theatres. Secondly, a more powerful cooling system was required for a 1.8 mm applicator as the insertion loss and therefore heat generation in coaxial cables increases for smaller diameters. Insertion losses of the cables used in the 1.8 mm and 2.4 mm applicators are 1.61 dB/m and 1.02 dB/m, respectively. Losses in the 1.8 mm device have therefore increased by 58 % compared to those of the 2.4 mm one, thus requiring a cooling system capable of extracting an additional approximate 58 % of heat energy. In addition to the rise in generated heat, the surface area of the smaller cable decreased reducing the contact area available for cooling. It was therefore concluded that a more powerful cooling was needed for use in the developed 1.8 mm applicator.

Passive Cooling System

Passive cooling as a protection against skin burns can also be achieved by simply creating a physical separation between the body wall and the applicator as depicted in figure 5.2. In these cooling types, single or multiple inflatable balloons are attached to the applicator shaft which, once inflated, force the tissue away from the device.

In cases of mild applicator heating, a passive cooling system like this one might offer a simple solution. However, in the case of the intense applicator and shaft heating in the 1.8 mm device, an active and much more powerful cooling mechanism is required.

Integrated Cooling System

An example of an integrated cooling system is displayed in the bottom right hand corner of figure 5.2. In this instance, two separate cooling channels are formed by two barriers located between the outer shaft and the coaxial cable which run along the full length of the device. The advantage of such a design is the ability to retain the original diameter of an applicator. Besides, it should offer excellent cooling capabilities since the coolant could be in direct contact with the coaxial cable. Furthermore, it is generally possible to produce a larger number of channels which would allow for constant cooling along the entire circumference. However, the major disadvantage of this design is seen in the manufactureability since water-proof seals are required between the barriers, shaft and cable.

Endothermic Sheath Cooling System

Endothermic sheath cooling system utilises chemical reactions between substances placed in sheaths around the applicator shaft to cool the device. The chemical reaction is initiated by penetrating or breaking the layers which initially separate the two chemicals. As long as the chemical reaction takes place in the surrounding layers, energy is transferred from the applicator to those layers and hence cooling the applicator shaft.

Cooling systems using endothermic chemical reactions can be a neat solution and might be useful in entirely different problems as they differ significantly from most of the traditional fluid cooling concept. However, they were not considered suitable as an active cooling of ablative devices.

Feed Cable Cooling

The main concepts for the cooling of the feed cable are multi-limen tubing and insulation spacers or tubes. In the first instance, the multi-lumen tubing is used as in the case shown in figure 5.2 except that the coaxial cable is now flexible rather than semi-rigid. In the second case, the hot cable is simply insulated or physically separated using spacers, tubes or spirals. Although the latter presents a simple solution for preventing patient skin burns, the use of spacers or spirals can make the device rigid and hence cumbersome to handle. Such a design was therefore not regarded desirable for the cooling the feed cable as part of this applicator development leading to the need of finding more convenient solution to this problem. Excessive heating of the feed cable presents one of the major problems and limiting factors concerning microwave ablation devices. Hence, providing adequate cooling of the feed cable had to be part of the design of a fully cooled applicator.

Conclusions

Some of the presented existing closed-cycle cooling systems such as gas cooling, tube-in-tube cooling or multi-lumen cooling were considered in the search of a suitable cooling system for the 1.8 mm applicator. However, none of the ones listed could ultimately deliver what was needed or couldn't be used for different reasons. The following section highlights some of the difficulties faced in trying to develop a successful cooling system for both applicator and feed cable.

5.3 Difficulties in the Development of a Closed-Cycle Applicator Cooling System

5.3.1 Size Restrictions

The first difficulty was faced when trying to scale down one of the reviewed existing cooling concepts. It quickly became obvious that tube-in-tube and similar concepts were not suitable for the 1.8 mm applicator due to the very small sizes needed – the

radial gap itself between coaxial cable and shaft was only 0.21 mm. It was concluded that as much as possible of the space between coaxial cable and shaft should be used for the active cooling and that no extra outer jacket or part should be added.

5.3.2 Difficulties in Manufacture

Some of the reviewed closed cycle cooling concepts were not pursued due to difficulties in manufacture. For instance, techniques for installing multi-lumen tubing or special barriers to from channels were limited. Furthermore, fragile structures such as the coaxial cable, ferrule and ceramic pieces were to be protected during the assembly in order to avoid damage caused by kinking, bending or breaking of the parts. Therefore, a relatively simple manufacturing process was required for fabricating the closed-cycle cooling system.

5.3.3 Infringement of Patents

In addition to the difficulties stated in the previous sections, the infringement of existing patents in relation to closed cycle cooling systems had to be avoided. In particular, the patent application publications [80] and [81] were of importance, concerning a large number of specific designs of water-cooled microwave ablation devices. To the best of the author's knowledge, none of the cooling solutions presented in this work infringe any existing patents.

5.3.4 Required Energy Dissipation

The cooling system had to dissipate heat energy stemming from two kinds of heat sources: heat conducted into the cooling system from the partly surrounding external hot ablation zone and heat generated due to losses in the coaxial cables including semi-rigid and flexible feed cable. In the assessment of the required energy dissipation of the cooling system the former heat source could be neglected when compared to the latter much greater heat source since most of the energy delivered to the ablation zone will be used to heat a volume of tissue with only a small fraction of that heat conducting back along the shaft. The following analysis estimates the quantity of heat that the cooling system was to dissipate and necessary flow rates to do so.

For the purpose of this analysis, a possible flexible feed cable for the applicator design was chosen having the following characteristics and dimensions: an outer diameter of 2.7 mm, a length of 2 m, and insertion loss of 1 dB/m. In addition to that, a length of multi-lumen tubing of OD 7.5 mm (major) and 5.5 mm (minor) was selected featuring two lumen with IDs of 4.1 mm (major) and 1.5 mm (minor) as illustrated in figure 5.3. The multi-lumen tubing is also referred to as 'umbilical tubing' in the remainder of this work. The flexible cable was intended to be inserted into the major lumen leaving enough space around it for water to flow past. The minor lumen was intended for coolant supply connecting the applicator handle.

The heat Q (J) generated per second in the coaxial cables can be determined by cal-

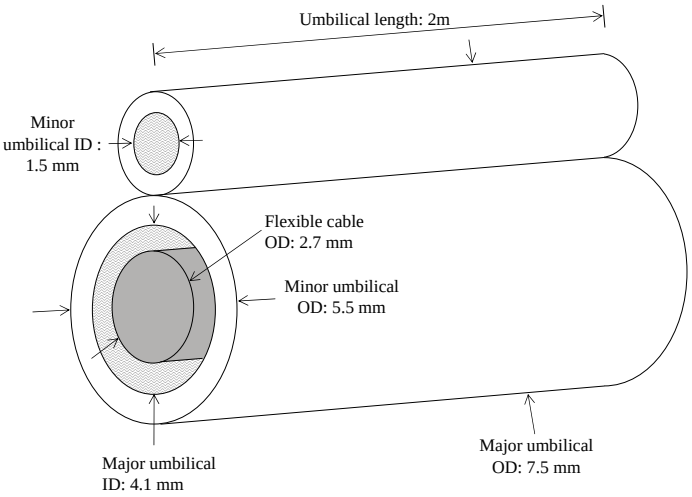

Figure 5.3: Dimensions of umbilical tubing cooling the flexible applicator feed cable.

culating the drop in power along the cables $P_0 - P_{tip}$ between input power P_0 and tip power P_{tip} using respective values of insertion losses in dB and cable lengths l_f and l_{sr} in m for flexible and semi-rigid cable, respectively. The total loss of connectors was assumed to be -0.2 dB, and the input power P_0 set to 148 W. This maximum input power was chosen in order to obtain a maximum tip power of 84 W which was the same maximum tip power allowed in the larger 5.6 mm applicator + 15 %. The total heat generated per unit time $\dot{Q}$ (J/s) is hence given by:

$$\begin{aligned} \dot{Q} = P_0 - P_{tip} &= P_0 - P_0 \cdot 10^{loss \cdot l/10} \\ &= P_0(1 - 10^{loss \cdot l/10}) \\ &= 148(1 - 10^{(-1.61 \cdot 0.168 + (-1) \cdot 2 + (-0.2))/10}) \\ &= 64 \end{aligned} \tag{5.1}$$

As can be seen, almost half of the input power is turned into heat due to cable losses. The majority of those losses are encountered in the long flexible cable. The cooling system therefore had to dissipate a total energy of 64 J per s.

Assuming there is no heat transfer between the coolant and the surrounding air, the coolant was water of temperature 27 ° (27 ° is the maximum allowable temperature for operating theatres as defined by regulatory bodies; the maximum temperature of the coolant may be assumed to be of the same value), density $\rho = 1000$ kg/m^3, and specific heat capacity $c_p = 4181$ J/(kg $\cdot$ K), and a total volume V in m^3 of water in the cooling system surrounding semi-rigid and flexible cable of:

$$\begin{aligned} V &= \pi l_{sr}((ID_{shaft}/2)^2 - (OD_{sr}/2)^2) + \pi l_f((ID_{umb}/2)^2 - (OD_f/2)^2) \\ &= \pi 0.168((1.6 \cdot 10^{-3}/2)^2 - (1.2 \cdot 10^{-3}/2)^2) + \pi 2((4.1 \cdot 10^{-3}/2)^2 - (2.7 \cdot 10^{-3}/2)^2) \\ &= 1.5 \cdot 10^{-5} \end{aligned} \tag{5.2}$$

, the coolant would experience a rate of heating $\frac{\Delta T}{t}$ in K/s of:

$$\begin{aligned} \frac{\Delta T}{t} &= \frac{Q}{mc_p t} \\ &= \frac{64}{1.5 \cdot 10^{-5} \cdot 1000 \cdot 4181 \cdot 1} \\ &= 1.0 \end{aligned} \tag{5.3}$$

Allowing a maximum temperature rise ΔT_{max} of the coolant of 10 K, that is from 27 ° to 37 °, a required minimum mass flow rate $\dot{m}$ (kg/s) for the coolant results according to:

$$\begin{aligned} \dot{m} &= \frac{V \cdot \rho}{\frac{\Delta T_{max}}{\Delta T / t}} \\ &= \frac{1.5 \cdot 10^{-5} \cdot 1000}{10/1.0} \\ &= 1.5 \cdot 10^{-3} \end{aligned} \tag{5.4}$$

which is equivalent to a volumetric flow rate of 5.4 l/hr. Using the cross-sectional areas A_{shaft} and A_{umb} of the cooling channels in shaft and umbilical tubing, the respective fluid velocities ν_{shaft} and ν_{umb} (m/s) can be computed. The cross-sectional area of one cooling channel in the shaft is hereby determined to be half of an approximate available 80 % of the total cross-sectional area giving $A_{shaft} = 3.6 \cdot 10^{-7}$ m^2; the cross-sectional area of the cooling channel in the umbilical tubing is $A_{umb} = 7.5 \cdot 10^{-6}$ m^2, the area of the coolant feed channel $A_{feed} = 1.8 \cdot 10^{-6}$ m^2. The fluid velocities in shaft, umbilical, and feed tubing can therefore be estimated to 4.2 m/s, 0.2 m/s, and 0.8 m/s according to:

$$\begin{aligned} \nu_{shaft} &= \frac{\dot{m}}{\rho A_{shaft}} = 4.2 \\ \nu_{umb} &= \frac{\dot{m}}{\rho A_{umb}} = 0.2 \\ \nu_{feed} &= \frac{\dot{m}}{\rho A_{feed}} = 0.8 \end{aligned} \tag{5.5}$$

These calculations show that in order to provide adequate cooling for the applicator a volumetric flow rate in the order of 5 l/hr will be necessary resulting in fluid velocities in the orders of 4 m/s and 1 m/s in shaft and umbilical cable, respectively. Thus, the syringe pump (Graseby 3100) used previously for open-cooled applicators would not be suitable to provide the required estimated flow rate of 5 l/h as its maximum flow rate was limited to a fraction of that, 0.199 l/h. A suitable pump would hence be required.

5.3.5 Required Pressure

The pressure drop between cooling system input and output was estimated in order to determine the necessary pump power. The cooling system can be split into two parts – shaft and umbilical tubing. Although most of the pressure will be dropped across the small cooling channels in the shaft, the contribution of all parts will be determined in

this section.

In fluid dynamics, a hydraulic diameter D_h is often used for non-circular channel geometries as it can then be used to calculated many of the parameters applicable to the circular tube case which are well-understood. Hence, the hydraulic diameter (m) of the cooling system in the shaft was determined using the cross-sectional area A_{shaft}, as calculated in the previous section, and a wetted perimeter U (m) of the cross-section which was defined in accordance to A_{shaft} as half of 80 % of the total perimeter for an annular disk made up by coaxial cable and shaft:

$$\begin{aligned} D_h &= 4 \cdot \frac{A}{U} \\ &= 4 \cdot \frac{A}{0.5 \cdot 0.8 \cdot 2 \cdot \pi(OD_{sr}/2 + ID_{shaft}/2)} \\ &= 4 \cdot \frac{3.6 \cdot 10^{-7}}{0.8\pi(0.6 \cdot 10^{-3} + 0.8 \cdot 10^{-3})} \\ &= 4.1 \cdot 10^{-4} \end{aligned} \tag{5.6}$$

Following that, the so-called Reynolds number Re was determined. Re is a dimensionless number and a measure of inertial forces to viscous forces for given flow conditions. Low Reynolds numbers mean the flow is laminar, whereas Reynolds numbers above 10^4 stand for fully turbulent conditions. The onset of turbulence is defined by the critical Reynolds number $Re_c = 2300$. In laminar flow viscous forces are dominant and the fluid flow is smooth and constant. In contrast to that, turbulent flow is dominated by inertial forces which lead to the formation of random eddies, vortices and other flow fluctuations. Using the fluid velocity ν_{shaft} from equation 5.5 and a viscosity μ of 0.001 kg/(m·s) for water, Re can be determined as follows:

$$\begin{aligned} Re &= \frac{\rho \cdot \nu_{shaft} \cdot D_h}{\mu} \\ &= \frac{1000 \cdot 4.25 \cdot 4.1 \cdot 10^{-4}}{0.001} \\ &= 1722 \end{aligned} \tag{5.7}$$

Thus, the flow in the shaft cooling channels was expected to be laminar. Respective Reynolds numbers for feed and umbilical tubing were 1307 and 288, hence resulting in laminar flow in all channels.

The pressure drop dp (bar) across the shaft cooling channel with length $l = 0.32$ m was then calculated according to equation 5.8 to 2.6 bar (equivalent to 256 kPa) [82, p.380]:

$$dp = \frac{8 \cdot \mu \cdot \nu_{shaft}}{(D_h/2)^2} \cdot l = 2.6 \tag{5.8}$$

Similar analyses for feed and umbilical tubing resulted in pressure drops of 0.4 bar and 0.1 bar, respectively. The total pressure drop of the cooling system could hence be estimated to approximately 3 bar.

The pump power P_p (W) required to overcome the resistance to flow associated with the pressure drop dp may be expressed in terms of the mass flow rate $\dot{m}$ (kg/s) and

density (kg/m^3) as:

$$P_p = dp \cdot \frac{\dot{m}}{\rho} \tag{5.9}$$

This results in a total required pump power P_p of approximately 0.5 W; 0.4 W of this total power is needed due to the pressure drop in the applicator shaft channels.

5.4 Development of Integrated Oval Design

5.4.1 Design Evolution

Although none of the reviewed existing cooling systems described in section 5.2 were suitable for the cooling of the 1.8 mm applicator, the first cooling concept for the applicator – the oval tube cooling system – developed while and through examining those other systems. During the manufacture and testing of this novel oval cooling system the subsequent versions, round tube cooling system, and round tube cooling system with internal thermocouple, evolved.

These three cooling concepts are described in the following sections in the order in which they were developed and built. The term 'cooling system' refers to a cooling system without antenna, and 'cooling system applicator' to a fully operational microwave ablation applicator including the respective cooling system design – oval, round, or round with thermocouple.

Oval Tube Design

The oval tube design rested on the concept of creating two coolant channels – one either side of the coaxial cable – by deformation of the stainless steel shaft into an oval shape. The minor diameter of the oval tube was made equal to the OD of the coaxial cable. Assuming pressure between the contacting areas of shaft and coaxial cable, two lateral sealed channels could be created; figure 5.4 displays a cross-section through such a design resulting in an oval tube. A cross-over region between channel one and two close to the applicator tip was also required in order to create a close cycle system and maximum shaft cooling. This cross-over region was accomplished by retaining the original circular shape of the tube at its distal end over a length of 3 mm to 5 mm such that coolant of channel one could circulate around the coaxial cable and into channel two.

A mere contact between shaft and cable would not achieve the necessary water-proof sealing. However, any leakage along the length of the seal was to be avoided as this would degrade the efficacy of the cooling at the distal end of the shaft. The concept of pressurising the contact areas to create a water-tight seal was realised by generating an initial slightly undersized tube. This tube could then be decompressed within its elastic limits to allow insertion of the coaxial cable. Once the temporary decompression was released, the shaft returned to its original deformed state, hence exerting permanent pressure on the coaxial cable.

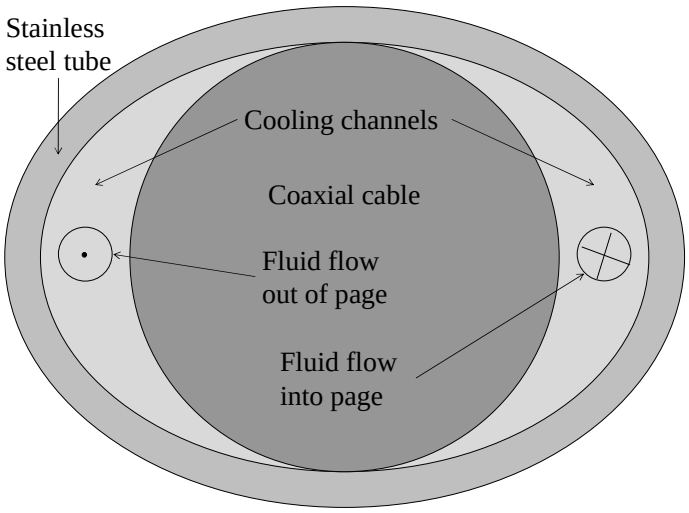

Figure 5.4: Cross-sections through oval cooling system design.

Material Considerations

The term 'stainless steel' is used for iron-based metals containing at least 10 % chromium. It is the chromium content that builds an invisible barrier of chromium oxide 'CrO' protecting the iron against most corrosion or rust, hence the term 'stainless' steel. There are over 150 grades of stainless steel. The stainless steel shaft of the 1.8 mm applicator is of type 304, the basic stainless steel type which is used in more than half of all applications including stainless steel. It is non-magnetic and exhibits high strength as well as good wear and corrosion resistance. In the medical field it is used for making hypodermic needles, cannulas, and hypodermic capillary tubing [83].

Another type of steel is spring steel. Objects made thereof return to their original shape after a load condition is removed. The key component of most spring steel alloys is a concentration of silicon between 1.50 % and 1.80 %, compared to a maximum of 1 % for 304 [84]. Such material characteristics would be beneficial for the design of the oval cooling system. However, a preformed oval tube of exact dimensions would involve a costly process of custom-made ordering which was not feasible at that time.

It was therefore decided to utilise the 304 stainless steel hypodermic tube (Small Parts Inc.; HTX-15X, OD (1.8288 $\pm$ 0.0127) mm, ID (1.5875 $\pm$ 0.0254) mm), since 304 offers a relatively high modulus of elasticity of 193 GPa to 200 GPa, compared to other softer metals, for instance copper, with a modulus of elasticity of around 110 GPa.

5.4.2 Manufacture of Cooling System

Prior to the manufacture of a fully operational microwave applicator, a test piece was made without a microwave antenna tip but incorporating the developed close-cycle cooling system. In the remainder of the document such test pieces are referred to as 'cooling system'.

Step 1 — Permanent Deformation

Taking a material beyond its limits of elasticity results in a permanent deformation of that object. This principle was used for altering the shaft dimensions from an initially circular to later oval shape. Deformation was achieved by placing the tube between the jaw beams of a vice of a milling machine (EMCO FB-2E). The vice had parallel steel jaws of 12 mm width and 110 mm length with flush surfaces. A 360° rotation of the vice handle reduced the distance between the jaws by 3.08 mm.

The length of the jaws had to be extended as to allow simultaneous compression along the full length of the tube minus the cross-over length. Jaw extensions were accomplished via the insertion of two steel plates with parallel faces cut to the required length of 150 mm. The stainless steel tube was positioned horizontally between the plates protruding at one end by 5 mm whilst flush at the other end.

The target minor outer diameter of the tube in the deformed state was determined by means of geometric considerations. As the initial ID of 1.59 mm was to be equal to the OD of the coaxial cable of 1.19 mm, a minimum compression of 0.40 mm was required, assuming a constant wall thickness. Using the thread pitch, the required minimum compression was then converted into a corresponding minimum rotation of 47°.

Step 2 — Elastic Deformation

The slightly undersized oval tube was reintroduced between the plates into the vice with the spherical end sticking out. Next, the tube was rotated so that its major axis was aligned horizontally and the vice closed sufficiently to hold the tube in place. Thereafter, the vice was slightly closed, exerting pressure across the major axis of the tube resulting in a widening and growing minor tube diameter as is illustrated in figure 5.5. The vice was further closed until the insertion of the coaxial cable became possible. The required rotation was recorded, the vice opened, and the assembly removed.

Determination of Optimum Permanent and Elastic Deformation

Prior to the application of this concept to full-length tubes and cables, a set of trial compressions were made with smaller piece of about 4 cm length. Therein, permanent deformation was generated for compression distances of 0.40 mm to 0.90 mm and cable fit tested afterwards. A compression distance of 0.40 mm did not produce enough distortion to stop the cable from moving freely inside the tube, whereas one of 0.90 mm resulted in a slight over-compression. An optimum compression distance of 0.84 mm was determined in this manner.

Thereafter, another set of trial compressions were made using short-length pieces. First, permanent deformation of the test tubes was produced for the distances above. Then, the pieces were subjected to the elastic deformation and cable lengths introduced if possible. The generated test assemblies were next investigated regarding two matters. Firstly, visual inspection of the tube-to-cable interface was conducted under a microscope (Meiji EMZ, magnification 10x). Visible gaps between the two items, as well as

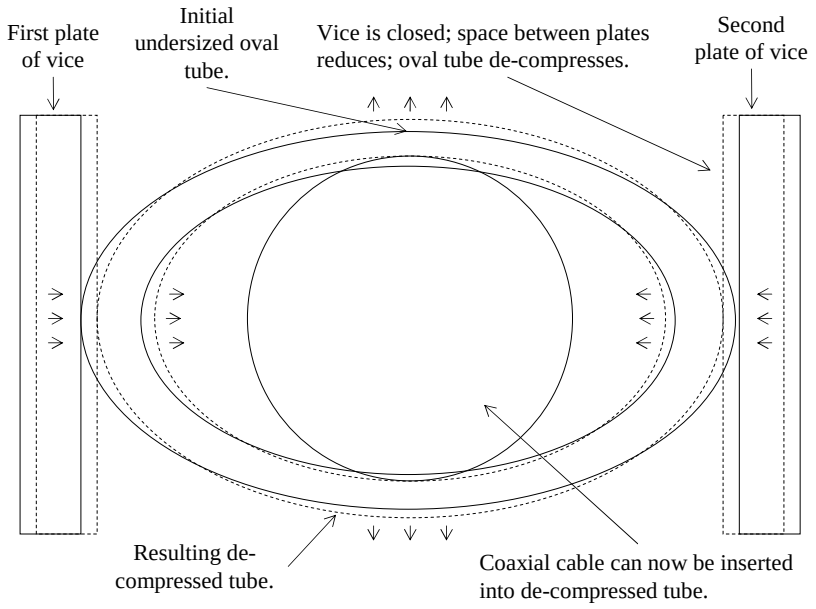

Figure 5.5: Illustration of elastic deformation process during oval cooling system manufacture.

possible movement relative to each other resulted in the assembly considered inadequate. Secondly, a pull test was performed to test the strength of the assembly. Again, any movement of the cable relative to the tube was regarded as unsatisfactory. In this way the optimum permanent to elastic compression was determined, consisting of an initial permanent compression of 0.84 mm (98°) followed by an elastic decompression of 0.26mm (30°).

Manufacture

The first cooling system test piece was then made from a set of handle pieces machined to provide separate inlet and outlet chambers for the coolant. The assembly of the oval cooling system was performed in the following sequence of actions using the deformation technique described above:

- Permanent deformation of tube into oval shape
- Drilling of two holes through strongly curved sides of tube at a distance of approximately 2 cm from each other
- Elastic deformation of tube and insertion of coaxial cable
- Sealing of one of the channel openings at the proximal end of the tube
- Sealing of distal end of tube close without blocking fluid cross-over region
- Affixing of handle parts in the order back to front and sealing all joints
- Bonding of luer locks in designated holes in handle

All joints and seal were made with epoxy adhesive and attention was paid to create water-proof joints. Figure 5.6 depicts different views of the deformed and prepared stainless steel tube including side and top views of the cross-over region and the holes acting as coolant inlet and outlet.

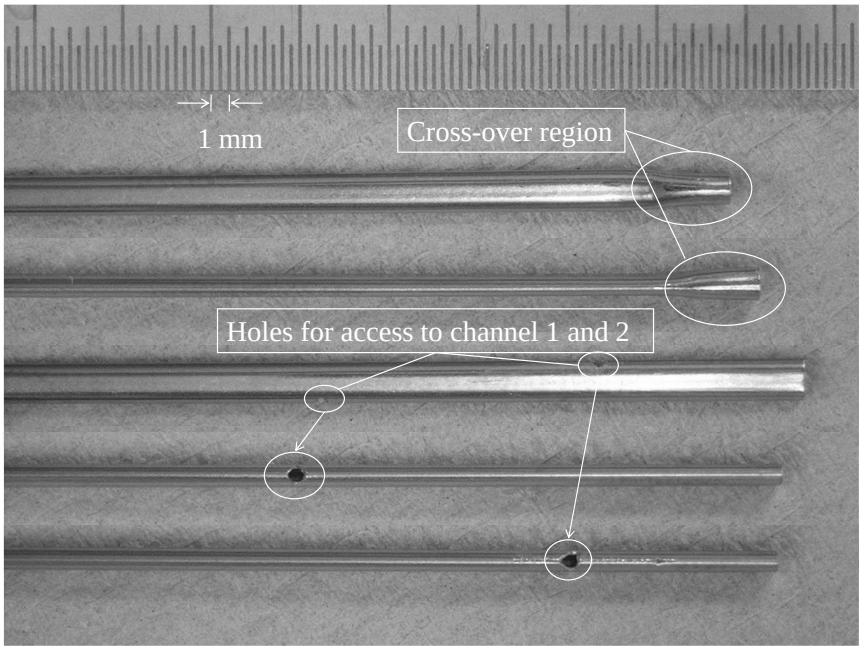

Figure 5.6: Deformed and prepared tube for manufacture of oval cooling system.

The envisaged fluid flow through the applicator is depicted in figure 5.7 as follows: coolant enters the handle through the input chamber; it then enters into the shaft through hole 1 and flows along the shaft towards the cross-over region; at the cross-over region it circulates around the coaxial cable into channel 2; the fluid then returns toward the handle inside channel two in the shaft, exists through hole 2 in the shaft and through the exit chamber in the handle.

Figure 5.8 shows the assembly after the insertion of the coaxial cable and glueing of the first handle piece. A picture of the fully assembled device will be shown in the next section.

5.4.3 Experimental Validation of Cooling System

Experimental Setup and Methodology

The experimental setup is shown in figure 5.9. A syringe pump was connected to the handle inlet via small diameter plastic tubing; a second length of tubing was connected to the handle outlet guiding the coolant to a collection container. The syringe was filled with water of approximately 20 °C. The cooling system was mounted vertically on a stand above a hot plate with the tip pointing downwards. A beaker filled with vacuum pump oil (Edwards Ultra Grade 19; flash point 230 °C) was placed on the hot plate and heated to approximately (100 ± 5) °C. Seven thermocouples TC2 to TC8 (T type; 0.25 mm diameter; OMEGA Engineering, Inc.; 5TC-TT-T-30-36) were attached along the shaft in order to record temperatures during the experiment as shown in figure 5.10. The locations of the TC beads with respect to the distal end of the shaft were 2 mm, 18 mm, 35 mm, 48 mm, 64 mm, 78 mm, and 93 mm, respectively. A cladding of polystyrene was installed around the shaft to insulate the thermocouples

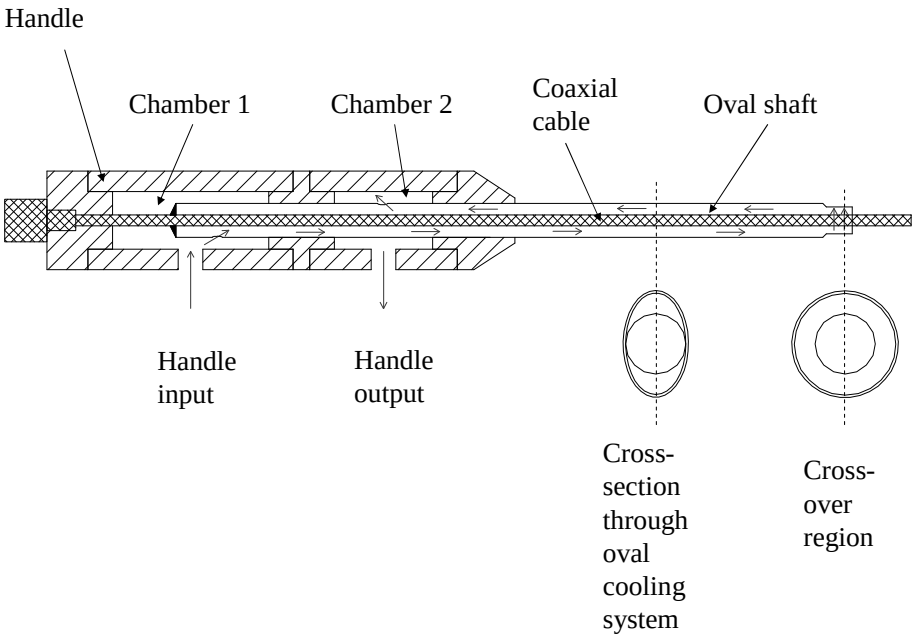

Figure 5.7: Section through major axis of oval closed cycle cooling system. Red arrows indicate the fluid flow path.

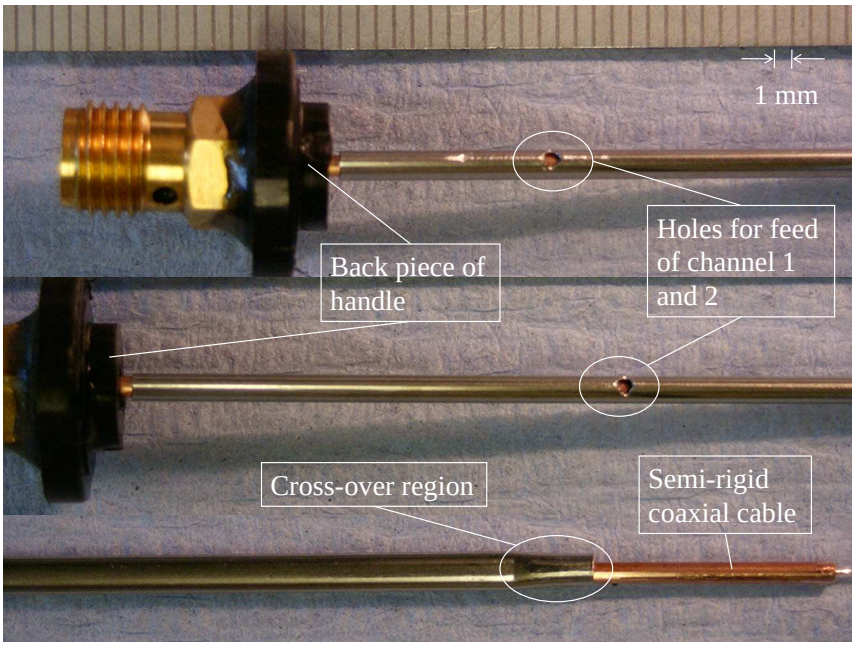

Figure 5.8: Intermediate stages in assembly of oval cooling system showing in- and outlet holes in shaft and fluid cross-over region.

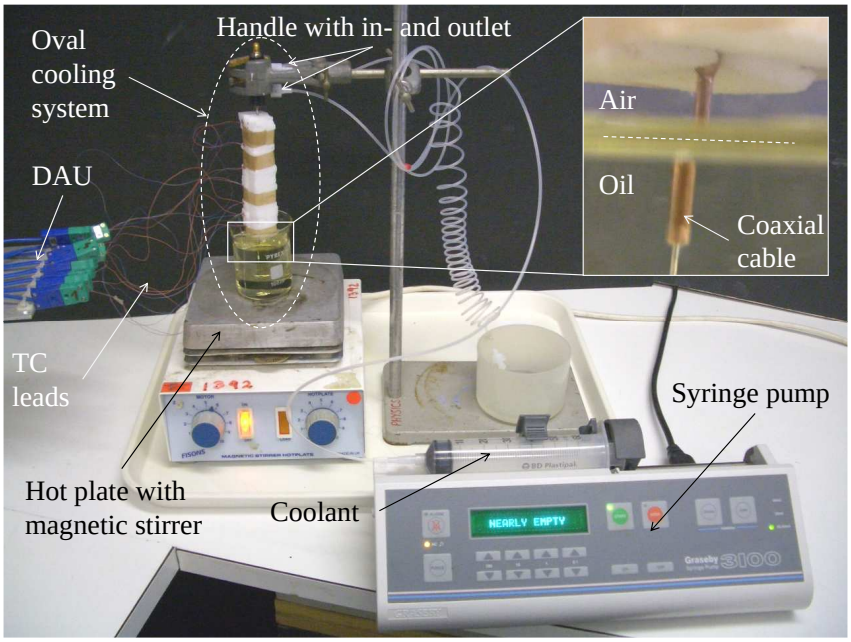

Figure 5.9: Experimental setup of oval cooling system validation.

from the environment and, in particular from rising hot air warmed by the beaker of hot oil during the experiment. Another thermocouple, TC1, was utilised to monitor the temperature of the hot oil. Temperature data was recorded with a data acquisition unit (DAU) of sampling rate 1/s (Anville Instruments; Series 410).

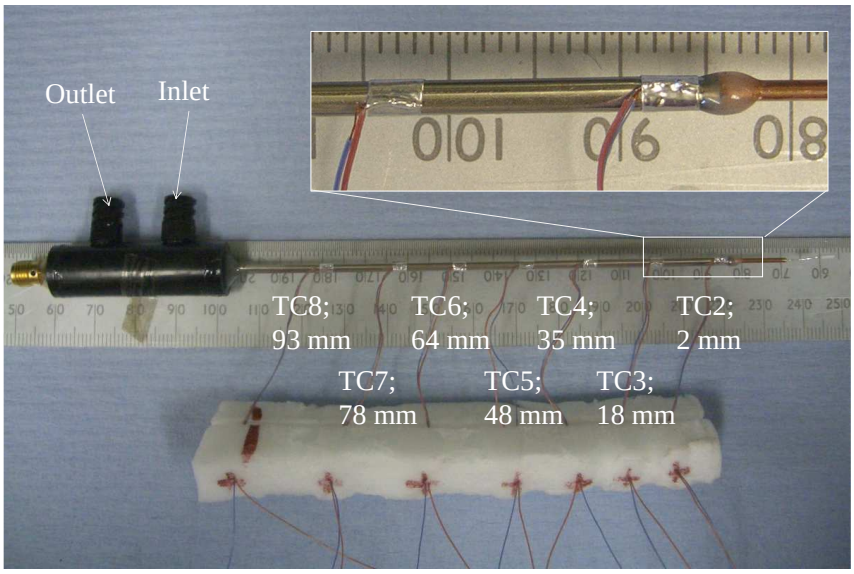

Figure 5.10: Oval closed cycle cooling system with 7 thermocouples attached along shaft to monitor temperatures.

At the beginning of each experiment, temperature logging was initiated. Thereafter, the tip of the cooling system was immersed such that the distal end of the cross-over region was located approximately 5 mm above the oil surface, that is, only the coaxial cable

was immersed into the hot load (as shown in the top right corner of figure 5.9). Once temperatures along the shaft had equilibrated, the cooling was turned on. The system was left in this state to develop a new steady-state before the cooling was switched off and temperatures allowed to equilibrate yet once more. In experiment one, this cycle was repeated three times for flow rates of 90 ml/h, 90 ml/h, and 190 ml/h; in experiment two, the cycle was repeated five times for the higher flow rate of 190 ml/h.

Results

Figure 5.11 and 5.12 depict the measured temperature data for TC1 to TC8 versus time for experiment 1 and 2. TC2 was located at the cross-over region and hence closest to the oil bath, TC3 to TC8 at increasing distances relative to the distal end of the shaft. The vertical dashed lines indicate the times when the cooling was turned on or off. The cooling flow rate was 90 ml/h for the first cycle, and 190 ml/h for the subsequent two cooling cycles.

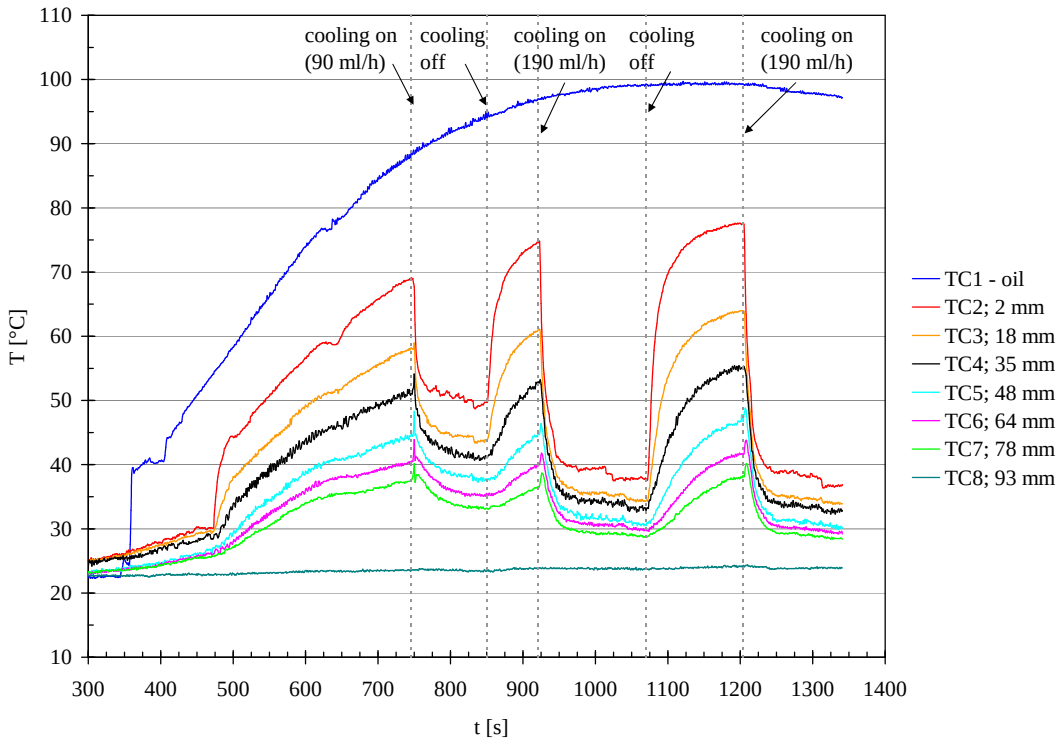

Figure 5.11: Recorded temperatures versus time (TC2 to TC8 along shaft); experiment 1. Dashed lines indicate times when cooling was switched on and off; cooling flow rates: 90 ml/h, 90 ml/h, and 190 ml/h.

Discussion

In both experiments, temperatures along the shaft dropped sharply as soon as cooling was switched on and rose equally fast when cooling was suspended. The magnitude and speed in temperature drop depended on the rate of cooling and location of measurement,

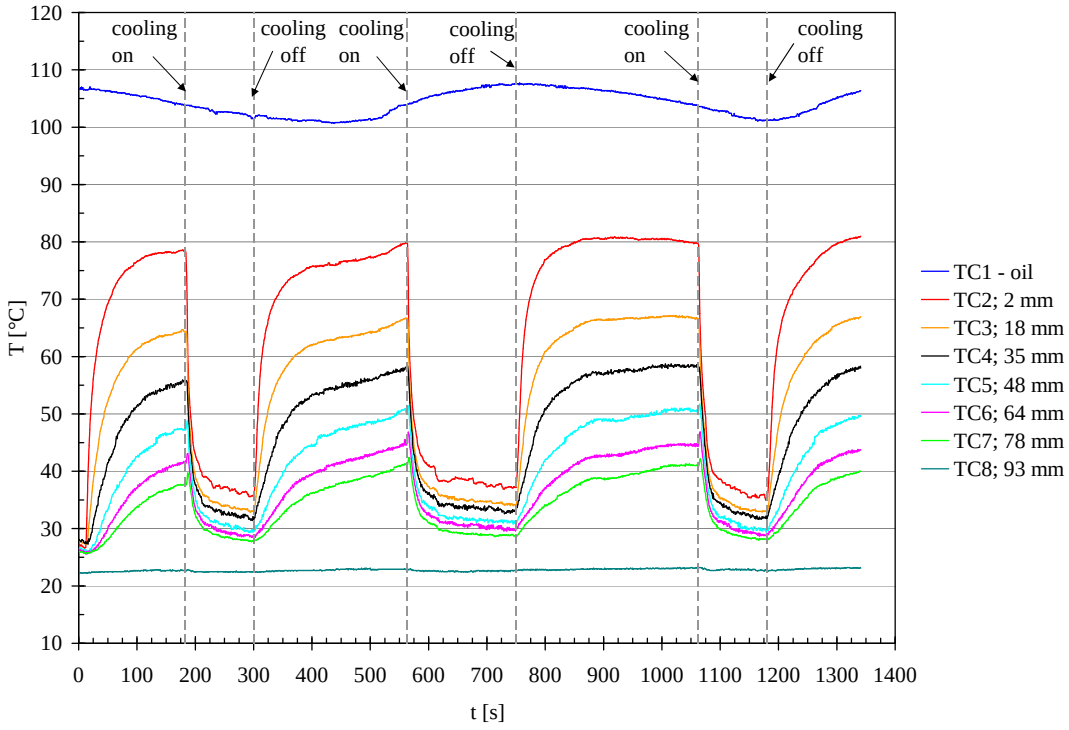

Figure 5.12: Recorded temperatures versus time (TC2 to TC8 along shaft); experiment 2. Dashed lines indicate times when cooling was switched on and off; cooling flow rate: 190 ml/h.

amounting to a maximum drop ΔT of -42 °C in 50 s. The order of highest temperatures during both cooling and non-cooling phases corresponded to the position of the TC, that is, the TC closest to the heat source, TC2 (red traces), experienced the highest overall temperatures, followed by TC3 (orange traces) located 16 mm further back along the shaft, then TC4 (black traces), TC5 (turquoise), TC6 (magenta), and finally TC7 (green). TC8 was faulty and hence not reading true temperatures of the shaft. The fluctuation of TC1 was due to the hot plate turning on and off in the attempt to keep the oil at a constant temperature of 105 °C.

In all cooling instances, the steady-state temperatures of the TCs settled within a certain temperature range, the span of which was affected by the rate of cooling. Those steady-state temperatures were 41 $\pm$ 8 °C in the case of the lower flow rate of 90 ml/h (see figure 5.11, 830 s), and 33 $\pm$ 5 °C for 190 ml/h (see figures 5.11 and 5.12). This behaviour was of importance as it indicated the lack of significant leakage in the cooling system. In addition to that, lower shaft temperatures could be expected for further increases in flow rate.

However, the cooling problem simulated in these experiments was simplified regarding two important aspects. Firstly, during an ablation some length of the applicator shaft would be in direct contact with surrounding hot tissue, giving rise to more intense heating. Secondly, additional heating of the shaft was expected in an ablation setup caused by direct electromagnetic heating of the stainless steel due to its lower values of electrical conductivity resulting in greater resistive losses.

Conclusion

The data recorded showed that the cooling system was capable of rapid and powerful cooling, even at locations close to the heated load. The cooling system produced a maximum ΔT of -44 °C in 110 s at TC2 at 2 mm, compared to a maximum ΔT of -28 °C in the case of the closed cycle air-cooling system with similar setup [64, p.80]. Besides, the efficacy of the cooling system could possibly be further increased by using higher flow rates and/or coolant of lower initial temperature. It was therefore decided to combine the cooling system and the applicator developed previously.

5.4.4 Manufacture of Oval Applicator

The combination of the oval cooling system and the applicator developed in chapter 4 produced an oval applicator with closed cycle cooling system. The process of integration was fairly straight-forward, presenting only a few difficulties during manufacture. The main steps in the assembly of the applicator were as follows:

- Deformation and preparation of shaft as described in section 5.4.2
- Full insertion of coaxial cable into elastically widened shaft through proximal opening
- Continue applicator tip assembly while fixed in vice:
  - Soldering of ferrule
  - Application of adhesive (Loctite 638) around proximal shoulder of ferrule
  - Bonding ferrule to shaft by sliding back cable assembly until proximal shoulder of ferrule fully inside shaft
- Opening vice, removing assembly
- Assembly of applicator tip was then continued as before (see appendix B) with altered handle design comprising two separate chambers. Adhesive for tip joint was Loctit 638
- Non-stick dip coating of applicator shaft

The main challenges were due to the generally small part sizes, additional obstruction in movement and view during fixation in vice, required water-proof seals on most glue joints, and the insertion of the ferrule into the distal opening of the shaft. The latter issue arose due to the fact that the tube had been deformed significantly beforehand, and any distortions in the nearby end would not allow the ferrule to be inserted. In addition, the adhesive around this joint was not to block the cross-over region inside the shaft. Figure 5.13 depicts the assembled applicator; the applicator tip including the cross-over region are shown below in magnified top and side views.

5.4.5 Experimental Validation of Oval Applicator

Introduction to Ex-Vivo Ablations

Ex-vivo ablations are generally carried out in fresh animal organs such as bovine liver, occasionally porcine liver or kidney, sourced from local butchers. Ideally, the ex-vivo

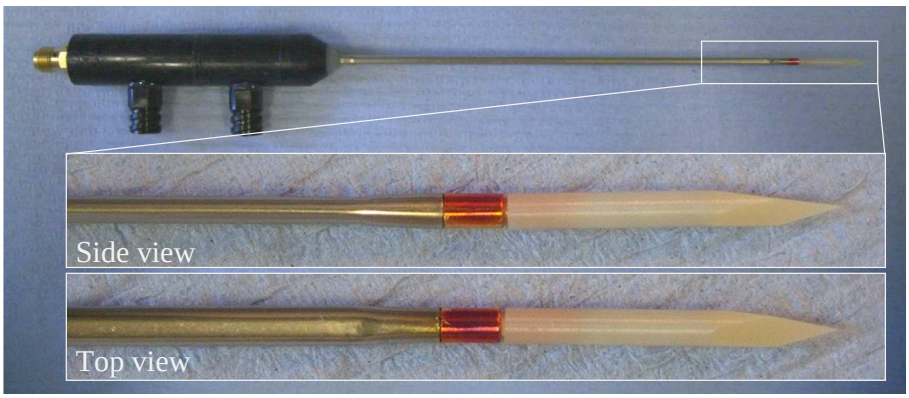

Figure 5.13: 1.8 mm applicator with integrated oval closed cycle cooling system.

tissue bulk is heated to body temperature of 37 °C since it then optimally mimics in-vivo conditions. However, for the sake of readiness, ex-vivo tissue is sometimes used as delivered, or from the fridge with temperatures between 7 °C to 20 °C. The applicator under test is placed into tissue, such that the entire radiating part of the antenna structure is well buried and surrounded by load material. Microwave power is turned on and applied for a set time period, generally 2 to 8 minutes. After the ablation, the applicator is removed immediately and a cut made along the applicator path and through the centre of the ablation. Coagulation boundaries are then determined by visible inspection relying on the apparent differences in colour and texture of ablated versus fresh liver tissue. Whereas fresh ex-vivo bovine liver tissue is dark red in colour, it changes into a shade of pale brown in the ablated state. All cells within an ablation zone discoloured in such a way have been taken beyond their cytotoxic limit and are consequently irreversibly damaged. The ablation zone is then measured on the basis of those visible boundaries. This method of ablation size determination is the most common technique of measuring lesions as the macroscopic difference of tissue colour corresponds accurately to the underlying cellular damage which was proven by pathologic analyses [85].

In this test, experimental validation consisted of testing the applicator's cooling system and determining ablation sizes as described above. Prior to the experiments, the $S11$ of the applicator was measured in 0.58 % w/v saline and found to be -10 dB.

Experimental Setup and Methodology

The performance of the closed cycle oval cooling system was tested in an ex-vivo ablation setting. Six thermocouples (T type; 0.25 mm diameter; OMEGA Engineering, Inc.; 5TC-TT-T-30-36) were used to record temperatures during ablations and were attached along the shaft at distances of 2.5 mm (TC1), 7 mm (TC2), 19 mm (TC3), 35 mm (TC4), 52 mm (TC5), and 73 mm (TC6) relative to the ferrule-tip interface as shown in figure 5.14. The error in TC placement was ± 1 mm.

Three ablations of 3 min were performed with input powers of 30 W, 50 W, and 60 W relative to the applicator input. For each ablation, the applicator was inserted into a large piece of fresh bovine liver tissue heated to (34 ± 4) °C. Temperature logging

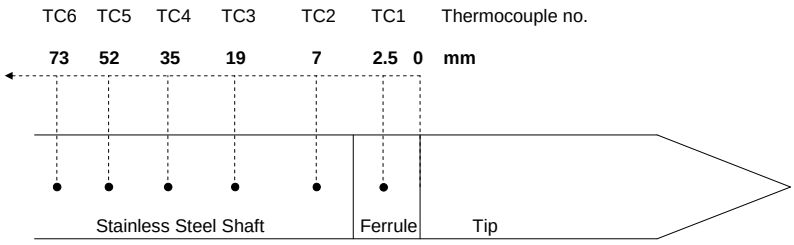

Figure 5.14: Locations of thermocouples of oval closed cycle cooling applicator during ex-vivo ablations; placement error ± 1 mm.

was activated first, followed by the switch-on of cooling and microwave power. The setup of the cooling circuit was retained from the previous experiment (see section 5.4.3). The flow rate of test 1 (30 W) was set to 190 ml/h, and was then increased to approximately 1900 ml/h for the latter tests. As the flow rate produced by the syringe pump was limited to 190 ml/h, the higher flow rates were achieved by manually driving the syringe itself. Upon test completion, the microwave power was turned off, the applicator carefully removed, and the ablation sectioned for measurement.

Results

Figures 5.15, 5.16, and 5.17 display the recorded shaft temperatures of the 30 W, 50 W, and 60 W ablations, respectively. TC4 failed and its data was therefore omitted in the graphs.

Ablation sizes were 27 mm × 40 mm (radial × longitudinal diameter), 37 mm × 39 mm, and 40 mm × 42 mm for 30 W, 50 W, and 60 W. The measurement error was ± 2 mm in all cases. Figure 5.18 shows the disclosed ablation of the 60 W test measuring 40 mm × 42 mm. The same ablation is also shown as found in the mass of ex-vivo bovine liver. The approximate locations of applicator and thermocouples are indicated by white dashed lines and white dots, respectively.

Discussion

Temperatures in experiment 1 (see figure 5.15) were rising for the first minute, then slowly approaching steady-state conditions. In the centre of the ablation, those steady-state values were (125 ± 5) °C for TC1, (130 ± 10) °C for TC2, and (95 ± 10) °C for TC3. Outside the ablation zone and probably in air, both TC5 and TC6 recorded (52 ± 5) °C. Sharp rises in temperature, as can be seen around 15 s and 100 s, lasting between several seconds to minutes, were most likely caused by direct electromagnetic heating of the thermocouple bead. Efforts were made to shield the beads from the radiation by using metallic tape made of aluminium for mounting, however a full protection could not be guaranteed. Another reason for sudden temperature rises in the ablation centre are bursts experienced in the tissue caused by the high power densities. Both, direct heating and burst events were therefore neglected in the discussion of shaft temperatures.

The effects of an increase in flow rate by a factor of 10 can readily be seen in the

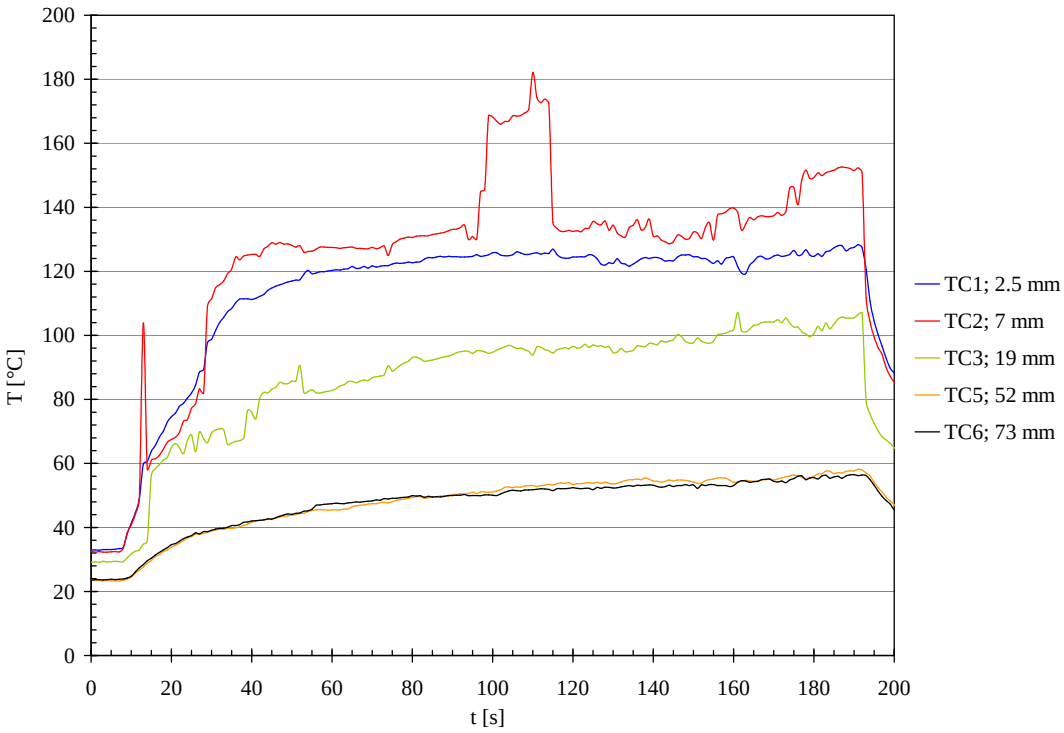

Figure 5.15: Temperatures along shaft of oval applicator during ex-vivo ablation of 30 W, 3 min, and flow rate 190 ml/h.

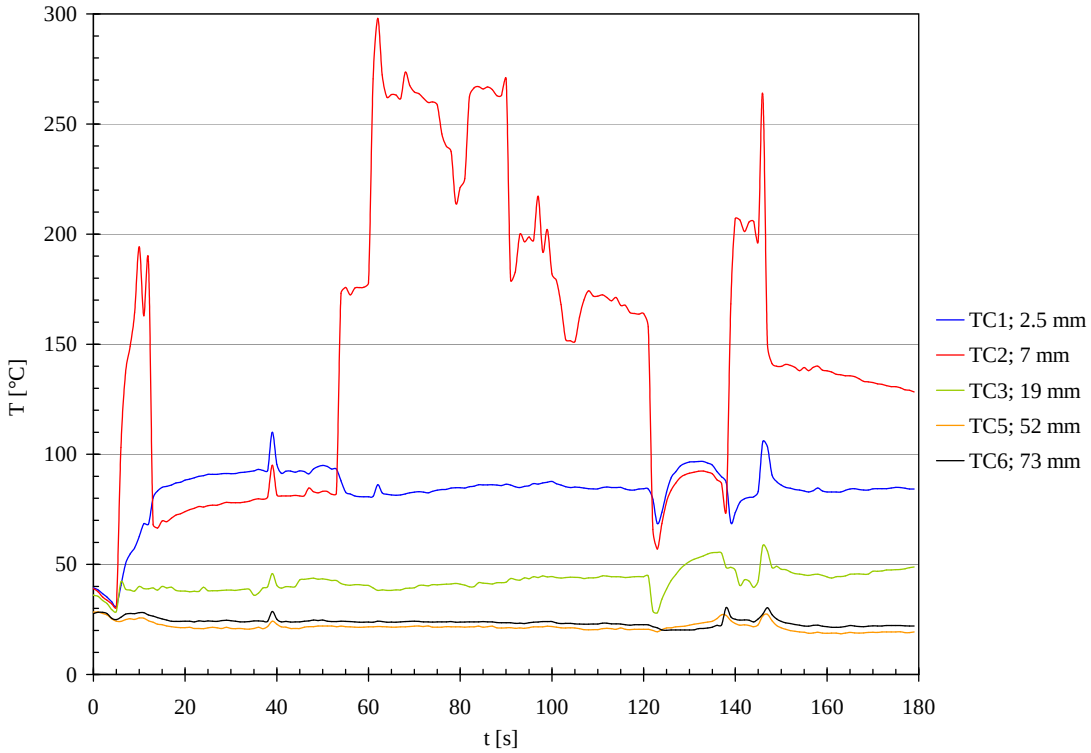

Figure 5.16: Temperatures along shaft of oval applicator during ex-vivo ablation of 50 W, 3 min, and flow rate of approximately 1900 ml/h.

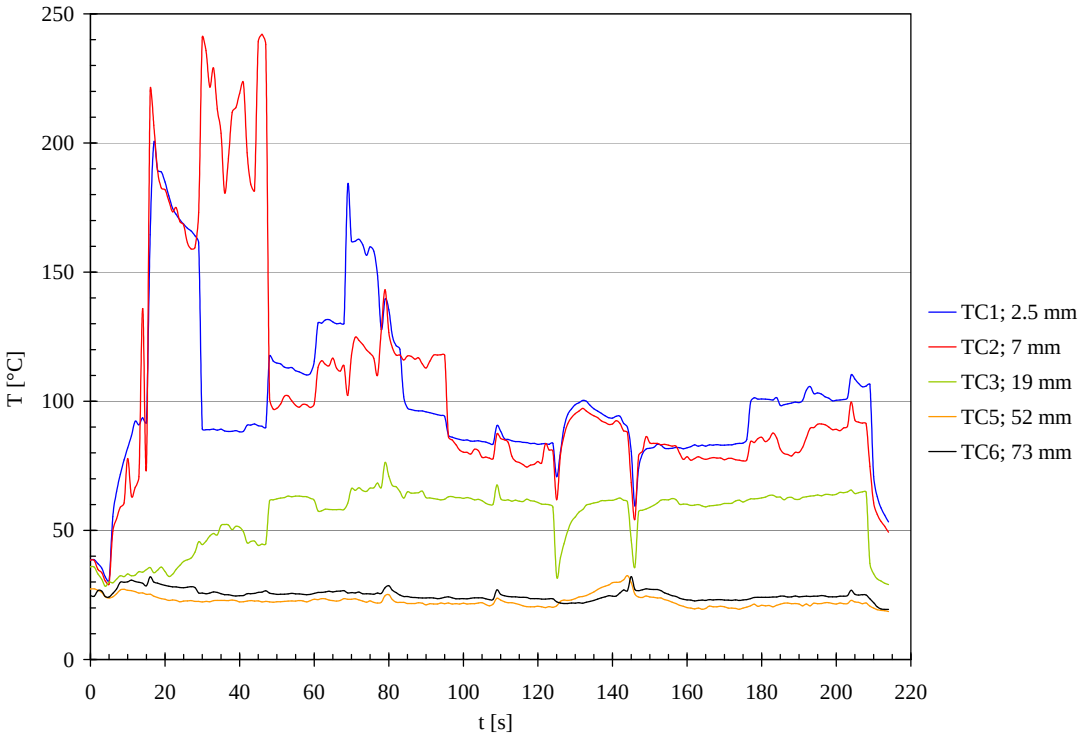

Figure 5.17: Temperatures along shaft of oval applicator during ex-vivo ablation of 60 W, 3 min, and flow rate of approximately 1900 ml/h.

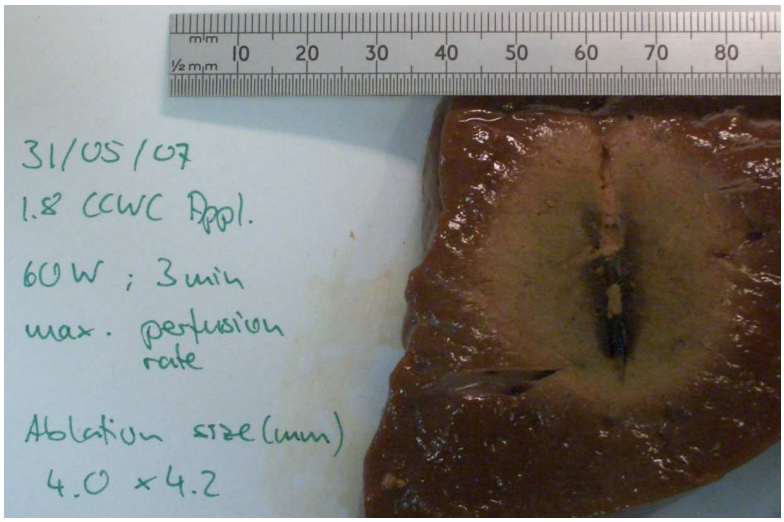

Figure 5.18: Ablation of size 40 mm × 42 mm produced with oval applicator (60 W, 3 min, 1900 ml/h). Measurement error ± 2 mm.

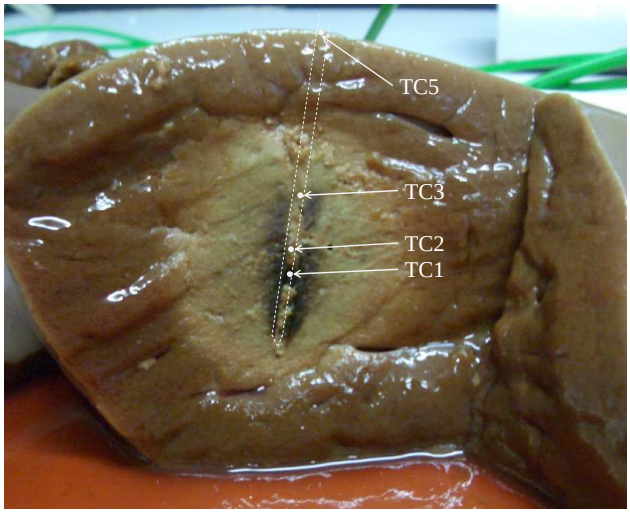

Figure 5.19: Ablation and applicator location of 60 W, 3 min in mass of ex-vivo bovine liver.

temperature traces of experiments 2 and 3 (see figures 5.16 and 5.17). Steady-state temperatures were (85 ± 5) °C for TC1, (40 ± 5) °C for TC3, and (24 ± 4) °C for TC5 and TC6. A steady-state temperature for TC2 was difficult to define due to the extensive occurrence of direct heating. The same problem existed in the traces of TC1 and TC2 in experiment 3. A best estimate of (100 ± 30) °C could be made for those sensors. TC3 settled to a value of (65 ± 5) °C, TC5 and TC6 to (24 ± 4) °C.

Small dips and rises in the temperature traces of experiments 2 and 3 were due to the varying flow rates of the non-perfect manual cooling. In addition, the syringe had to be refilled during ablation 2 and 3. The microwave power was therefore turned off to allow the refill which caused the top temperatures along the shaft to drop sharply (see figure 5.16 from 123 s to 138 s and figure 5.17 from 125 s to 145 s).

The benefit of using higher flow rates becomes evident when comparing the temperatures of the two different cases. Shaft temperatures outside the ablation zone (TC5 and TC6) were falling from (52 ± 5) °C in the case of the low flow rate to (24 ± 4) °C for the higher rate. This reduction is of importance as it prevents harmful burns at locations outside the target area. Despite being positioned inside the ablation zone, the traces of TC3 also show a significant lowering for higher flow rates ((95 ± 10) °C to (65 ± 5) °C) indicating that at places shortly outside the area of necrosis temperatures could fall below the cytotoxic limit. Unfortunately, the thermocouple to prove that instance, TC4, had failed and no definite conclusion could be drawn at this stage. Similarly, the implications of increased flow rates on tip temperatures (TC1, TC2) were inconclusive due to the occurrence of major events of direct heating. However, some increase in tip cooling for higher rates of cooling was likely to occur due to a greater heat flow towards parts at lower temperatures.

The radial diameter for the 30 W ablation, 27 mm, agreed well with a previously performed ablation size of 25 mm with the open cooled applicator (30 W, 4 min; ablation not shown or discussed in this thesis). However, the longitudinal diameter differed distinctly between 60 mm (30 W, 4 min) previously to now 40 mm (30 W, 3 min),

39 mm (50 W, 3 min), and 42 mm (60 W, 3 min). This reduction in ablation length resulted in almost perfectly spherical ablations as can be seen in figure 5.19.

5.4.6 Conclusions

The oval cooling system was capable of significant cooling along shaft and ferrule. Higher flow rates produced greater cooling in all areas. A flow rate of approximately 1900 ml/h was hence recommended for future use. In addition, the oval cooling system affected the ablation shape favourably. Again, a higher flow rate induced greater effects. The flow rate of 1900 ml/h generated a near spherical ablation for an application of 60 W for 3 min.

During the tests, an issue concerning the ovality of the cooling system emerged. The concern regarding the cooling system and therefore applicator shaft was in connection with the difficulty of specifying the device diameter. Being of oval shape, it could not be classified as a device of 1.8 mm diameter, since the major axis increased to approximately 2 mm during the deformation process. As the device diameter was of major importance, the current solution was considered unsatisfactory and work on the design of the cooling system continued.

5.5 Development of Round Design

5.5.1 Design Evolution and Concept

The oval cooling system and applicator were shown to operate successfully and reliably but were lacking the symmetry of a tubular round design. The design was therefore revised, resulting in a second generation closed cycle cooling system intended for use with the 1.8 mm applicator.

The principle of seal formation by pressurising associated interfaces had proven viable by the initial oval design and was hence maintained. However, instead of permanently deforming the stainless steel tube, the required contacts between shaft and cable were realised via the insertion of an additional structure.

The simplest modality found meeting those criteria was the insertion of a thin wire into the shaft. The wire shifts the coaxial cable towards one side of the tube creating two separate channels. Figure 5.20 illustrates this concept. The difference in size of tube ID and cable OD measured (0.39 ± 0.05) mm, calculated according to the dimensions and tolerances given. A slightly over-sized wire was therefore needed in order to provide the necessary pressure between wire, shaft, and cable. The insertion of both wire and cable could be realised by applying a weak elastic compression on the tube. Once both parts were positioned correctly, the compression could be released, generating the required pressure between the parts. The cross-over region between the two channels could also be retained by terminating the wire approximately 5 mm in front of the proximal end of the ferrule.

The two most common units specifying wire sizes are American Wire Gauge (AWG) and

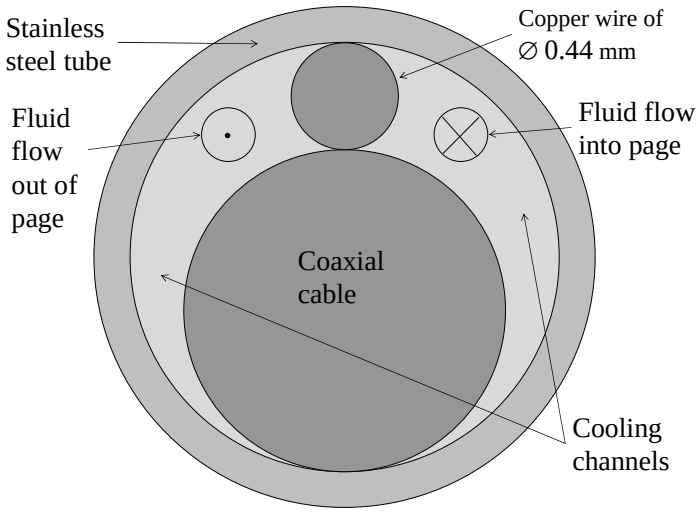

Figure 5.20: Cross-section through round closed cycle cooling design.

a metric scale. An increase in AWG size thereby denotes a decrease in wire diameter. In order to provide permanent pressure across wire and cable in all instances, a wire diameter equal to the maximum possible gap size was required. The nearest AWG sizes were 25 (0.45 mm) and 26 (0.40 mm). Due to the reason stated above, a bare copper wire of the larger size AWG 25 was selected.

5.5.2 Manufacture of Cooling System

The assembly of the round cooling system was similar to the preceding one in the oval case. The stainless steel tube was introduced between the plates and vice used previously, its position aligned horizontally with one end protruding the steel plates by 5 mm. The vice was slowly closed until insertion of cable and wire became possible. Attention was paid as to not compress the tube any further than required. Since the thin wire was prone to kinking, it was introduced first, and then the coaxial cable. Since no compression took place over the last 5 mm of the tube, wire and cable could not advance completely through the tube. The wire was therefore retreated until its end lay approximately 8 mm behind the distal end of the tube. The coaxial cable was then passed through entirely. After that, the vice was opened and the cooling system completed as in the oval design case (see page 80). The shaft was slightly deformed by the manufacturing process giving rise to minor and major diameters of (1.77 $\pm$ 0.02) mm and (1.87 $\pm$ 0.02) mm.

5.5.3 Experimental Validation of Cooling System

Experimental Setup and Methodology

The experimental setup employed for validation of the oval cooling system detailed in section 5.4.3 was recreated for the testing of the round cooling system. Four thermocouples were utilised for measuring temperatures of oil (TC1) and shaft. The positions

of TC2 to TC4 relative to the distal end of the shaft were 10 mm, 40 mm, and 80 mm with a placement error of ± 3 mm. The immersion depth of the cooling system was such that the distal end of the shaft was located approximately 5 mm above the surface of the hot oil. Water of (20 ± 3) °C was used as coolant and driven at flow rates of 90 ml/h, 190 ml/h, and approximately 400 ml/h.

Results

Figure 5.21 depicts the recorded temperature data for TC1 to TC4. The coolant flow rates were gradually increased from 90 ml/h (syringe pump driver) to approximately 400 ml/h (manual drive), in the sequence of 90 ml/h, 90 ml/h, 190 ml/h, ∼400 ml/h, and ∼400 ml/h. Cooling was turned off between runs to allow temperatures to rise again.

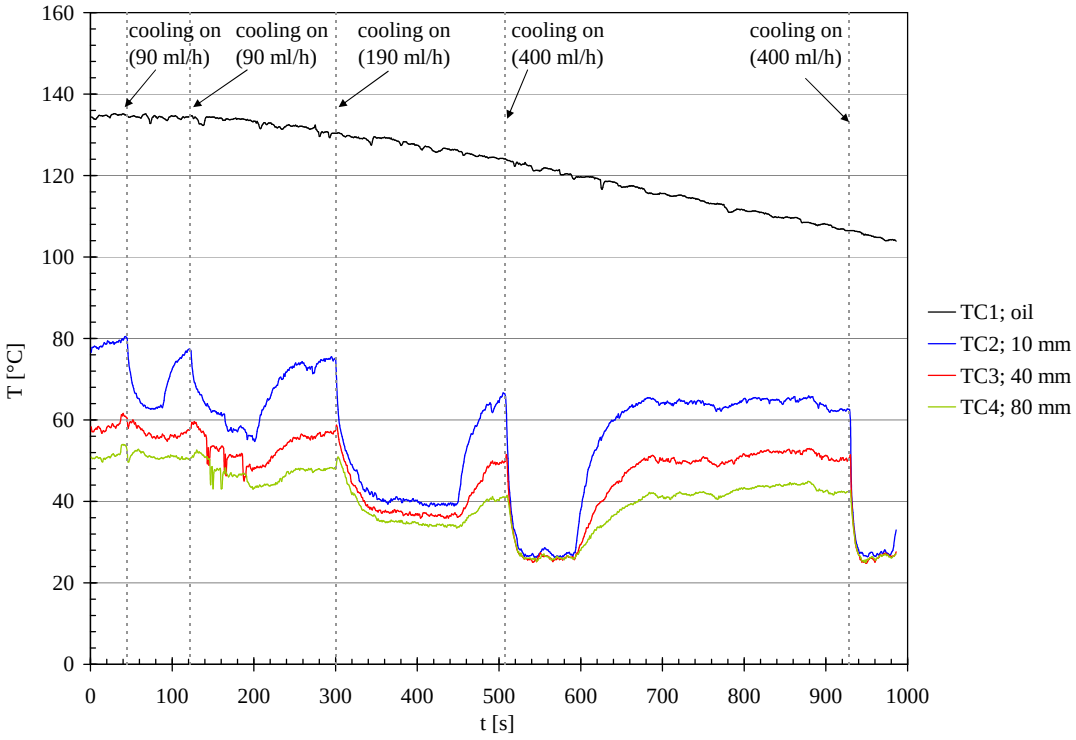

Figure 5.21: Recorded temperatures versus time. TC1 in oil; TC2 to TC4 along shaft. Flow rates in order: 90 ml/h, 90 ml/h, 190 ml/h, ∼400 ml/h, ∼400 ml/h; start of cooling indicated by vertical dashed lines.

Discussion

The results obtained closely mirrored those of the oval cooling system test. Temperatures along the shaft dropped sharply as soon as the cooling was engaged. The lowest final temperature of (26 ± 2) °C for all thermocouples on the shaft was achieved for the highest flow rate of ∼400 ml/h. The temperature data also suggested that no significant leakage occurred.

Conclusion

The round cooling system was capable of rapid powerful cooling along the shaft. Its performance was comparable to that of the previous oval cooling system. In addition to that, the concern regarding the ovality of the device had hence been resolved. The round cooling system thus met all requirements and was subsequently integrated into the applicator design.

5.5.4 Manufacture of Round Applicator

The main challenge in building the applicator was encountered in the attempt to merge ferrule and shaft. Once insertion of the coaxial able was completed, the solder joint of the ferrule was produced. Thereafter, glue was applied around the back end of the ferrule, and the cable carefully pushed backwards until the ferrule barely contacted the tube. Due to the asymmetric arrangement of cable and wire inside the tube, the cable and ferrule required centralising before full insertion into the tube became feasible. Once the gap between ferrule and shaft was closed, the vice was opened and the applicator completed as described before (see section 5.4.2).

5.5.5 Experimental Validation of Round Applicator

Introduction

The applicator was first tested in the hot oil setup in order to determine the pressure in the cooling system for various flow rates. This was necessary in order to select a suitable pump as the syringe driver had not been capable of providing the required pressures in earlier experiments. After that, ex-vivo experiments were conducted and temperatures of ferrule and shaft recorded. S11 was recorded prior to testing.

Measurement of Cooling System Pressure

Figure 5.22 illustrates the experimental setup for determining pressures in the round cooling system. The pressure in the system was measured using a pressure transducer (2200SGA4001D3FA from Gems Sensors & Controls) of range 0-4 bar relative to atmospheric pressure. The transducer was installed in the cooling circuit and its output (0-10 V) read with a voltmeter. The voltage was then translated into pressure p (bar) by means of a conversion table. Volumetric flow rates Q (l/h) were determined using a measuring cylinder. A pump (Milli-RQ Pump System from Millipore) with constant flow rate was driven by a voltage source with variable output between 0 % and 100 % of the input voltage of 230 V (Variable Transformer from Regulac Transformer). In that way, variable flow rates between 0.1 l/h and 4.4 l/h were realised. The central range between 1 l/h and 3.6 l/h however, could not be used as the variable voltage source was not stable at these outputs.

The applicator was prepared with three thermocouples attached along the shaft at distances of 1.5 mm (TC1), 24 mm (TC2), and 54 mm (TC3) relative to the distal end

of the shaft (error ± 2 mm). A beaker with vacuum pump oil (Edwards Ultra Grade 19; flash point 230 °C) was heated on a hot plate to approximately 110 °C. TC4 was inserted into the oil load and TC5 into the coolant reservoir. The applicator shaft and thermocouples were again insulated using the polystyrene cover. Seven experiments were conducted as described previously using flow rates of 0.15 l/h, 0.42 l/h, 0.78 l/h, 0.9 l/h, 0.96 l/h, 3.72 l/h, and 4.38 l/h.

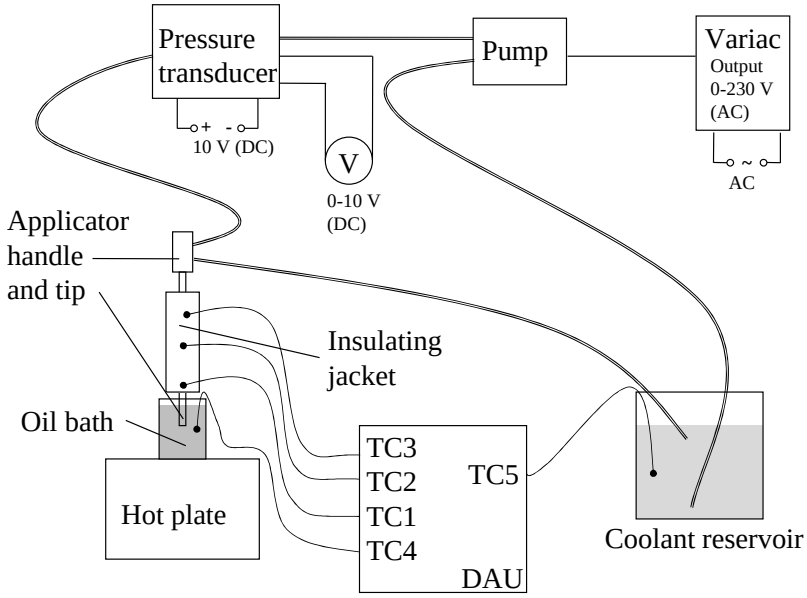

Figure 5.22: Experimental setup for measuring pressure in the round cooling system for various flow rates.

Figure 5.23 displays the results as temperature T (°C) and pressure p (bar) versus volumetric flow rate Q (l/h) for all experiments. TC1, TC2, and TC3 represent the steady-state temperatures developed for a given flow rate, TC4 and TC5 the respective temperatures of the hot oil and coolant.

It can be seen that a low flow rate of 1 l/h required a pressure of (0.5 ± 0.1) bar, whereas for the highest flow rate of 4.5 l/h a pressure of (2.9 ± 0.2) bar was necessary. The relationship between flow rate and pressure in the system was hence roughly linear. The drop in pressure is the result of friction of the fluid against the tube. The tube dimensions, turns in the channel which change the directions of the fluid flow, and other physical properties also affect the pressure drop. Generally, high flow rates are associated with small tubes resulting in larger pressure drops whereas low flow rates in large tubes give lower pressure drops.

The ferrule temperature TC1 dropped from (45 ± 2) °C for a flow rate of 0.15 l/h to (25 ± 2) °C for 0.96 l/h, however did not decrease any further for higher flow rates. Since the heating of the shaft was purely due to heat conduction from the tip, the cooling was expected to be of greater efficacy in the case of microwave ablations. For this reason, a higher flow rate of approximately 4 l/h was chosen for the subsequent ex-vivo experiments.

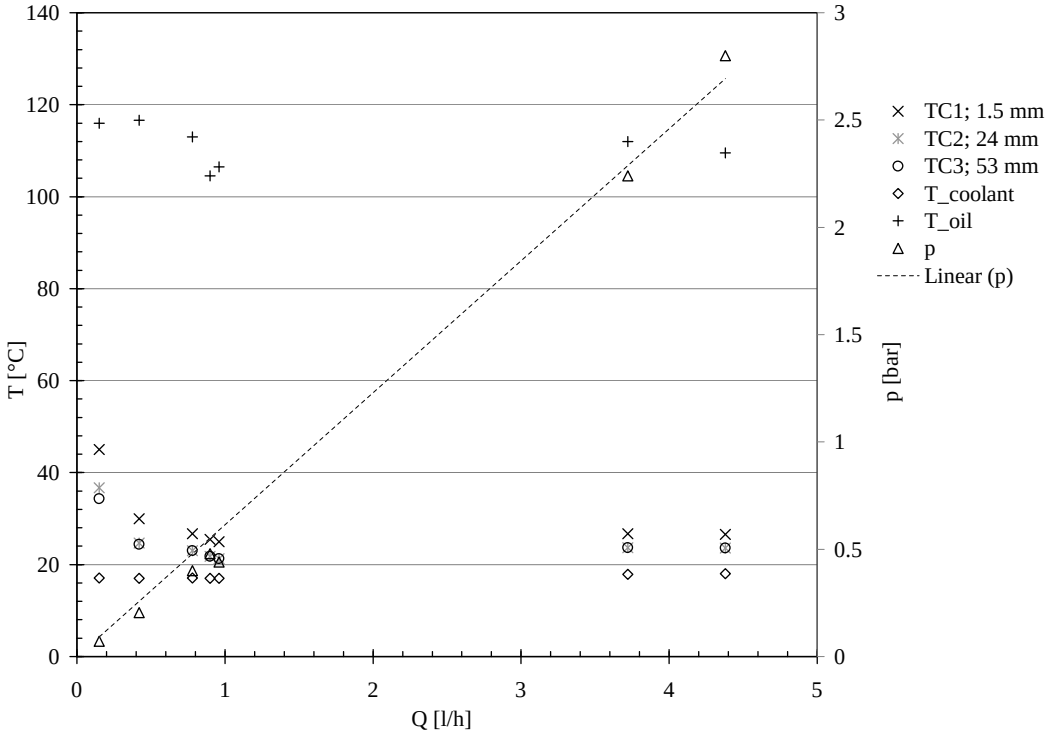

Figure 5.23: Recorded temperatures T and pressures p versus volumetric flow rate Q of round applicator in hot oil bath experiment. TC1 to TC3 along shaft; TC4 in hot oil bath ; TC5 in coolant reservoir.

Temperature Measurements During Ex-vivo Ablations

The thermocouples along the applicator shaft were retained from the previous experiments (TC1 at 1.5 mm, TC2 at 24 mm , and TC3 at 54 mm; ± 2 mm). TC4 and TC 5 were used to measure temperatures of ex-vivo bovine liver and coolant, respectively. S11 was measured prior to testing to -12 dB in ex-vivo bovine liver heated to (30 ± 2) °C. Two 3 min ablations of 30 W and 45 W were undertaken with a flow rate of 3.72 l/h.

Recorded temperatures in the case of the 30 W ablation are shown in figure 5.24. A steady-state temperature of (73 ± 3) °C was reached after approximately 50 s at the ferrule (TC1). TC2 rose to (29 ± 2) °C, TC3 to (25 ± 2) °C.

Figure 5.24 also identifies the ferrule as the location of highest temperatures during the ablation experiencing (73 ± 3) °C. Compared to the steady-state temperature of (125 ± 5) °C obtained with the oval applicator during a 3 min ablation of 30 W and flow rate 0.19 l/h (see page 91), this presented a reduction in peak temperature of 20 %. The reason for that reduction was the use of a significantly higher flow rate of 3.72 l/h in the latter experiment. Similarly, the temperatures along the shaft were also substantially lowered, for instance from (52 ± 5) °C to (25 ± 2) °C for the thermocouple positioned at 53 mm.

In comparison to the hot oil experiment the ferrule and shaft temperatures of the round

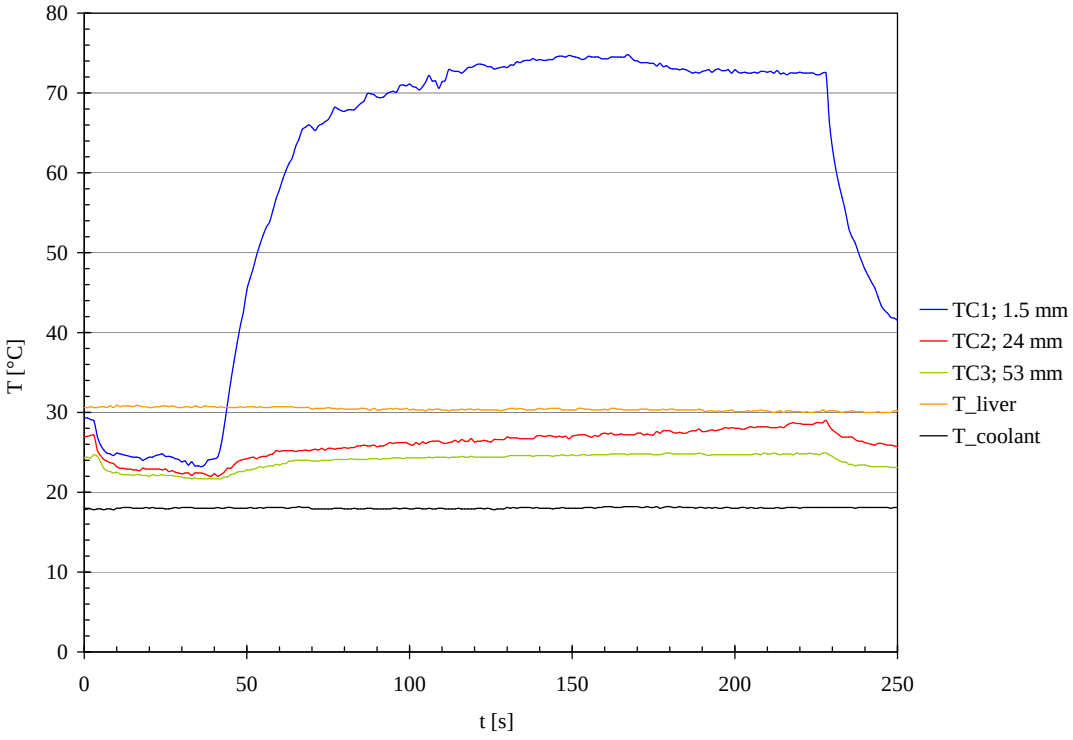

Figure 5.24: Temperatures along shaft of round applicator during ex-vivo ablation of 30 W, 3 min, 3.72 l/h. TC1 at ferrule; TC2 and TC3 at shaft.

applicator had increased. This was expected however, as the heating was simplified in the case of the oil experiments hence underestimating the real temperatures experienced during ablations.

5.5.6 Conclusion

The performance of the round cooling system was shown to be equivalent to that of the preceding oval system. The use of a high flow rate of approximately 4 l/h maximised the cooling potential along the applicator shaft and ferrule. Furthermore, the round design eliminated the concern regarding the shape associated with the oval applicator.

The instantaneous and powerful cooling of the designed systems were highlighted during the hot oil experiments. On the one hand this meant powerful and rapid cooling when needed, on the other hand however, it meant that an unintended interruption of the cooling had to be avoided. Such an instance of cooling failure would cause temperatures in the applicator and shaft to escalate, potentially leading to serious patient harm, applicator damage or even failure. For safe device operation it was hence considered necessary to ensure instant detection of cooling failures. For this reason, a mechanism for the detection of cooling failures was developed next.

5.6 Development of Round Design with Cooling Failure Detection

5.6.1 Introduction

As stated in the list of requirements in the design brief (see page 40), superficial skin burns caused by hot cables had to be prevented. Hence, the instance of a cooling failure had to be detected before shaft or cable temperatures could rise above 48 °C. Tests conducted in the previous hot oil experiments showed a rise in temperature on the outside of the shaft to 60 °C within 10 s after cooling was stopped (see figure 5.12). The objective of the cooling failure detection system was to identify any instance of cooling failure within a maximum delay time of approximately 10 s.

In order to design a suitable failure detection system, a list of design requirements was generated which is given in the subsequent section.

5.6.2 Design Requirements and Concept

The cooling failure detection system had to meet the following requirements:

- Detection of all kinds of cooling failure modes including:
  - General coolant leakage anywhere in the system
  - Pump failure
  - Channel blockage
  - Internal leakage from one applicator handle chamber to the other bypassing the applicator shaft
  - Coolant bypass around wire in shaft
- Response time less than 10 s
- Direct measurement preferred to indirect needing additional mapping procedures
- Minimal failure probability of sensor.
- Compatibility with current applicator design

5.6.3 Difficulties in the Development of a Cooling Failure Detection System

The major difficulty faced during the development of the cooling failure detection system for the microwave applicator was due to the small part sizes and resulting restrictions in available space. Since the direct measurement of parameters such as flow rate or temperature was required, other possibly simpler measurements such as cooling system pressure were not acceptable. This led to the main effort of finding a method of measuring temperature inside the shaft and as close to the tip as possible.

Possible design options were sought; for instance a setup in which a temperature sensor was inserted into the applicator shaft. Such a temperature sensor had to be smaller than 0.4 mm in diameter since this was the maximum distance available between coaxial cable and shaft. Ideally, its diameter would be as small as possible so as to minimally restrict coolant flow.

A bare thermocouple junction could possibly be inserted into the cooling channel and used to sense temperatures close to the applicator tip. The wires of the thermocouple

however had to be insulated and mechanically well protected to avoid short circuits or damage during manufacture and use. Therefore, the ideal case would be to use hypodermic tubes through which the insulated wires could be fed. However, considering the diameter of insulated thermocouple wires, the required inner diameter of such hypodermic tubing, the restricted outer diameter of the thermocouple assembly and the requirement for a two-wire setup rendered this design idea unfeasible.

Following those considerations, the next obvious concept was to use ready-made commercially available hypodermic needle thermocouples which house a thermocouple junction at the tip of a stainless steel needle probe. The smallest available and most suitable commercial product found was a mini hypodermic thermocouple needle probe of diameter 0.2 mm from Omega Engineering Limited [86]. However, it's length is restricted to only 2.5 cm and the probe handle is even larger. Furthermore, costs are relatively high. Due to these limitations, the use of the mini hypodermic needle thermocouple was not considered suitable.

Another option was to install a temperature sensor on the outside wall of shaft or handle which would circumvent the difficulty of restricted space. However, the risk of damaging or breaking off such sensors which could lead to serious patient injury was considered too great and was hence not pursued either.

5.6.4 Development of Temperature Sensor

A innovative solution was found that satisfied all criteria stated in section 5.6.2 . It was based on the introduction of a thermocouple into the applicator shaft with its junction located directly next to the cross-over region. With this design, the direct measurement of temperature itself was realised without the need for further conversion, as would have been necessary, for instance, in the event of recording the system pressure. Furthermore, all types of failure could be detected, since pump failure, channel blockages, coolant bypass, as well as all other general leakages would lead to rising temperatures at the location of the thermocouple bead. The strongest and fastest increase of temperature for any such event would be produced around the location of the ferrule as shown in previous experiments (see, for instance, figure 5.11). Although the thermocouple would be located inside the shaft rather than on its outer surface, temperatures were expected to rise similarly to those recorded previously. Lastly, the issue of compatibility with the present applicator design was regarded doable since the currently unused volume taken up by the copper wire could be utilised. A thermocouple junction is generated by joining two dissimilar metals and is usually achieved by means of welding. However, an active process such as welding could not be utilised in the scope of this work without the need for major changes in the manufacturing procedure.

In order to generate a thermocouple junction, the process of electroplating was investigated. In electroplating a metallic coating is deposited onto an object of choice. The object is connected to the negative pole of a voltage source, hence forming the cathode. It is then immersed in a solution containing a salt of the metal to be deposited, copper sulphate ($CuSO_4$) in this case. An anode made of the same material as the desired coating is connected to the plus pole of the voltage source and is also immersed into the solution. Positively charged copper ions Cu^{2+} are reduced to metallic copper at the

cathode, whereas hydroxide ions OH^- are oxidised at the anode forming water H_2O, hence removing electrons from the copper metal and oxidising it to the Cu^{2+} state. The copper anode metal dissolves as Cu^{2+} ions thus retaining the concentration of the solution. Utilising the process of electroplating for copper, a thermocouple junction was generated at the uninsulated end of a thin constantan wire creating a T-type thermocouple junction constantan-copper. More details on the electroplating procedure can be found in appendix C.

Instead of using a second thermocouple wire made of copper to close the thermocouple circuit, the outer conductor of the coaxial cable was utilised as second thermocouple wire closing the circuit. This innovative yet simple setup had the advantage of minimising the reduction in cross-sectional area of the cooling channels as well as all benefits associated with a rugged design, for instance, no risk of damage to the wire during manufacture. A copper wire could then be soldered to the outer conductor of the coaxial cable at the proximal end of the cable and hence outside of the narrow shaft region. Both wires, constantan and copper, were then guided along the applicator feed cable towards the microwave generator where an appropriate interface could be installed. Figure 5.25 displays the circuit diagram of the developed thermocouple. The top diagram represents the functional diagram of the thermocouple design; the lower diagram the detailed make-up of the thermocouple including the constantan wire, the copper plated end of the constantan wire, the electrical contact of the plating to the outer conductor of the semi-rigid coaxial cable acting as second thermocouple wire and the copper wire with its respective solder joint connecting to the outer conductor.

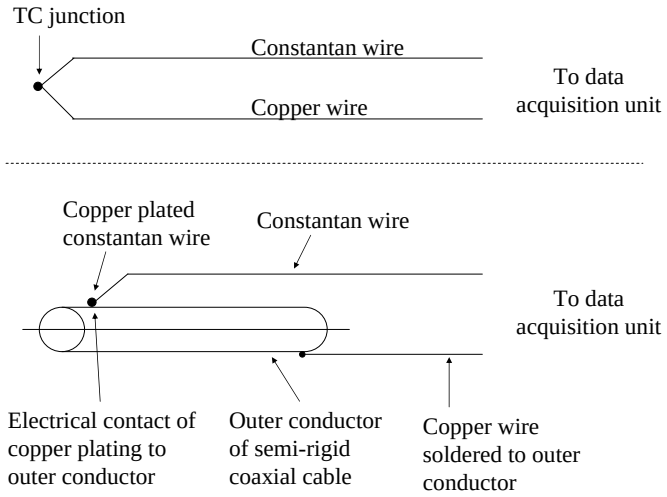

Figure 5.25: Detailed circuit diagram of developed thermocouple being part of the designed cooling failure detection system.

5.6.5 Manufacture of Round Cooling System with Temperature Sensor

The sensor design described was subsequently incorporated into the existing round cooling system. The current copper wire forming the two cooling channels was exchanged for an insulated constantan wire of correct diameter (OD 0.45 mm) and 3 mm copper

plating on one end. The assembly of the cooling system was performed according to the instructions given in 5.4.2. The pressure exerted on coaxial cable and tube established the necessary electrical contact for the operation of the thermocouple between copper plating and outer conductor.

Difficulties in the assembly were encountered due to the friction of the wire insulation which complicated the insertion of the coaxial cable considerably. Furthermore, the wire insulation was damaged at various places during the process. However, an electrical contact between constantan wire and outer conductor had to be avoided in order to ensure that the thermocouple junction was located close to the ferrule as intended reading valid temperatures and not at some point further down the cable due to unwanted electrical shorts. Damage to the wire insulation therefore had to be avoided in future assemblies.

5.6.6 Experimental Validation of Temperature Sensor

The temperature of a hot water load was measured simultaneously with a commercially available T-type thermocouple (TC1; 0.25 mm diameter; OMEGA Engineering, Inc.; 5TC-TT-T-30-36; accuracy ± 1 °C) and the developed cooling system with internal thermocouple (TC2). An extension wire made of copper was soldered to the proximal end of the outer conductor of the semi-rigid cable and connected, together with the constantan wire, to the digital acquisition unit (DAU). TC1 and TC2 were then simultaneously introduced into hot water load of (51 ± 1) °C, and temperature data of both TCs recorded.

Figure 5.26 displays the temperature traces for both commercial thermocouple (TC1) and fabricated thermocouple (TC2). In air, TC1 and TC2 recorded (16.3 ± 0.2) °C and (16.8 ± 0.2) °C, respectively. Inserted into the hot water load, TC1 read (51 ± 0.2) °C and TC2 (51.4 ± 0.2) °C.

The delay in reaching the final temperature in the case of TC2 can be explained by considering the respective locations of the thermocouple junctions. The junction of TC1 was located at the very tip and hence in direct contact with the water. In contrast to that, the junction of the plated wire TC2 was shielded from the water by the stainless steel tube. The final temperature was therefore reached approximately 5 s after that recorded by TC1.

Within the limits of the measurement accuracy, both thermocouples recorded the same temperatures. The operation of the manufactured plated thermocouple junction was hence validated.

5.6.7 Improvement of Temperature Sensor Design

Due to the difficulties encountered during the fabrication of the previous design, a more robust and reliable design was required. The main problems in the initial design were linked to:

- Large coefficient of friction of polyamide wire insulation.
- Kinking of the wire due to its small diameter (0.45 mm).

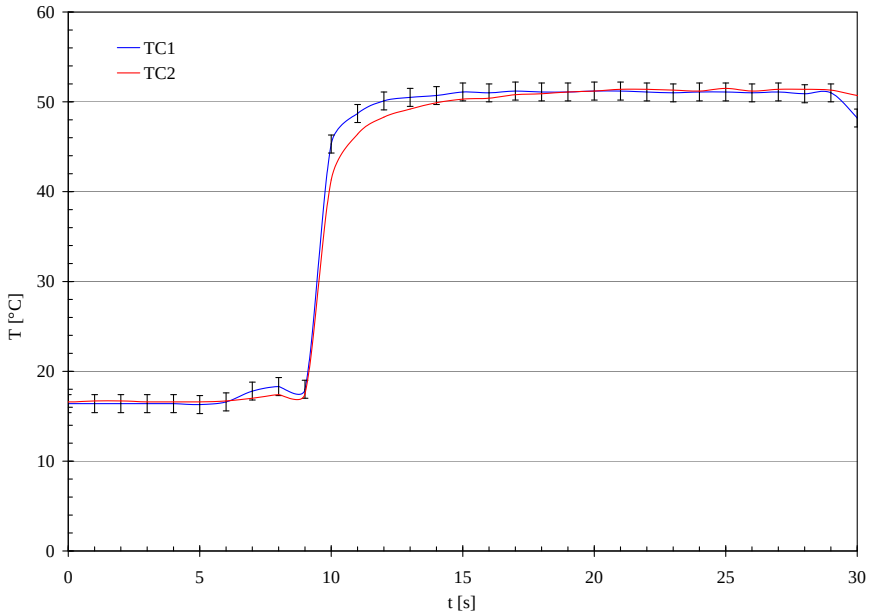

Figure 5.26: Temperatures of water load recorded with commercial (TC1) and manufactured thermocouple (TC2).

- Missing rugged wire insulation preventing electrical contact to neighbouring structures.

A solution was found in the use of a hypodermic stainless steel tube through which the constantan wire was threaded. Suitable sizes of stainless steel tube and enamelled constantan wire were available: 0.46 mm OD, 0.31 mm ID, 144 mm in length (from T/W; 26 gauge; Cooper's Needle Works Ltd.), and 0.14 mm OD constantan wire (Scientific Wire Company).

Experimental validation was undertaken in the following chapter 7, in conjunction with the validation of a batch of prototype systems built following the latest applicator and cooling system designs.

5.7 Conclusion

This chapter presented three designs of closed cycle cooling systems, oval, round, and round with cooling failure detection. The latest design, round with cooling failure detection, met the requirements listed in the design brief (see p.40) concerning the applicator's cooling system: providing a powerful cooling system for safe high-power device operation, preventing skin burns by keeping maximum shaft temperatures below 48 °C, facilitating material selection due the lowering of applicator temperatures, and improving the sphericity of ablations.

The next step in the device development was a prototype batch build using the latest design round with thermocouple in order to validate the complete prototype system. Prior to the batch build however, a brief analysis of applicator service failure is given.

Chapter 6

Analysis of Applicator Service Failures

6.1 Introduction

Up to this point several 1.8 mm and 2.4 mm applicators had been built and tested in various ways apart from those mentioned in previous chapters. During these experiments a number of device failures occurred. Since device reliability plays a critical role in the design and development of any medical device, failures of any kind must be avoided. Failures of the 2.4 mm applicator were included due to the similarity in design of 2.4 mm and 1.8 mm devices. Any failures observed in the 2.4 device were hence expected to also be of critical importance for the reliability of the smaller device. The major failure types are discussed in this chapter, including the nature, cause, and where possible, remedial measures taken.

6.2 Types of Failures

6.2.1 Fracture of Tip

The fracture of an applicator tip during operation belongs to the most severe failure modes. The failure displayed in figure 6.1 occurred after 150 s of a planned 4 min ablation of 60 W with a round closed cycle cooling applicator and flow rate of approximately 3 l/h. It can be seen that the cylinder, washer and part of the trocar tip of the applicator were completely separated from the main applicator body. The cylinder as well as the trocar piece were discovered in the ablated tissue after the failure, both abnormally blackened. Both pieces were found approximately 1 cm in front of their expected locations and in non-ablated tissue. The washer however could not be found.

The failure was most likely caused by the melting of the washer to centre conductor solder joint. The melting point of the solder utilised (Surface Mount Solder Paste from Electrolube) was 183 °C, a temperature which could have been exceeded during the ablation procedure. Melting of the solder could have resulted in sparking and subsequent shorting of centre and outer conductor as molten solder spread throughout the inside of the tip and cylinder. In the event of a spark, very high temperatures would

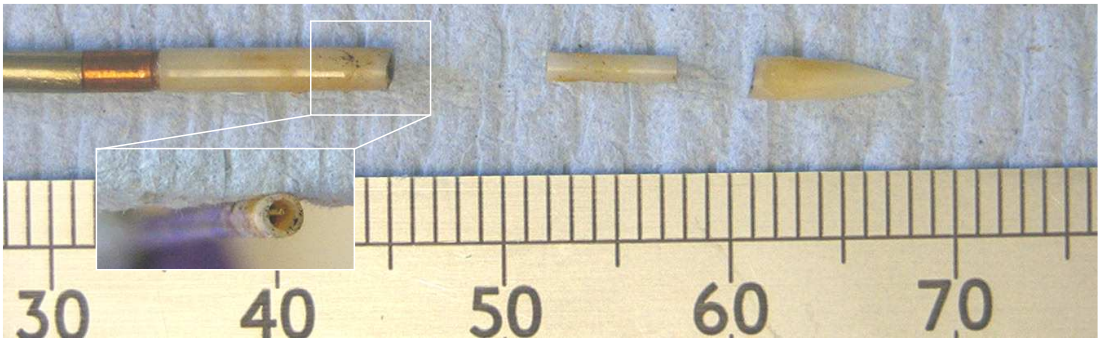

Figure 6.1: Fractured applicator tip and recovered trocar piece and cylinder. Failure occurred during an ex-vivo ablation of 60 W, 4 min, 3 l/h with a round closed cycle cooling applicator.

result leading to the fracture of the tip and the dislocation of the cylinder. Such an event could also explain the darkening of the cylinder which could be a thin layer of re-solidified solder. Failures of this kind had already been observed several times for the 2.4 mm applicator.

Solution Concept 1 — Solderless Design

The first solution concept consisted of a design without solder around the washer since eliminating the presence of solder in the high temperature region of the tip would resolve the root of the problem.

Computer simulations as described in chapter 4 were performed in order to assess the feasibility and effect of the solderless design. The analysis was solved for ID washer values of 0.2 to 0.4 mm with air assigned in the gap between washer and centre conductor. The resulting $S11$ showed promising results for very small gaps. However a slight increase in air gap size resulted in a non-operational device. The model hence indicated a possible but sensitive solderless design.

The solderless design was tested using a 2.4 mm applicator since no parts for building 1.8 mm applicators were available at that time. The applicator was assembled as usual, omitting the step of soldering the washer. S11 was then recorded in saline. At first, the S11 agreed well with expected values for that device. However, when turning and moving the applicator, S11 proved unstable. In certain positions, S11 was only measured to -5 dB. Furthermore, the sound of a lose part could be heard when turning the applicator. Due to those reasons, the solderless design was considered inadmissible and discarded.

Solution Concept 2 — Conductive Epoxy

The second option comprised the use of a metal-loaded high temperature epoxy (Permabond Bondmaster ESP110) with recommended service temperature range of up to 180 °C. Due to its metallic content the paste was electrically conductive. Its main function however was to locate the washer in order to avoid movement. Epoxy adhesives

are thermosetting glues forming cross-links when mixed with a catalyst or hardener. If taken beyond their service temperature limits, epoxies do not re-melt but at some point begin to char or even burn. The danger of molten conductive material in the tip was hence averted, the possibility of charring or burning however did not improves matters much. So, in order to make sound decisions on the use of adhesives in this region, better understanding of maximum tip service temperatures was required.

6.2.2 Ferrule Puncture

During experiments with the 2.4 mm applicator a failure occurred during an ablation of 60 W. Subsequent inspection revealed a puncture through the lateral wall of the ferrule. The puncture diameter was measured to (0.5 ± 0.1) mm and its vertical position to 1.5 mm with respect to the ferrule to tip intersection. The centre conductor was truncated some millimetres above the puncture contacting the outer conductor via a mass of resolidified copper measuring (0.47 ± 0.02) mm in diameter.

Possible causes include the presence of impurities inside the ferrule void, distortion of the centre conductor towards the inner surface of the ferrule and burrs on the cut surface of the outer conductor. Any of those cases would have led to a reduction in gap between centre and outer conductor or ferrule, thus increasing the risk of arcing. The fact that part of the ferrule and centre conductor had melted and re-solidified supported this assumption. Since an electrical contact between centre and outer conductor had been created, the applicator was short-circuited and hence no longer operational.

Cleanliness and visual inspections during applicator assembly presented the best precaution to this kind of failure. Although small burrs, some impurities, and minute bends in the centre conductor could not entirely be avoided, these measures were considered adequate.

6.2.3 Failure of Tip Bond

During the development and validation of the preceding 2.4 mm applicator, a number of cases of tip bond failure were encountered resulting in the complete detachment of the ceramic tip from the applicator. The adhesive used for the tip joint in all those devices was a two-component high temperature ceramic adhesive (Ceramabond™ 571-VFG from Aremco Products, Inc.) featuring a maximum service temperature of 1760 °C.

The most likely reason of failure was considered to be connected to an imperfect bond. The ceramic powder consisted of high purity fine grains of particle sizes between 1 µm and 5 µm and recommended glue line thickness between 0.05 mm and 0.2 mm. A glue line thickness of less than 0.05 mm prevents uniform adhesion [87]. The gap size between tip and cylinder/ferrule in the 2.4 mm device measured between 0.07 mm and 0.28 mm due to machining tolerances (see appendix A), hence close to the lower limit for acceptable glue line thicknesses. Furthermore, the assembly of that glue joint was commonly presented with difficulties due to the rapid setting of the ceramic adhesive within seconds. Once the paste had been applied into the hole of the ceramic tip, the

applicator had to be inserted immediately and in one movement. Any delay during that process would lead to a failed assembly since removal of the ceramic paste was practically impossible. Lastly, ceramics are generally brittle materials and hence prone to fracturing. All of these issues could have contributed to low quality ceramic bonds and subsequent failures.

Due to an even lesser glue line thickness of 0.05 mm to 0.21 mm in the 1.8 mm applicator, the difficulty of creating a good and strong bond using the ceramic paste had only increased. To this point in the development of the 1.8 mm applicator, a retaining compound (Loctite 638 from Henkel Technologies) had been used for all tip bonds with a maximum bond strength at room temperature. Loctite 638 looses half its strength at 145 °C and all its strength if heated to 250 °C or above. Due to indications such as high-level carbonisation of the ablation centre, the likelihood of temperatures exceeding 200 °C was high which severely weakens the bond strength. Alternative solutions for the fabrication of the tip bond were hence necessary.

Investigations into mechanical joints were made including designs featuring sliding fit, locks, bolts, or threaded ferrules, however, none presented a feasible solution. The remaining option was seen in the use of a better suited adhesive. A high performance epoxy for ultra high temperature applications was found (Aremco-Bond™ 526N-C from Aremco Products, Inc.). This high temperature (HT) epoxy had the benefit of a temperature resistance up to 300 °C, however it required a relatively long curing schedule of 4 h at a temperature of 163 °C. The HT epoxy bond strength was tested on a copper – ceramic sample and resulted in a thin strong bond line. It was hence adopted for use in the manufacture of new 1.8 mm applicators.

6.2.4 Degradation of Non-Stick Coating

Discolouration and degradation of the coating was observed around the washer and lower tip after performing ex-vivo ablations. The degradation process started during the first ablation and proceeded to a point of complete material loss within around five further ablations. The continuing loss of non-stick coating around the applicator tip had a negative effect on the withdrawal of the applicator after ablations as the tip began to adhere severely to the surrounding ablated tissue exerting additional strain on the tip bond.

The degradation of the non-stick coating was induced by the exposure to high temperatures during ablations. The regions of maximum temperature around ferrule and washer were hence most affected. Degradation could be lessened by lowering tip service temperatures. However, the effect of the cooling on lowering those temperatures had not as yet been determined.

Investigations into finding superior coatings were hence undertaken. Three coatings were tested: a polytetrafluoroethylene (PTFE) dispersion coating (DuPont PTFE TE 3893-N; 59.94 % solids; continuous operating temperature 260 °C), a PTFE based dry-film lubricant coating (Xylan 8110/G2599; grey/black; Whitford Plastics Ltd.; operating temperature up to 285 °C intermittent), and a PTFE micropowder (Dyneon TF 9207 PTFE; peak melting temperature 329 °C) added to a polyamide dispersion.

Each coating was applied on test pieces and cured according to schedule. Thereafter, the non-stick properties were analysed by heating the test pieces to temperatures of approximately 200 °C whilst in contact with tissue. Adhesion of tissue to the object under test upon removal was classified as failure, whereas a clean surface was considered evidence for the applicability of the non-stick coating. Figure 6.2 depicts the condition of the PTFE based dry-film lubricant coating (Xylan) after being subjected to the test procedure, showing cracks in the coating, chipping, and substantial tissue adhesion.

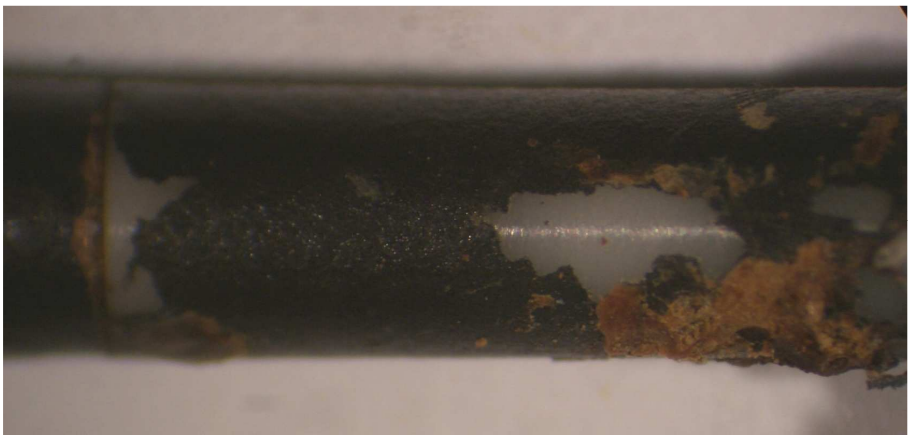

Figure 6.2: Condition of the PTFE based dry-film lubricant coating (Xylan) after testing.

None of the coatings passed the test but presented performances inferior to that of the existing non-stick coating (NuSil MED10-6600). In discussion with NuSil a similar but slightly tougher version of the silicone dispersion was recommended (NuSil MED10-6400). The initial curing schedule remained unchanged, but a last curing step of 20 min at 200 °C was added to increase the wear resistance of the coating.

6.3 Conclusions

Two of the four failures discussed could be attributed to the exposure of the applicator tip to high service temperatures: the failure of the washer solder joint leading to tip fractures and the degradation of the non-stick coating. Remedial measures were suggested for the washer solder joint in the use of a conductive epoxy and for the non-stick coating in the change to a slightly tougher dispersion. The ferrule puncture was regarded avoidable by following appropriate measures during the assembly process. In addition, tip bonds failures could be prevented by the application of a new high temperature epoxy. All issues discussed were factored into the design of the prototype system which will be discussed in the following chapter 7.

Chapter 7

Development of 1.8 mm Prototype System

7.1 Introduction and Definition of Prototype System

Seven 1.8 mm prototype systems were built and tested. The following sections describe their design, manufacture, and experimental validation. The prototype systems were built in sequence in order to allow for material and design changes between successive devices. All prototype designs were devised in collaboration with the MDTG at the University of Bath.

The prototype system consists of three main components (see figure 7.1): the applicator based on the design from chapter 4, comprising the latest cooling system design (round shaft, internal thermocouple); a flexible coaxial feed cable with surrounding cooling tube (umbilical tubing) connecting applicator to a so-called local control station (LCS); and an exit manifold where coolant is separated from the flexible feed cable. The flexible cable and umbilical tubing were introduced in chapter 5 (see figure 5.3) when flow rates and pressure values were estimated for the developed closed-cycle cooling system. Both flexible coaxial cable and umbilical tubing defined were retained for the design and manufacture of these prototypes.

The microwave source, coolant, and LCS were not considered part of the prototype system. The LCS houses the pump and a microwave disconnection unit connecting microwave source and flexible cable. The coolant flows from the reservoir through the pump into the applicator handle, up and down the shaft, and returns in the cooling jacket surrounding the flexible cable to the coolant reservoir via the exit manifold as indicated by arrows in figure 7.1. In this setup, all applicator surfaces (shaft, handle, feed cable) that are likely in contact with patients are being actively cooled. This design presented the first fully-cooled microwave ablation device developed in the MDTG group as well as a significant improvement compared to cooling systems installed in other commercially available microwave devices due to the reasons given in section 5.2.

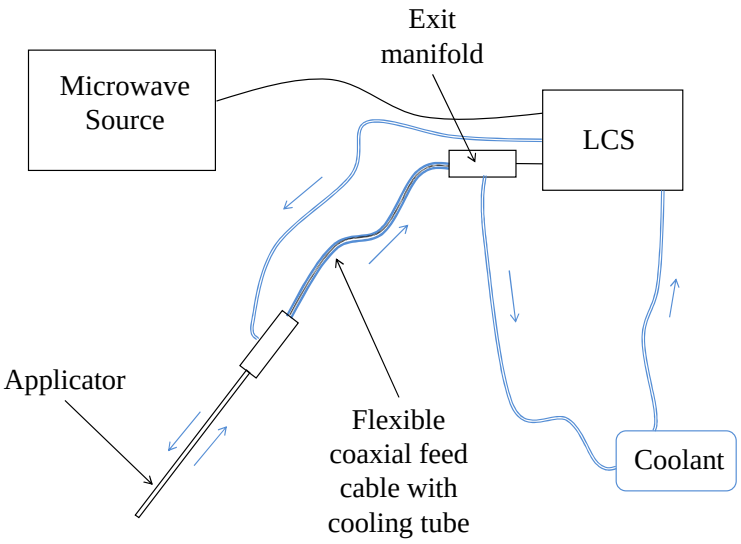

Figure 7.1: Components of 1.8 mm Prototype System. Direction of coolant flow indicated by arrows.

7.2 Objectives

The objectives of the batch build included general design optimisation, debugging of the assembly procedure, and overall device validation. Device validation consisted of several experiments including $S11$ measurements, calorimetry, measurements of service temperatures at tip, ferrule, and shaft locations, determination of optimum power-time setting, determination of optimum flow rate, investigations of temperature rises in the applicator in the event of a simulated cooling failure, applicator reliability tests, determination of ablation size and shape, assessment of coating degradation over time, validation of tip bond strength, and elimination of water leakages in the system. Table 7.1 lists the experiments, the applicator(s) utilised for the particular task, and the section of the document addressing them.

The main objectives of prototypes 1 and 2 were the testing of the overall system design in terms of correct and fitting part dimensions and suitability of bonding agents for the manufacture of the handle and exit manifold. Both prototypes were fully operational after manufacture and were hence used for further testing as outlined in section 7.5.

7.3 Design

The engineering drawing of the complete prototype system is shown in figure 7.2. The design comprises the applicator antenna, handle, flexible feed cable with cooling tube, and exit manifold. Individual system components are also specified in the bottom left hand corner. Prototypes 1 to 5 were built according to this design, prototypes 6 and 7 with minor changes of, for instance, part length or choice of adhesive in order to simplify

Table 7.1: Objectives of prototype batch built and testings

Objective	Applicator(s)	Section
Optimisation of system design	All (1 to 7)	7.3
Debug assembly procedure	All	7.4
Measurement of $S11$	1 to 6	7.5.1
Calorimetry	4, 5	7.5.2
Measurement of shaft service temperatures	1	7.5.3
Measurement of tip and ferrule service temperatures	1, 4, 5	7.5.3
Determination of optimum power-time setting	3	7.5.3
Determination of optimum flow rate	1	7.5.3
Validation of cooling failure detection system	1	7.5.4
Validation of applicator reliability	3	7.5.5
Validation of ablation size and shape	1	7.5.6
Determination of coating degradation	3	7.5.7
Validation of tip bond strength	All	7.5.8
Elimination of water leakages	All	7.5.9

the manufacturing process. However, none of those changes altered the performance of the microwave system.

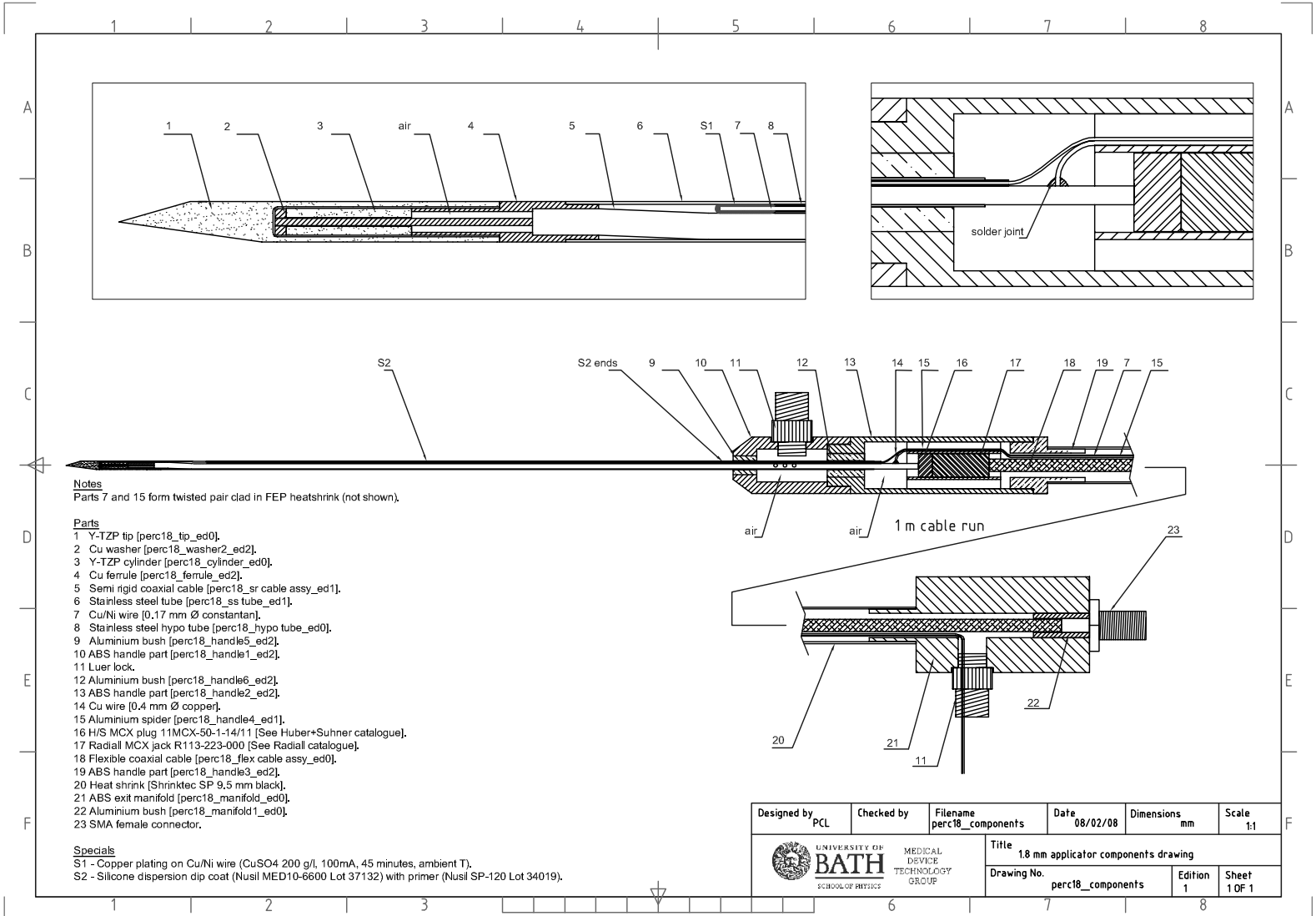

Figure 7.2: Design drawing of first 1.8 mm Prototype System.

The handle was designed to fulfil a number of purposes. First of all, it had to serve its primary purpose of handling during use. In addition it provided a connection to the high-pressure coolant input from the LCS, two separate chambers for coolant input and output to the shaft, mechanical and water-proof protection of the MCX microwave connectors linking semi-rigid and flexible coaxial cable, and lastly a passageway for the coolant from the handle into the tube surrounding the flexible feed cable.

All handle and exit manifold parts were made of acrylonitrile butadiene styrene plastic resin (ABS), a material easy to bond and machine with a melting point of 105 °C. Spider (part 15) and bushes (parts 9, 12, and 22; see figure 7.2) were made of aluminium for better thermal conduction and mechanical strength. Both microwave coaxial cables, semi-rigid and flexible were supplied by Rhophase Microwave Ltd.

7.4 Assembly

7.4.1 Assembly of Prototype 1

First, the antenna structure of the prototype system was assembled including the manufacture of applicator tip and cooling system. Thereafter, the exit manifold was fabricated, followed by the connection between flexible cable assembly to applicator and enclosing handle structure. Figure 7.3 identifies the locations, order, and nature of all bonds and joints made during the assembly of prototype 1. A complete and detailed description of the manufacture of the first prototype system can be found in appendix D.

Different stages in the fabrication process of prototype 1 are displayed in figures 7.4. The top figure shows aluminium bushes separating input and output chambers in the handle. The left centre figure shows the aluminium spider protecting the MCX microwave connectors whilst providing a passageway for coolant and thermocouple wires from the handle output chamber into the tubing surrounding the flexible feed cable. The bottom figure displays the proximal handle part and the beginning of the flexible cable tubing made of black heat shrink tubing. The figure on the right depicts the assembled, bare antenna structure consisting of coaxial cable, ferrule, and tip; the thermocouple made of copper plated constantan wire inside a thin stainless steel tube; and the applicator shaft. Figure 7.5 displays the first fully assembled 1.8 mm prototype system.

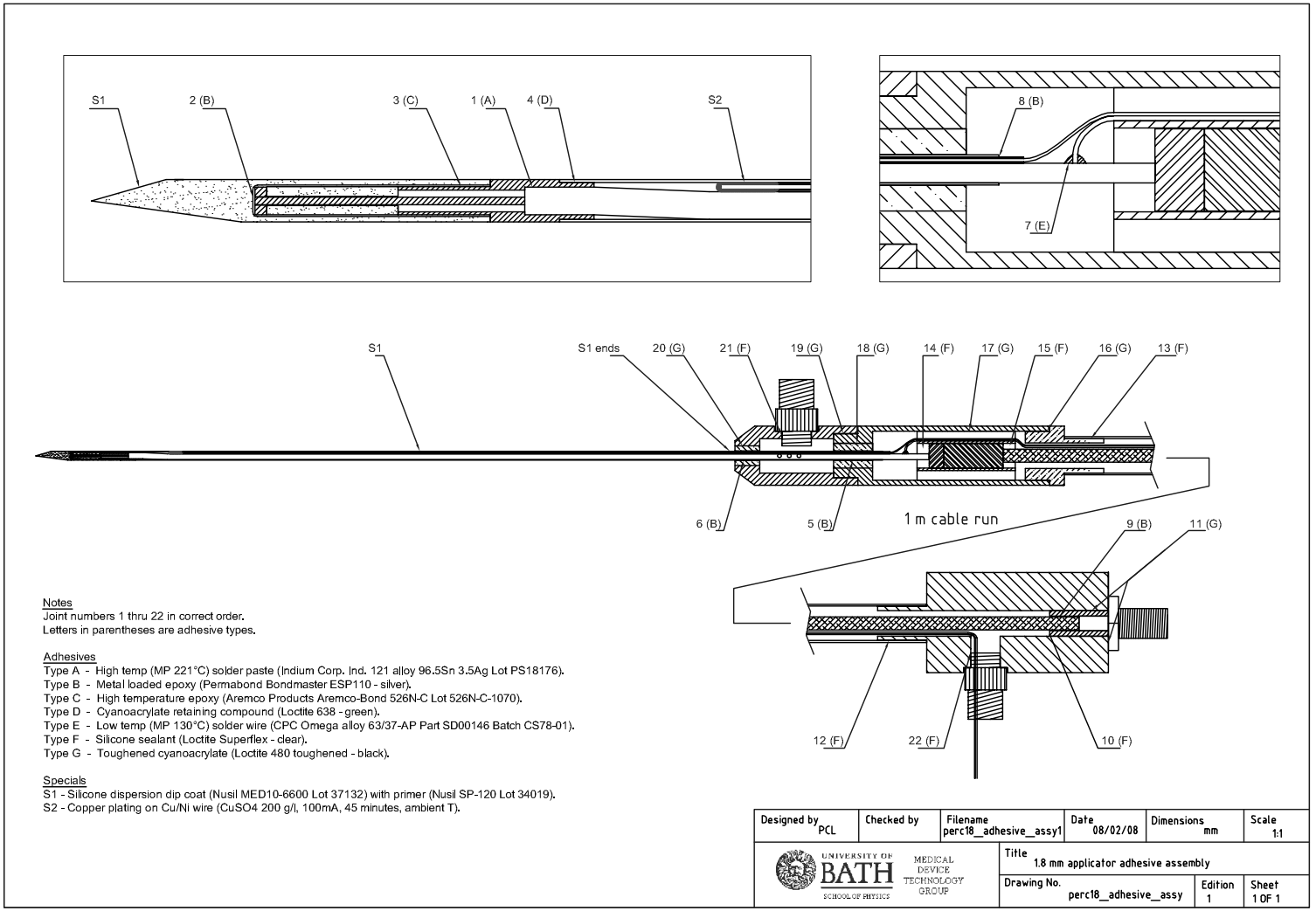

Figure 7.3: Location, order, and type of bonds of 1.8 mm prototype 1.

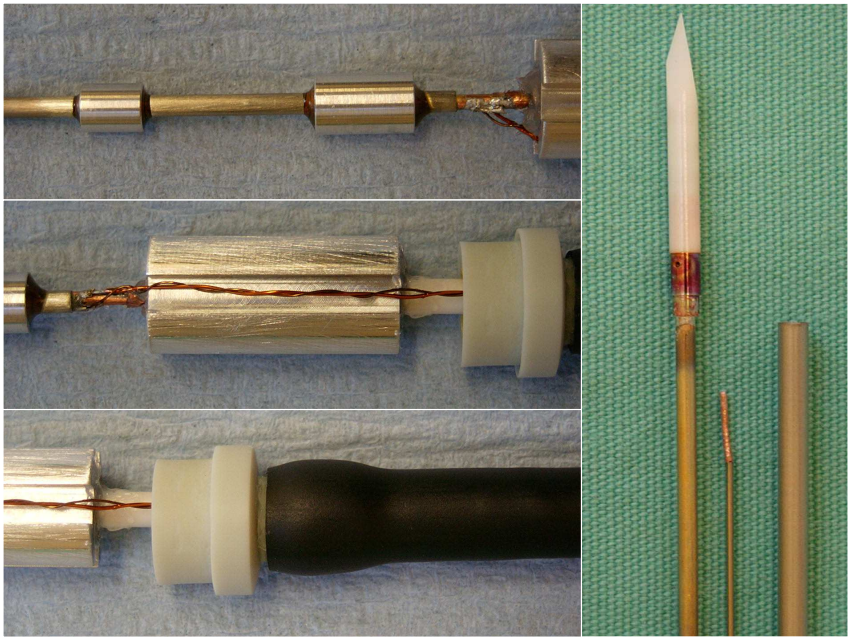

Figure 7.4: Fabrication of handle (left) and antenna (right) during assembly of 1.8 mm prototype system.

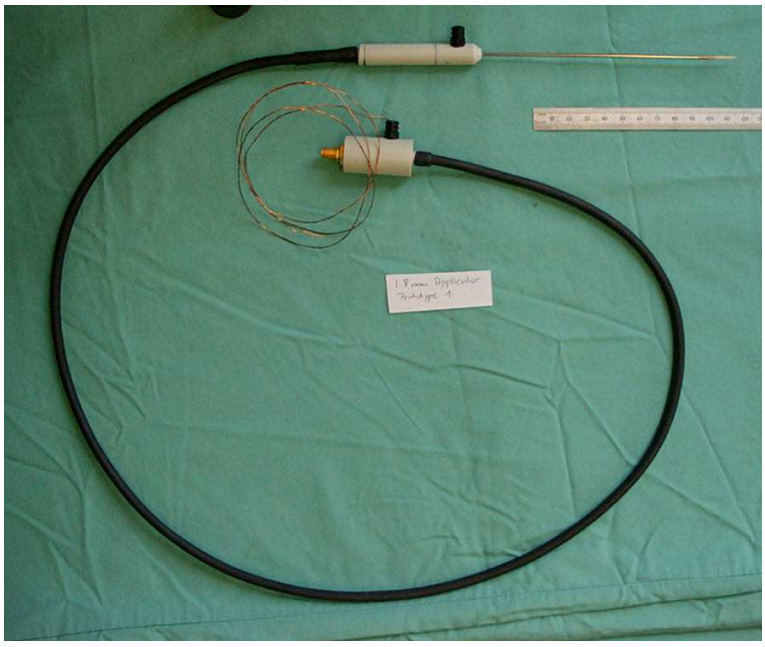

Figure 7.5: Fully assembled first 1.8 mm prototype system.

7.4.2 Assembly of Prototypes 2 to 5

As a result of difficulties encountered during the assembly and validation of the first prototype, several changes were made in the manufacturing process for prototypes 2 to 5:

1. Silver brazing for washer to centre conductor

2. HT epoxy used for:
    (a) Ferrule to shaft bond
    (b) Sealing of cooling channel (prototype 2 only)
    (c) All handle joints
3. Sealing of cooling channel for prototype 3 to 5: permabond
4. 3 mm (prototype 2) and 5 mm (prototype 3 to 5) copper plating lengths

The technique of brazing is similar to that of soldering but uses higher temperatures. In brazing, parts that are closely fitting are joined by heating an alloy or filler metal above its melting temperature (425 °C or higher). The filler material then flows into the gap between the parts induced by capillary action. Once molten, the filler and flux interact with a thin layer of the base metal forming a strong joint. The joint is thus made up of a number of different layers, each linked metallurgically to its adjacent layers. By definition, the melting temperature of the materials to be joined has to exceed that of the braze alloy by some significant amount. If silver is used as alloy, the process is also referred to as 'silver brazing' or 'hard soldering'. The gap size in silver brazing should not be greater than a few micrometres to assure a sufficiently strong capillary force. Furthermore, to produce a joint of high strength, the base metals must be particularly clean and free of oxides or greases. Flux is often required to prevent oxides from being formed while heating the base metals [88].

The silver braze chosen for joining washer and centre conductor featured a melting point of approximately 960 °C. The risk of melting, charring, or burning during device operation should thus have been eliminated. Resistance soldering tweezers were utilised to achieve the necessary temperatures required for silver brazing without damaging the cable.

7.4.3 Assembly of Prototype 6

Silver brazing of the washer had proven successful during the test with the previous prototypes. It was hence retained for all subsequent assemblies. However, the HT epoxy used in the tip joint was being displaced during curing. The most likely cause for this was the expansion of the air inside the ferrule void due to the higher temperatures during the curing schedule. Furthermore, the use of HT epoxy for all handle bonds resulted in unnecessarily long curing times during handle assembly.

Solutions to the problems encountered were sought. A conical hole of 0.2 mm to 0.3 mm diameter was drilled through the lateral wall of the ferrule to allow for the balance of air pressure during the curing of the tip bond. This hole was closed with solder upon the cure of the tip joint. In addition, the HT epoxy was replaced with Loctite 480 for all handle joints.

7.4.4 Assembly of Prototype 7

In an attempt to close the ferrule drill hole, hot solder was pushed out during the assembly of prototype 6. A possible cause for that was that during soldering the ferrule was heated causing the air inside the ferrule to heat up, thus exerting pressure on the

solder applied to fill the hole. In the assembly of prototype 7, the metal loaded epoxy (Permabond Bondmaster ESP110) was used for closing the hole in the ferrule. The prototype was mounted in a curing block with temperature controller, therefore heated to a temperature of 110 °C. Whilst kept at this constant temperature, the epoxy was applied into the hole and the assembly left to cure for about 1 h. In that way, the formation of bubbles in the adhesive caused by air expansion inside the ferrule was prevented.

7.5 Experimental Validation

7.5.1 $S11$ Measurements

The return loss $S11$ (dB) was measured for prototypes 1 to 6 in order to verify proper device operation. $S11$ was measured as detailed earlier (see page 63) using the network analyser (Wiltron 37269A). $S11$ was recorded in the frequency domain from 1 GHz to 10 GHz in 0.58% w/v saline.

The mean of the recorded return losses for prototypes 1 to 6 in is displayed in figure 7.6 (black line) together with the corresponding standard deviation (grey lines). At 2.45 GHz the return loss read (-11 ± 0.5) dB. Using the acceptance threshold of -10 dB, all devices passed.

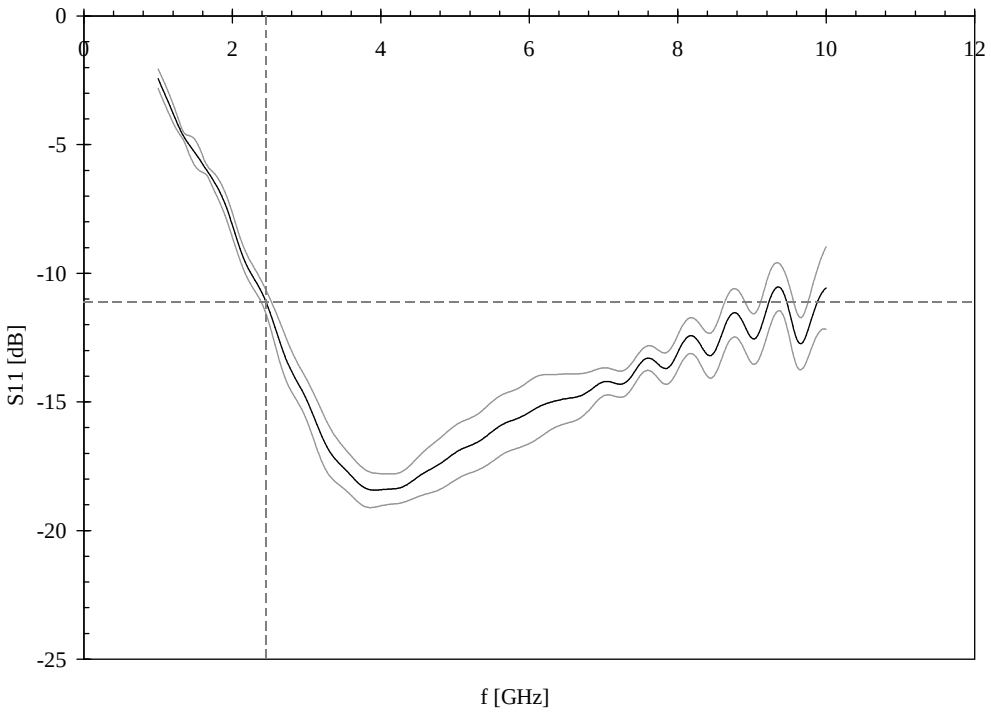

Figure 7.6: Mean $S11$ of prototypes 1 to 6 measured in 0.58 % w/v saline; standard deviation displayed in grey lines; dashed lines cross at (2.45 GHz; -11 dB).

7.5.2 Calorimetry

Objective

Calorimetry was conducted in order to determine the efficiency of the device and validate it against theoretical predictions.

Theory

The theoretical efficiency, η, is defined as useful power output divided by the total electrical power consumed (see equation 7.1). In the scope of this work the useful power output denotes the power deposited in the load, P_d (W), causing its temperature to rise, and the total power consumed corresponds to the applicator system input power, P_0 (W). The applicator input was defined as the input to the flexible cable rather than the applicator antenna itself. Calculation of the efficiency required knowledge of all cable and connector losses as well as the reflection coefficient of the applicator.

$$\eta = \frac{P_d}{P_0} \tag{7.1}$$

Using the network analyser, the loss of the extension feed cable was measured via the cable's $S12$ parameter to be -1 dB, and the sum of two connector losses to approximately -0.2 dB. The insertion losses of flexible and semi-rigid coaxial cable were taken as stated by the manufacturers, -1.0 dB/m and -1.61 dB/m, respectively. The total loss in the prototype system, including 1 m flexible cable, 0.18 m semi-rigid cable, and one connector was therefore equal to $-1.0+(-0.1)+(-0.29)$ dB $= 1.39$ dB. Lastly, using the measured $S11$ of -11 dB for saline, the theoretical power P_d absorbed by the water could be calculated. Table 7.2 shows the calculation for an output power P_{out} of a microwave generator of 30 W.

Table 7.2: Energy balance and theoretical efficiency of prototype system.

Power at generator P_{out}	30 W
Loss feed cable and connector	-1.1 dB
Power P_0 at prototype input	23.29 W
Total loss prototype	1.39 dB
Power at applicator tip	16.91 W
$S11$ of prototype	-11 dB
Power reflected at tip	1.34 W
Power P_d deposited in water	15.57 W
Theoretical efficiency η	0.67

Experimental Setup and Methodology

The prototype system was connected via a feed cable of insertion loss -1 dB to the microwave generator. A polystyrene insulated container filled with water was used in order to reduce heat losses during the experiments. The water temperature T_0 and mass m were measured using a digital thermometer (measurement error $\pm$ 0.1 °C) and

Table 7.3: Experimental results of prototype efficiency via calorimetry measurements.

Test no.	m [g]	T_0 [°C]	T_1 [°C]	ΔQ [J]	P_d [W]	η_{exp}	η_{th}
4-1	137.87	18.4	20.0	923.6	15.39	0.66	0.67
4-2	161.73	18.1	19.7	1083.5	18.06	0.78	0.67
4-3	157.83	18.5	20.0	991.5	16.53	0.71	0.67
5-1	168.51	18.5	19.9	987.8	16.46	0.71	0.67
5-2	164.03	18.7	20.1	961.5	16.03	0.69	0.67
5-3	181.18	19.1	20.5	1062.0	17.70	0.76	0.67

precision scales (measurement error ± 0.01 g), respectively. The applicator tip was then immersed into the water, the generator output power set to 30 W, and microwave power applied for a length of time (Δt) of 60 s. Immediately after test completion, the raised water temperature (T_1) was measured and recorded. This process was repeated three times for both of the prototypes utilised (#4 and #5). After the experiments, the energy deposition ΔQ was calculated according to equation 7.2, where c_p denotes the specific heat capacity of water (4181 J/(kg·K) at 25 °C) and ΔT = T_1 - T_0 the temperature rise in K. Finally, the efficiency of the prototype system was computed using $\eta = P_d/P_0 = \Delta Q/(\Delta t \cdot P_0)$.

$$\Delta Q = m \cdot c_p \cdot \Delta T \tag{7.2}$$

Results

Table 7.3 presents the results of the calorimetry experiments including the experimental power deposition P_d, as well as experimental and theoretical prototype efficiencies. The mean experimental efficiency was determined to 0.72 ± 0.04.

Discussion

The experimental and theoretical efficiencies were statistically different. Since the temperature and mass of the water load were determined with small measurement errors, and the insertion loss of the coaxial transmission line known, the most likely reason for the difference in results lay in the unstable output of the microwave generator. The power output was measured and controlled with a power meter connected directly to a sample port. However, the generator was designed for a high power output (100 W or more) at frequencies between 2.5 GHz and 10 GHz. According to the operation manual, the output was hence most stable at the centre frequency of 5 GHz. Although efforts were made to calibrate the generator output at 2.45 GHz, no definite conclusions could be drawn. Furthermore, the power output had to be continually adjusted during operation leading to errors especially during the start of an experiment. The error in generator output power was therefore estimated to 30 W ± 5 W. Assuming an output power P_{out} of, for instance, 33 W in the calorimetry experiments would result in a mean experimental efficiency of 0.65 ± 0.04 close to the theoretical value.

Figure 7.7 illustrates the energy balance of the prototype system in percentages for the theoretical efficiency of 0.67. It can bee seen that 21 % of the input power is lost in

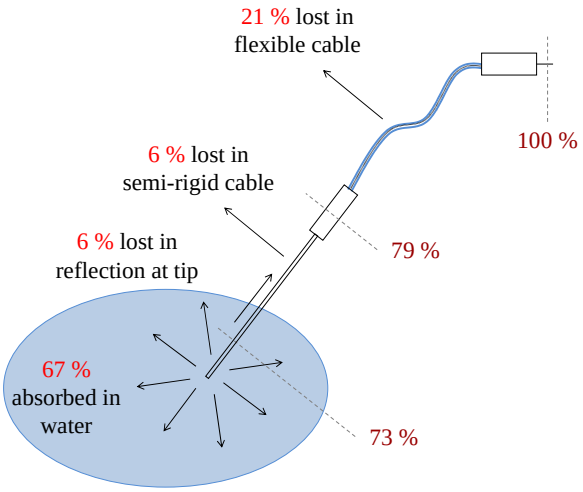

Figure 7.7: Energy balance of prototype system for the theoretical efficiency of 0.67. The reference point was the flexible cable input, as stated by the value of 100 % at this point.

the flexible feed cable, 6 % in the semi rigid coaxial cable, and a further 6 % due to the reflection at the tip; 67 % of the applicator input power is hence absorbed by the water.

Conclusion

Apart from the difficulty regarding the output power of the microwave source, the calorimetry experiments were useful for obtaining an energy balance for the prototype system. Furthermore, no unknown power losses occurred which might have been caused by poor connections or damaged cables in the system.

7.5.3 Measurement of Prototype Service Temperatures

Introduction

Prototype service temperatures were measured during ex-vivo ablations in order to obtain the optimum power-to-time setting for the system. Optimum in this context meant maximising ablation size for a maximum ablation time of 8 min whilst ensuring device survival. Since device temperatures were closely linked to the coolant flow rate, the optimum flow rate was also required and hence determined during the tests.

Experimental Setup and Methodology

Six bare thermocouples (TC1 to TC6; 0.127 mm diameter; T Type; OMEGA Engineering, Inc.) were utilised to measure tip, ferrule and shaft service temperatures. Figure 7.8 displays the locations of TC1 to TC5 attached along the applicator, as well as internal thermocouple TC6 inside the shaft. TC2 was attached to the centre section of

the ferrule and its lead wires attached to the shaft. TC3 to TC5 were affixed likewise at positions of 20 mm, 40 mm, and 80 mm from the centre of the ferrule, respectively.

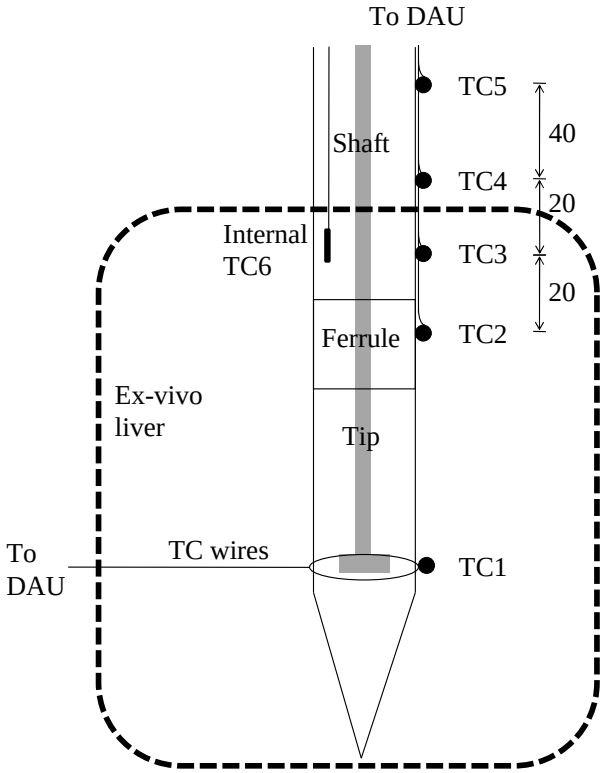

Figure 7.8: Experimental setup for measuring applicator service temperatures at tip, ferrule, and shaft locations during ex-vivo ablations. Dashed black lines represent the ex-vivo liver load.

TC1 recorded the applicator tip temperatures. In order to reduce the incidences of direct heating in the thermocouple, its lead wires were laid out perpendicularly to the applicator axis. Furthermore, the wires were formed into a loop at the junction, threaded over the applicator tip and guided into the correct position. In this way, the thermocouple wires of TC1 were located perpendicularly to the electric field during device operation hence minimising direct heating. Direct heating in metallic objects is caused in parts positioned parallel to the electric field leading to current generation and therefore heat generation. The junction of TC1 was coated with a second layer of non-stick silicone dispersion, yielding protection and insulation for the sensor.

In order to place the applicator as outlined in figure 7.8, a vertical cut was made in the ex-vivo liver and the applicator inserted at the very end of that cut so that the wires of TC1 could exist the tissue perpendicularly. After applicator placement, the cut was closed and experiments were started.

Ablations were performed for input powers P of 30 W to 89 W relative to the input of the flexible cable and times t ranging from 4 min to 10 min. A temperature limit T_{lim}, measured at either tip or ferrule, was defined prior to the first experiment; if

reached during an ablation it resulted in a power switch-off. Cooling flow rates were varied between 1.3 l/h and 4.4 l/h. Power, time, temperature limit, and flow rate were sequentially increased between successive tests in order to find the applicators maximum performance limit whilst minimising device losses due to failures. The value of T_{lim} was hence increased from initially 180 °C, to 250 °C, and finally 300 °C (see table 7.4).

The first set of 4 min tests (tests 1 to 8) was carried out with thermocouples TC1 to TC6 attached as discussed. Tests 2, 9, and 10 were conducted to determine the optimum flow rate of the system. Tip temperatures were continued to be measured for other applicators (applicators 4 and 5; tests 11 to 24) and increasing ablation times. For those tests, a different microwave source was utilised with fixed increments in input powers leading to slightly different levels than those set previously. A final ablation of 89 W, 10 min was performed in order to test the applicator survival.

Results

Table 7.4 lists the sequence of tests performed including test parameters P, t, T_{lim}, Q, T_{max}^{tip} and where applicable T_{max}^{ferr}. Input power P, ablation time t, and flow rate Q were gradually increased in order to find the optimum settings for the system. No failures occurred during testing. The maximum service temperatures of both tip (T_{max}^{tip}) and ferrule (T_{max}^{ferr}) were recorded after each test and are also listed in table 7.4.

Table 7.4: Sequence of experiments performed. Input power P and ablation time t were steadily increased in order to determine the optimum power-time setting of the prototype system.

Test	P [W]	t [min]	T_{lim} [°C]	Q [l/h]	T_{max}^{tip} [°C]	T_{max}^{ferr} [°C]	Measurements; applicator number
1	30	4	180	1.3	110	100	tip, ferrule, shaft temperatures; # 1
2	30	4	180	3.2	130	84	tip, ferrule, shaft temperatures; try to decrease T_{max}^{ferr}; # 1
3	40	4	180	3.2	150	90	tip, ferrule, shaft temperatures; # 1
4	50	4	180	4.0	180	107	tip, ferrule, shaft temperatures; T_{lim} reached at 187 s; # 1
5	60	4	180	4.0	180	95	tip, ferrule, shaft temperatures; T_{lim} reached at 83 s; # 1
6	60	4	250	4.0	195	105	tip, ferrule, shaft temperatures; # 1
7	70	4	250	4.4	230	110	tip, ferrule, shaft temperatures; # 1
8	80	4	250	4.4	275	120	tip, ferrule, shaft temperatures; # 1
9	60	6	250	3.2	250	N/A	Q increased to 4.0 l/h at 231 s; # 1
10	40	4	300	5.0	115	N/A	tip temperatures; # 5
11	48	4	300	4.3	118	N/A	tip temperatures; # 5
12	64	4	300	4.3	140	N/A	tip temperatures; # 5
13	79	4	300	4.3	174	N/A	tip temperatures; # 5
14	64	4	300	4.3	160	N/A	tip temperatures; # 4
15	79	4	300	4.3	210	N/A	tip temperatures; # 4
16	79	4	300	4.3	211	N/A	tip temperatures; loose TC1; # 4
17	48	8	300	4.2	148	N/A	tip temperatures; # 5
18	64	8	300	4.2	170	N/A	tip temperatures; # 5
19	79	8	300	4.2	182	N/A	tip temperatures; # 5
20	48	8	300	4.2	140	N/A	tip temperature; # 4
21	64	8	300	4.2	203	N/A	tip temperature; # 4
22	79	8	300	4.2	174	N/A	tip temperature; # 4
23	89	10	300	4.2	294	N/A	applicator survival test; # 4

Shaft temperatures recorded for the minimum and maximum ablation settings of 30 W, 4 min, 1.3 l/h (test 1; solid lines) and 80 W, 4 min, 4.4 l/h (test 8; dashed lines) are shown in figure 7.9.

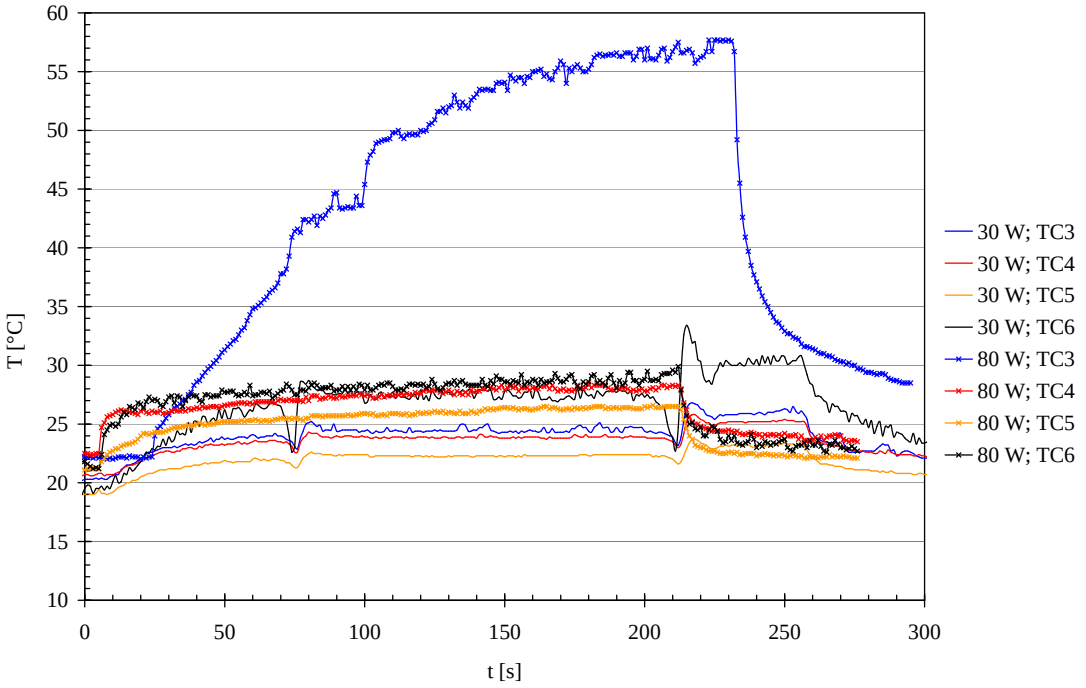

Figure 7.9: Temperatures recorded along shaft for a 30 W, 4 min, 1.3 l/h and 80 W, 4 min, 4.4 l/h ablation. TC3 at 20 mm, TC4 at 40 mm, TC5 at 80 mm from ferrule; TC6 internal TC.

Figure 7.10 displays the measured data for tip and ferrule service temperatures recorded during ablations of 4 min at 40 W, 60 W, and 80 W. The data shown has been averaged; it was taken from experiments performed at these settings (see table 7.4). Likewise, tip temperatures have been recorded for ablations of 8 min at 50 W, 60 W, and 80 W which are shown in figure 7.11.

Figure 7.12 compares the prototype temperatures for two ablations performed at 30 W using different flow rates, 1.3 l/h and 3.2 l/h (tests 1 and 2). Both ablations were performed at the onset of prototype testing, hence the low input power of 30 W.

The effects of an increase in flow rate from 3.2 l/h to 4.0 l/h on applicator temperatures during an ex-vivo ablation of 60 W (test 9) is depicted in figure 7.13. Flow rate was increased at approximately 230 s.

Discussion

During the 30 W ablation, all temperatures recorded at the shaft stayed below 35 °C (see figure 7.9). The highest temperature was experienced by the internal thermocouple TC6, then by TC3, TC4, and TC5. The order hereby corresponds to increasing distances of respective thermocouple from the ablation centre (see figure 7.8). The dips at

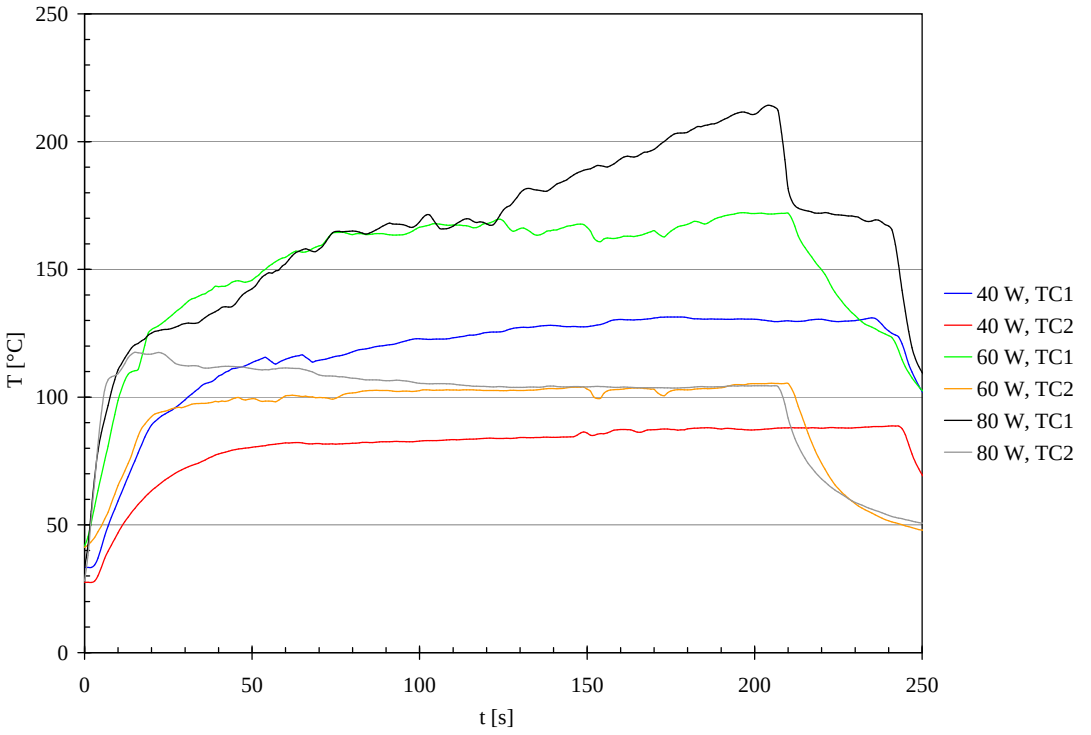

Figure 7.10: Tip (TC1) and ferrule (TC2) temperatures recorded during ex-vivo ablations of 4 min at 40 W, 60 W, and 80 W.

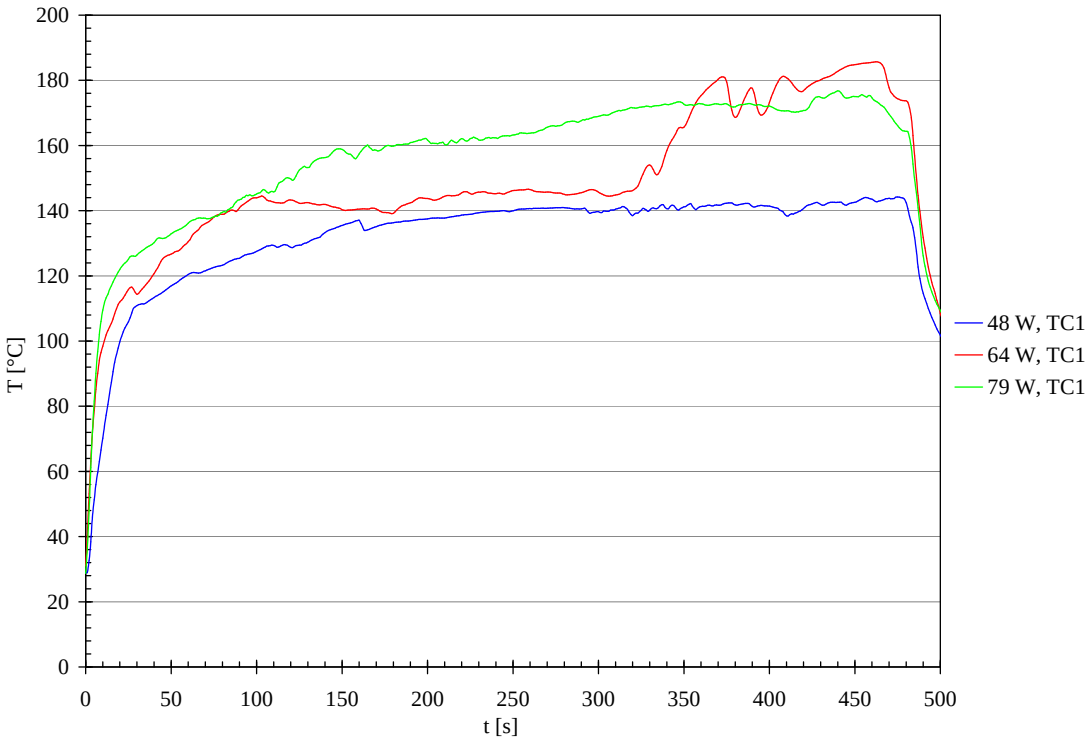

Figure 7.11: Tip temperatures recorded during ex-vivo ablations of 8 min at 48 W, 64 W, and 79 W.

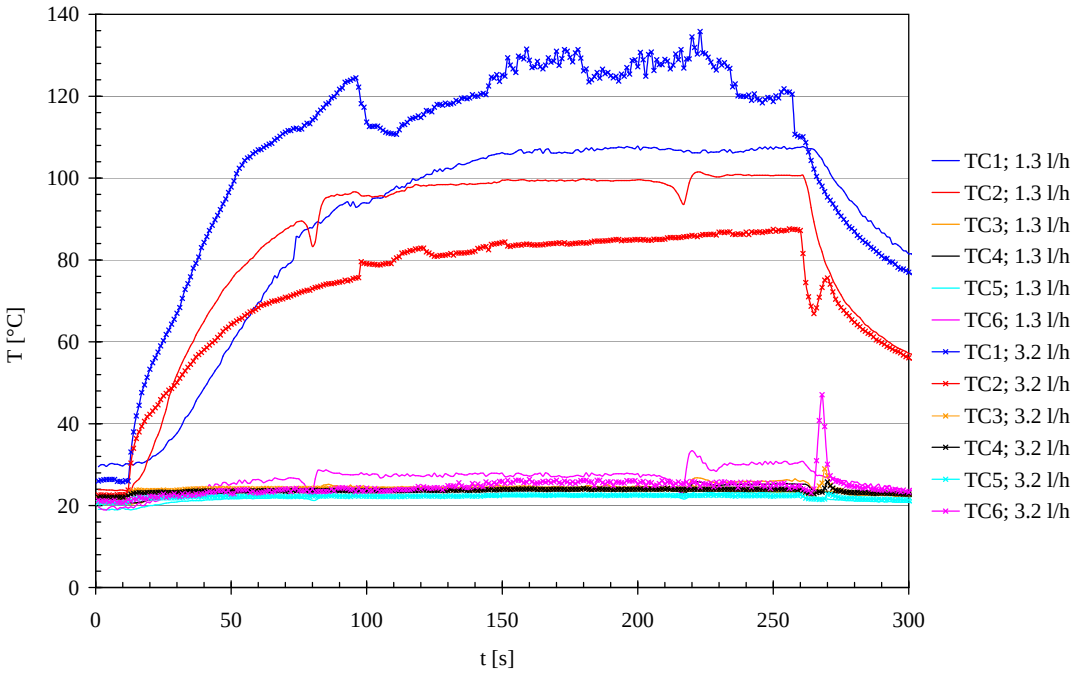

Figure 7.12: Comparison of prototype temperatures during ex-vivo ablations of 30 W for different flow rates of 1.3 l/h and 3.2 l/h.

times 74 s and 211 s were caused by a sudden automatic switch-off of microwave power. The time it took to reset the power in those two instances was added to the ablation time, hence a total ablation time of approximately 250 s.

Temperatures of the 80 W ablation were similar (see figure 7.9), in that temperatures of TC6 were higher than TC4, and TC4 higher than TC5. The exception was TC3, reading up to 58 °C. These high readings of TC3 can be explained by considering the location of TC3 and the input power level. An ablation of 80 W results in a longitudinal ablation diameter of at least 40 mm (ablation sizes will be determined in section 7.5.6). Since TC3 was attached 20 mm from the ferrule, it was situated inside the ablation zone, hence experiencing cyto-toxic temperatures. In this case, TC4 was the first thermocouple outside the ablation recording a maximum temperature of 28 °C.

It was hence shown, that shaft temperatures could be kept below 48 °C for input powers up to 80 W and ablation time 4 min, when using appropriate flow rates. Furthermore, since the highest shaft temperatures were measured with the internal thermocouple, thermocouples TC3 to TC5 were not utilised any longer in subsequent tests.

Temperatures at the ferrule reached steady-state conditions of (85 ± 4) °C, (104 ± 4) °C, and (108 ± 4) °C for 4 min ablations of 40 W, 60, and 80 W, respectively (see figure 7.10). Temperatures did therefore not significantly increase for 80 W ablations compared to those of 60 W. Since those steady-state conditions had been reached within 2 min, ferrule temperatures were not continued to be measured for the subsequent ablations of 8 min.

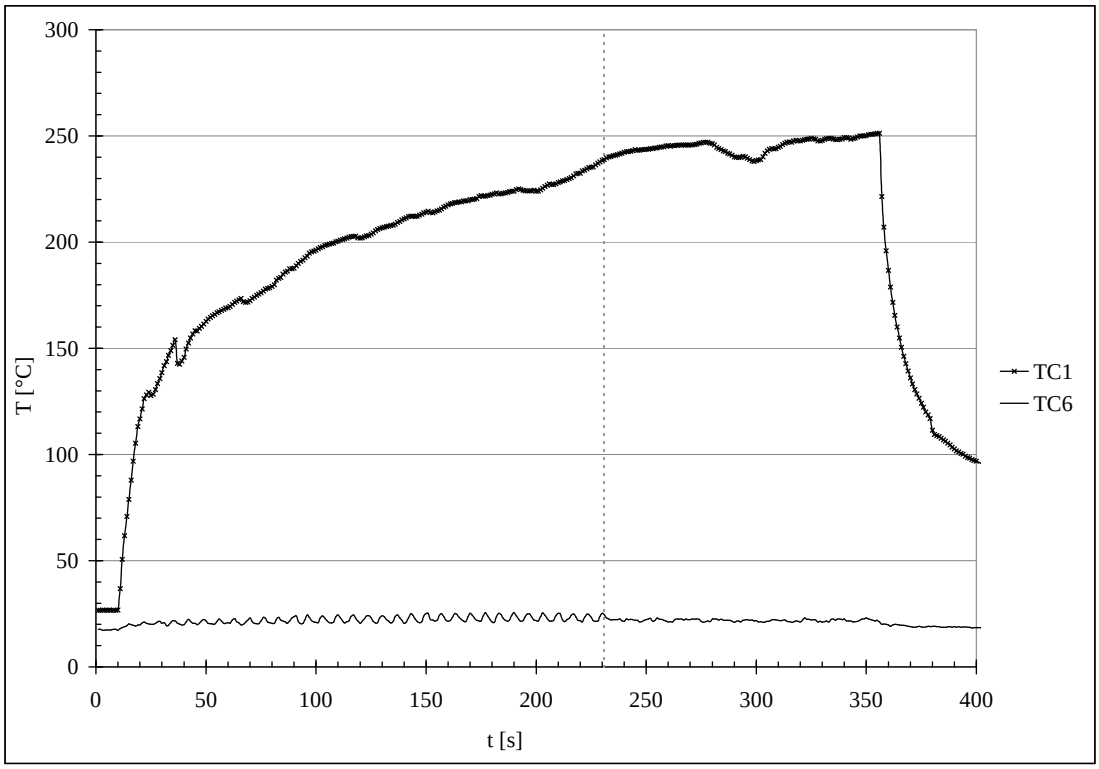

Figure 7.13: Effects of increase in flow rate from 3.2 l/h to 4.0 l/h on applicator temperatures during ex-vivo ablations of 60 W; flow increased at 231 s (dashed vertical line).

Figure 7.10 shows that tip temperatures were generally higher than those recorded at the ferrule and rising for higher input powers. The difference in ferrule to tip temperature was due to the direct cooling of the ferrule but not tip. Since coolant is flowing across the surfaces of the lower part of the ferrule, heat convection in the fluid contributes to the general heat transfer via conduction. At locations further up the tip, the effects of the cooling were limited to heat conduction alone. The maximum temperatures at the tip were 133 °C, 172 °C, and 214 °C for 4 min ablations of 40 W, 60 W, and 80 W, respectively.

The maximum tip temperatures during the 8 min ablations of 48 W, 64 W, and 79 W were 144 °C, 186 °C, and 176 °C, respectively (see figure 7.11). Hence, maximum mean tip temperatures increased for greater input powers with the exception of the last test (79 W, 8 min). In this case, a higher maximum temperature actually resulted for 60 W than for 80 W. The maximum temperature during the 80 W ablation was unexpectedly low, which was highlighted by the fact that temperatures during the 80 W, 4 min ablations exceeded those performed over 8 min.

The most likely cause for this inconsistency in power-to-tip-temperature relation was seen in the large inherent variations in tip temperature measurements during individual experiments, the reason for which were probably due to imperfect experimental conditions in ex-vivo ablations. Bovine liver tissue is an inhomogeneous medium with structures such as blood vessels. In ex-vivo experiments, 'empty' blood vessels can act

as tubes guiding steam away from the ablation centre and towards locations beyond the ablation zone. In the test, steam could have escaped in such a way, or through the cut made in the tissue for thermocouple placement. Furthermore, the cut in the tissue could have led to instances at which the applicator was not fully surrounded by tissue, giving rise to varying load conditions, hence changing S11, and lastly power deposition in the tissue.

Figure 7.12 compares prototype temperatures during ablations of 30 W for different coolant flow rates of 1.3 l/h and 3.2 l/h. The effects of the higher flow rate (3.2 l/h) can be seen at the ferrule (TC2) and internal thermocouple (TC6) where temperatures dropped from 100 °C to 87 °C and 31 °C to 26 °C, respectively. Tip temperatures however, were not positively affected by the increase in flow rate as they actually rose from 107 °C to 135 °C. This rise in tip temperature was not attributed to the higher flow rate, but rather to variations in these measurements as discussed in the previous section.

Lastly, the effect of increasing the flow rate during an ablation on tip temperatures is shown in figure 7.13 where an increase at 231 s from initially 3.2 l/h to 4.0 l/h had no significant effect, neither on tip temperatures (TC1) nor on internal temperatures (TC6). However, the oscillations in the trace of TC6, caused by the frequency of the pump, were lessened. The higher flow rate was hence preferred.

Conclusion

Applicator service temperatures were validated by means of prototype temperature measurements. The defined service temperature limit of 300 °C for any part of the applicator lead to the following decisions regarding the optimum power and time setting. Since a tip temperature of 275 °C was already measured in the ablation of 80 W and 4 min (tests 8 in 7.4), and a tip temperature as high as 294 °C in the 89 W, 10 min ablation (test 23), the optimum power-time was set to 80 W and 8 min in order to accommodate a margin of safety regarding input power and time. In addition, the optimum flow rate was defined as 4.0 l/h, as this rate eliminated temperature oscillations at the internal thermocouple. Service tip temperatures, however, could not be significantly lowered by using higher flow rates.

7.5.4 Cooling Failure Detection System

A cooling failure was simulated during an ablation procedure to determine the response time of the cooling failure detection system. The cooling failure detection system consisted of the internal applicator thermocouple developed in section 5.6.4. The time required for shaft temperatures to exceed the critical value of 48 °C during a cooling failure was sought and compared to the response time of the thermocouple.

An ex-vivo ablation of 60 W and flow rate 4.0 l/h was performed with prototype 1. Shaft and internal temperatures (TC3 to TC6) were recorded as described before. Cooling was switched off after 1 min and the temperature responses recorded. In order to prevent device damage, the input power was discontinued once TC6 exceeded 50 °C.

Figure 7.14 displays the recorded temperatures of shaft and internal thermocouples for the simulated cooling failure. Cooling was turned off at 68 s, the input power at 71 s. The figure shows a dramatic rise in temperature at TC6 as soon as cooling was switched

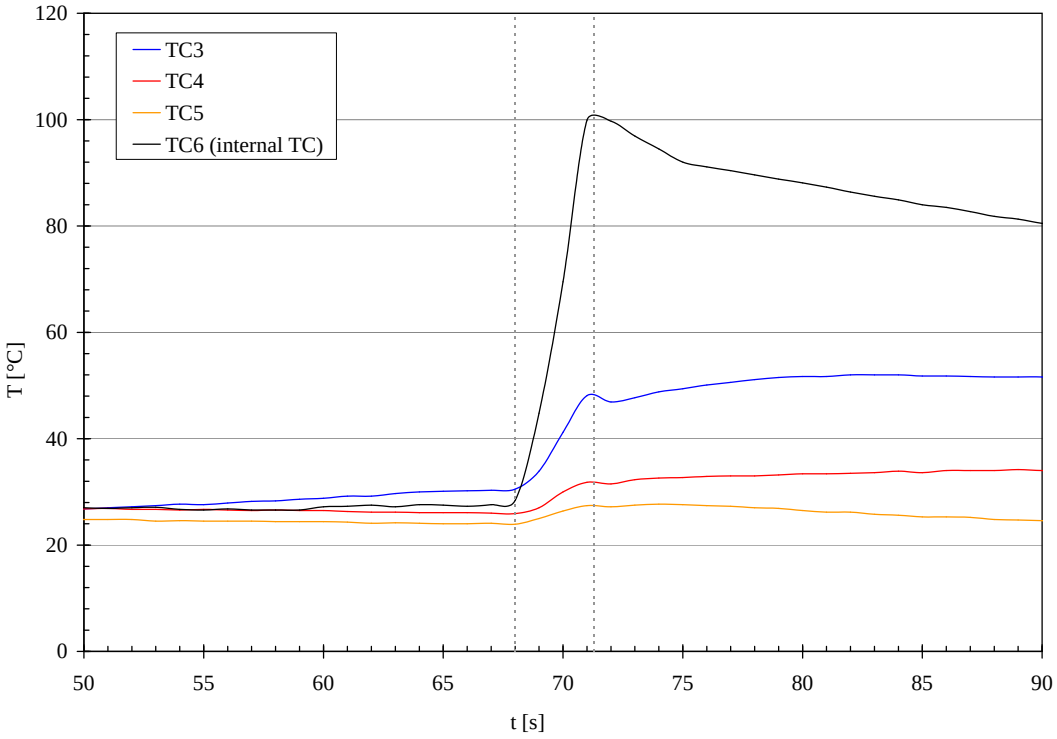

Figure 7.14: Temperatures of shaft (TC3 to TC5) and internal thermocouple (TC6) recorded for simulated cooling failure during ex-vivo ablation of 60 W; 4.0 l/h. Cooling was turned off at 68 s; input power turned off at 71 s.

off, from 28 °C to 100 °C within 3 s, or 24 °C/s. Temperatures at TC3, TC4, and TC5 also rose but at significantly slower rates of 6 °C/s, 2 °C/s, and 1 °C/s, respectively.

Depending on the location of TC3, either within the ablation zone or outside, different response times were required to avoid temperatures at the shaft exceeding 48 °C. Since it is likely for the shaft at TC3 to lie inside the ablation, TC4 would be the thermocouple to consider. Assuming the rise of 2 °C/s for TC4, the time to reach 48 °C would have been 11 s. Within those 11 s, TC6 would have risen by 264 °C, assuming its respective rate of 24 °C/s.

Test results therefore showed that shaft temperatures could be kept below 48 °C if the termination of the input power was triggered by a value between 40 °C and 250 °C read at TC6. The sensitivity of the detection methods was hence high, making its implementation easily achievable.

7.5.5 Applicator Reliability

Applicator reliability was validated by means of repetitive testing. 10 successive ablations were performed at optimum power-time setting of 80 W, 8 min with one particular prototype. After each ablation the prototype integrity was examined which included vi-

sual inspection of the antenna structure and $S11$ measurements to ensure undiminished electrical performance.

Two prototypes (# 3 and # 5) were tested in this manner. Ablations with prototype 5 were undertaken over a period of several days, those with the former device in direct succession.

Both applicators passed the reliability test without failures. Degradation of the coating was noted, however it neither adversely affected applicator performance nor applicator withdrawal.

The successful validation of the prototype reliability was of highest importance as it presented the validation of the complete prototype design covering many design aspects. Device failures had occurred during the development phase and were subsequently corrected thorough a number of design changes. Hence, all of those alterations had also been validated as part of the applicator reliability tests. The fact that both devices survived was hence a significant result.

7.5.6 Ablation Size and Shape

Ablation sizes were recorded for all tests listed in 7.4 and those of the reliability experiments. Figure 7.15 displays the measured minor (radial) and major (longitudinal) ablation diameters versus applied energy. The energy was calculated from the input power P and ablation time t, using the power level measured at the input of the flexible cable.

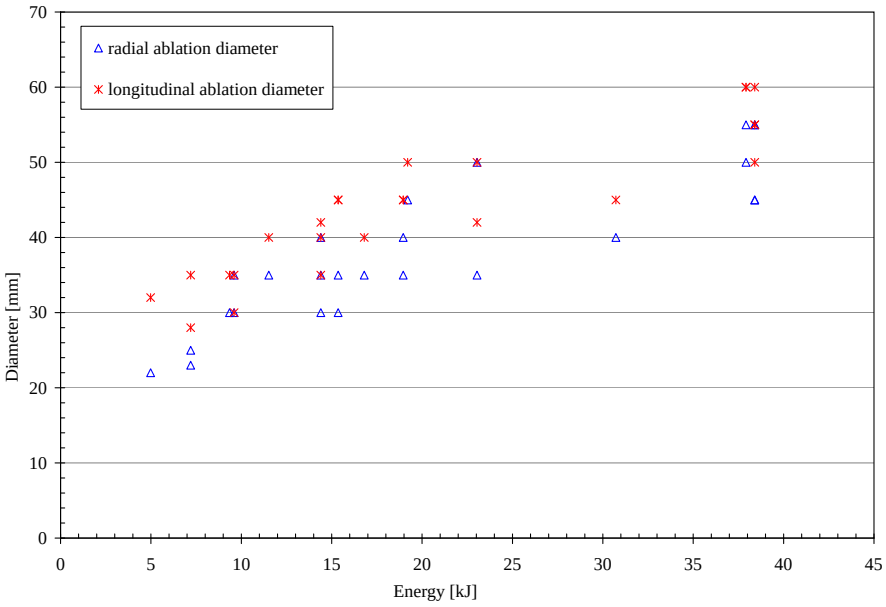

Figure 7.15: Minor and major ablation diameter versus applied energy for various input powers and ablation times; measurement error ± 2 mm.

The relatively large discrepancies in ablation size (see figure 7.15) were due to the fact that the ablation sizes were measured from ablations which were often conducted with

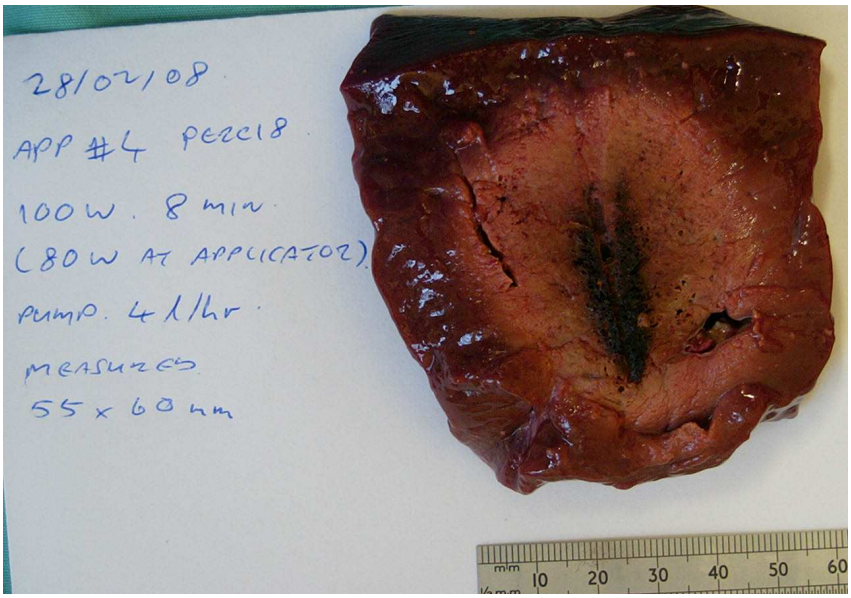

Figure 7.16: Ex-vivo ablation of 80 W, 8 min. Ablation size 55 mm × 60 mm; measurement error ± 2 mm.

a different primary purpose than ablation size measurement, as listed in table 7.4. For instance, the initial temperature of tissue should always be close to body temperature if accurate information regarding the ablation size is sought. However, in these tests, the initial temperature of bovine liver was between 16 °C to 37 °C due to practical reasons. Ablations performed in cold liver will therefore result in comparatively smaller lesion diameters. Furthermore, tissue inhomogeneities such as blood vessels interfered frequently with ablations, also resulting in smaller ablation sizes. In addition, the placement of thermocouples along the applicator for temperature measurements affects ablation size negatively, as cuts had to be made in tissue which mostly resulted in non-symmetrical ablation shapes. However, the data still shows the general trend of growing ablation sizes for larger energy input. Small quantities of energy of about 10 kJ therefore result in an ablation size of approximately 30 mm to 35 mm diameter; the highest energy deposition of 38 kJ in ablation sizes of approximately 50 mm to 55 mm.

At optimum power-time (80 W, 8 min), the ablation size was determined to 55 mm × 60 mm. This ablation measurement was performed in a separate experiment with the sole aim of lesion size determination. Hence, no thermocouples, cuts, or other detrimental factors were allowed in that test. Figure 7.16 displays such an ablation, measuring 55 mm × 60 mm, which was performed in ex-vivo bovine liver of (35 ± 5) °C. The requirement of generating ablation sizes of ≥ 50 mm as stated in the design brief (see page 40) had hence been met by the current prototype design.

Furthermore, the sphericity of the ablation was calculated to 0.999 which satisfied the requirement concerning the ablation sphericity defined in the design brief (see page 40). Generally, the sphericity Ψ of an object is defined as the ratio of the surface area of a sphere of volume equal to the given object to the surface area of the object [89]. It hence is a measure for how spherical an object is. Sphericity can be determined using

equation 7.3, where V_o is the volume of the object and A_o the surface area of the object. Sphere and cube, for instance, have sphericities of 1 and 0.806 respectively.

$$\Psi = \frac{\pi^{1/3}(6V_o)^{2/3}}{A_o} \tag{7.3}$$

In order to determine the sphericity of an ablation, the ablation shape was approximated to an ellipsoid with semi-major axis r and semi-minor axis q equal to 30 mm and 27.5 mm, respectively. The sphericity of the ablation was therefore calculated according to equation 7.4 which defines the sphericity of an ellipsoid. The resulting sphericity of 0.999 satisfied the required lower limit of 0.98.

$$\Psi = \frac{\pi^{1/3}(6V_o)^{2/3}}{A_o} = \frac{2\sqrt[3]{rq^2}}{r + \frac{q^2}{\sqrt{r^2-q^2}}\ln(\frac{r+\sqrt{r^2-q^2}}{q})} = 0.999 \tag{7.4}$$

Both ablation size and shape of the prototype devices were hence validated in the ex-vivo setup.

7.5.7 Durability of Non-Stick Coating

Coating degradation was observed over a number of 10 successive ablations undertaken at optimum power-time (80 W, 8 min, 4 l/h). Tests were conducted with a previously unused prototype (# 3) with a non-stick coating of pristine condition. After each ablation a picture was taken of the applicator tip to record the condition of the coating over time.

Figure 7.17 shows the ceramic applicator tip and non-stick coating (NuSil MED10-6400) after 0 to 10 ablation procedures. Pictures were taken through a microscope for greater magnification.

The sequence of pictures show that the coating started to degrade in the form of discolouration with the first ablation and continued throughout all subsequent tests (see figure 7.17). Furthermore, coating material was being removed from the tip, beginning at approximately the fourth ablation. However, despite of this loss of material, a very thin layer of non-stick coating remained in the areas where the wear occurred. After ablation 9 and 10, tissue began to adhere to the tip as can be seen in pictures 9 and 10; however those tissue parts could easily be wiped off with a damp cloth. Although the coating looked fairly damaged after the last test, no adhesion to the carbonised ablation zone occurred during applicator withdrawal. In addition, the quality and durability of the coating could most likely be further improved by using professional mixing and applying techniques which were not available during construction of this prototype.

As the primary aim of the coating was to provide a non-stick applicator surface, which none of the other types of non-stick coatings that had been tested previously could provide (see chapter 6), the NuSil MED10-6400 silicone dispersion coating was regarded as the most suitable material for the application purpose. The test showed that it provided non-stick properties throughout the most severe test conditions of maximum device input power, maximum ablation time, and maximum number of repetition for a

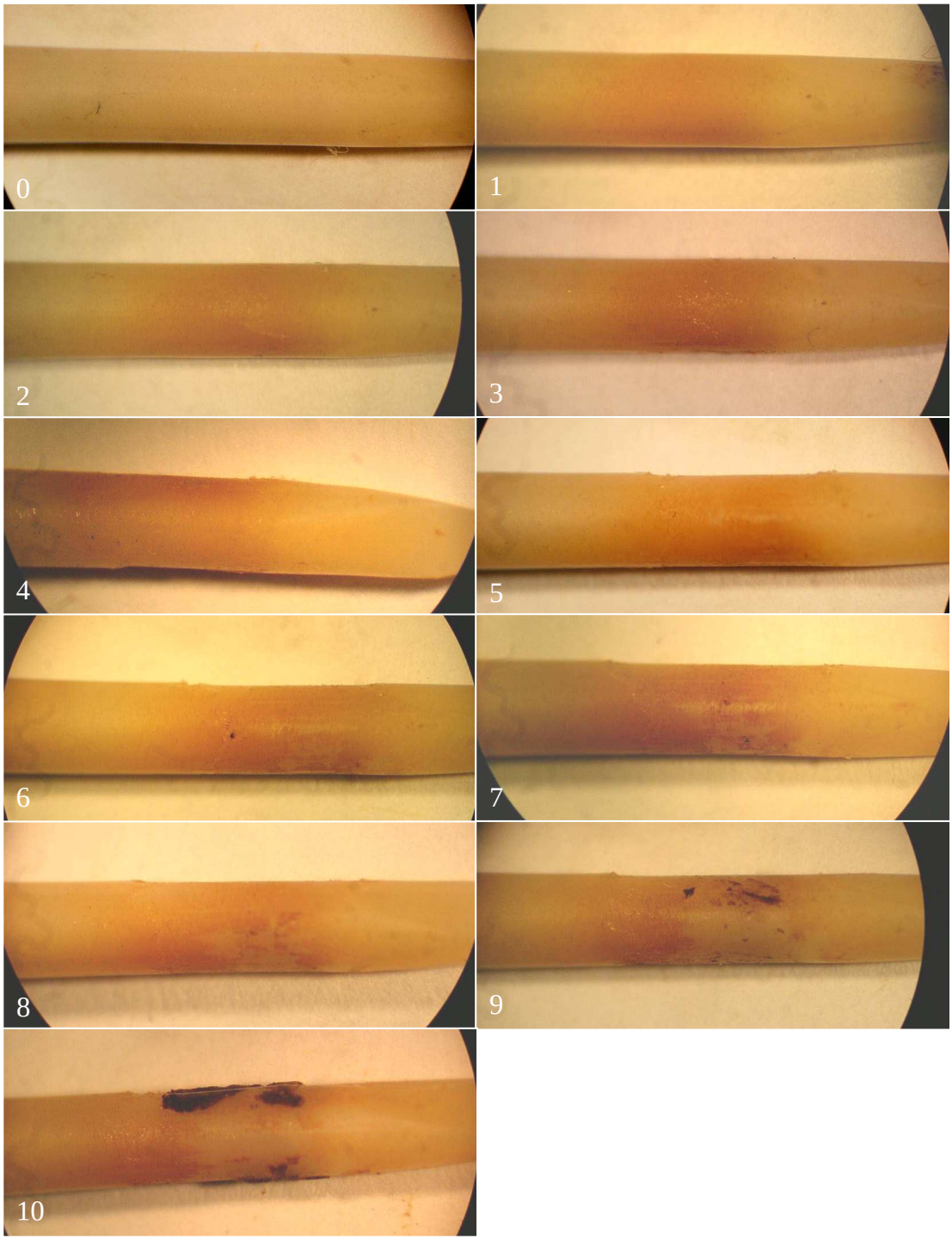

Figure 7.17: Condition of non-stick applicator coating after 0 to 10 ablations of 80 W, 8 min; numbers indicate after how many ablations (0 to 10) the respective picture was taken.

single device.

7.5.8 Tip Bond Strength

The tensile strengths of all prototype tip joints were tested prior to first operation. The intactness of the tip joint was important with regards to preventing tip detachments or water penetration into the tip during later ablation experiments. The tip joint strengths were therefore tested by applying a tensile force axially on the tip. Tensile forces of approximately 10 N were exerted manually on the ceramic tip.

None of the tip joints failed. It was therefore concluded that the HT epoxy (Aremco-Bond 526N-C) utilised in all prototypes provided a reliable and strong bond between ceramic tip and copper ferrule.

7.5.9 System Water Leakage

Prior to and during the experimental validation no significant water leakages occurred in the prototype systems. Some minor leakages around handle luer locks and front handle pieces took place, however due to the small leakage volumes (drops), those occurrences were considered to not compromise the performance of the cooling system during testing. Furthermore, they were easily eliminated by improving bonding techniques or changing adhesives between successive prototype assemblies.

7.6 Conclusions

The design of the prototype system was optimised with regards to manufacture, device reliability and ease of application. The mean return loss of the system was measured to be (-11 ± 0.5) dB. The experimental efficiency was determined to 0.72 ± 0.04, slightly higher than the theoretical efficiency of 0.67. The discrepancy was allocated to the unstable power output of the microwave amplifier. Furthermore, measurements of shaft service temperatures showed that the cooling system kept all prototype surfaces below 48 °C. Also, tip and ferrule service temperatures were recorded and led to the definition of an optimum power-time setting and optimum flow rate of 80 W, 8 min, 4 l/h in order to limit peak service temperatures to a maximum of 300 °C. In addition, it was shown that the cooling failure detection system detects any kind of cooling failure in a matter of seconds by monitoring temperatures of the internal shaft thermocouple. Applicator reliability was validated for a maximum load of 10 successive ablations at optimum power-time. Ablation size was measured to 55 mm × 60 mm at optimum power-time leading to an ablation shape with sphericity 0.999. Besides, the non-stick coating was validated at maximum load (10 ablations; 80 W; 8 min). The tensile strength of the tip bond was validated as fit for purpose. Lastly, water leakages in the system had been eliminated by alterations in design and assembly procedure. The prototype system had hence been validated and was ready for use. An electromagnetic-thermal FEM model of the prototype system was developed and is presented in the following chapter 8.

Chapter 8

Electromagnetic-Thermal Computer Simulations of 1.8 mm Prototype

8.1 Introduction

An electromagnetic-thermal analysis of the applicator was performed using the finite element method (FEM) with the objective of predicting applicator temperatures encountered during microwave ablation in various media. In order to predict such applicator service temperatures, the device's $S11$, SAR, and electric field shape had to be simulated beforehand since the thermal response in tissue is initiated by the absorption of emitted EM waves. The two fields – electromagnetic and thermal – become interdependent or coupled due to the assignment of temperature-dependent load material data. In this case, a coupled electromagnetic-thermal analysis is required whereby the results of one analysis (EM) is assigned as initial condition in the second analysis (thermal). Also, the active cooling of the applicator cooling system affected the device's service temperatures. Hence, the cooling effect was included in the simulation by means of utilising a heat transfer coefficient which was assigned in the thermal analysis.

In order to be able to predict the temperatures encountered by the applicator during an ablation the use of advanced non-linear material properties for ex-vivo bovine liver was required since service temperatures were expected to be largely determined by surrounding tissue temperatures as well as the active device cooling. Tissue temperatures during microwave or radiofrequency ablation are best modelled using non-linear material properties [73, 67, 55, 68, 90]. First, published non-linear data for ex-vivo bovine liver was used in the model, however the resulting modelled temperature data did not agree with measured values. Efforts were hence focussed on defining a suitable set of non-linear material properties of ex-vivo bovine liver in order to be able to better predict applicator and tissue temperatures during microwave ablation. This study resulted in the proposal of novel temperature-dependant material properties of ex-vivo bovine liver between 20 °C and 300 °C for microwave ablation. The coupled-field electromagnetic-thermal FEM models presented in this chapter were developed in COMSOL Multiphysics 3.5.

8.2 Coupled Electromagnetic-Thermal Model

8.2.1 Application Modes and Physics

Two application modes were utilised to simulate the electromagnetic-thermal problem:

- The Transverse Magnetic (TM) Waves mode to simulate the applicator's electric field and SAR distributions.
- The Bioheat Equation (BHE) mode to simulate the transient temperatures of applicator and load due to absorption of EM energy, heat flux due to the active cooling, and energy transfer through heat conduction.

Both application modes are based on the same model geometry with independent variables being coordinates r, z, φ, and time t. Application mode properties, boundary settings, and subdomain settings for TM and BHE mode are discussed in sections 8.2.5 and 8.2.6, respectively.

8.2.2 Solution Process of Coupled-Field FEM

Figure 8.1 illustrates the solution process of a coupled-field electromagnetic-thermal analysis with temperature-dependent material properties. Firstly, the construction of the model itself is undertaken which includes drawing of the model geometry, definition and assignment of material properties and assignment of boundary conditions, excitation and spatial heat source for each mode. The first step of the solution process is then taken by solving for the TM mode under steady-state conditions to obtain the SAR distribution. Here, the SAR distribution is termed initial spatial heat source distribution $Qext(t_0)$ (W/kg). Next, $Qext(t_0)$ is read into the BHE mode, due to its assignment during the model construction, and also stored as part of the model solution. A transient analysis of the BHE mode follows for a duration set by a defined parameter called time step, computing the temperature distribution $T(r, z, t_i)$ of the model geometry. $T(r, z, t_i)$ is also added to the results file and used to update the temperature-dependent material properties if the current analysis time t_i is smaller than the total analysis time t_{max}. Changes in material properties however invalidates the steady-state solution of the TM mode. Therefore, the steady-state solution for the TM mode has to be re-solved under the new conditions resulting in a modified heat source distribution $Qext(t_1)$. $Qext_1$ is then read into the BHE mode and the solution process continued in cyclic iterations until t_i equals the total analysis time t_{max}. Once t_{max} has been reached, the solution process finishes, yielding a results file containing $Qext(t_i)$ and $T(r, z, t_i)$ for each time step.

To ensure convergence of the EM solver solution, the model mesh was optimised in a convergence analysis (see section 8.2.4). During the solution process of the time-dependant analysis, convergence was controlled by the software. In order to obtain convergence between consecutive solutions, the software may divide the time steps defined by the user into smaller sections. The purpose of convergence control is to compute accurate results while minimising the computational time needed.

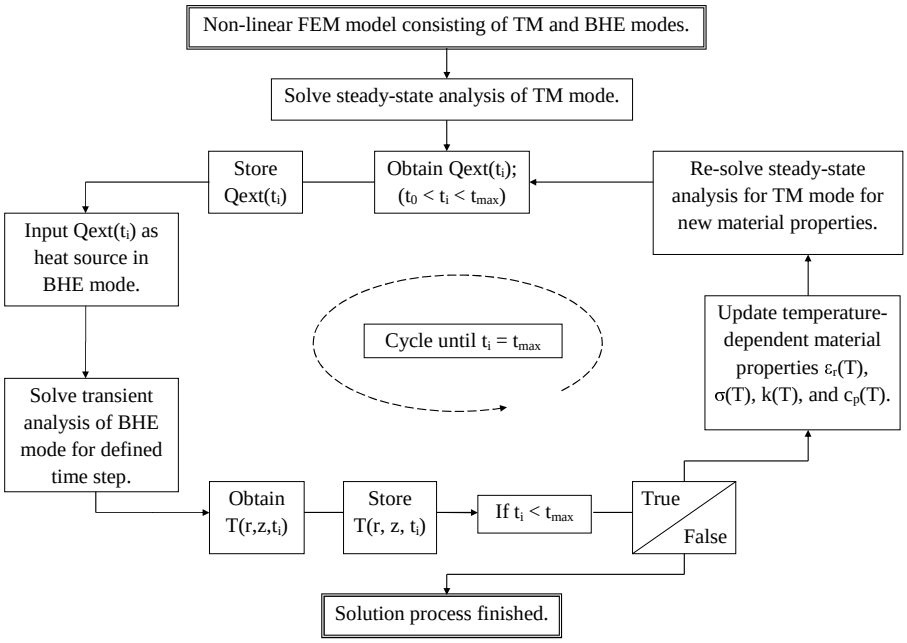

Figure 8.1: Solution diagram of coupled-field electromagnetic-thermal FEA.

8.2.3 Model Geometry

Due to the availability of axially symmetric elements and the axially symmetric nature of the applicator, the model geometry could be reduced to two dimensions (2D) using cylindrical coordinates r, z as indicated in figure 8.2 where the computational domain appears as a rectangle (dashed lines) in the rz-plane. This computational domain presents the model geometry. The model geometry is shown in figure 8.3. It was created by defining 2D areas called subdomains which are interconnected by shared boundaries. The symmetry axis was defined by the r = 0 axis.

As before, the applicator consisted of semi-rigid coaxial cable with LD PTFE dielectric, stainless steel shaft, copper ferrule, air void inside the ferrule, ceramic cylinder, copper washer, and ceramic tip and was embedded in a rectangular load. The model geometry and dimensions matched the latest 1.8 mm prototype design described in section 7.3 except for a small number of changes that had been made to the design during the time of model creation:

- A small quartz tube (ID (0.60 ± 0.05) mm; OD (0.84 ± 0.02) mm; l (5.00 ± 0.5) mm) was added. It was threaded onto the extended centre conductor contacting the end of the cable dielectric, centralising the centre conductor and preventing shorting.
- The tip bore hole was increased to a length between 10.20 mm and 10.45 mm. In the model 10.3 mm was used which created a gap of 0.35 mm between washer and tip. This gap was divided into an air gap at the washer of height 0.05 mm and a volume of glue filling the remaining gap (height 0.3 mm).
- Exterior ferrule lengths of formerly 1.5 mm, 3 mm, 4 mm changed to 1.5 mm, 3.25 mm, and 3.75 mm (proximal to distal sections). Hence, the overall length remained at 8.5 mm but the middle section increased by 0.25 mm and the distal

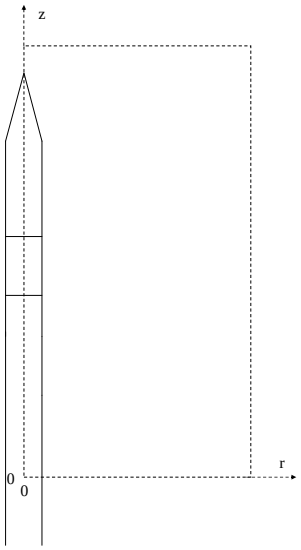

Figure 8.2: Computational domain of FEA.

section decreased by that same amount (0.25 mm).

- Ceramic paste was used for tip to ferrule bond. Its main constituent is magnesium oxide (MgO).
- The length of the flexible feed (umbilical) cable was increased to 2m.

8.2.4 Free Mesh Parameter Setting

A free mesh is readily generated and refined in COMSOL Multiphysics 3.5. However, a mesh created in such a way does not take into account the particular needs of a model, and usually leads to inaccurate solution data. An improved mesh can be produced for a particular model by comparing solution data (e.g. $S11$) resulting from different mesh densities [66] and limiting the allowed change in solution data between subsequent solutions. This concept was taken into consideration and led to a convergence analysis with the aim to define the optimum mesh density for different parts of the model.

The solution data $S11$ (dB) and power input level P_{in} (W) were monitored for different mesh cases. The mesh density in each region was adjusted individually and numerical convergence resulted when a uniform change of less than 0.1 % in the reflected power $S11$ and power input level P_{in} was reached. A number of analysis were solved sequentially and mesh parameters along critical parts steadily increased until the convergence criteria were met. The optimum mesh density found in this manner is shown in figure 8.3. The maximum element size was limited to 3 mm globally, to 0.15 mm in the cable dielectric, and to 0.1 mm on the inner boundary of the cable dielectric. A total of 11 414 elements resulted for this mesh and geometry.

Figure 8.3 also displays mesh quality on a coloured scale from 0 (blue) to 1 (red), with 1 representing maximum element quality. Element qualities should not fall below 0.5 in order to maintain model accuracy [91]. With the exception of very few and non-critical

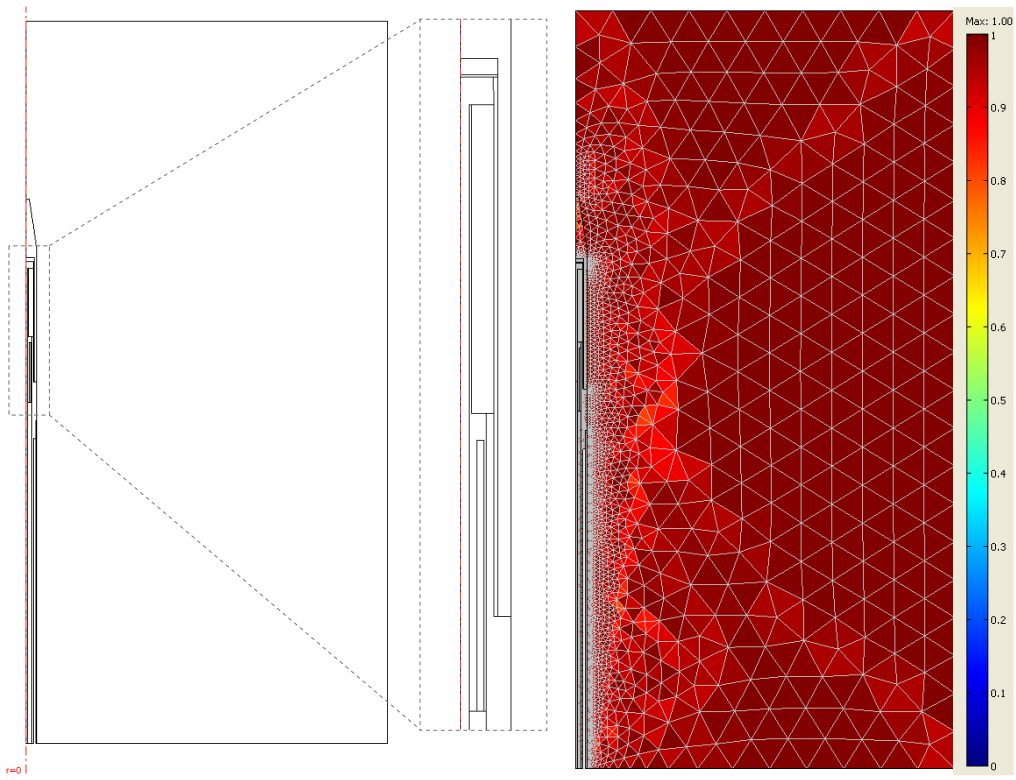

Figure 8.3: 2D axisymmetric model geometry of coupled electromagnetic-thermal FEA (left) and mesh (right).

elements along the tip structure, element quality exceeded the threshold everywhere in the model.

8.2.5 Transverse Magnetic (TM) Waves Application Mode

The mode of propagation of an electromagnetic wave in coaxial cables is the TEM mode which is characterised by transverse electromagnetic fields. The appropriate equations for electric and magnetic field assuming time-harmonic fields with complex amplitudes are given by [92]:

$$\vec{E} = \vec{e}_r \frac{C}{r} e^{i(\omega t - kz)} \tag{8.1}$$

$$\vec{H} = \vec{e}_\phi \frac{C}{rZ} e^{i(\omega t - kz)} \tag{8.2}$$

where C is the capacitance per unit length (F/m) of the coaxial line, r, ϕ, and z the cylindrical coordinates, ω the angular frequency, k the propagation constant given by $2\pi/\lambda$, Z the characteristic impedance of the coaxial cable, and z the direction of propagation. Z is defined as [1, p.59]:

$$Z = \sqrt{\frac{L}{C}} \tag{8.3}$$

where L is the self-inductance per unit length of the coaxial line (H/m). L and C are given by [1, p.62]:

$$L = \frac{\mu}{2\pi} \ln(r_0/r_i) \tag{8.4}$$

and:

$$C = \frac{2\pi\varepsilon'_r}{\ln(r_o/r_i)} \tag{8.5}$$

where r_i and r_o are the inner and outer radii of the dielectric. The characteristic impedance hence is:

$$Z = \ln(r_o/r_i)\frac{1}{2\pi}\sqrt{\frac{\mu}{\varepsilon'_r}} \tag{8.6}$$

The power flow $\vec{P}$ in the cable may be computed from the Poynting vector as [1, p.65]:

$$\vec{P} = \frac{1}{2}\int_{r_i}^{r_o} (\vec{E} \times \vec{H}^*) 2\pi r dr = \vec{e}_z \pi \frac{C^2}{Z} \ln\frac{r_o}{r_i} \tag{8.7}$$

In the load material, the electric field also has an axial component, the magnetic field however remains purely in azimuthal direction. The applicator could hence be modelled using an axisymmetric transverse magnetic formulation (TM wave), representing the wave propagation in both cable and load. The electric and magnetic fields in tissue take the form of

$$\vec{E}(r, z, \varphi, t) = (\vec{E}_r(r, z) + \vec{E}_z(r, z))e^{i\omega t} \tag{8.8}$$

$$\vec{H}(r, z, \varphi, t) = \vec{H}_\varphi(r, z)e^{i\omega t} \tag{8.9}$$

where $\vec{E}_r$ and $\vec{E}_z$ are the r and z components of the electric field, and $\vec{H}_\varphi$ the azimuthal component of the magnetic field.

The boundary conditions applied consisted of the following assignments. Firstly, axial symmetry was defined on all boundaries lying on the axis r = 0 (see figure 8.2). The outer boundaries of the coaxial cable were set to perfect electric conductor (PEC). A PEC boundary condition forces the electric field to be normal to the respective surface (see equation 8.10). Interior boundaries were not specified. In addition, a port of coaxial type was defined across the cable dielectric boundary with electric and magnetic fields defined according to equations 8.1 and 8.2, and input power P_{in} defined by equation 8.7.

$$\vec{n} \times \vec{E} = 0 \tag{8.10}$$

The applicator radiates into tissue where a damped wave propagates. The load volume was hence truncated at a distance sufficiently large to absorb nearly all of the wave. Lastly, a scattering boundary condition was assigned on all remaining external load boundaries, absorbing any part of the wave that reaches the boundary by setting magnetic and electric fields equal to zero.

The default element type selected by the software was retained , the analysis type set to harmonic wave propagation, and the frequency of operation defined as 2.45 GHz. Except for the definition of material properties including electrical conductivity σ and real and imaginary part of the complex permittivity ε'_r and ε''_r, no further subdomain settings were necessary for the TM mode. Material properties for both TM and BHE

modes will be defined in section 8.2.8.

8.2.6 Bioheat Equation (BHE) Application Mode

Heat transfer in the tissue was simulated using Pennes' bioheat equation, as defined in chapter 2, page 32. In the context of this work, all variables in the BHE were space and time dependent, for instance, temperature $T(r, z, t)$, defined at the point in space with coordinates (r,z) and time t (s). Heat transfer due to blood perfusion was neglected in the model since ex-vivo tissue was utilised in the experimental setup. Similarly, the metabolic heat generation Q_m was set equal to zero in ex-vivo tissue.

The SAR generated by the electromagnetic waves in the TM waves mode was input in the form of a spatial heat source $Qext$ (W/kg). $Qext$ was assigned in the subdomain settings of the load material, tip, cylinder, and glue gaps. $Qext$ is given by the equation 2.32 defined in chapter 2 for SAR.

The initial temperature of all subdomains was set to 20 °C. Thermal insulation was assigned at all external model boundaries (refer to figure 8.3) in the form of:

$$\vec{n} \cdot \nabla T = 0 \tag{8.11}$$

Material properties required for the BHE mode consisted of thermal conductivity k (W/(m·K)), density ρ (kg/m^3), and specific heat c_p (J/(kg·K)). Furthermore, the default element type was retained and the analysis type set to transient.

8.2.7 Heat Transfer Coefficient

So far, the heat transfer in tissue and applicator consisted of heat conduction and electromagnetic heating. The cooling effect of the applicator cooling system whereby the fluid cools the internal surfaces by convective cooling had not been taken into account as yet.

Convection cooling can be divided into four categories depending on the conditions (natural or forced) and the geometry (internal or external flow). The flow conditions for those four cases can either be laminar or turbulent flow, resulting in eight types of convection cases [56]. In natural convection, the fluid is driven by buoyancy forces induced by temperature differences and thermal expansion. Forced convection conditions apply when the fluid flow is created by an external force. The flow in the applicator cooling system is forced, as it is created by applying a pressure differential across the cooling circuit.

Modelling convection processes is generally possible in two ways, either by using a heat transfer coefficient on the convection-cooled surfaces, or by extending the model to describe the full fluid flow and heat transfer in the cooling fluid [93]. As mentioned earlier, no separate fluid analysis was undertaken for solving the fluid flow and temperature field since the memory required for solving this type of analysis was not available on the workstation used. The forced convection cooling was hence modelled using a heat transfer coefficient.

The heat transfer coefficient was included in the model by assigning a heat flux boundary condition on all cooling system surfaces. The inward heat flux through a boundary is given by:

$$\vec{n} \cdot \vec{q} = -q_0 \tag{8.12}$$

where $\vec{n}$ is the normal unit vector of the boundary, $\vec{q}$ the total heat flux vector ($\mathrm{W/m^2}$) given by $-k\nabla T$, and q_0 the inward heat flux ($\mathrm{W/m^2}$) normal to the boundary.

In order to include convective cooling in the model, a term accounting for the heat flux due to the forced convection cooling q_{cool} given by $q_{cool} = h(T_0 - T)$ can be added to the inward heat flux q_0, where h is the heat transfer coefficient ($\mathrm{W/(m^2{\cdot}K)}$), T_0 the fluid temperature, and T the surface temperature. The heat flux can therefore be written as:

$$-\vec{n} \cdot \vec{q} = q_0 + h(T_0 - T) \tag{8.13}$$

The main difficulty in using heat transfer coefficients is the definition of an appropriate value. Many parameters influence the value of h, including the fluid's material properties, the surface temperature, the fluid flow rate and flow regime, and the geometrical configuration of the cooling channel. A vast number of empirical equations have been published for different flow conditions by various researchers, however they are applicable only to the specific conditions and parameters defined in each case [94], [95], [96]. Since, both the geometry of the applicator channel and the heating conditions were unique, none of the cases found in literature were applicable. In this model, the heat flux into the coolant originated from two main sources, internally from the electromagnetically heated coaxial cable, and externally from the electromagnetically heated tissue load. For these reasons, the numerical determination of heat transfer coefficients for both internal and external cooling surfaces would have involved a significant amount of time and was hence, with regards to the aim of this work for developing a working device, neglected. However, typical values of h for forced convection cooling using liquids range from 50 to 20,000 $\mathrm{W/(m^2{\cdot}K)}$ [56], or even up to 100,000 if convection with phase change (boiling or condensation) is applicable. Section 8.4 will discuss how the value of the heat transfer coefficient used in the model was determined.

8.2.8 Material Properties

Applicator Material Properties

Material properties of the applicator are specified in table 8.1. All properties were approximated as linear. Unless otherwise stated, material properties are taken from [97]. The properties of 3Y-TZP zirconia and ceramic paste were defined where possible according to the data provided by the manufacturers [98], [87]. The electrical properties of the applicator materials were defined via real and imaginary part of the relative complex permittivity ε_r' and ε_r'', or conductivity σ in the case of metals. Values marked with * were estimated.

Table 8.1: Material properties of applicator employed in coupled-field FEA; values marked with * are estimated.

Material	ε_r'	ε_r''	σ (S/m)	c_p (J/(kgK))	k (W/(mK))	ρ (kg/m^3)
Copper	1	0	6.0e7	397	395	8960
LD PTFE	1.7	0.0001	0	840*	0.19*	960*
St. steel	1	0	1.4e6	500	16	7800
Air	1	0	0	1000	0.03	1.1
3Y-TZP zirconia	32	0.032	0	400	2	6050
Ceramic paste	2*	0.01*	0	100*	0.5*	1500
Quartz	3.78	0	0	830	7	2200

Material Properties of Ceramic Tip and Cylinder

The dielectric properties of zirconium oxide ($Zr0_2$; zirconia) were measured by [73] to $\epsilon_r' = 18$ and $tan\delta = 0.005$. These values have been used previously for yttria stabilised tetragonal zirconia (3Y-TZP) in computer models. However, during a recent study comparing modelled and measured $S11$ of a 2.45 GHz surface applicator developed by the MDTG ([99]), the dielectric constant of 3Y-TZP was found to be 32 ± 1.

Consequently, the literature was reviewed with the aim of establishing correct dielectric properties for 3Y-TZP. Not surprisingly, other researches had also stated that there seemed to be considerable variation in the reported values for both the permittivity and the loss tangent of yttria stabilised zirconia (YSZ) [100]. Researches have found that the concentration of yttria doping played a major role in the definition of the molecular structure, being either single crystal, cubic, or tetragonal, which in turn altered the respective values for permittivity and loss tangent [101].

The dielectric properties of yttria stabilised zirconia (YSZ) were measured at 5.5 GHz and 300 K to $\epsilon_r' = 33.4$ and $tan\delta = 9 \cdot 10^{-4}$ [100]. Furthermore, the permittivity and loss tangent of YSZ was determined at 10 GHz and 300 K for yttria doping concentrations of 0 %, 2 %, and 9 % by other researchers [101]. The results obtained are listed in table 8.2 which explain the wide variation in the published permittivity values of YSZ, as the permittivity of YZP was found to be highly dependent on the concentration of yttria doping. It was concluded that the yttria doping determines the structure of the YSZ as it affects the stability of the different phases.

Table 8.2: Dielectric properties of YSZ at approximately 10 GHz and 300 K [101].

Yttria doping [%]	Structure	ε_r'	$tan\delta$
0	Monoclinic and polycrystalline	17.9	$7 \cdot 10^{-4}$
2	Cubic and tetragonal	34.5	$9 \cdot 10^{-4}$
9	Single crystal (cubic phase)	27.2	$47 \cdot 10^{-4}$

Temperature-dependent dielectric properties of zirconia were also determined [102]. At (0 , 100, 200, 300) °C the permittivity and loss tangent were measured to 19, 19, 19.3, 19.5, and 0, 0, 0, 0.01, respectively. However, further details on the material were not given.

It has to be noted that pure zirconium oxide ZrO_2, or zirconia, has very different

properties to those of yttria stabilised zirconia. Pure zirconia exists in three crystal phases depending on the temperature: cubic at T $\geq$ 2370 °C, tetragonal at 1170 °C $\leq$ T $\leq$ 2370 °C, and monoclinic at T $\leq$ 1170 °C. The transformation from tetragonal to monoclinic is rapid and is accompanied by a 3 % to 5 % increase in volume causing significant cracking in the material. A solution to slow down or eliminate these crystal structure changes was found in the use of specific oxides dissolving in the zirconia crystal structure. Oxides commonly used for this purpose are magnesium oxide (MgO), calcium oxide (CaO), and yttrium oxide (Y_2O_3; or yttria). If sufficient amounts are added to the zirconium oxide, the cubic structure connected to high temperatures can be maintain for room temperature. Cubic stabilised zirconia hence became a useful technical material [103].

A complex fabrication process of controlled, stress induced volume expansion of the tetragonal to monoclinic inversion can produce a very high strength, hard, and tough variety of zirconia – tetragonal zirconia polycrystal ceramics (TZP). TZP is a pure tetragonal phase stabilised with rare earth oxides, mostly yttria and less commonly ceria. The yttria stabilised form is often referred to as YTZP, the ceria stabilised one as CeTZP. However, the properties of TZP degrade rapidly when exposed to environments of high temperature water vapour of 200 °C to 300 °C. The general maximum operating temperature is usually set to 800 °C [103].

The permittivity value of 17.9 (see table 8.2) matched the initial measurement of 18 taken by Hardie [73] surprisingly well. It was hence assumed that Hardie [73] measured the dielectric properties of pure zirconia and not yttria stabilised tetragonal zirconia.

The properties of 3Y-TZP for the FEA were therefore taken from [100] who measured a permittivity ϵ_r' of 33.4 and a loss tangent $tan\delta$ of $9 \cdot 10^{-4}$ for yttria stabilised zirconia.

Frequency-Dependent Saline Properties

In order to validate the electromagnetic model results, frequency-dependent saline properties were assigned as load and the FEA solved from 1 GHz to 10 GHz. The saline properties for 20 °C and 0.1 N saline were given in table 4.6 in chapter 4 [74].

Ex-vivo Bovine Liver Properties from Literature

In contrast to the applicator materials, the properties of ex-vivo bovine liver were assumed non-linear over temperature. Researchers like [73], [104], [105], and [106] have studied and partly measured tissue properties at elevated temperatures. Tissue permittivity was measured for temperatures up to 140 °C [73]. The temperature of tissue samples was hereby elevated using a conventional convection oven. Furthermore, the density of ablated tissue was measured by Yang [106] at various distances from the ablation centre. Tissue density was then translated into tissue water content, and tissue properties k and c_p defined as functions of tissue water content using the mixing theory. The mixing theory states that the heat capacity in composite materials can be estimated as the sum of heat capacities of each fractional component [55]. In like manner, k was derived. The tissue water content itself was related to tissue temperature

on the basis of the following assumptions:

- Tissue water exists in two forms – free water and bound water. Bound water refers to water molecules combined with other chemical molecules. Unlike free water, bound water requires extra kinetic energy to break chemical bonds. Bound water hence evaporates at higher temperatures than free water. Approximately 50 % of the tissue water is free water, the remaining 50 % bound water [105], [104].
- Initial water volume fraction of 0.778 [55].
- Evaporation of tissue water begins between 70 °C and 80 °C [107].
- 50 % of the tissue water is boiled off at 104 °C [104].
- Bound water starts evaporating at 104 °C [106].
- At 180 °C the water volume fraction reaches approximately 0.06 [106].

A variable $c_{p.lat}$ was defined for taking into account the vaporisation of water. The vaporisation of free and bound water was approximated to take place between 100 °C and 180 °C. In this manner, the latent heat of vaporisation of 2260 kJ/kg was spread over 80 °C for a total of 0.6 kg water per unit mass of tissue (0.4 kg free and 0.2 kg bound water) giving a value of 2260·0.6/80 kJ/(kg·K) = 16.95 kJ/(kg·K).

Figures 8.4 display the resulting temperature-dependent properties of ex-vivo bovine liver whereby data for water volume fraction w_v, density ρ (kg/m^3), specific heat capacity c_p (J/(kg·K)), thermal conductivity k (W/(m·K)) was taken from [106], and data for real and imaginary part of the relative complex permittivity, $\varepsilon_r^{'}$ and $\varepsilon_r^{''}$ from [73]. Dotted lines represent extrapolation of the data to higher temperatures.

Proposed Properties of Ex-vivo Bovine Liver

Solving the computer model for the temperature-dependent tissue properties taken from literature and discussed in the previous section showed great discrepancies between measured and modelled applicator temperatures of up to 400 °C (see page 154) rendering the material properties found in literature unsuitable for the simulation of high-temperature microwave ablations. Reasons for possible errors in published tissue permittivity could be due to one or more of the following issues:

- Permittivity was measured using tissue samples. During the heating process, the water content could decrease significantly due to the length of time required (10-20 min) and the small, unsealed sample pieces.
- Permittivity was measured at the sample surface where the tissue water content was least. However, during ablations, the volume of tissue heated is surrounded by further tissue which could oppose the decrease in water content.
- The water content of tissue is not only a function of temperature but also of time. The time required to raise the tissue temperature in the centre of an ablation to 100 °C is usually below 20 s, compared to the much longer heating times for convection heating. The drop in tissue permittivity measured in this manner could hence be overestimated resulting in values too low for elevated temperatures.

Similar errors could have occurred when measuring tissue densities at the end of an ablation as the remaining water content is a result of the time history of the tissue, that

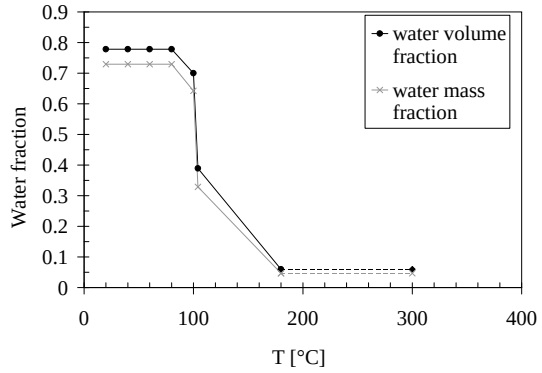

(a) Tissue water volume fraction $w_v(T)$.

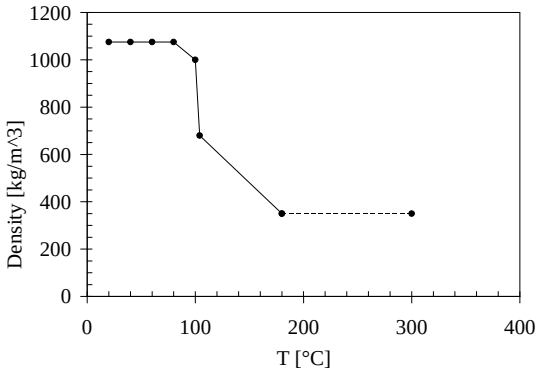

(b) Density $\rho(T)$.

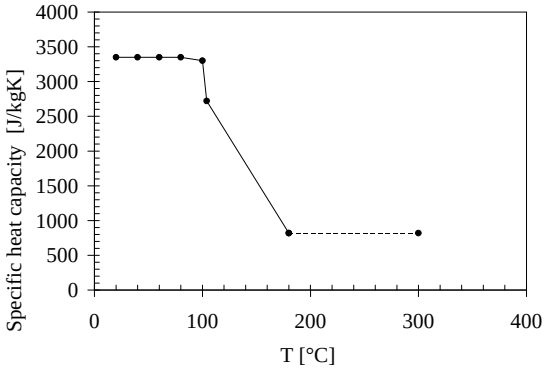

(c) Specific heat capacity $c_p(T)$

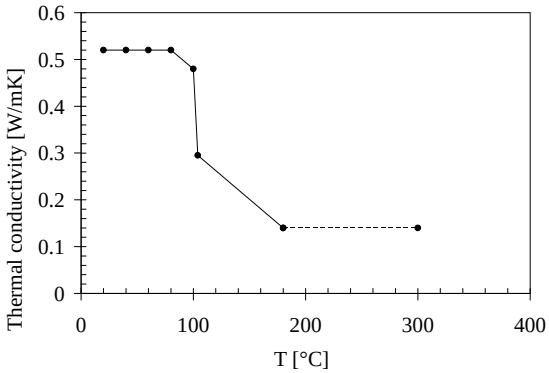

(d) Thermal conductivity $k(T)$

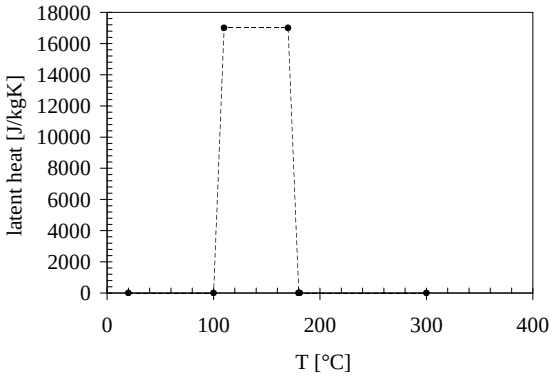

(e) Latent heat of vaporisation $c_{p.lat}(T)$.

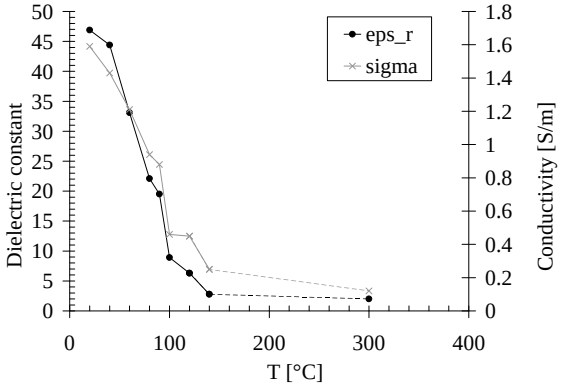

(f) ε'_r and σ

Figure 8.4: Material properties of ex-vivo bovine liver as functions of temperature as defined in literature. Data extrapolated to 300 °C (dotted lines).

is how long the tissue remained at particular temperatures. Hence, the tissue water content was related to a distinct length of time and degree of high temperature exposure. Relating tissue water content to temperature in this way could also overestimate the initial variations in tissue properties ρ, c_p, and k.

Apart from those measurements and estimation mentioned above, data for temperature-dependent liver tissue did not exist for temperatures above 80 °C, to the author's knowledge. Also, the measurement thereof proves extremely difficult, as outlined above in the discussion of possible errors during data recording.

As a consequence, modified temperature-dependent ex-vivo bovine liver properties are proposed as part of this work with the aim of improving modelling capabilities of high-temperature microwave ablations. These material properties were established iteratively: First, all properties were reset to their initial values at room temperature. For higher temperatures, material properties were then varied according to the trends described above for a particular property. The model was solved and resulting temperature data compared to measured data. If necessary, material properties were adjusted and the model re-solved until agreement between modelled and measured data existed within the error limits. This process was then repeated for the next higher temperature range. In this manner, the material properties were established step by step for all temperature regimes up to 300 °C. It was noted during computer modelling that permittivity and thermal conductivity appeared to be the major factors in influencing the temperature gradient. Figure 8.5 depicts both the data from section 8.2.8 taken from the literature (black lines) and the new proposed properties resulting from the FEA study (red lines).

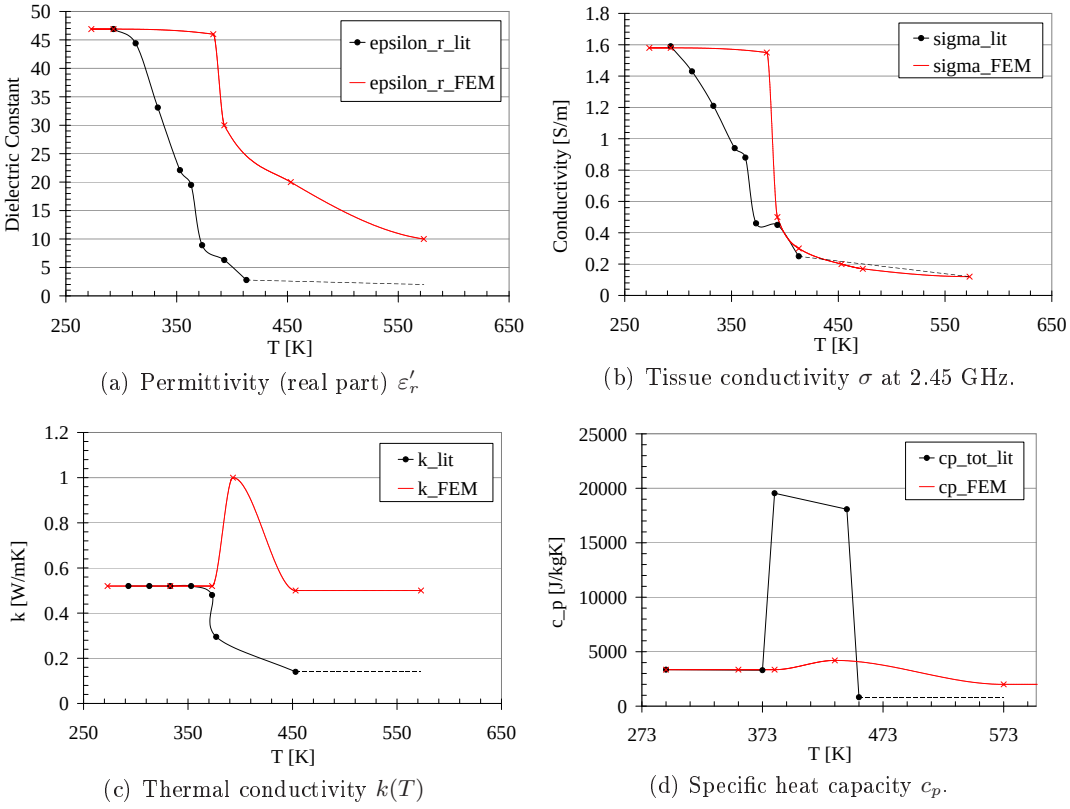

(a) Permittivity (real part) ε'_r

(b) Tissue conductivity σ at 2.45 GHz.

(c) Thermal conductivity $k(T)$

(d) Specific heat capacity c_p.

Figure 8.5: Published (black lines; label 'lit') and proposed material properties of ex-vivo bovine liver as functions of temperature (red lines; label 'FEM').

Table 8.3 lists the proposed tissue properties in a tabular fashion, needed for the definition of the functions shown in figure 8.5 which were assigned in the FEA.

The following assumptions were made for defining the proposed liver tissue properties:

- Permittivity values can drop to below 15 % of their initial values at room temperature for temperatures above 100 °C [73].

Table 8.3: Proposed tissue properties in tabular format; assigned in FEA of 1.8 mm applicator.

T (°C)	T (K)	$\epsilon_r^{'}$	$-\epsilon_r^{''}$	ρ	c_p	k
20	293	46.9	11.6	rho	3350	0.52
100	373	N/A	N/A		N/A	0.52
110	383	46	11.4		3350	N/A
120	393	30	3.7		N/A	1
140	413	N/A	2.2		N/A	N/A
160	433	N/A	N/A		4200	1
180	453	20	1.5		N/A	0.5
200	473	N/A	1.2		N/A	N/A
300	573	10	0.9		2000	0.5

- Thermal conductivity increases due to the generation of steam above 100 °C but decreases again for very high temperatures above 200 °C.
- The specific heat capacity also increases above 100 °C to take into account the latent heat of vaporisation needed for steam generation.
- Since tissue density and specific heat capacity are linked, tissue density was approximated constant (1075 kg/m^3) and the effects included in the specific heat capacity.

8.2.9 Solver Settings and Solution Process

The analysis type in the solver settings was set to harmonic propagation for the TM mode and to time-dependent solver for the BHE. The transient analysis required the definition of the total analysis time and appropriate intermediate time steps. The total analysis time was set equal to the maximum ablation time of 6 min. A short time step of 1 s was defined after which the current solution data was stored by the model.

The model was first solved for the electromagnetic problem only in order to obtain $S11$ as a function of frequency. This was achieved by utilising frequency-dependent properties for saline as load. The results were then compared to experimental $S11$ data in order to validate the model. Upon successful validation, the analysis was then run for linear bovine liver properties and applicator temperatures compared to experimental data. Following the linear analysis, the material properties were changed to temperature-dependent ones and the coupled-field analysis re-solved. The solution process of the coupled-field analysis was described in detail in section 8.2.2.

8.3 Analysis 1: $S11$ in Saline

The load material properties were defined according to the frequency-dependent saline properties given in table 4.6. A parametric analysis was started for the TM mode in order to allow solving for various frequencies between 1 GHz and 10 GHz. Figure 8.6 displays the model results and $S11$ measurements. $S11$ in 0.1 M saline was recorded for two different applicators. The results were averaged and smoothed (grey line with

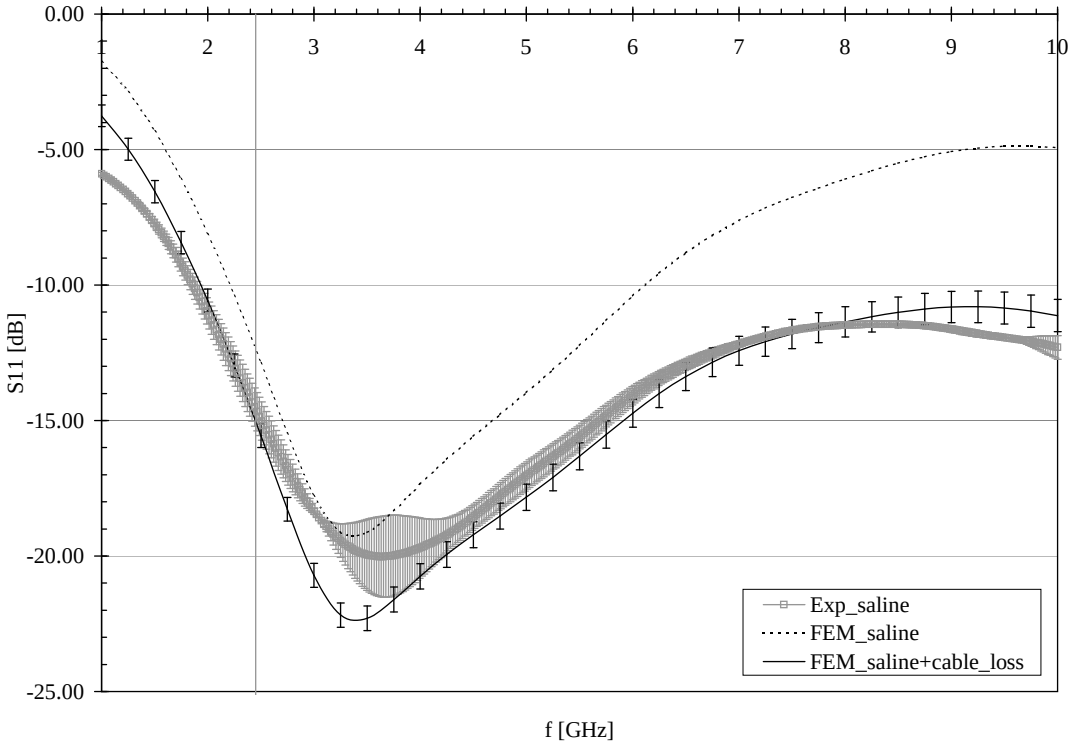

Figure 8.6: Comparison of modelled $S11$ (dashed trace) for frequency-dependent saline properties to measured data (grey trace); cable loss included in FEM results (black trace).

markers). The black dashed trace indicates the model basic results, the black solid line the model result taking into account of the umbilical cable loss and error. The umbilical cable loss was measured to (-0.5 ± 0.1) dB/m at 1 GHz, and (-1.55 ± 0.15) dB/m at 10 GHz and assumed to increase linearly in the given range. Since the umbilical cable was of length 2 m, the total cable loss in $S11$ measurements was twice the cable loss for 2 m, that is, -2 dB at 1 GHz and -6.4 dB at 10 GHz. This loss was added to the $S11$ model results. Within the error given, measured and modelled data were in good agreement.

8.4 Analysis 2: T in Ex-vivo Bovine Liver for Linear Material Properties

After the electromagnetic model was validated using $S11$, an number of electromagnetic-thermal analyses were run with linear material properties in order to determine the heat transfer coefficient of the cooling system.

The heat transfer coefficient h was determined by solving the model for various values of h and comparing the resulting model ferrule temperatures to those of the measurement (tip temperatures were hardly influenced by cooling). Also, a dead zone in the cooling of length 4 mm was added in the model representing the dead zone in the applicator due to

the gap between end of internal thermocouple and ferrule. The best agreement between model data and measured temperatures were thus obtained for heat transfer coefficients of 5000 W/(m^2·K) along shaft and cable, and 1000 W/(m^2·K) within the dead zone. A heat flux boundary condition was therefore assigned on outer conductor and interior shaft using h = 5000 W/(m^2·K), and on ferrule surfaces using 1000 W/(m^2·K). The external temperature, meaning the fluid temperature, was set to 293 K.

Figures 8.7 and 8.8 display the measured and modelled temperature data for locations at tip and ferrule for 66 W and 88 W tip powers (6 min ablations). Tip and ferrule temperatures were measured using the technique described in 7.5.3, except that the applicator was inserted horizontally into tissue with a weight placed on top of the liver-applicator-liver sandwich. This setup was chosen in order to prevent the tissue from withdrawing from the applicator surface and steam to escape through the cut in the tissue. For each power setting, the measurement was repeated 5 times and the recorded data averaged. The figures show measured and modelled temperatures over the total ablation time of 6 min. The error bars plotted for the experimental data (grey bars) is the standard deviation derived from the set of measurements.

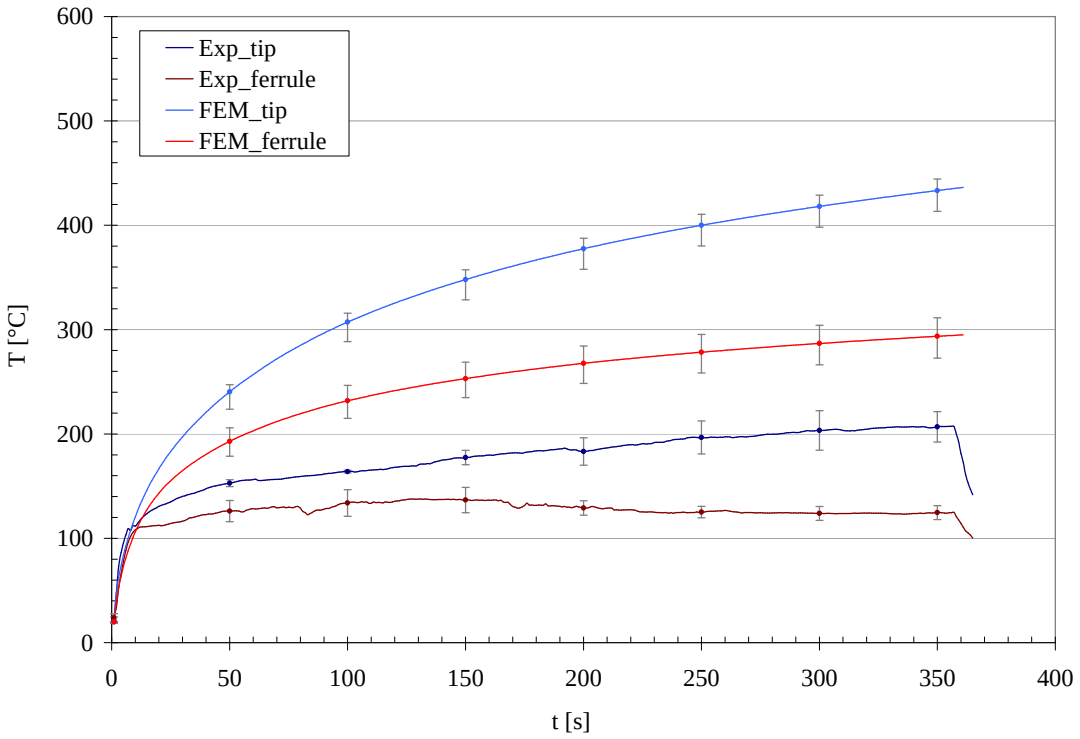

Figure 8.7: Measured (exp) and modelled (FEM) tip (blue) and ferrule (red) temperatures for linear tissue properties; 66 W tip power; error bars in grey.

The following assumptions were made concerning the error present in the modelled temperature data: Δz of 0.5 mm and 1.6 mm in respective placements of tip and ferrule thermocouples. The radial placement error Δr was determined to be equal to the diameter of the thermocouple bead, that is 0.127 mm. The error of the modelled data was then obtained by finding the points of minimum and maximum temperatures within the described areas. The coordinates (r,z) (m) of test points for minimum, target,

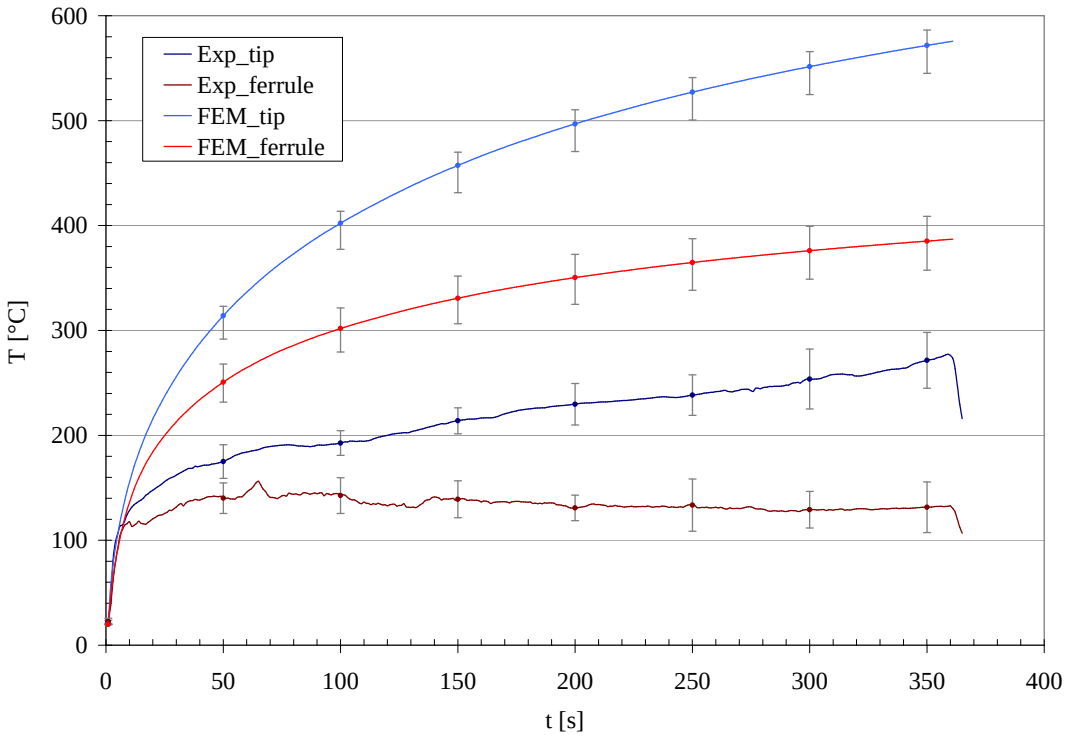

Figure 8.8: Measured (exp) and modelled (FEM) tip (blue) and ferrule (red) temperatures for linear tissue properties; 88 W tip power; error bars in grey.

and maximum values were (0.915e-3,0.03), (0.95e-3,0.0186) and (1.042e-3,0.0295) for tip and (0.915e-3,0.0176), (1.042e-3,0.0192), and (0.95e-3,0.0186) for ferrule. Figure 8.9 illustrates the position of those test points.

Good agreement between measured and modelled data was achieved for temperatures up to approximately 100 °C. The discrepancies for temperatures beyond 100 °C were expected since no temperature-dependent properties had been included as yet.

Further errors in measured and modelled data were induced by the following issues. The applicator non-stick coating was not included in the FEM model. The model hence lacked the thermal barrier provided by the coating between applicator and tissue. Also, the thermocouple bead was insulated and protected from the tissue with a second layer of silicone (tip) and layers of tape (ferrule). However, in the case of the tape, liquid (blood) could penetrate between TC and tape hence distorting the measurements.

8.5 Analysis 3: T in Ex-vivo Bovine Liver for Non-linear Material Properties

The temperature-dependent properties of ex-vivo bovine liver found in literature and defined in section 8.2.8 were assigned in the model. The FEA was then solved initially for a tip power of 88 W. Figure 8.10 shows the resulting tip and ferrule temperatures together with the corresponding measured data. The error in the computed data was determined as in the linear case.

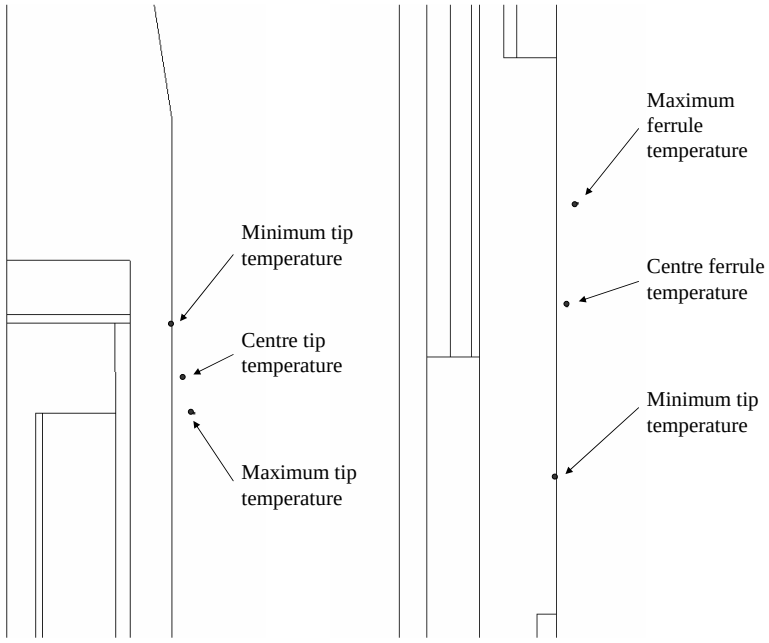

Figure 8.9: Locations of temperature test points in FEM model for tip and ferrule temperatures.

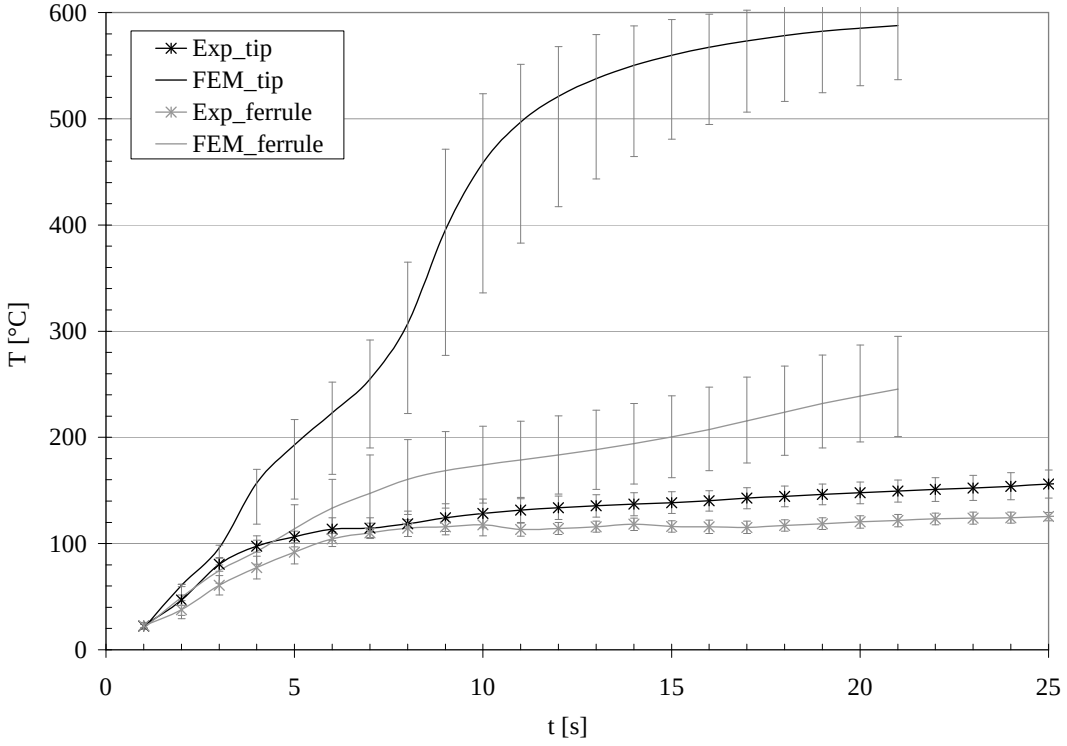

Figure 8.10: Measured (exp) and modelled (FEM) tip and ferrule temperatures for temperature-dependent tissue properties taken from literature. 88 W tip power.

It can be seen, that modelled temperatures at the tip exceed 500 °C after 10 s. Due to these unrealistic data, the analysis was not completed for the remainder of the ablation duration. Reasons for the extreme heating beginning at approximately 100 °C must be due to underestimating the tissue density and/or thermal conductivity. The material properties of ex-vivo bovine liver used in the model were defined from the scarce data found in literature. However, as shown in the figure, these material properties could not accurately predict temperatures experienced in the tissue during microwave ablation. For this reason, new non-linear temperature-dependent tissue properties were proposed as described previously (see section 8.2.8).

8.6 Analysis 4: T in Ex-vivo Bovine Liver for Proposed Material Properties

The novel temperature-dependent properties of ex-vivo bovine liver proposed in section 8.2.8 were assigned and the model solved for the same power settings of 66 W and 88 W relative to the tip. Figures 8.11 to 8.14 display the resulting tip and ferrule temperatures together with the corresponding measured data. Modelled data for tip and ferrule is displayed in dark blue and dark red respectively, corresponding measured data in light blue (tip) and light red (ferrule). The error in the computed data was determined as in the linear case.

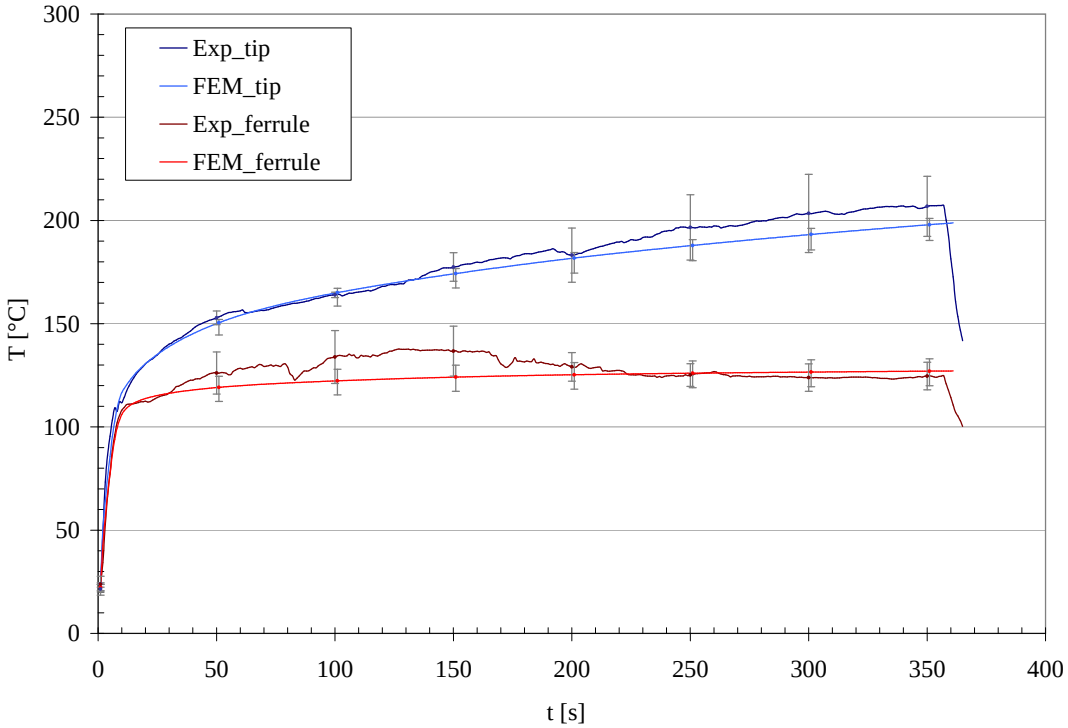

Figure 8.11: Measured (exp) and modelled (FEM) tip (blue) and ferrule (red) temperatures for novel temperature-dependent tissue properties proposed in this work; 66 W tip power; error bars in grey.

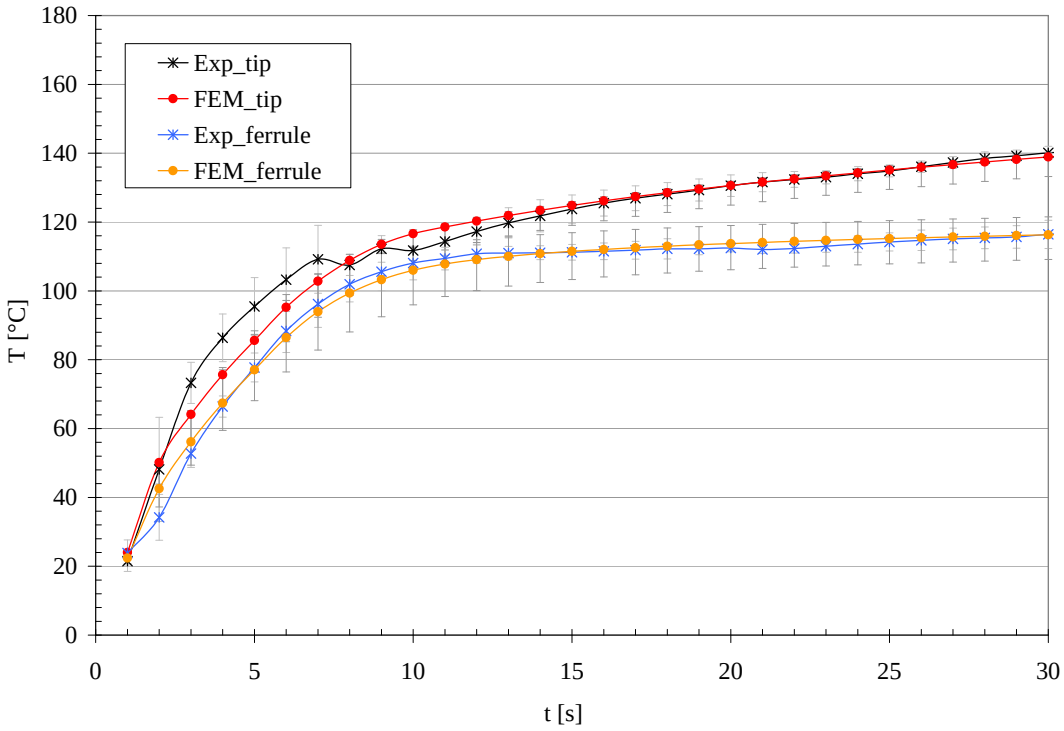

Figure 8.12: Initial temperature rise at 66 W tip power for proposed temperature-dependent tissue properties; error bars in grey.

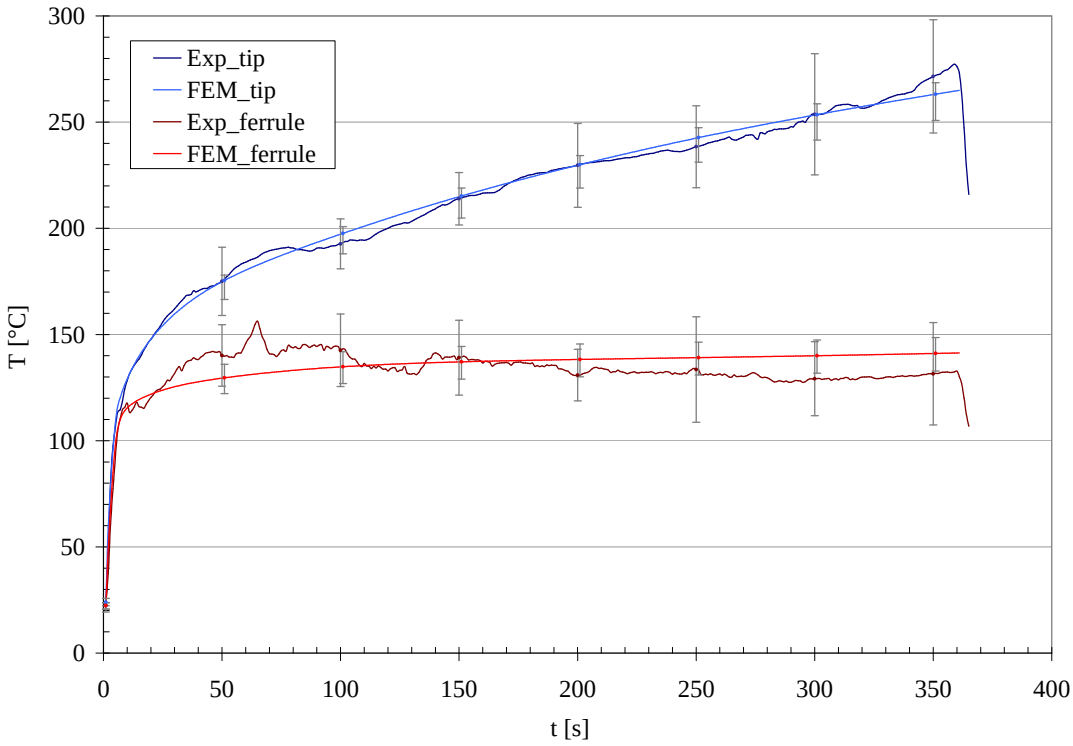

Figure 8.13: Measured (exp) and modelled (FEM) tip (blue) and ferrule (red) temperatures for proposed temperature-dependent tissue properties. 88 W tip power.

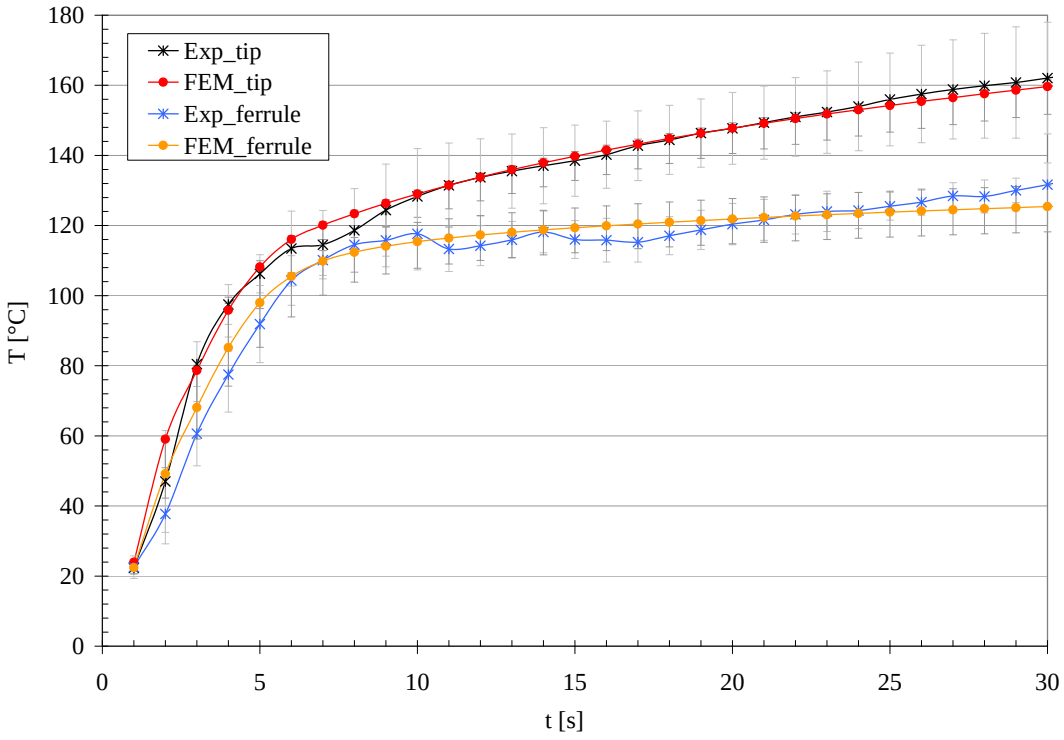

Figure 8.14: Initial temperature rise at 88 W tip power.

Good agreement between experimental and theoretical data was achieved for the entire ablation duration for both power levels. Measured temperatures at the ferrule initially rose to 130 °C and 140 °C for 66 W and 88 W, respectively, and dropped back to a steady-state of (125 ± 10) °C and (130 ± 20) °C beyond 3 min. This effect was most likely due to the drying out of the tissue. Since material properties in the model were only defined as functions of temperature, this time-dependent change in tissue properties was not considered. However, the final temperatures did again agree within the error limits.

Figures 8.15 and 8.16 show the resulting temperature distributions in both applicator and load for a 6 min, 88 W ablation at intervals of 60 s. It can be seen that the hottest point in the applicator is in the tissue at washer level. Tip temperatures were measured at this location. Furthermore, shaft temperatures are kept low due to the active cooling. It can hence be concluded that the highest temperatures in the applicator occur at the washer. These are (195 ± 6) °C for 66 W and (265 ± 12) °C for 88 W tip power, respectively.

Furthermore, figure 8.17 displays final temperatures of 88 W ablation at time 360 s along lines in radial direction from r = 0 mm to r = 30 mm and at nine different z values; the exact locations of these lines are shown in figure 8.18 whereby the colour of line matches the corresponding trace in figure 8.17. It can be seen that the highest temperatures are found in close proximity to the washer giving rise to a steep temperature gradient of approximately 25 °C/mm in radial direction in this area.

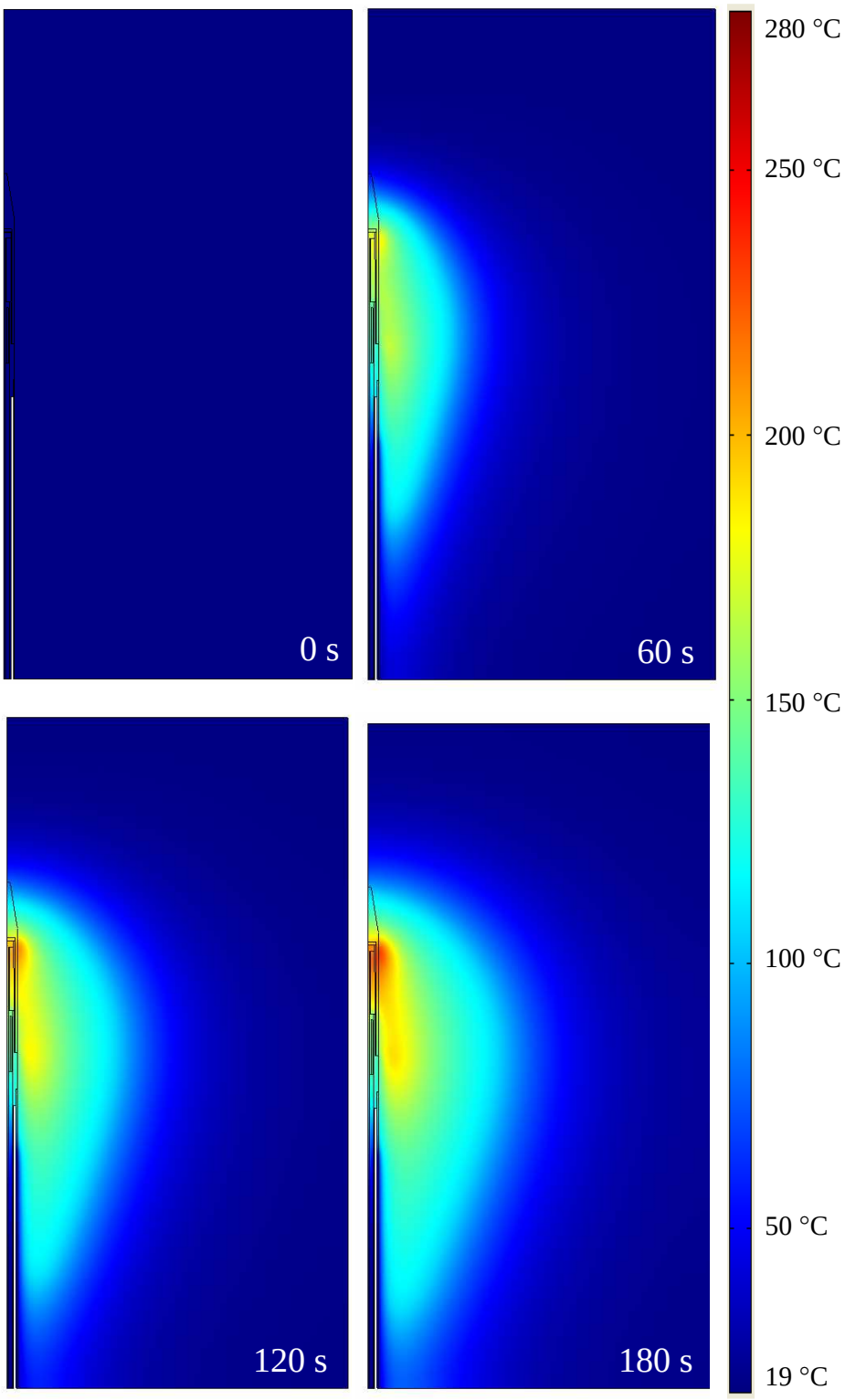

Figure 8.15: Modelled temperature distribution in applicator and tissue at 0 s, 60 s, 120 s, and 180 s of a 6 min, 88 W ablation for proposed ex-vivo bovine liver properties.

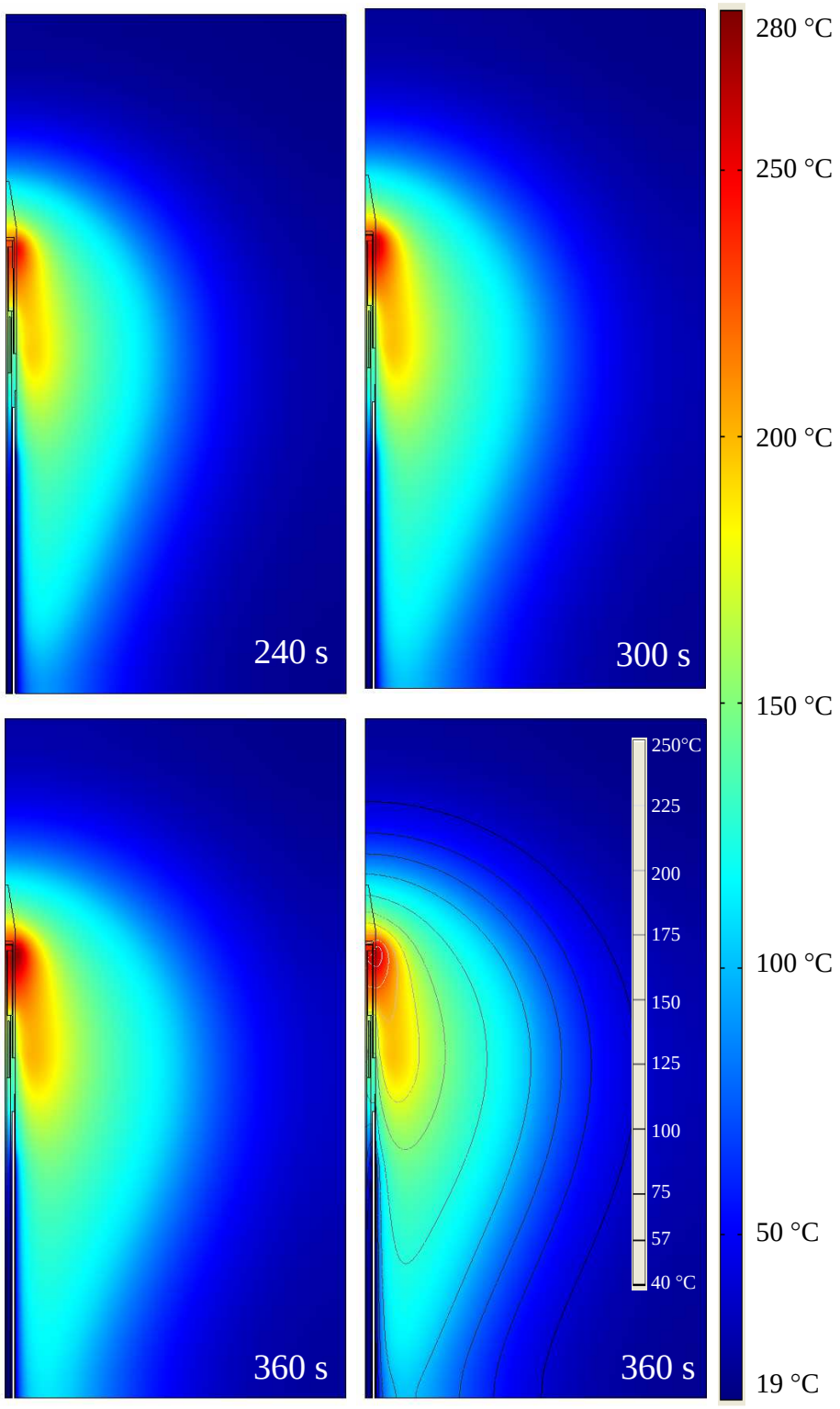

Figure 8.16: Modelled temperature distribution in applicator and tissue at 240 s, 300 s, and 360 s of 6 min, 88 W ablation for proposed ex-vivo bovine liver properties. Last figure depicts final temperature distribution with additional temperature contour lines.

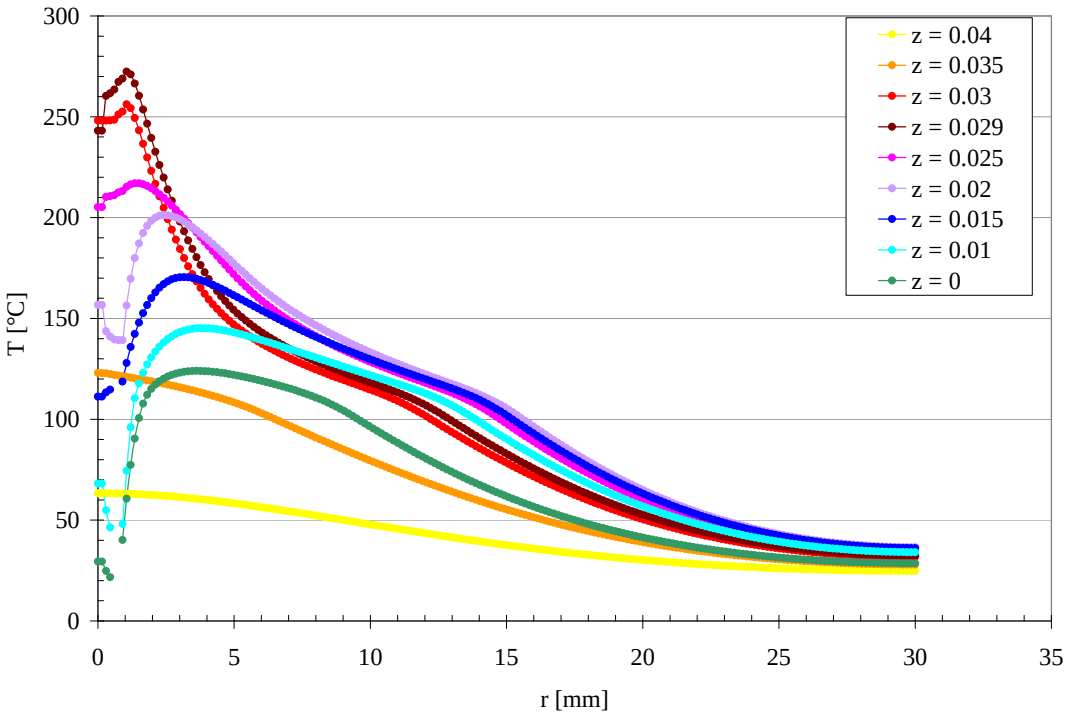

Figure 8.17: Temperature in applicator and tissue at 360 s of 88 W ablation plotted along lines in radial direction for heights z = 0, 0.01, 0.015, 0.02, 0.025, 0.029, 0.03, 0.035 and 0.04 m.

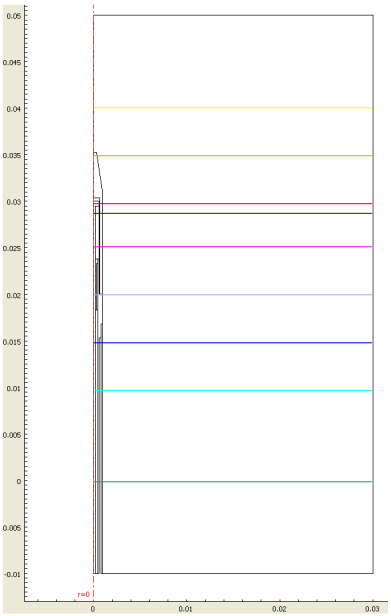

Figure 8.18: Position of lines along which temperature is plotted in figure 8.17; r = 0 to 30 mm; z = 0, 0.01, 0.015, 0.02, 0.025, 0.029, 0.03, 0.035 and 0.04 m.

8.7 Conclusion

The main challenge in the development of a FEA model of the applicator concerned the definition of the largely unknown temperature-dependent tissue properties and heat transfer coefficient. Novel material properties of ex-vivo bovine liver were proposed as a result of comparing modelled and measured temperatures and adjusting relevant properties accordingly, since the data sourced from the available literature led to marked disagreement between modelled and measured temperature distributions. These proposed material properties were then used in the FEM model to analyse tissue and applicator temperatures. Also, a heat transfer coefficient for the closed-cycle cooling system of the applicator was established.

The resulting transient temperatures of the FEA showed good agreement with recorded temperature data for 6 min ablations of 66 W and 88 W. Highest applicator temperatures were shown to be experienced in the applicator tip around the washer, reading (195 ± 6) °C and (265 ± 12) °C for 6 min ablations of 66 W and 88 W, respectively. Due to the selection of suitable high-temperature applicator materials reported in previous chapters, the device was capable of withstanding these extreme conditions repeatedly. The FEA model can hence be used to predict applicator and tissue temperatures for high-temperature microwave ablation devices at various settings of power level, cooling rate, ablation time, or even antenna designs. For instance, any effects on applicator service temperatures due to changes made to the antenna design can now be readily assessed using the developed model with proposed non-linear tissue properties prior to the manufacture of prototype devices.

Chapter 9

Conclusion

This chapter concludes the work presented as part of this thesis. First, a summary of the thesis and individual chapters is given. This is followed by some recommendations regarding future research and an overall conclusion regarding the thesis subject, process and outcome.

9.1 Summary of Thesis

In the following subsections, an overview of the activities undertaken and results obtained in each chapter is given.

9.1.1 Introduction

Primary and secondary cancer of the liver is a major concern in today's world with a total number of approximately 1 million new cases each year. The prognoses of untreated HCC or hepatic malignancies are poor with 5-year survival rates between 0 % and 10 %. Liver resection and liver transplantation remain the best curative options for the treatment of HCC and hepatic metastases with 5-year survival rates ranging from 20 % to 60 % and 40 % to 60 % depending on factors such as the type, size and number of tumours or the age of the patient treated.However, only an approximate 20 % of all patients are eligible for these surgical procedures. Local ablative techniques target the vast number of patients unable to receive major surgery. Within this category of local ablative techniques, MWA still holds a relatively small but rising percentage of all treatments. The main advantages of MWA over other techniques include fast treatment times, large ablation diameters, repeatable ablation geometry, ablation not limited by tissue charring and inducement of complete tumour death within the ablation zone. These benefits are the basis for the development of MWA devices with the aim to provide a fast and effective treatment of both HCC and hepatic metastases.

9.1.2 Theory

In MWA at 2.45 GHz, energy absorption or heating of soft tissues is achieved by coupling of an EM wave to the permanent dipole of water molecules. Under the influence

of a microwave electric field water molecules tend to re-orient themselves to the applied field, however the molecules are unable to follow the extremely rapid reversals of the electric field which leads to the power dissipation and hence heating of the tissue. The EM wave emitted by MW antennae is obtained by solving Maxwell's equations and the wave equation. The degree of responsiveness of a certain material to microwave radiation is defined by the material's complex permittivity at a given frequency. The specific absorption rate (SAR) is a measure of energy deposition in tissue in units of W/kg caused by the absorption of electromagnetic waves leading to heating in the affected region. Following the initial temperature rise induced by the absorption of microwaves, the second important mechanism in MWA begins - heat conduction. Heat conducting from the ablation centre towards colder surrounding areas is responsible for further ablation growth. Both mechanisms, direct electromagnetic heating and heating due to conduction, are taken into account of in the Bio-heat equation which therefore allows computational analyses and simulations of tissue temperature during MWA. The difficulty in theoretical analyses of MWA are mainly due to the strong temperature-dependence of tissue properties, which are still largely unknown for temperatures above 100 °C. Theoretical predictions are therefore limited in terms of final ablation temperatures but produce nevertheless satisfying data concerning final ablation size and the assessment of initial reflected power at the applicator.

9.1.3 Detailed Design Brief of 1.8 mm Applicator

Prior to the commencement of the applicator development, a detailed design brief was presented. In it, the desired device performances were identified and subsequently defined in terms of 21 specific applicator requirements. The major requirements included a restriction of device diameter to below 2 mm, a flexible and light-weight coaxial feed cable, a restriction of cable and shaft temperatures in use to below 48 °C, a return loss of below −10 dB, a possible ablation time of up to 8 min, an input power of at least 60 W, an applicator survival over 8 consecutive ablations at maximum power and maximum time settings as well as a closed-cycle cooling system.

9.1.4 First 1.8 mm Applicator Design and Electromagnetic Analysis

Taking those requirements into consideration, an initial applicator design was proposed and its EM performance analysed in a FEA of the device. The design of the applicator with a reduced diameter of 1.8 mm was based on that of a dipole antenna, continuing on the successful development of earlier larger diameter devices by the group.

The FEA was solved for a number of combinations of possible lengths for the most critical applicator dimensions in order to optimise the antenna design. The most suitable combination was then selected featuring a return loss of −15 dB at 2.45 GHz. Furthermore, the SAR of the antenna was analysed leading to an acceptable absorption pattern around the applicator tip.

Following the theoretical design phase, two applicators were built according to the specifications obtained from the computer simulations. $S11$ of the devices were measured and compared to theoretical values which highlighted the need to take into account a

minute air gap between washer and tip. Re-solving the computer model with such an air gap resulted in good agreement between theoretical and measured $S11$ across the frequency range of 1 GHz to 10 GHz. At the operating frequency of 2.45 GHz, both modelled and measured $S11$ were -14 dB.

9.1.5 Development of Applicator with Integrated Closed Cycle Cooling System

Before applicators could be tested in an ex-vivo setup, a suitable cooling system had to be developed in order to protect the devices from failure caused by the high temperatures which were most expected during the operation of the applicator. The cooling system to be developed also had to meet a number of requirements; it had to be closed cycle in order to prevent unwanted and potentially harmful coolant input into the ablation centre; it was not allowed to increase the diameter of the existing 1.8 mm applicator; it must not infringe on existing patents concerning the cooling of microwave applicators; it had to provide adequate cooling to enable high-power operation of the device; it had to cool the applicator feed cable maintaining surface temperatures below the allowable limit of 48 °C; and lastly it had to be manufacturable with regards to required pressure, costs, and overall design complexity.

Several existing cooling concepts were considered, however none of which met all requirements stated. A novel solution was found in the design of an oval tube cooling system relying on pressurised contact areas between oval outer stainless steel tube and inner circular semi-rigid coaxial cable for providing waterproof seals. The pressure was created by releasing a previously elastically deformed tube. This concept was subsequently improved until it met all requirements stated earlier resulting in the following design: The stainless steel tube remained in its initial round state and a piece of wire was introduced to form the required pressurised contacts between shaft and cable. In the following, a thermocouple of novel design was developed consisting of a single constantan wire with copper plated end, utilising the outer conductor of the semi-rigid coaxial cable as second lead wire. The piece of wire utilised previously was then exchanged with the developed TC assembly. The final design of cooling system with integrated temperature sensor provided a sensitive mechanism for detecting cooling failures of all conceivable kinds.

Lastly, the shaft cooling was extended over the applicator handle and, by means of umbilical tubing, over the full length of the coaxial feed cable. This setup presented the final design of the closed cycle cooling system developed as part of this work meeting all specifications. The performance of the cooling system was validated as part of the subsequent prototype build and testing.

9.1.6 Analysis of Applicator Service Failures

Prior to the prototype batch build, a brief analysis of applicator failures was presented. Typical failures included fracture of ceramic tip, ferrule puncture, failure of tip bond and degradation of the non-stick coating over time. Remedial measures such as improved assembly processes and the use of better suited materials, adhesives, or coatings were taken to limit the risk of failures to a level as low as reasonably possible.

9.1.7 Development of 1.8 mm Prototype System

Following those considerations, a batch of 7 prototype applicators were built according to the latest designs of antenna and cooling system. During the fabrication of the prototypes, the assembly procedure was de-bugged and optimised with regards to obtaining a greater yield and reducing the assembly time of initially 1-2 weeks to several days per applicator. The performance of the prototype devices was then validated using appropriate tests regarding $S11$ (to (-11 ± 0.5) dB), maximum service temperatures of tip, ferrule and shaft (to 300 °C, approximately 120 °C and $\leq$ 30 °C, respectively), detection of cooling failures, ablation size and shape (typically 55 mm x 60 mm for a 80 W, 8 min ablation with sphericity of 0.999), survival of non-stick coating over the maximum number of 8 repetitive ablations performed at highest power and time (80 W, 8 min), and lastly overall prototype survival over maximum number of ablation repetitions at maximum power and maximum time. Since measurements of applicator service temperatures were undertaken during the prototype validation testing, computer simulations were performed to predict the thermal applicator response.

9.1.8 Electromagnetic-Thermal Computer Simulations of 1.8 mm Prototype

A computational FEM model of the applicator was developed to analyse the thermal conditions in applicator and load during operation. Until that point in time, computer simulations of MW devices were limited to either their EM behaviour only or to electromagnetic-thermal analysis predicting temperatures just beyond the boiling point of water, with exception of [106] who defined temperature-dependent ex-vivo bovine liver properties to simulate load temperatures up to 180 °C. However, using those material properties for this device did not yield good results. The reason for this is most likely the operation of the device at much higher input powers and the rapid rise in tissue temperature associate with it.

The creation of a FEM model which would allow the prediction of both applicator and load temperatures throughout the entire ablation time was then anticipated. A coupled-field electromagnetic-thermal FEM model was generated in the following, including the effects of the cooling system by defining a heat transfer coefficient. The material properties of ex-vivo bovine liver were adjusted at higher temperatures according to defined trends and the resulting temperature data compared with experimental data. This process was repeated for several temperature regimes until all necessary data was defined. This led to the establishment of novel temperature-dependent properties for ex-vivo bovine liver up to 300 °C including dielectric constant, electrical conductivity, thermal conductivity, and specific heat capacity. Using those newly defined parameters, the FEM model was recomputed and very good agreement between modelled and measured data achieved.

9.2 Conclusion of Thesis Project

The research undertaken was very interdisciplinary in nature which required knowledge in many different subject areas such as electrical engineering, physics, biology, material

science, medical knowledge. The best way to acquire the necessary information is seen in the study of previous theses which cover the area of microwave ablation. Furthermore, skills needed for working in collaboration with industry were necessary; all of those made the project interesting and challenging. Tasks such as computer simulations, practical manufacture of devices, experimentation and testing as well as incorporating design changes stemming from the consumer or end user allowed the growth of an all-round view of the project. Besides, the usefulness and purpose of the project was rewarding knowing that potentially many people might benefit from the development of the device in the future.

The initial decision to develop a small-diameter microwave applicator for microwave soft tissue ablation was in line with efforts made by other MWA companies who also focussed their research and development on designing applicators with smaller diameters. This trend still holds true at this time and is likely to continue for the next couple of years.

Although many obstacles were met during the design, development and manufacturing phases of the 1.8 mm percutaneous microwave applicator, mainly due to the miniaturisation of the device and cooling system and as discussed in respective chapters, the 21 design requirements stated at the onset were finally achieved through various design changes and also the development of novel design elements.

The latest design of the 1.8 mm internally cooled percutaneous microwave applicator - except minor changes regarding adhesive selection and more significant changes regarding handle and cooling pump design - is currently being developed into a commercial product by Acculis Limited in collaboration with Runfold Medical Limited under the name of Percutaneous Microwave Tissue Ablation applicator or 'pMTA' applicator. The pMTA product will include the applicator and a Local Cooling Station 'LCS' which houses a pump supplying coolant to the flexible cable and applicator shaft. The pMTA applicator is designed for single-use, the LCS for multiple usage. The pMTA product will be supplied to hospitals in conjunction with an existing separate control unit 'Sulis V' containing the microwave generator as well as control software. The latest stage of the pMTA product development is depicted in figure 9.1 showing the three components - pMTA applicator in too lengths, LCS and control unit. It is anticipated to receive product clearance in the UK and the rest of the world through CE marking and product approval in the US through the US Food and Drug Administration by the end of 2009. Once the product has been cleared it can be sold and used in sites around the world.

Figure 9.1: Latest pMTA system design consisting of pMTA applicators of two lengths, pump and connection unit LCS, coolant, and microwave source Sulis V (from Acculis Limited).

Chapter 10

Future Work

This final chapter on future work comments on the most important developments and possibilities in the research of microwave ablation. In the following sections, four aspects of future work as seen by the author will be discussed: recommendations for future PhD projects, the immediate future work concerning the research and development of microwave ablation, the future work concerning ablative techniques in general, and lastly the overall future work with respect to tumour treatment.

10.1 Recommendations for Future PhD Projects

Computer models were used repeatedly during the research project to assess the prospects of possible applicator designs. Learning to use such computer simulations confidently can take several months to a year depending on the complexity of the program. It therefore seems to be appropriate to only engage in computer modelling if it will be used frequently during the project, since computer simulations do not supersede the subsequent manufacture and experimental validation of a device. However, for the design of new applicators with possibly new intended uses, computer modeling is useful and should remain the starting point for predicting terms such as $S11$, temperature, and associated data in the design process.

One problem which will most likely remain for the time being is the lack of material data for human living tissues, especially cancerous, as such data is needed for computer modelling. So, in many instances approximate values have to be used.

Understanding the requirements of the medical environment regarding, for instance, operating theatre design, operating procedures, required dimensions, safety or user-friendliness is another key factor which can slow down the initial learning process. However, having full knowledge of those requirements is essential for defining accurate and appropriate applicator design requirements early on in the project in order to ensure that a device is developed which will be suitable for its intended use.

Furthermore, the selection of suitable materials is critical for a successful device development. Materials used must be suitable for use in high-power microwave fields, under high-temperature conditions of 300 °C or higher, in liquids and must be either biocompatible or otherwise coated with a biocompatible material. This severely limits

the number of suitable materials. As a consequence, the introduction of new materials and coatings into the marketplace should be monitored continuously.

10.2 Future Work in Microwave Ablation

The major piece of future work regarding the pMTA project is the execution of clinical trials to assess the overall performance of the pMTA system in the clinical in-vivo setting. For instance, the dose-response curve for in-vivo ablations has to be determined mapping final ablation size to applied power and time. Reliable data on ablation size versus applied energy is very important and will be used as part of the operating instruction for the pMTA system.

Another important part of future work is the design of new applicators. Due to a frequency-dependence of the applicator antenna length, a device operating at a frequency between 8 GHz-10 GHz would be optimal for creating small spherical ablations. Computer simulations of an applicator designed for operation at 9.2 GHz showed that the expected ablation sizes lie in the range of 0 cm to 3 cm and treatment times between several seconds to a few minutes. The small spherical ablation geometries are due to the short antenna length of approximately 4 mm at 9 GHz. Also, input powers required to achieve such small scale ablations range from 10 W to about 40 W, which means the device can be based on thin coaxial cables. The design characteristics and applicator outputs would be ideal for the treatment of tumours that are located in organs such as lung or bone where minimal damage during access must be achieved and required ablation sizes are usually small.

Regarding the design of new applicators, a further parameter could be utilised in the future to improve the device's power deposition over the duration of an ablation. During this project, the applicator's $S11$ was monitored over the span of an ex-vivo ablation. It was noted that the reflected power at the applicator tip increased from initially 3 % to approximately 20 % at the end of a full-power and full-time ablation (180 W; 6 min; pMTA system). Such data could potentially be used in the design of future devices to ensure continued power deposition. For instance, the applicator could be designed for operating best in partially or fully desiccated tissue. Approximate values of desiccated ex-vivo bovine liver tissue could be taken from the non-linear data proposed in chapter 8 (see page 149) for temperatures around 200 °C or higher.

Another challenge in future computer modelling is the prediction of ablation sizes near blood vessels as these can act as heat sinks distorting the final ablation geometry. Part of such a project would be the assessment of the cooling effect of blood flow onto final ablation geometry using suitable measurement techniques.

The continued improvement of computer simulations of MWA is also seen as a possible piece of future work. As discussed in detail, temperature-dependent material properties are of highest importance whenever thermal aspects of ablations are to be simulated. Using suitable measurements, the knowledge of material properties should be further refined in the future including ex-vivo as well as in-vivo data where possible. Furthermore, the construction of patient-specific models including the individual architecture of the liver would be a massive improvement. These could be fed into the overall treat-

ment planning of tumour management. This issue is explained in more detail in the following.

Complete treatment planning is becoming more and more popular and also realistic due to advances in monitoring and guidance systems for clinical products. Emerging intraoperative guidance relies on electromagnetic and optical tracking of interstitial equipment such as applicators and probes during the surgical procedure. For instance, the 'Pathfinder' product from Pathfinder Therapeutics Inc provides navigation during liver surgery which allows a new type of treatment planning. Firstly, the affected organ is scanned during an open liver procedure and the data used for creating a 3D model of that organ including all major vascular structure. Secondly, the optimum path invoking minimal damage and risk is determined by the software using the data of the 3D liver model. Once the optimum path has been defined, the actual placement and advancement of the applicator is monitored in real-time to ensure correct positioning along the pre-defined path until the target area has been reached. At this point the ablation is performed. The pathfinder product significantly reduces the risk of misplacing surgical tools and damaging blood vessels or other important nearby structures. Bringing different technologies together in such a way will play an important role in the future perception of microwave ablation devices as flexible and high-tech products.

10.3 Future Work in Ablative Techniques

The future of ablative techniques in general depends on several developments. Firstly, the effectiveness of ablation treatments over time must be assessed using randomised controlled clinical trials. The aim of such clinical trials is to compile data regarding complication, local recurrence and survival rates for ablative techniques such as microwave or RF ablation as well as the current 'gold standard' of surgical resection in order to be able to compare the different procedures. However, patient selection for trials like this are usually difficult as many factors such as age, tumour size, tumour location, total number of tumours and general health must be the same in order to ensure comparability. So, the presence of MWA in the future as part of a pool of tumour treatment options will depend on data showing that the 5-year survival is indeed the same or even higher for MWA compared to other treatments.

Another challenge is seen in the real-time monitoring of microwave ablations as the theoretical ablation size can vary from the actual in-vivo ablation and from person to person. Developments into the real-time monitoring of ablation growth are one of the major requests from clinical partners and would bring huge benefits for all types of thermal ablation techniques.

In addition, further research could be focussed on possibilities of protecting structures in cases where a tumour is located near-by a major vessel or structure. Thermal ablation of tumours which are located too close to either major blood vessels, biliary tree, or neighbouring organs is currently almost impossible.

Furthermore, research could be performed into the potential treatment of 'fatty' and 'cirrhotic' liver, both of which describe a particular hepatic disease with currently limited treatment options.

Also, microwave applicators could potentially be used in a new treatment setting of 'ablate and cut' whereby short-time and low-power pulses of microwave energy could be used to ablate a thin region of approximately 5 mm which would subsequently be cut. Repeating such a process could result in a clean non-bleeding cut since the tissue would be first coagulated and then cut. The first question to answer here is whether using a microwave applicator in such a way would exceed the allowable electromagnetic leakage from the device which could pose a risk for user and patient.

So far, all ablative techniques have been regarded as curative treatments. However, a further potential significant use of ablations might be that of life extending treatments rather than curative treatments. Whereas curative treatments aim to completely destroy a tumour, life extending treatments focus on shrinking tumours by repeated application, thereby prolonging patient survival. Microwave ablation performed with small percutaneous applicators is ideally suited to such tasks, as treatments are minimally invasive, fast and readily repeatable.

Similarly, ablative techniques are also candidates for palliative treatments. Palliative treatments are performed to alleviate a patient's pain rather than to obtain a permanent cure. Ablations as palliative treatments will be increasingly used in areas such as benign or malignant bone cancer, where pain is associated with a build-up of pressure in the bone which can be significantly reduced by shrinking of the tumour mass using, for instance, heat [12, 108].

Lastly, ablative techniques play an important role in the area of liver transplantation. As mentioned earlier, donor organs are relatively rare compared to the number needed and patients therefore often have to wait a significant period of time before suitable organs become available. In this situation, ablative techniques are an important tool to ensure patient survival until the time of transplantation as they can be used to shrink and hence manage the tumour during the waiting time. Again, multiple or repeated ablations are generally possible to achieve the necessary result.

10.4 Future Work in Tumour Treatment

Again, randomised controlled clinical trials are needed to compare various treatment methods such as resection, radiotherapy, chemotherapy, RF ablation and MW ablation with regards to long-term patient survival, disease-free survival rate and complication rates. As mentioned before, attempting to conduct such trials one is faced with the need of ethical patient selection criteria. Besides, long-term follow-up data can be scarce. All those reasons make the direct comparison very challenging and time consuming but nevertheless necessary.

As scanning equipment and technology improves, the smallest detectable tumour size is likely to be reduced in the future. This creates the need for a new type of treatment outcome where small ablation sizes (1 cm to 3 cm) are required. As discussed in the previous section those requirements could be best met by a thin, low-power microwave applicator operating around 10 GHz.

More commercial partnership between different providers offering complementary equip-

ment such as optical tracking system, tumour ablation system and real-time monitoring of ablation growth will be formed in the future in order to increase treatment areas, treatment effectiveness and treatment safety. This is seen as a major part of future MWA systems. Partnerships between various and complementary companies will create systems that are compatible with each other offering the customer the possibility of an integrated approach to treatment planning, treatment monitoring and treatment performance.

The ultimate question that needs to be answered is whether MWA is likely to play a significant role in the future management of cancer. On the one hand critics might say that MWA is and will be a treatment too imprecise and unspecific and ablation sizes will never be exactly the same but vary from patient to patient which is unacceptable. To some degree this is true since every person has a unique immune system and responds slightly differently to major treatments such as MWA. On the other hand, it could be argued that being unspecific is of advantage as any type and location of soft tissue can be treated as long as the tissue water content is similar. Also, monitoring applicator placement and ablation growth will have a significant impact on the safety and efficacy of MWA and will contribute greatly to its wider acceptance and hence use. In addition, current microwave technology continues to be refined so that specific applicators are designed for specific purposes and treatments offering purpose driven performances in terms of applicator dimensions, ablation size, and operating frequency. Furthermore, MWA will be of use in other treatments apart from the curative treatments such as life-extending treatments, palliative treatments, and treatments to ensure patient survival during the waiting time up to liver transplantation. These areas of application are regarded as very significant and are expected to grow in the future as small percutaneous microwave applicators are ideally suited for the tasks. In conclusion, MWA is thought to become an increasingly important part of tumour treatment which might concentrate on the treatment of specific tumour types, sizes, shapes, and locations, where MWA has proven to be the best treatment choice in terms of long-term and disease-free patient survival. In addition to that, life-extending treatments, palliative treatments and treatments to ensure patient survival during waiting times will rise in the near future adding MWA to a new treatment category.

References

[1] D. Pozar, Microwave Engineering. Wiley, 2nd ed., 1998.

[2] S. Labonte, H. Ali, and L. Roy, "Monopoles for microwave catheter ablation of heart tissue," IEEE Trans Microwave Theory Tech.-S International Microwave Symposium Digest, vol. 1, pp. 303–306, 1995.

[3] S. Labonte, A. Blais, S. Legault, H. Ali, and L. Roy, "Monopole antennas for microwave catheter ablation," IEEE Trans Microwave Theory Tech, vol. 44, pp. 1832–1840, 1996.

[4] S. Labonte, A. Blais, and L. Roy, "Metal-tip monopoles for microwave ablation," Proc Annu Int Conf IEEE Eng Med Biol Soc, vol. 17, pp. 279–280, 1995.

[5] W. Hurter, F. Reinbold, and W. Lorenz, "A dipole antenna for interstitial microwave hyperthermia," IEEE Trans Microwave Theory Tech, vol. 39, pp. 1048–1054, 1991.

[6] K. Saito, "Heating characteristics of array applicator composed of two coaxial slot antennas for microwave coagulation therapy," IEEE Trans Microwave Theory Tech, vol. 48, pp. 1800–1806, 2000.

[7] C. Brace, D. v. d. Weide, F. Lee, P. Laeseke, and L. Sampson, "Analysis and experimental validation of a triaxial antenna for microwave tumor ablation," IEEE Trans Microwave Theory Tech.-S Int Microwave Symp Dig, vol. 3, pp. 1437–1440, 2004.

[8] J. Lin and Y. Wang, "The cap-choke catheter antenna for microwave ablation treatment," IEEE Trans Biomed Eng, vol. 43, pp. 657–660, 1996.

[9] J. Chen, "Numerical simulation of annular-phased arrays of dipoles for hyperthermia of deep-seated tumors," IEEE Trans Biomed Eng, vol. 39, pp. 209–216, 1992.

[10] P. Cherry and M. Iskander, "Calculations of heating patterns of an array of microwave interstitial antennas," IEEE Trans Biomed Eng, vol. 40, pp. 771–779, 1993.

[11] H. Chiu, A. Mohan, and D. Guy, "Coaxial slot array antenna for microwave catheter ablation," Int Symp Recent Advances Microwave Tech Proc, pp. 203–206, 1999.

[12] G. Carrafiello, D. Lagana, and C. Pellegrino, "Ablation of painful metastatic bone tumours: A systematic review," Int J Surg, vol. doi:10.1016/j.ijsu.2008.12.035, 2009.

[13] P. Liang and Y. Wang, "Microwave ablation of hepatocellular carcinoma," Oncology, vol. 72, no. Suppl 1, pp. 124–131, 2007.

[14] T. Wonnell, P. Stauffer, and J. Langberg, "Evaluation of microwave and radio frequency catheter ablation in a myocardium-equivalent phantom model," IEEE Trans Biomed Eng, vol. 39, no. 10, pp. 1086–95, 1992.

[15] J. Lin, Y. Wang, and R. Hariman, "Comparison of power deposition patterns produced by microwave and radio frequency cardiac ablation catheters," Electronics Letters, vol. 30, no. 12, pp. 922–923, 1994.

[16] D. Iannitti, "2.45 GHz microwave ablation of liver tumors." Presentation at AHPBA 2009, March 2009.

[17] W. Helton. Presentation at AHPBA 2009, March 2009.

[18] S. Goldberg, G. Gazelle, C. Compton, P. Mueller, and K. Tanabe, "Treatment of intrahepatic malignancy with radiofrequency ablation," Cancer, vol. 88, pp. 2452–2463, 2000.

[19] G. Dodd, M. Soulen, R. Kane, T. Livraghi, W. Lees, Y. Yamashita, A. Gillams, O. Karahan, and H. Rhim, "Minimally invasive treatment of malignant hepatic tumors: At the threshold of a major breakthrough," Radiographics, vol. 20, pp. 9–27, 2000.

[20] S. Jain, D. Dupuy, G. Cardarelli, Z. Zheng, and T. DiPetrillo, "Percutaneous radiofrequency ablation of pulmonary malignancies: Combined treatment with brachytherapy," AJR, vol. 181, pp. 711–715, 2003.

[21] G. Garcea, T. Lloyd, C. Aylott, G. Maddern, and D. Berry, "The emergent role of focal liver ablation techniques in the treatment of primary and secondary liver tumours," Euro J of Cancer, vol. 39, pp. 2150–2164, 2003.

[22] F. Bosch, J. Ribes, M. Diaz, and R. Cleries, "Primary liver cancer: Worldwide incidence and trends," Gastroenterology, vol. 127, no. 5, pp. S5–S16, 2004. Supplement 1.

[23] H. El-Serag and A. Mason, "Rising incidence of hepatocellular carcinoma in the united states," N Engl J Med, vol. 340, pp. 745–750, 1999.

[24] S. Taylor-Robinson, G. Foster, S. Arora, S. Hargreaves, and H. Thomas, "Increase in primary liver cancer in the UK 1979–94," Lancet, vol. 350, pp. 1142–1143, 1997.

[25] H. El-Serag and A. Mason, "Risk factors for the rising rates of primary liver cancer in the united states," Arch Intern Med, vol. 160, pp. 3227–3230, 2000.

[26] M. Jansen, R. van Hillegersberg, R. Chamuleau, O. van Delden, D. Gouma, and T. van Gulik, "Outcome of regional and local ablative therapies for hepatocellular carcinoma: a collective review," Euro J Surg Oncol, vol. 31, pp. 331–347, 2005.

[27] S. Winawer, "Colorectal cancer screening," Best Practice and Research Clinical Gastroenterology, vol. 21, no. 6, pp. 1031–1048, 2007.

[28] S. Winawer and P. Sherlock, "Colorectal cancer screening," Best Practice & Research Clinical Gastroenterology, vol. 21, no. 6, pp. 1031–1048, 2007.

[29] J. Niederhuber, "Colon and rectum cancer. patterns of spread and implications for workup," Cancer, vol. 71, pp. 4187–4192, 1993.

[30] H. Alexander, D. Fraker, and S. Libutti, "Regional treatment strategies for unresectable primary or metastatic cancer confined to the liver," Principles Pract Oncol Update, vol. 10, pp. 1–19, 1996.

[31] D. Haemmerich, L. Chachati, A. Wright, D. Mahvi, F. Lee, and J. Webster, "Hepatic radiofrequency ablation with internally cooled probes: Effect of coolant temperature on lesion size," IEEE Transactions on Biomedical Engineering,, vol. 2003, no. 4, pp. 493–500, 2003.

[32] T. Livraghi, L. Bolondi, L. Buscarini, M. Cottone, A. Mazziotti, A. Morabito, and G. Torzilli, "No treatment, resection and ethanol injection in hepatocellular carcinoma: a retrospective analysis of survival in 391 patients with cirrhosis," Journal of hepatology, vol. 22, no. 5, pp. 522–526, 1995.

[33] H. Bismuth, P. Majno, and R. Adam, "Liver transplantation for hepatocellular carcinoma," Semin Liver Dis, vol. 19, pp. 311–22, 1999.

[34] D. August, P. Sugarbaker, R. Ottow, F. Gianola, and P. Schneider, "Hepatic resection of colorectal metastases," Ann Surg, vol. 201, pp. 210–218, 1985.

[35] R. Poon, S. Fan, and C. Lo, "Improving survival results after resection of hepatocellular carcinoma: a prospective study of 377 patients over 10 years," Ann Surg, vol. 234, pp. 63–70, 2001.

[36] H. Stone, W. Long, R. Smith, and C. Haynes, "Physiologic considerations in major hepatic resections," Am J Surg, vol. 117, pp. 78–84, 1969.

[37] No authors listed, "Primary liver cancers in japan," 1980.

[38] W. Lau, T. Leug, S. Yu, and S. Ho, "Percutaneous local ablative therapy for hepatocellular carcinoma," Ann Surg, vol. 237, no. 2, pp. 171–179, 2003.

[39] N. Saguira and M. Ohto, "Treatment of small hepatocellular carcinoma by percutaneous injection of ethanol into a tumour with real-time ultrasound scanning," Acta Hepatol Jpn, vol. 24, p. 920, 1983.

[40] K. Ohnishi, "Comparison of percutaneous acetic acid injection and percutaneous ethanol injection for small hepatocellular carcinoma," Hepatogastroenterology, vol. 45, no. Suppl. 3, pp. 1254–1258, 1998.

[41] H. Liang, C. Yang, and H. Pan, "Small hcc: safety and efficacy of single high-dose percutaneous acetic acid injection for treatment," Radiology, vol. 214, pp. 769–774, 2000.

[42] J. Baust, A. Gage, H. Ma, and C. Zhang, "Minimally invasive cryosurgery–technological advances," Cryobiology, vol. 34, no. 4, pp. 373–384, 1997.

[43] T. Ravikumar, "Interstitial therapies for liver tumours," Surg Oncol Clin N Am, vol. 5, no. 2, pp. 365–377, 1996.

[44] J. Seifert and D. Morris, "World survey on the complications of hepatic and prostate cryotherapy," World Journal of Surgery, vol. 23, no. 2, pp. 109–114, 1999.

[45] W. Chen, C. Lafon, T. Matula, S. Vaezy, and L. Crum, "Mechanisms of lesion formation in high intensity focused ultrasound therapy," Ultrasonics Symposium 2002. IEEE, vol. 2, pp. 1443–1446, 2002.

[46] G. Vallancien, M. Haroumi, and B. Veillon, "Focused extracorporeal pyotherapy: feasibility study in man," J Endourol, vol. 6, pp. 173–181, 1992.

[47] R. Illing, J. Kennedy, F. Wu, G. ter Haar, A. Protheroe, P. Friend, F. Gleeson, D. Cranston, R. Phillips, and M. Middleton, "The safety and feasibility of extracorporeal high-intensity focused ultrasound (hifu) for the treatment of liver and kidney tumours in a western population," British Journal of Cancer, vol. 93, pp. 890–895, 2005.

[48] H. Parmentier, Melodelima, A. N'Djin, S. Chesnais, Y. Chapelon Jean, and M. Rivoire, "High-intensity focused ultrasound ablation for the treatment of colorectal liver metastases during an open procedure: Study on the pig," Annals of Surgery, vol. 249, pp. 129–136, 2009.

[49] J. McGhana and G. Dodd, "Radiofrequency ablation of the liver: current status," Am J Roentgenol, vol. 176, no. 1, pp. 3–16, 2001.

[50] S. Goldberg, G. Gazelle, E. Halpern, W. Rittman, P. Mueller, and D. Rosenthal, "Radiofrequency tissue ablation: importance of local temperature along the electrode tip exposure in determining lesion shape and size.," Acad Radiol, vol. 3, pp. 212–218, 1996.

[51] T. Aloia, J.-N. Vauthey, and E. Loyer, "Solitary colorectal liver metastasis," Arch Surg, vol. 141, pp. 460–467, May 2006.

[52] L. Blumgart and Y. Fong, Surgery of the liver and biliary tract. WB Saunders Co., 3rd ed., 2000. 1565–1576.

[53] B. Al-Sakere, F. Andre, C. Bernat, E. Connault, P. Opolon, R. Davalos, B. Rubinsky, and L. Mir, "Tumor ablation with irreversible electroporation," PLoS ONE, vol. 2, p. e1135, Nov 2007.

[54] M. Sadiku, Elements of Electromagnetics. Oxford University Press, 3rd ed., 2001. pp.419.

[55] F. Duck, Physical properties of tissue: A comprehensive reference book. New York: Academic, 1990.

[56] F. Incropera and D. DeWitt, Fundamentals of Heat and Mass Transfer. Wiley, 4 ed., 1996.

[57] H. H. Pennes, "Analysis of tissue and arterial temperatures in the resting human forearm," J Appl Physiol, vol. 1, pp. 93–122, 1948.

[58] J. Baish, "Perspectives on recent advances in micro vascular heat transfer," Proceedings of The First Joint BMES/EMBS Conference Serving Humanity. Advancing Technology, 1999. Atlanta. USA.

[59] K. Alexander and P. Clarkson, "A validation model for the medical devices industry," J Eng Design, vol. 13, no. 3, pp. 197–204, 2002.

[60] Medicines and Healthcare Products Regulatory Agency, "Medical devices directive." http://www.mhra.gov.uk/Howweregulate/index.htm, March 2009.

[61] The International Organization for Standardization, "Sterilization of medical devices." http://standards.mackido.com/en/en-standards24_view_6520.html, 2009.

[62] European Committee for Electrotechnical Standardization, "British standard. medical electrical equipment; part 1: General requirements for basic safety and essential performance," Nov 2006. BS EN 60601-1:2006.

[63] R. Nevels, G. Arndt, G. Raffoul, J. Carl, and A. Pacifico, "Microwave catheter design," IEEE Trans Biomed Eng, vol. 45, pp. 885–90, 1998.

[64] B. Lepers, Development of Gas Cooled Applicators for Microwave Ablation. PhD thesis, Department of Physics, University of Bath, July 2008.

[65] A. P. O'Rourke, M. Lazebnik, and J. M. Bertram, "Dielectric properties of human normal, malignant and cirrhotic liver tissue: in vivo and ex vivo measurements from 0.5 to 20 ghz using a precision open-ended coaxial probe," Phys Med Biol, vol. 52, pp. 4707–19, 2007.

[66] J. Bertram, D. Yang, M. Converse, J. Webster, and D. Mahvi, "Antenna design for microwave hepatic ablation using an axisymmetric electromagnetic model," BioMedical Engineering OnLine, 2006. doi:10.1186/1475-925X-5-15.

[67] I. Chang, "Finite element analysis of hepatic radiofrequency ablation probes using temperature-dependent electrical conductivity," BioMedical Engineering OnLine, vol. 2, 2003. doi:10.1186/1475-925X-2-12.

[68] E. Berjano, "Theoretical modeling for radiofrequency ablation: state-of-the-art and challenges for the future," BioMedical Engineering OnLine, vol. 5, 2006. doi:10.1186/1475-925X-5-24.

[69] Micro-Coax, "Semi-rigid coaxial cable." http://www.micro-coax.com/index.asp, 2007. Coaxial cable P/N UT-047C-LL.

[70] MatWeb Material Property Data, "Loctite 638 maximum strength retaining compound." http://www.matweb.com/index.aspx, 2009.

[71] Ansoft, "Simulation software for high-performance electronic design." http://www.ansoft.com/products/hf/hfss/, 2009.

[72] J. Jin, The Finite Element Method in Electromagnetics. Wiley-IEEE Press, 2nd ed., June 2002.

[73] D. Hardie, Non-linear modelling of microwave soft-tissue ablation using the finite element method. PhD thesis, Engineering and Physical Sciences, Heriot-Watt University, Sept 2006.

[74] J. Saxton and J. Lane, "Electrical properties of seawater," Wireless Engineer, pp. 269–275, October 1952.

[75] C. Brace, D. van der Weide, F. Lee Jr., P. Laeseke, and L. Sampson, "Analysis and experimental validation of a triaxial antenna for microwave tumor ablation," IEEE MTTS Int Microw Symp, vol. 3, pp. 1437–1440, June 2004.

[76] R. Nevels, G. Arndt, G. Raffoul, J. Carl, and A. Pacifico, "Microwave catheter design," IEEE Transactions on Biomedical Engineering, vol. 45, pp. 885–890, July 1998.

[77] S. Goldberg, M. Ahmed, G. Gazelle, J. Kruskal, J. Huertas, E. Halpern, B. Oliver, and R. Lenkinski, "Radio-frequency thermal ablation with nacl solution injection: Effect of electrical conductivity on tissue heating and coagulation – phantom and porcine liver study," Radiology, vol. 219, pp. 157–165, 2001.

[78] Precision Extrusion, Inc., "Multi-lumen plastic tubing." http://www.precisionextrusion.com/multilumen.html, 2009.

[79] Zeus, Inc., "Extruded tubing products – multi-lumen tubing." http://www.zeusinc.com/extrusionservices/products.aspx, January 2009.

[80] R. Turovskiy, S. Kim, M. Prakash, and F. Rossetto, "Devices and methods for cooling microwave antennas." http://www.wikipatents.com/ca/2532979.html, July 2005.

[81] E. Rudie and S. Kluge, "Microwave ablation device." http://www.wipo.int/pctdb/en/wo.jsp?IA=US2002029604&DISPLAY=STATUS, March 2003. International Publication Number WO 03/024309 A2.

[82] F. Incropera and D. DeWitt, Fundamentals of Heat Transfer. Wiley, 1981.

[83] Bo'sun Supplies Co., "Stainless steel info. what you need to know." http://www.bosunsupplies.com/StainlessInfo2.cfm, 2008.

[84] Globalspec, "The engineering search engine." http://www.globalspec.com/, 2009.

[85] Y. Wang, Y. Sun, L. Feng, Y. Gao, X. Ni, and P. Liang, "Internally cooled antenna for microwave ablation: Results in ex vivo and in vivo porcine livers," Euro J Radio, vol. 67, pp. 357–361, 2008.

[86] Omega Engineering Limited, "Thermocouple probes and assemblies." http://www.omega.co.uk, April 2009.

[87] Aremco Products, Inc., "High temperature ceramic adhesives and pastes." Technical Bulletin A2, 2006.

[88] Fusion, Inc., "Silver brazing." http://www.fusion-inc.com/silver-brazing.htm, 2008.

[89] H. Wadell, "Volume, shape and roundness of quartz particles," Journal of Geology, vol. 43, pp. 250–280, 1935.

[90] I. Chang and U. Nguyen, "Thermal modeling of lesion growth with radiofrequency ablation devices," BioMedical Engineering OnLine, vol. 3, no. 27, 2004.

[91] COMSOL AB, RF Module User's Guide, 2009.

[92] K. Saito, T. Taniguchi, H. Yoshimura, and K. Ito, "Estimation of sar distribution of a tip-split array applicator for microwave coagulation therapy using the finite element method," IEICE TRANSACTIONS on Electronics, vol. E84-C, no. 7, pp. 948–954, 2001.

[93] COMSOL AB, COMSOL Multiphysics Modeling Guide, 2009.

[94] M. Golriz and B. Sunden, "An analytical-empirical model to predict heat transfer coefficients in circulating fluidized bed combustors," Heat and Mass Transfer, vol. 30, pp. 377–383, September 1995.

[95] D. Mikielewicz, J. Mikielewics, and J. Tesmar, "Improved semi-empirical method for determination of heat transfer coefficient in flow boiling in conventional and small diameter tubes," International Journal of Heat and Mass Transfer, vol. 50, no. 19–20, pp. 3949–56, 2007.

[96] C. Wanga, Y. Hwang, and Y. Lin, "Empirical correlations for heat transfer and flow friction characteristics of herringbone wavy fin-and-tube heat exchangers," International Journal of Refrigeration, vol. 25, pp. 673–80, 2002.

[97] National Physical Laboratory, "Kaye&laby - tables of physical & chemical constants." http://www.kayelaby.npl.co.uk/general_physics/2_3/2_3_6.html, 2008.

[98] Dynamic-Ceramic Ltd., "Dynamic-ceramic technical information series technox zirconia." http://www.dynacer.com/zirconia.htm, 2006.

[99] P. J. Clegg, Microwave Ablation Therapy for Live Cancers. PhD thesis, Department of Physics, University of Bath, 2002.

[100] P. Smith and L. Davis, "Dielectric loss tangent of yttria stabilised zirconia at 5.6 ghz and 77 k," Electronics Letters, vol. 28, pp. 424–25, Feb 1992.

[101] T. Lanagamin, J. Yamamoto, A. Bhalia, and S. Sankar, "The dielectric properties of yttria-stabilized zirconia," Materials Lett, vol. 7, no. 12, pp. 437–440, 1989.

[102] M. Arai, J. Binner, G. Carr, and T. Cross, "High temperature dielectric measurements on ceramics," Dielectric Materials, Measurements and Applications, 1992. University of Nottingham UK.

[103] Accuratus, "Zirconium oxide zro2." http://www.accuratus.com/zirc.html, 2005.

[104] T. Ramachandran, K. Sreenivasan, and R. Sivakumar, "Water vaporization from heated tissue: an in vitro study by differential scanning calorimetry.," Lasers Surg Med, vol. 19, pp. 413–5, 1996.

[105] P. Morris, Nuclear Magnetic Resonance Imaging in Medicine and Biology. Oxford: Oxford University Press, 1986. 256–260.

[106] D. Yang, Measurements, Antenna Design and Advanced Computer Modeling for Microwave Tissue Ablation. PhD thesis, Electrical Engineering, University of Wisconsin-Madison, 2005.

[107] D. Haemmerich, "In vitro measurements of temperature-dependent specific heat of liver tissue.," Med Eng Phys, vol. 28, pp. 194–197, 2006.

[108] C. Simon and D. Dupuy, "Percutaneous minimally invasive therapies in the treatment of bone tumors : Thermal ablation," Seminars in musculoskeletal radiology, vol. 10, no. 2, pp. 137–144, 2006.

Appendix A

Engineering Drawings of First Applicator Design Components

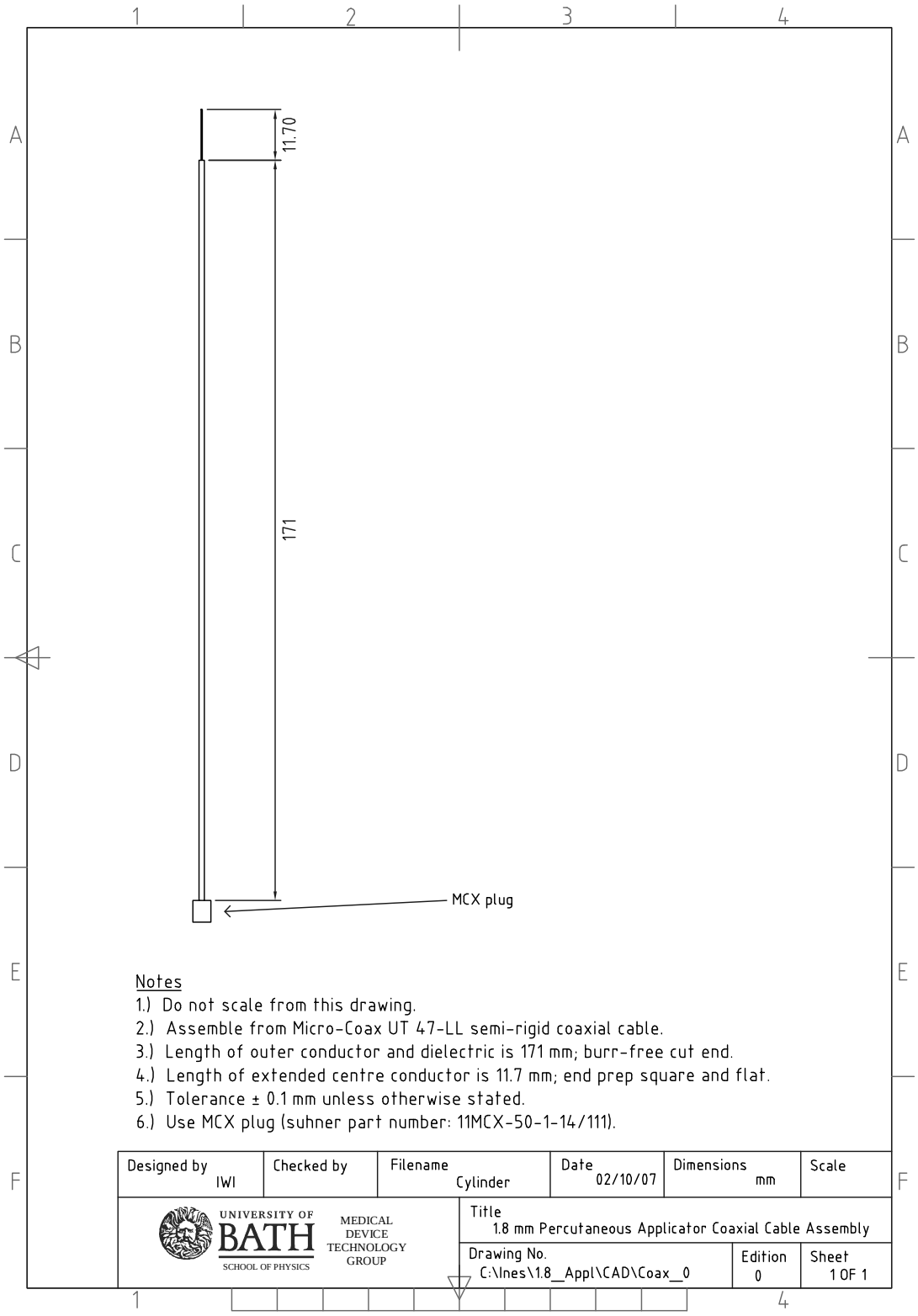

Figure A.1: Drawing of customised semi-rigid coaxial cable for first applicator manufacture.

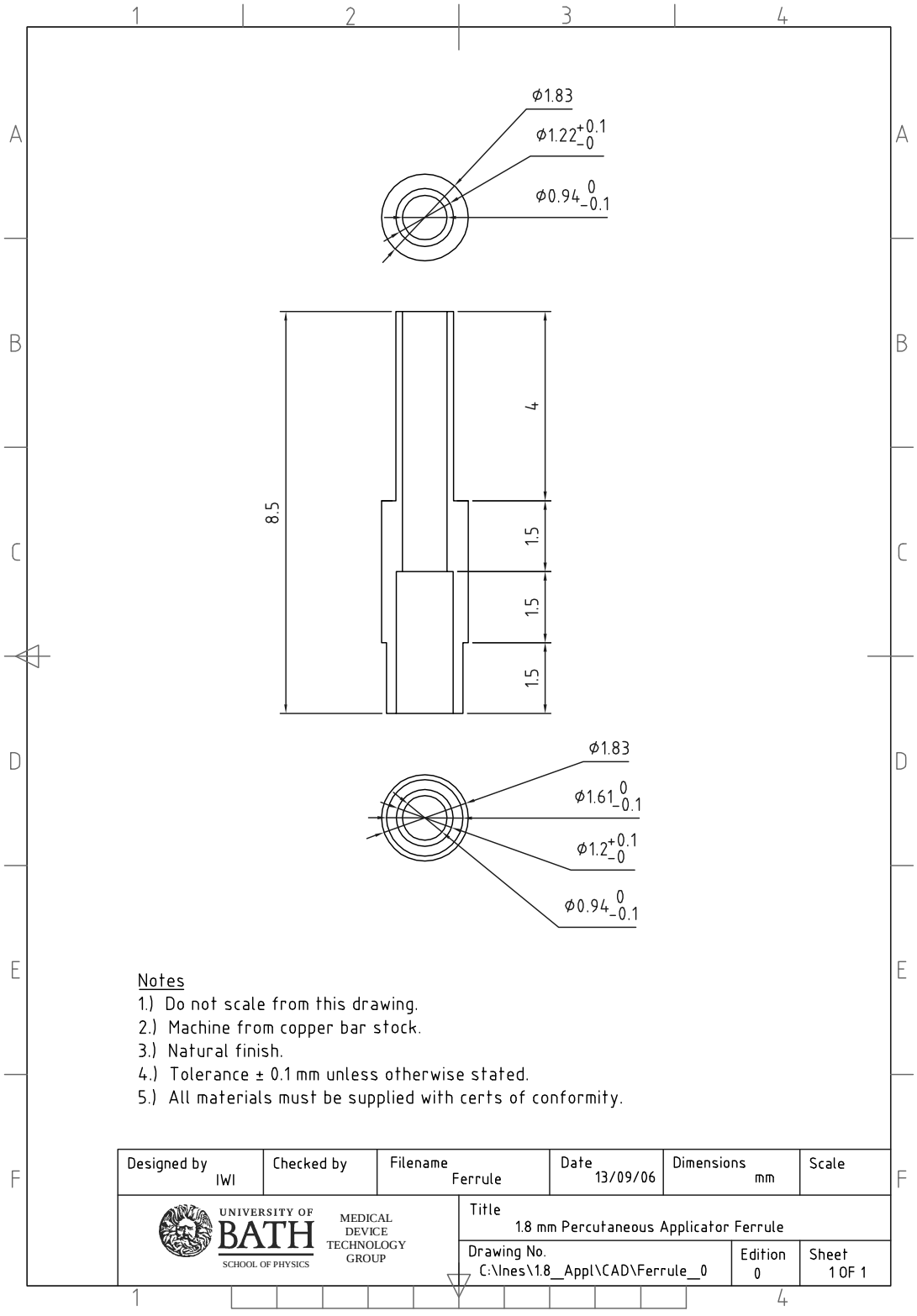

Figure A.2: Drawing of ferrule for first applicator manufacture.

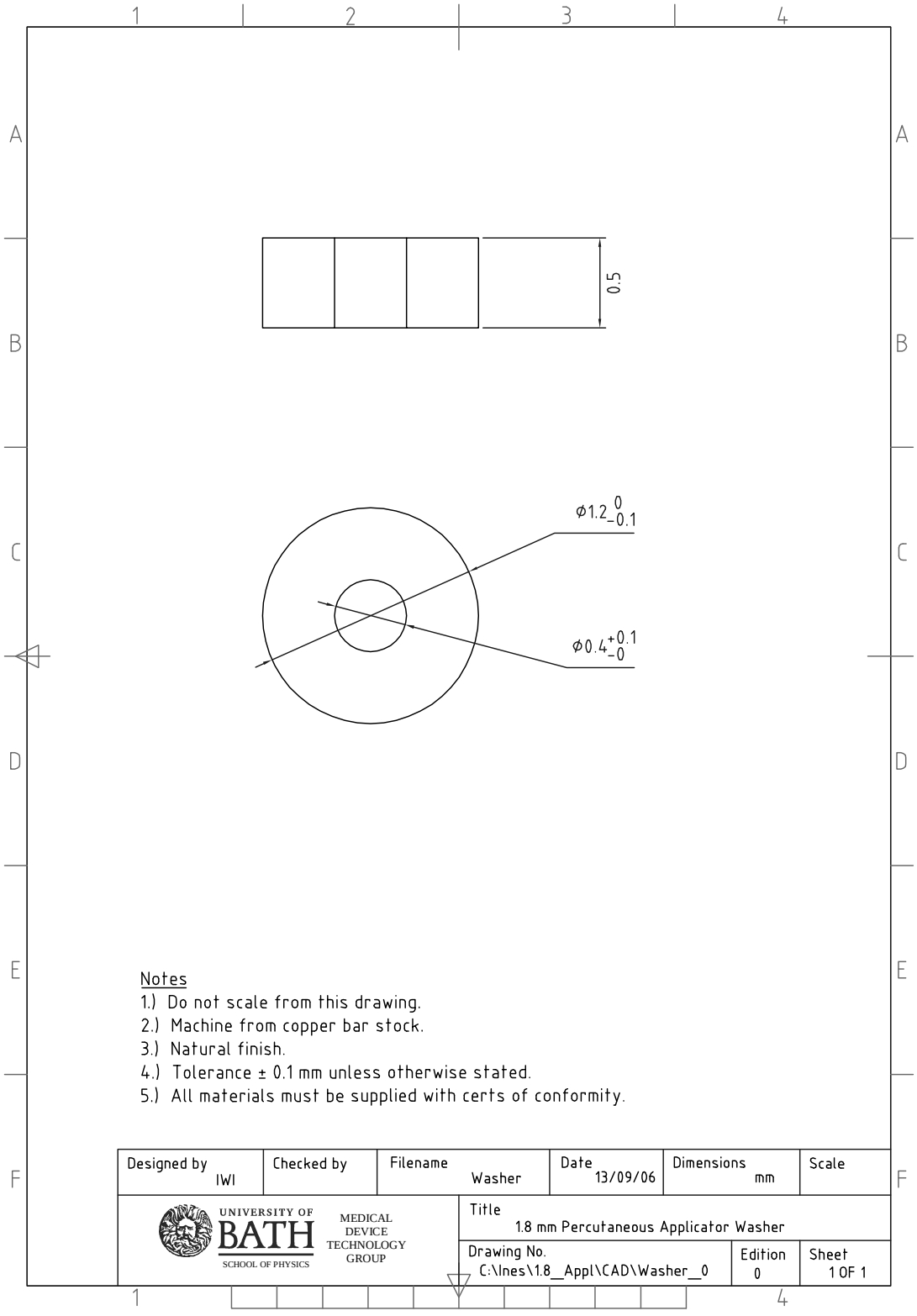

Figure A.3: Drawing of washer for first applicator manufacture.

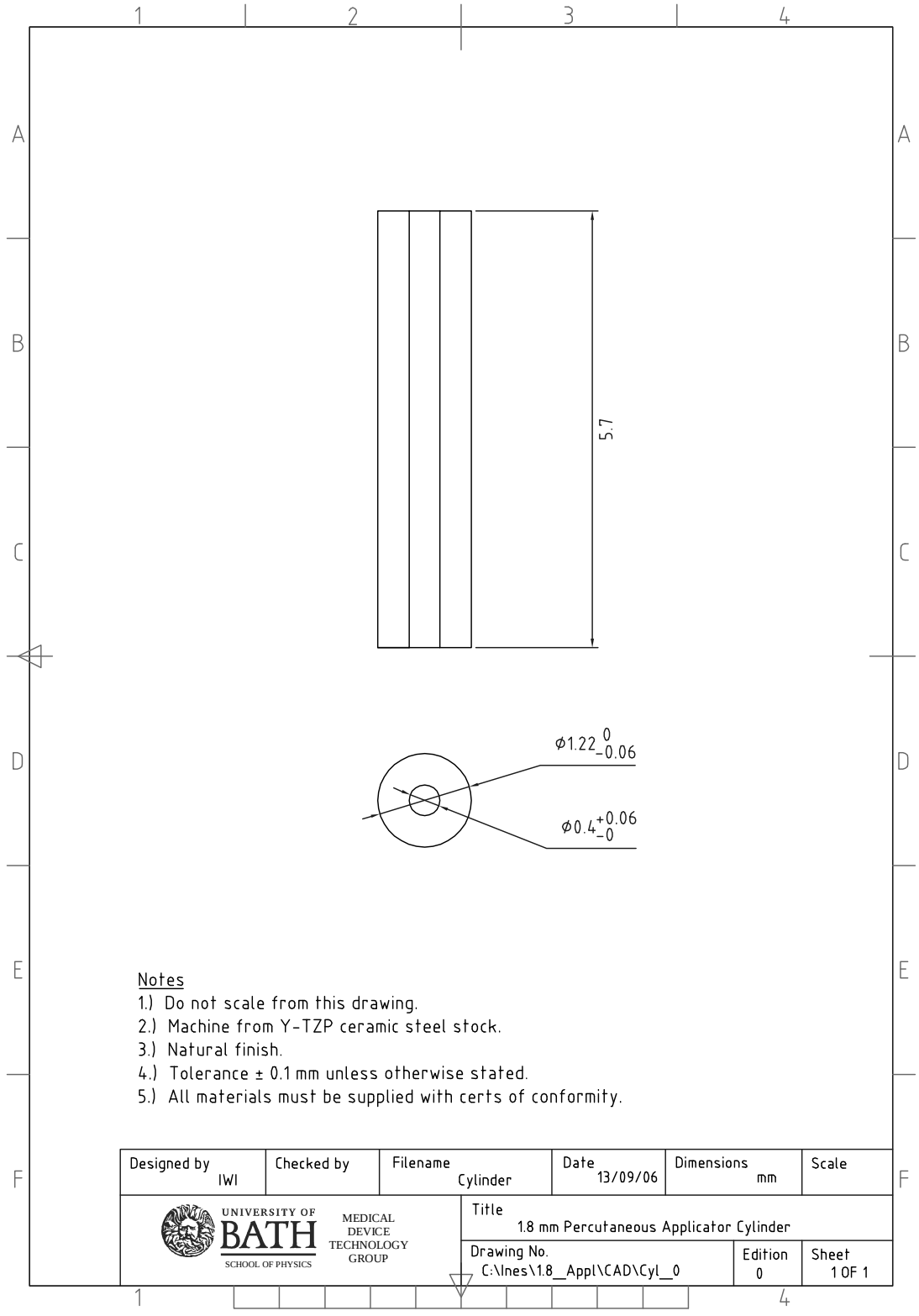

Figure A.4: Drawing of cylinder for first applicator manufacture.

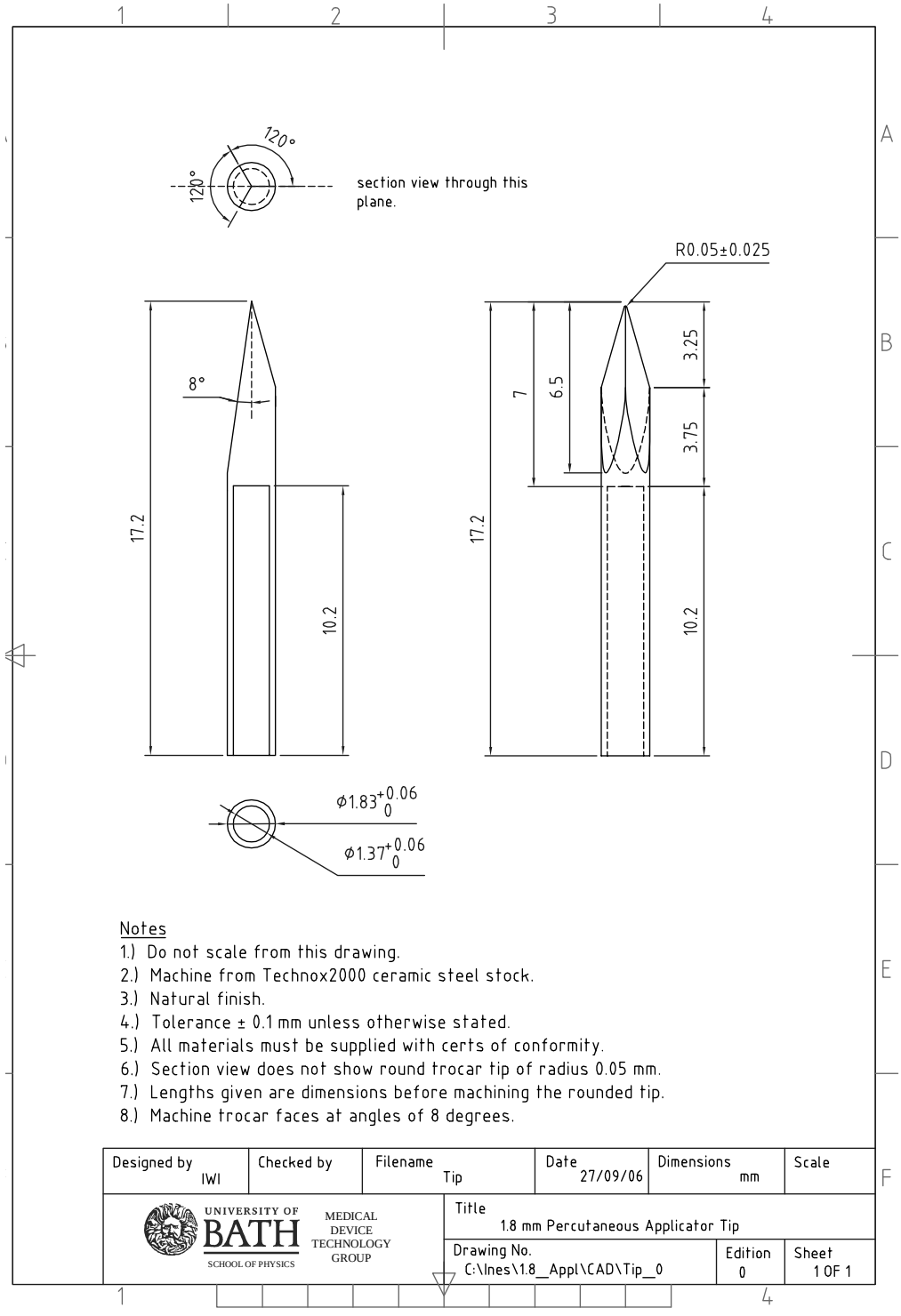

Figure A.5: Drawing of tip for first applicator manufacture.

Appendix B

Assembly Procedure of First 1.8 mm Applicator

1. Check fits of:
   (a) Shaft – coax
   (b) Coax – ferrule
   (c) Shaft – ferrule
   (d) Ferrule +cylinder + washer – tip
2. Drill holes in stainless steel tube (0.5 mm diameter, 2 - 4 holes), widen inside diameter.
3. Machine seal rings for input and output of handle.
4. Degrease ferrule, cylinder, washer, and tip in ultrasonic bath:
   (a) TCE (1-2 min)
   (b) A (1-2 min)
   (c) IPA (1-2 min)
5. Slip both handle parts over coax cable.
6. Degrease shaft with A, I and encase coax cable with stainless steel shaft.
7. Solder ferrule:
   (a) Degrease (A,I) end of coax cable.
   (b) Slide ferrule onto outer conductor of coax.
   (c) Slightly pull back ferrule. Apply solder paste accurately with a needle all the way around. Leave no gaps.
   (d) Push ferrule in place
   (e) Keeping ferrule and coax pressed together, melt solder paste by passing with flame of 'micro jet'. Wait briefly to cool down.
   (f) Check solder joint under microscope - has all solder melted, are there any visible gaps? It is very important that there are no gaps as the seal has to be water-tight. If necessary, add a little solder paste and reheat. Take great care not to overheat cable PTFE.
8. Glue cylinder to centre conductor. Apply glue to centre conductor sparing the top 1 mm where the washer will be soldered to. Slide cylinder over centre conductor checking that no glue is squeezed into the ferrule.
9. Solder washer:

(a) Slide ceramic cylinder over centre conductor.
(b) Apply solder paste into central hole of washer using a needle.
(c) Slip washer on end of centre conductor with burred side facing up (level side facing down), sitting on cylinder.
(d) Carefully melt solder paste using the same torch 'micro jet'. Leave to cool down.
(e) Check solder joint by applying medium force on washer trying to pull it off.

10. Glue joint tip:
    (a) Degrease distal end of applicator assembly (A, I).
    (b) Dry with heat gun level 1 - take care that all is dry (inside cylinder tec.).
    (c) Apply Loctite 638 to all surfaces - top of washer, sides of cylinder and ferrule and sparingly inside tip.
    (d) Slide tip over applicator end in a rotating manner and as far as possible.
    (e) Wipe off any excess glue. Do not pull back tip any length.
11. Glue joint shaft. Also glue shaft to ferrule using Loctite 638 (take care not to block any holes in the shaft) and cure together (40 °C for 1 hour).
12. Handle
    (a) Unscrew handle. Apply metal loaded epoxy to the screw thread with a needle. Screw handle together and wipe off any excess glue.
    (b) Apply metal loaded epoxy to the connector of coax cable and slide handle onto it. Press and wipe off excess glue.
    (c) Apply metal loaded epoxy or epoxy glue to the thread of a shortened lock connector and screw tightly onto handle. Wipe off any excess glue.
    (d) Check if little plastic ring (machined) fits over stainless steel shaft and inside the top end of the handle on spare parts. Then, slide the ring over the shaft in place.
    (e) Mask off shaft and handle with tape.
    (f) Mix 'blue rubber' (silicone):
        i. Spoon a spatula of white rubber into a small container.
        ii. Mix well for some minutes with a much smaller amount of blue hardener to get a pale blue mixture.
        iii. Apply glue to shaft at a distance of roughly 1 cm above the beginning of the handle. Leave to run down into place.
        iv. During the first hour, leave to air cure (alternatively use heat gun for approximately 1 min) taking care all air bubbles forming in the glue are destroyed by piercing with needle.
    (g) Remove masking tapes.
    (h) Cure metal loaded epoxy at 110 °C for 1 hour.
13. Degrease shaft with A,I. Mask off cooling holes in shaft.
14. Coating with silicone (NuSil Med10-6607)
    (a) Dip applicator NuSil silicone primer (clear) SP-120 for some seconds.
    (b) Air-dry for 1 min (inside fume cupboard).
    (c) Dip in silicone.
    (d) Retreat out and let silicone drip off.
    (e) Then turn and leave to dry for about 8 hours (inside fume cupboard).
    (f) Cut out masking tape.

Adhesives, solder, and coating:

1. Paste solder (MP 180 °C).
2. Cyanoacrylate retaining compound (Loctite 638 – green)
3. Metal loaded epoxy (Permabond Bondmaster ESP110 – silver)
4. Medical grade silicone dispersion coating (NuSil MED-6607)

Appendix C

Electroplating

Copper plating of the stripped end (3 mm to 5 mm) of a 0.2 mm diameter constantan wire was performed as follows:

1. Equipment and materials needed:
   (a) Copper Sulphate $CuSO_4$
   (b) deionised water
   (c) 2 copper pieces acting as anode and cathode
   (d) DC Voltage source
   (e) Lead wires with alligator clips
   (f) Multimeter
2. Mix plating solution with concentration of 200 g/l $CuSO_4$ and 5 g/l H_2SO_4.
3. Quantities for a beaker filled with 100 ml DI water: 20 g $CuSO_4$; no H_2SO_4 was added.
4. Connect large surface area load in parallel, thus plating both items at the same time.
5. Connect positive pole of DC voltage source to parallel load part one; the negative pole to back end of constantan wire and parallel load part two.
6. Stir solution. Insert cathode and anode so that they do not contact each other directly. Immerse wire enough to just submerse bare constantan end.
7. Trial plating of wires:
   (a) Wire 2 plated with I = 150 mA for about 3 1/2 hours.
   (b) Plate new wire (wire 3) with 150 mA for 1 h. Finished (diameter 0.45 mm).
   (c) Decrease current to 100 mA to allow for smaller grain sizes thus increasing the plating time. Plate wire 4. Plate for 1 h 10 min; over plated (OD 0.45-0.5 mm); sand down to OD 0.40-0.44 mm.
   (d) Wire 5; 100 mA; 30 min.

Appendix D

Assembly of Prototype 1

1. Stainless steel tube (part 1):
   (a) Widen distal tube opening to create fit over ferrule. Use 1.6 mm diameter drill.
   (b) Mark positions of centres of three holes serving as inlets, and positions of part 10 and 11 on tube using a scribe (measure distances from proximal end of tube (1):
      i. Hole 1 at 17 mm
      ii. Hole 2 at 19 mm
      iii. Hole 3 at 21 mm
      iv. Part 10 from 2 to 10 mm
      v. Part 11 from 25 to 30 mm
   (c) Position tube (1) in vee-block and drill holes at marked positions with 0.8 mm drill.
2. Ferrule (part 2) and washer (part 5):
   (a) De-burr interior face of ferrule by drilling through with 0.9 mm drill (ID ferrule: 0.94 mm; 1.2 mm).
   (b) De-burr and clean up manually with smaller drill.
   (c) De-burr washer if necessary using a scalpel or fine file.
3. Check fits of:
   (a) Ferrule – semi-rigid coaxial cable (part 3; referred to as 'coax')
   (b) Ferrule/coax – cylinder/washer/tip.
   (c) Ferrule – Shaft
4. Degrease coax with A (Acetone) and IPA (Isopropanol).
5. Degrease ferrule, cylinder, washer (placed on jig to avoid losing), and tip (placed on jig to prevent damage due to knocks with glass wall) in ultrasonic bath:
   (a) TCE (1-2 min)
   (b) A (1-2 min)
   (c) IPA (1-2 min)
6. Keep in separate container filled with IPA for short-term storage.
7. Joint 1 (solder paste 121 (MP 221 C) ; ferrule – coax):
   (a) Take out ferrule and blow dry for approx. 1 min using a heat gun (low level).
   (b) Check fit of ferrule to coax.

(c) Apply solder paste around distal end of outer conductor of coax over a length of 1mm. Push on ferrule.
(d) Carry out solder joint by gripping the coax with soldering tweezers close to joint and gently press down ferrule with a pair of tweezers. Keep still and apply power (30-40 W) until solder has melted completely. This should take a few seconds only. If soldering process takes more than 3 to 4 seconds, stop and repeat with a slightly higher power level.
(e) Once cooled check solder joint under microscope for gaps, impurities, or unsoldered parts.
(f) Ensure that entire solder joint is of high quality as it must remain watertight under pressures of 2-3 bar.
(g) Remove flux from solder joint by dipping the ferrule into IPA and manually cleaning the outside.
(h) Oven-dry at 85 °C for approximately 5 min.

8. Joint 2 (Permabond Bondmaster ESP110; silver; washer – centre conductor):
   (a) Take out cylinder, washer, and tip. Blow dry as before.
   (b) Thread cylinder on centre conductor followed by washer.
   (c) On top of cylinder, hold washer using precision tweezers. Apply a very small amount of adhesive onto the centre of the washer using a scalpel. Wipe off any excess adhesive with the scalpel blade.
   (d) Oven-cure for 30 min at 150 °C.
9. Joint 3 (HT epoxy; ferrule – tip):
   (a) Carefully roughen surface of distal end of ferrule with emery paper. Pay attention not to allow particles enter into the applicator through either the cylinder-ferrule or the ferrule-washer interface.
   (b) Clean with IPA. If IPA went inside applicator, oven-dry for approximately 5 min at 85 C.
   (c) Meanwhile, mix HT epoxy (mix resin and hardener 1:1 by weight).
   (d) Apply epoxy evenly around half to $\frac{3}{4}$ of circumference of distal end of ferrule using a small wire (e.g. 0.13 mm), leaving a gap for air to escape from the bottom of the tip when pushing on tip.
   (e) Slide on tip without rotating so as to not destroy air path.
   (f) Place assembly in oven set to 100 °C for 2-3 min.
   (g) If possible inside oven, rotate tip clock-wise and anti-clock-wise a few times. Fill up gap between ferrule and tip with more adhesive.
10. Cure 1 (joints 2 and 3): Cure at 163 °C for at least 2 hours.
11. Constantan wire (part 7):
   (a) Use enamelled constantan wire (0.17 mm diameter; OD with enamel 0.2 mm).
   (b) Cut to a length of 2 m.
   (c) Inspect the entire length of wire for defects in the enamel.
   (d) Remove enamel over a length of 3 mm at the distal end of the wire using a scalpel or sharp tweezers. Remove enamel at proximal end of wire over a length of a few centimetres.
   (e) Plate the bare constantan wire with copper (see C) until the plating reaches a diameter of 0.4 mm, slightly smaller than the diameter of the small stainless steel tube (part 8) of 0.457 mm (26 gauge).

(f) Once finished ensure that plating does not chips off.
(g) Carefully straighten the wire by hand. Do not insert into tube (1) yet.

12. Small stainless steel tube (part 8):

(a) Lay both tubes (1 and 8) next to each other so that distal end of tube (1) protrudes by 8 mm (5 mm plus plated length of 3 mm). Mark location of proximal end of tube (1) on small tube (8) using a 2 mm wide thin tape so that the distal end of tube is aligned with mark made.
(b) Cut tube (8) at proximal end of tape, i.e. approximately 2 mm behind the mark from 12.a. using a small square file (length should be 144 mm - check if correct). Start filing using an edge of the file until half way through tube (8), then break off tube by hand. Sand down break point.
(c) Insert wire (7) into small tube (8) starting with proximal end of wire and distal end of tube. Feed wire through until plating is in contact with distal end of small tube.
(d) Assembly acts as a thermocouple and is referred to as 'thermocouple' in the remainder of the document.

13. Deformation:

(a) Insert jaws into vice. Position spacer (spacer 1) in the centre and between the jaws plus a second thinner spacer (spacer 2) on top of spacer 1.
(b) Place stainless steel tube (1) on top of both spacers with holes facing up and exposing distal end of tube by 5mm.
(c) Keeping horizontally aligned, twist tube (1) clockwise by 45 . Check position and alignment. Then, close vice just enough to take hold of the tube.
(d) Remove spacer 2 and start closing the vice slowly. Continue squeezing until spacer 1 impedes any further turns.
(e) Insert coax into tube beginning at distal end of tube and with proximal end of coax until ferrule touches distal end of tube - do not leave any space between ferrule and tube.
(f) Release coax so that it arranges itself at the bottom of the tube.
(g) Take hold of the small tube thermocouple (7 and 8) with the left hand. With right hand fixate coax in its position at the bottom of the tube. Start introducing distal end of thermocouple in proximal end of tube (1). Continue insertion of thermocouple sliding along the top of the coax until the marking tape is in direct contact with the proximal end of the tube (1).

14. Joint 6 (Loctite 638; ferrule – stainless steel tube):

(a) Apply adhesive using a needle around proximal end of ferrule (2) in order to form joint 6. Ensure that adhesive is applied evenly as this joint must provide a watertight seal under pressures of 2-3 bars.
(b) Hold both coax (3) and thermocouple (7 and 8) with left hand and tip with right hand. Simultaneously, pull with left hand and push with right, shifting ferrule inside distal end of tube (1) thus forming adhesive joint 6.
(c) If necessary, straighten tip carefully by hand.
(d) Release vice, take out applicator assembly, and wipe off any excess adhesive.
(e) Check that the positions of the inlet holes in tube (1) are located correctly to form inlet for one channel but not the other channel. Cooling channels must be isolated from each other. Remove tape.

(f) Leave to air-dry for 30 min.

15. MCX Connector (part 9):

    (a) Send off applicator assembly to Rhophase to fit MCX connector.
    (b) Upon return, connect carefully to flexible cable and check S11 on network analyser:
        i. S11 for applicator and cable: -25 dB
        ii. S11 for applicator (use gating): -18 dB
    (c) Length of semi-rigid has changed compared to drawing! Update drawing accordingly for next assembly.

16. Joints 7and 8 (Permabond Bondmaster ESP110; silver; parts 10 and 11 – tube (1)):

    (a) Degrease applicator with A + IPA.
    (b) Apply just enough adhesive on tube (1) at marking made for part 10. Slide part 10 over distal end of applicator assembly and twist in correct position. Be careful not to block the cooling channels.
    (c) Repeat process for part 11.
    (d) Check position of parts relative to handle parts 19 and 20.
    (e) For this applicator 1, parts 10 and 11 had to be moved back by 1.5 mm to allow correct position of spider.
    (f) Problem: proximal end of part 10 now level with end of tube (1) - danger of blocking cooling channel with adhesive applied for fixing part 10.
    (g) Oven-cure for 30 min at 130 °C. Lie horizontally.
    (h) Once cured, check joints. If necessary, fill any gaps with permabond and cure with silicone in the next step.

17. Coating 1 (NuSil MED10-6600 silicone dispersion; applicator):

    (a) Degrease applicator with A + IPA.
    (b) Mask off part 11 with high temperature masking tape.
    (c) Dip applicator in silicone primer (NuSil SP-120) until approximately 1 cm to part 11. Air-dry for 1-2 min.
    (d) Thoroughly stir individual components prior to addition to ensure homogeneity.
    (e) Mix part A and B 1:1 by weight in appropriate dish. Stir well.
    (f) Dip applicator into dish and turn to ensure full coating.
    (g) Remove and hold up side down for approximately 1 min to drain silicone. Once silicone stopped dripping, turn applicator upright and place in holder.
    (h) Cure at:
        i. 25 °C for 30 min
        ii. 75 °C for 45 min
        iii. 150 °C for 10 h (applicator 1: 16 h)

18. Joint 9 (solder wire with MP 130 °C (Omega; Combined Precision Components; Alloy; 63/37-AP; Flux); copper wire - outer conductor):

    (a) Centred between proximal end of tube (1) and MCX connector (9), solder enamelled copper wire (diameter 0.4 mm bare) and length 2 m (part 12) to outer conductor of coax using low temperature solder wire and resistance soldering tweezers.
    (b) Once cooled, twist copper and constantan wires into a twisted wire pair.

19. Joint 10 (Permabond Bondmaster ESP110; silver; cooling channel):
    (a) Under the microscope, seal off cooling channel at the proximal end of the tube (1) with permabond using a fine needle. Ensure that the channel to be sealed is the one with the three holes.
    (b) Oven-cure for 45 min at 150 °C.

    HANDLE AND FLEXIBLE CABLE ASSEMBLY

    Note: Difficulties in handle assembly of applicator 1 due to tight fits of aluminium collars (parts 10 and 11) and spider (part 18) to handle pieces (parts 19 and 20). Widening of holes in handle parts 19 (with 10 mm and 5 mm diameter drills) and 20 (with 4 mm drill) might relieve assembly in future cases. Also, a suitable epoxy could be used instead of loctite 638 as it:
    (a) Would allow time to correct relative position of parts.
    (b) Had gap filling properties.
    (c) Would not spoil appearance of handle if clear/yellow in colour.
20. Check fits of all handle parts:
    (a) Tight fits of aluminium collars (parts 10 and 11) and spider (part 18) to handle pieces (parts 19 and 20). Widen or de-burr holes in handle part 19 with 10 mm and 5 mm diameter drills, part 20 with 4 mm drill.
    (b) Roughen all glue joint surfaces with emery paper.
    (c) Clean plastic handle parts in warm soapy solution.
    (d) Roughen surface of spider; degrease.
21. Joint 11 (Permabond Bondmaster ESP110 + Loctite Superflex Sealant; aluminium ring – connector):
    (a) Degrease back end of connector and aluminium cylinder (part 14); clean flexible cable.
    (b) Apply permabond adhesive around connector on proximal end of flexible cable. Slide aluminium cylinder (part 14) onto connector. Remove any excess glue.
    (c) Oven-cure at 150 °C for 45 min.
    (d) Apply silicone around distal end of aluminium cylinder (14) - not onto sides - to create a watertight seal.
    (e) Oven-cure at 90 °C for 30 min. Full cure after 24 hours at RT.
22. Joint 12 (Loctite 480; exit manifold – connector):
    (a) Apply loctite 480 around aluminium cylinder (part 14) and back end of connector. Thread exit manifold (part 15) over flexible cable assembly onto back of connector.
    (b) Clamp/hold for 2 min without moving.
    (c) Oven-cure at 80 °C for 30 min.
23. Mark positions of following parts on flexible cable, measured from the proximal end of the connector (of length 12 mm):
    (a) Distal end of part 17: 4.5 mm.
    (b) Proximal end of spider (part 18): 2.5 mm.
    (c) Distal end of heat shrink tubing: 12.5 mm.
24. Joint 13 (Loctite Superflex Sealant; heat shrink – exit manifold):

(a) Cut heat shrink tubing (part 16) to length of 960 mm (length needed in shrunk state is 962.5 mm, corresponding to 948.3 mm unshrunk).
(b) Feed flexible cable and wire plus cord (for pulling back thermocouples wires later) through heat shrink using a tube of right size to ease insertion. Remove guiding tube.
(c) Slide collar (17) onto flexible cable.
(d) Connect thermocouple wires to cord and pull back through collar, heat shrink and out through exit in exit manifold.
(e) Apply silicone paste around socket of part 15.
(f) Shrink proximal end of heat shrink onto silicone using a heat gun set to low heat. Pay attention to not melt plastic handle part (melting point: 100 °C).
(g) Continue to shrink heat shrink moving towards distal end. Discontinue approx. 5 to 10 cm before the distal end leaving the last section unshrunk.
(h) Check whether marking made on flexible cable can be seen. If not, trim back heat shrink carefully until marking is revealed.

25. Joint 14 (Loctite Superflex Sealant; heat shrink – part 17):

(a) Apply silicone around socket of part 17 and slide into heat shrink so that distal end of part 17 is level with marking made on flexible cable. Fasten to keep relative alignment.
(b) Complete shrinking tubing onto part 17. Ensure position of part 17 is correct concerning the marking, i.e. a small gap between the shoulder of part 17 and the beginning of the heat shrink is acceptable.
(c) Note for Applicator one: Heat shrink was to short, slipped off part 17. Forced part 17 lined with superglue back into heat shrink; protect with second layer of (larger) heat shrink.

26. Joints 15 and 16 (Loctite Superflex Sealant; MCX connectors – spider):

(a) Degrease MCX connectors.
(b) Slide spider onto MCX connector of applicator (part 9) and connect to MCX connector of flexible cable assembly (13) inside spider.
(c) Take up slack of twisted wire pair.
(d) Apply silicone inside void in proximal end of spider and slide spider in place, aligning with mark on flexible cable.
(e) Fill up distal space with silicone.
(f) Fasten and leave to air cure for 24 hours.
(g) Note: Silicone joint does not harden but remains flexible; might cause problems when trying to push on outer handle part 19.

27. Joints 17, 18, and 19 (Loctite 480; part 17 – part 19, 18 – 19, and 10 – 19):

(a) Check fit of part 19 and 20 onto 9, 10, and 11 (use spare parts).
(b) Apply adhesive around distal end of part 17, sparingly on the outside faces of spider. Also apply adhesive extremely sparingly on part 10 since any excess adhesive will be push towards end of tube (1) potentially blocking the cooling channels.
(c) Carefully push part 19 into position, keeping the assembly up side down.
(d) Wipe off any excess adhesive on the outside.
(e) Air-dry for 2 min.

(f) Note: Difficulty in assembly of applicator 1. Additional problem in that once part 19 is in place there is no means to check if channels got blocked or silicone joint in spider has broken or torn.

28. Joints 20 to 23 (Loctite 480; part 19 – part 20, and 11 – 20):
    (a) Apply adhesive around distal end of part 19 and sparingly on part 11.
    (b) Slide part 20 over applicator and into position. Wipe off excess adhesive.
    (c) Air-dry for 2 min.
    (d) Keep up side down to air-dry for 24 hours.

Adhesives:

1. High temperature (MP221 °C) solder paste (Indium Corp. Ind. 121 alloy 96.5Sn 3.5Ag Lot PS18176)
2. Metal loaded epoxy (Permabond Bondmaster ESP110 – silver)
3. High temperature epoxy (Aremco-Bond 526N-C Lot526N-C-1070)
4. Cyanoacrylate retaining compound (Loctite 638 – green)
5. Low temperature solder (CPC Omega alloy 63/37-AP Part SD00146 Batch CS78-01)
6. Silicone sealant (Loctite Superflex – clear)
7. Toughened cyanoacrylate (Loctite 480 toughened – black)